IRAQI JOURNAL OF APPLIED PHYSICS

The *Iraqi Journal of Applied Physics (IJAP)* is a peer reviewed journal of high quality devoted to the publication of original research papers from applied physics and their broad range of applications. IJAP publishes quality original research papers, comprehensive review articles, survey articles, book reviews, dissertation abstracts in physics and its applications in the broadest sense. It is intended that the journal may act as an interdisciplinary forum for Physics and its applications. Innovative applications and material that brings together diverse areas of Physics are particularly welcome. Review articles in selected areas are published from time to time. It aims to disseminate knowledge; provide a learned reference in the field; and establish channels of communication between academic and research experts, policy makers and executives in industry, commerce and investment institutions. IJAP is a quarterly specialized periodical dedicated to publishing original papers, letters and reviews in: Applied & Nonlinear Optics, Applied Mechanics & Thermodynamics, Digital & Optical Communications, Electronic Materials & Devices, Laser Physics & Applications, Plasma Physics & Applications, Quantum Physics & Spectroscopy, Semiconductors & Optoelectronics, Solid State Physics & Applications, Alternative & Renewable Energy, and Environmental Science & Technology. Sub-disciplines include Dielectrics, ferroelectrics, and multiferroics; Electrical discharges, plasmas, and plasma-surface interactions; Emerging, interdisciplinary, and other fields of applied physics; Energy and Sustainability; Magnetism, spintronics, and superconductivity; Organic-Inorganic systems, including organic electronics; Photonics, plasmonics, photovoltaics, optical phenomena, materials, and metamaterials; Physics of devices and sensors; Physics of materials, including electrical, thermal, mechanical and other properties; Physics of matter under extreme conditions; Physics of nanoscale, 2D materials, and low-dimensional systems; Physics of semiconductors; Quantum technology; Soft matter, fluids, and biophysics; Thin films, interfaces, and surfaces.

ISSN (Print): 1813-2065, ISSN (Online): 2309-1673

EDITORIAL BOARD

Editorial Office:
P. O. Box 88052, Baghdad 12631, IRAQ
Mobile: +964 7832 360 114 (Telegram, Viber, WhatsApp)
Website: www.ijap-iq.com
Emails: info@ijap-iq.com, editor_ijap@yahoo.co.uk, ijap.editor@gmail.com

ADVISORY BOARD

SPONSORED AND PUBLISHED BY
AMERICAN QUALITY FOR SCIENTIFIC PUBLISHING INC.
1479 South De Gaulle Ct, Aurora, CO 80018, United States

IRAQI JOURNAL OF APPLIED PHYSICS

INSTRUCTIONS TO AUTHORS

CONTRIBUTIONS

Contributions to be published in this journal should be original research works, i.e., those not already published or submitted for publication elsewhere, individual papers or letters to editor.
Manuscripts should be submitted to the editor at the mailing address:

Iraqi Journal of Applied Physics, Editorial Board, P. O. Box 88052, Baghdad 12631, IRAQ
Mobile: +964 7832 360 114 (Telegram, Viber, WhatsApp)
Website: www.ijap-iq.com
Email: info@ijap-iq.com, editor_ijap@yahoo.co.uk, ijap.editor@gmail.com

MANUSCRIPTS

Two hard copies or a soft Word copy on a CD or DVD should be submitted to the Editor in the following configuration:

- **One-column** Double-spaced one-side A4 size with 2.5 cm margins of all sides
- Times New Roman font (16pt bold for title, 14pt bold for names, 12pt bold for headings, 12pt regular for text)
- Manuscripts presented in English only are accepted.
- English abstract not exceed 150 words
- 4 keywords (at least) should be maintained on (PACS preferred)
- Author(s) should express all quantities in SI units
- Equations should be written in equation form (*italic* and symbolic) NOT in plain text
- Tables and Figures should be separated from text and placed in new pages after the references
- Charts should be indicated by the software used for generating them (e.g., Excel, MATLAB, Grapher, etc.)
- Figures and diagrams can be submitted in original colored forms for assessment and they will be returned to authors after provide printable copies
- Only original or high-resolution scanner photos are accepted
- For electronic submission, articles should be formatted with MS-Word software
- Figures, charts, photos, images or pictures **SHOULD NOT** be grouped in Word file
- Figure caption should be written as plan text **NOT** inside a text box

AUTHOR NAMES AND AFFILIATIONS

It is IJAP policy that all those who have participated significantly in the technical aspects of a paper be recognized as co-authors or cited in the acknowledgments. In the case of a paper with more than one author, correspondence concerning the paper will be sent to the first author unless staff is advised otherwise.
Author name should consist of first name, middle initial, last name. The author affiliation should consist of the following, as applicable, in the order noted:
- Company or college (with department name or company division), Postal address, City, Governorate or State, zip code, Country name, contacting telephone number, and e-mail

REFERENCES

The references should be brought at the end of the article, and numbered in the order of their appearance in the paper. The reference list should be cited in accordance with the following examples:

[1] F.H. Al-Berkdar, D.N. Raouf and F.H. Hamza, “A Line Tuned TEM_{00} Mode CW CO_2 Laser”, *Iraqi J. Appl. Phys.*, 1(1) (20025) 8-10.
[2] W. Demtröder, **“Atoms, Molecules, and Photons”**, Springer-Verlag (Berlin, 2006), Ch. 4, p. 130.
[3] Y. Lee, S.A. Korpela and R. Horne, "Structure of Multi-Cellular Natural Convection in a Tall Vertical Annulus", Proceedings of 7th International Heat Transfer Conference, U. Grigul et al., eds., Hemisphere (NY), 2 (1982) 221–226.
[5] M. Hashish, "Waterjet Technology Development", High Pressure Technology, PVP-Vol. 406 (2000) 135-140.
[6] D.W. Watson, "Thermodynamic Analysis", ASME Paper No. 97-GT-288 (1997).
[7] Z. Cheng, "Vibrational Discrete Action Theory", Ph.D. thesis, Columbia University, USA (2021).

PROOFS

Authors will receive proofs of papers and are requested to return one corrected copy as a WORD file on a compact disc (CD) or by email. New materials inserted in the original text without Editor’s permission may cause rejection of paper unless the handling editor is informed.

COPYRIGHT FORM

Author(s) will be asked to sign the IJAP Copyright Form and hence transfer copyrights of the article to the Journal soon after acceptance of it. This will ensure the widest possible dissemination of information.

OFFPRINTS

Authors will receive electronic offprint free of charge and any additional reprints can be ordered.

SUBSCRIPTION AND ORDERS

Annual fees (4 issues per year) of subscription are:
50 US$ for individuals inside Iraq; **200** US$ for institutions inside Iraq; **100** US$ for individuals abroad; **300** US$ for institutions abroad.

Roaa J. Mohammed
Jasim M. Mansoor
Asaad A. Kamil

Department of Physics,
College of Science,
University of Diyala,
Diyala, IRAQ

A Detailed Evaluation of Zn:Cu Co-Doping Impacts on the Performance of Nanostructured CdO Thin Films

This study focuses on the production and analysis of nanostructured CdO films co-doped with zinc (Zn) and copper (Cu) using the sol-gel spin coating technique. X-ray diffraction analysis revealed that these films have a cubic crystalline structure typical of CdO. Surface morphology showed that both the doping ratio and the type significantly influence the microstructure of the films. The presence of O, Cu, Cd, and Zn in the initial solution was confirmed. The absorbance values of the prepared samples exhibit a positive correlation with the Cu content. In addition, the energy gap values were shown to be dependent on the Zn:Cu ratio. Conductivity, measured via the Hall effect, increased notably with Cu doping up to a 10% ratio. The results demonstrate the impact of Zn:Cu co-doping on the structural, optical, and electrical properties of CdO films, indicating their potential for optoelectronic applications.

Keywords: Spin coating; Cadmium oxide; Energy gap; Nanostructures
Received: 29 January 2024; **Revised:** 25 March 2024; **Accepted:** 01 April 2024

1. Introduction

Owing to their unparalleled properties for various nanotechnology applications, transparent conducting oxides (TCOs) have garnered considerable technological and scientific interest [1-3]. Cadmium oxide (CdO) is a significant constituent of the transparent conductive oxide (TCO) group, garnering considerable contemporary interest because of its noteworthy electrical and optical characteristics. CdO is classified as an n-type semiconductor because of its notable electrical conductivity. In addition, it shows exceptional optical transparency within the visible spectrum. CdO possesses a direct band gap energy ranging from 2.2 to 2.7eV [4]. The characteristics of CdO films make them advantageous for several applications, including but not limited to smart windows, heat mirrors, gas sensors, phototransistors, and optical communications [5-10].

By doping CdO films with varying metallic ions, the morphological, optical, and structural properties of the films can be changed. The process of introducing ionic impurities into CdO films results in substantial modifications to the band structure and, so, the physical properties. The process of introducing ions with radii different from those of Cd^{2+} into CdO, known as doping, can be achieved by incorporating ions such as Mn, Pr, Al, Cr, Ce, Sn, and Gd, resulting in significant improvements in bandgap energies as well as morphological and structural properties [11-14]. Therefore, doping is typically associated with improving the electrical and optical characteristics of CdO films. The practice of employing two different dopant ions on a single CdO film, commonly referred to as double doping, is being investigated, has recently been seen to result in CdO films with unique properties [15-17].

Metal-organic chemical vapor deposition (MOCVD) [18], successive ionic layer adsorption and reaction (SILAR) method [19], spray pyrolysis [20], pulsed laser deposition [21], RF magnetron sputtering [22], chemical bath deposition [23], and sol–gel processes [24] have all been reported for CdO thin film deposition. The sol–gel spin coating method has several advantages, including simplicity, composition control, and homogeneity [25]. Sol-gel method Zn:Cu co-doped CdO films have not been reported in the literature, to the best of our knowledge. Therefore, this study focuses on assessing the effects of Zn and Cu co-doping on the morphological, structural, electrical, and optical characteristics of CdO films. Here, we present a detailed examination of the properties of nanostructured CdO thin films co-doped with Zn and Cu for the first time.

2. Experimental Work

Using the sol-gel spin coating method, we prepared pure and co-doped CdO thin films on glass substrates. Cadmium acetate $Cd(CH_3COO)_2{\cdot}2H_2O$, was dissolved in 10 ml of 2-methoxyethanol to form a 0.5M solution. Copper acetate $Cu(CH_3COO)_2{\cdot}2H_2O$ and zinc acetate $Zn(CH_3COO)_2{\cdot}2H_2O$ were added to this solution in varying Zn:Cu ratios (10% Zn, 7.5% Zn:2.5% Cu, 5% Zn:5% Cu, 2.5% Zn:7.5% Cu, 10% Cu) to create a homogeneous solution. Monoethanolamine (MEA) was then introduced to the stirred mixture to achieve the desired viscosity and stability. The mixture was heated at 75°C for 2 hrs while stirring. This process yielded a clear, light-yellow solution, which was then left to stand at room temperature for 24 hrs.

Earlier research has shown that solution anesthetics can improve the morphology, crystallization, and pore structure of spin-coated thin film electrodes [26]. Prior to depositing the solution onto the glass substrates by spin coating, the substrates were cleaned in an ultrasonic water bath with diluted detergents, acetone, 99% pure ethanol, and deionized water for 20 min, then dried with nitrogen gas and preheated in an oven at 75°C. The aged solutions were filtered through a 0.1µm filter to remove any agglomerated particles, ensuring standardized thin-film deposition by spin coating.

All samples were spin-coated at 3300 rpm for 35s onto soda-lime glass substrates. Each layer was covered with a 200 mL solution and dried for 15 min on a heated plate set to 200°C. This coating and drying process was repeated five times. Subsequently, the samples were annealed in a furnace at 475°C for 1 hour and gradually cooled to room temperature. The structural, morphological, optical, and electrical properties of the pure and co-doped CdO thin films were characterized using XRD, FE-SEM, UV-visible spectroscopy, and the Hall effect.

3. Results and Discussion

XRD analysis was conducted to investigate the influence of co-doping Cu with Zn on the crystalline structure and crystallite dimensions of CdO specimens.

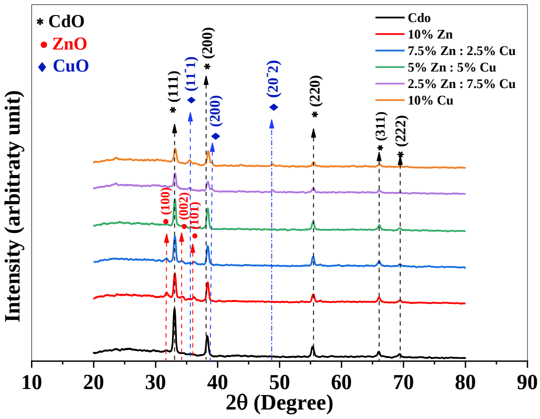

Fig. (1) XRD patterns of CdO and (Zn:Cu) co-doped thin films

The XRD patterns depicted in Fig. (1) prove that all the CdO samples show distinctive peaks associated with the cubic polycrystalline structure of CdO, as showed by ICDD card no. 75-0592. The presence of well-defined diffraction peaks indicates a high degree of crystallinity. The films co-doped with Cu and Zn show a pronounced preferential orientation along the (111) crystallographic plane, which is comparable to the orientation saw in the original CdO film. The Cu with Zn co-doped CdO films show markers associated with ZnO oxide and CuO oxide, which may be detected using an XRD setup with a specified detection limit. New peaks were seen in films having 10% Zn and 7.5% Zn:2.5% Cu, specifically corresponding to the (100), (002), and (101) planes of ZnO (ICDD 079-2205). Similarly, three peaks were shown in films having 10% Cu and 7.5% Cu:2.5% Zn, specifically corresponding to the (11^{-}1), (200) and (20^{-}2) planes of CuO (ICDD 080-1268). This implies that the successful incorporation of Cu and Zn ions into the CdO matrix was achieved [27]. A shift of 2θ toward higher diffraction angles is seen in the (111) diffraction, as depicted in Fig. (2). The observed phenomenon of a slight shift in the diffraction peak can be attributed to the presence of structural strain and changes in the stoichiometric composition resulting from the process of doping. The primary cause of this structural influence can be attributed to the disparity in the ionic radii between the host elements Cd^{+2} and the dopant ions Cu^{+2} and Zn^{+2}. Other researchers have also seen observed shifts in diffraction peaks when using other doping elements [28,29]. These findings show that a significant portion of Cu^{+2} and Zn^{+2} ions were integrated into the CdO lattice [30]. Moreover, the variability in the placement of the peaks shows that the lattice parameter undergoes alterations due to the disparity in the ionic sizes of the atoms [31].

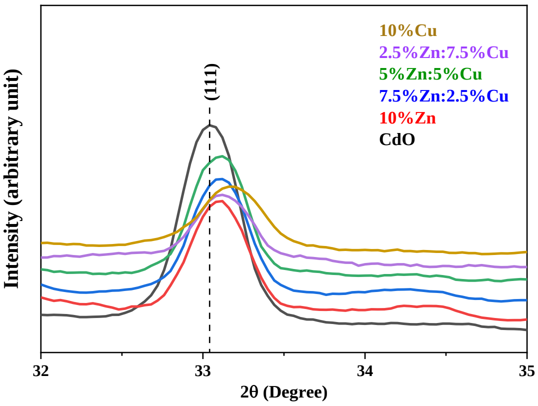

Fig. (2) XRD patterns of the preferential orientation of CdO and Zn:Cu co-doped CdO thin films

The crystallite sizes of the CdO thin films co-doped with Zn:Cu were determined using the widely recognized Scherrer's formula below [32]:

$$D = \frac{0.94\lambda}{\beta cos\theta} \qquad (1)$$

In the given equation, the symbol D represents the dimension of the crystallite, β denotes the full-width at half maximum of the XRD peak, λ represents the wavelength of the x-ray (1.5406Å), and θ signifies the Bragg's angle. The calculation of additional microstructural parameters, including lattice spacing (d), lattice constant (a), strain (ε), and dislocation density (δ), can be achieved by the using of equations (2), (3), (4) and (5) [33,34]

$$d = \frac{n\lambda}{2dsin\theta} \qquad (2)$$

$$\frac{1}{d^2} = \frac{h^2+k^2+l^2}{a^2} \qquad (3)$$

$$\varepsilon = \frac{\beta cos\theta}{4} \qquad (4)$$

$$\delta = \frac{1}{D^2} \qquad (5)$$

In the context of XRD, the variable *n* denotes the degree of diffraction, λ indicates the wavelength associated with the XRD pattern, and θ signifies the diffraction angle. The values of D, ε, and δ that were acquired are displayed in table (1). The variations in the ε, D, and δ values of the CdO films are seen to be contingent on the different doping percentages of Cu:Zn, as depicted in table (1). The observed phenomenon can likely be attributed to the replacement of Cd^{+2} ions with Cu^{+2} or Zn^{+2} ions inside the CdO lattice structure. This substitution occurs because the ionic radii of Cu^{+2} (0.72Å) and Zn^{+2} (0.74Å) deviate from that of Cd^{+2} (0.97Å) when considering metals with a coordination number of 6 [35]. Several researchers have similarly reported these findings [36,37]. The literature clearly sets up a relationship between crystallite size, microstrain, and dislocation density, indicating an unfavorable correlation [38].

The analysis of surface morphology plays a crucial role in understanding the surface characteristics of nanostructured films. To investigate the alterations in the surface morphology of CdO films induced by double-doping, FE-SEM was performed as in Fig. (3) as the modification of the surface characteristics and particle dimensions of the films by the process of doping are proved. These images reveal that the surface of the CdO films showed a remarkable state of roughness. The CdO films are characterized by a significant quantity of nanoparticles that are spread in a random manner across the substrates made of soda-lime glass. The morphology of the pure CdO thin film shows a cauliflower-like shape, while the CdO thin films co-doped with Cu:Zn exhibit nanospherical granules. Earlier studies conducted by researchers [34] have also saw comparable structural characteristics in CdO films. Variations in the particle thicknesses of the films were seen upon co-doping with Cu and Zn, as depicted in Fig. (3). These changes showed a strong correlation with the variations in crystallite size, as determined by XRD analysis. The particle size values for the films of CdO, 10% Zn, 7.5% Zn:2.5% Cu, 5% Zn:5% Cu, 2.5% Zn:7.5% Cu, and 10% Cu are approximately 43.71-69.08nm, 37.07-101.5nm, 29.24-55.91nm, 36.43-267.1nm, 27.69-86.23nm, and 25.81-48.57nm, respectively.

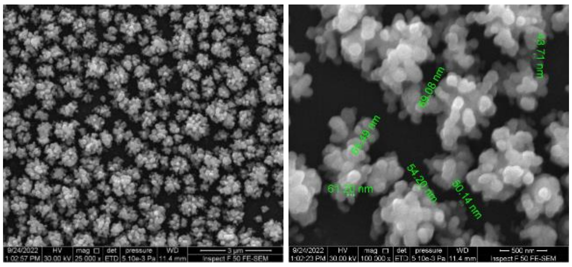

CdO

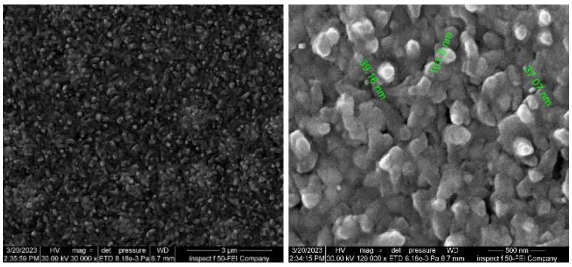

10% Zn

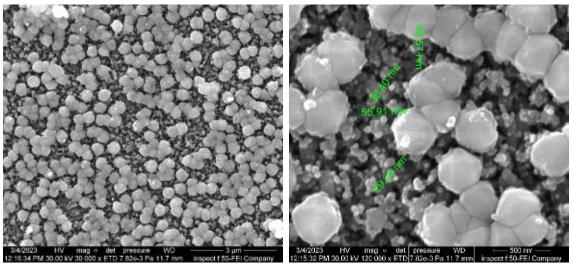

7.5% Zn:2.5% Cu

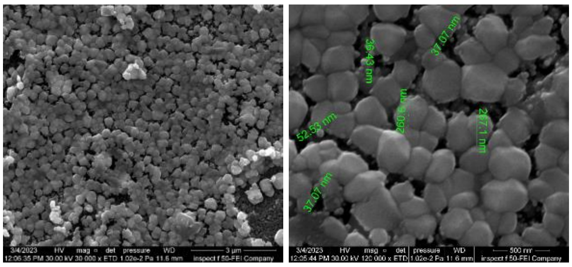

5%Zn:5%Cu

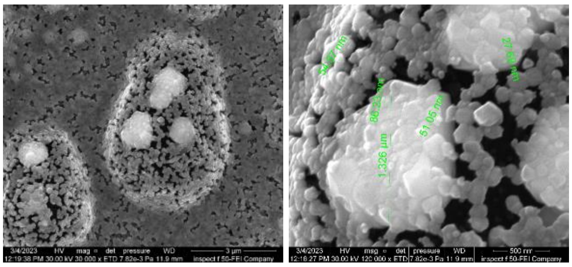

2.5% Zn:7.5% Cu

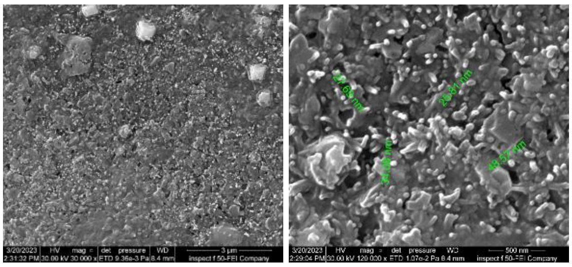

10% Cu

Fig. (3) FE-SEM images of the CdO and (Cu:Zn) co-doped CdO thin films

The variation in morphologies observed can be attributed to disparities in the electronegativity and ionic radius between the dopants and the host metal. These differences influence the growth process and the crystal plane surfaces of CdO films [35,36]. The researchers used the EDS analysis to find the elemental compositions of the samples that were generated. Figure (4) shows the elements in the nanostructured CdO films demonstrating the presence of the expected O, Cu, Cd, and Zn elements in the first solution.

The absorption spectra for the CdO thin films and 10% co-doped CdO thin films with varying Cu:Zn ratios (10%Zn, 2.5%Cu:7.5%Zn, 5%Cu:5%Zn, 7.5%Cu:2.5%Zn, and 10%Cu) are presented in Fig. (5). The spectra were recorded in the wavelength range of 300-900 nm. The figure demonstrates that the absorbance edge is consistently positioned at approximately 500 for all samples. Moreover, there is a discernible pattern in which the absorption spectrum demonstrates an upward trend as the ratio of copper to zinc increases. The presence of elevated copper content in the co-doped CdO films results in the generation of supplementary energy levels situated within the bandgap. The presence of these energy levels enables a more effective process of light absorption, leading to an amplification of the absorption spectrum. Consequently, the degree of absorbance of films becomes more prominent when the ratio of copper to zinc in the doping composition increases. The simultaneous incorporation of both copper (Cu) and zinc (Zn) dopants in co-doped CdO films results in a synergistic phenomenon. The introduction of Cu doping results in the incorporation of deep energy levels, while Zn doping functions as a donor of shallow levels. Variations in the optical characteristics of dual-doped CdO films can be attributed to the influence of the specific Cu:Zn ratio, which figures out the dominance of one effect over the other. The ability to customize the composition of CdO thin films by adjusting the percentages of Cu and Zn allows the optimization of these films for various applications in optoelectronics, sensors, and other electronic devices [39].

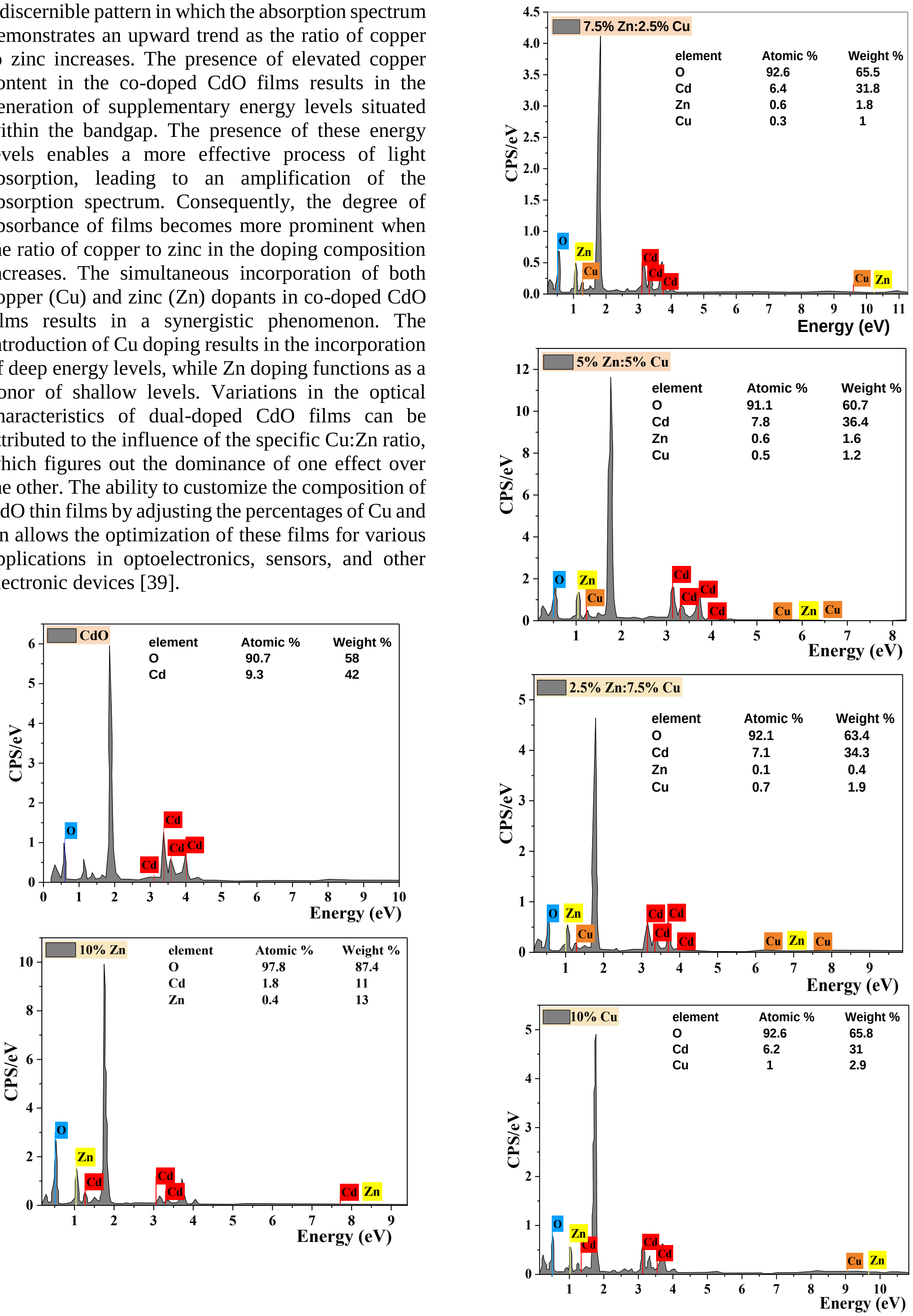

Fig. (4) EDS spectra of the prepared CdO and Zn:Cu co-doped CdO thin films

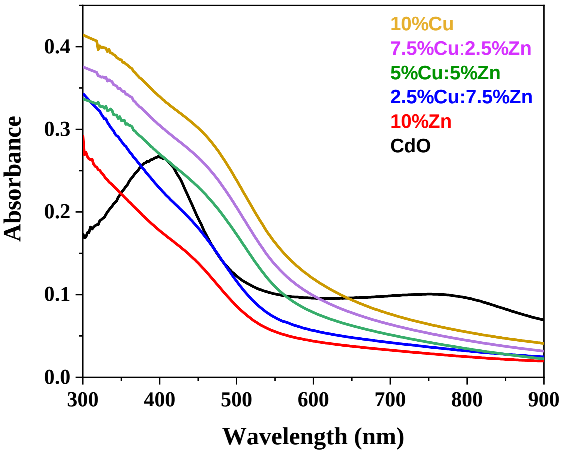

Fig. (5) Absorption spectrum of the CdO and Zn:Cu co-doped CdO thin films

The determination of the optical bandgap ($E_{g(opt)}$) for the thin films of dual-doped CdO with varying Zn:Cu ratios was performed using the Tauc formula below, described in reference [34].

$$\alpha h\nu = A(h\nu - E_g)^{1/2} \qquad (6)$$

In the previous equation, α represents the coefficient of absorption, A denotes a constant, $h\nu$ represents the energy of the photon, and E_g signifies the optical energy gap

According to the data presented in Fig. (6), the energy bandgap of the 5% Cu:5% Zn composition sample was measured to be 2.57eV. Furthermore, it is noteworthy that when the Cu:Zn ratio increases, the energy bandgap experiences a modest drop, reaching a value of 2.45eV. Nevertheless, there was an observed rise in the energy bandgap to 2.92eV as the Zn content increased compared to Cu. The inclusion of copper (Cu) in the co-doped CdO films introduces supplementary energy levels within the bandgap.

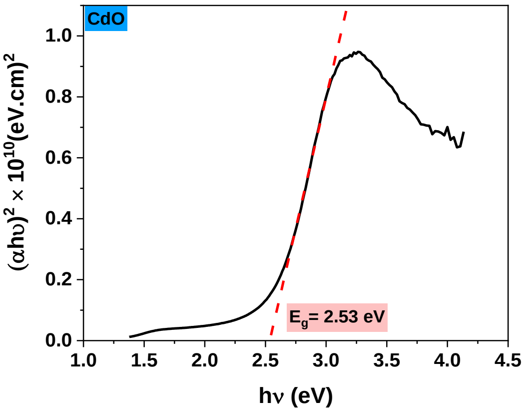

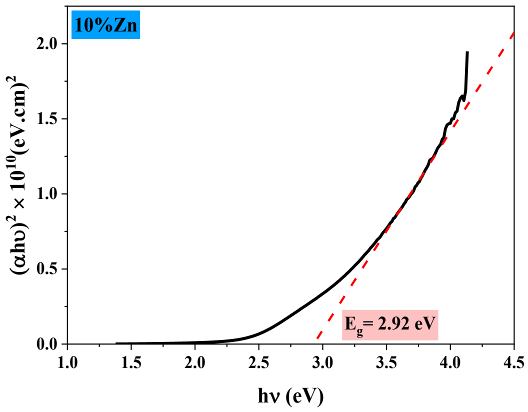

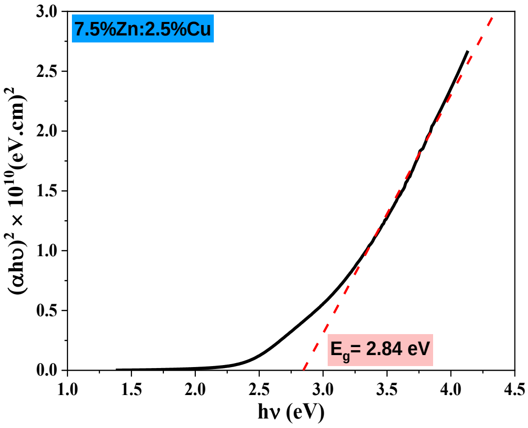

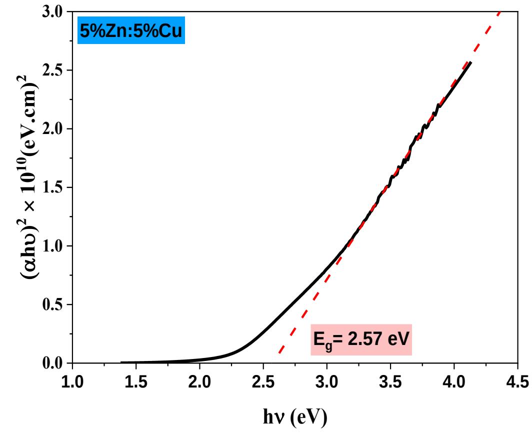

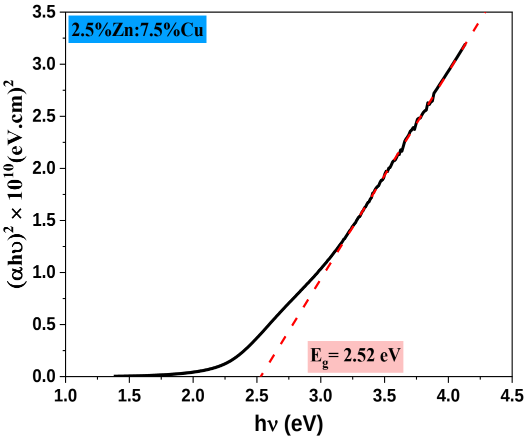

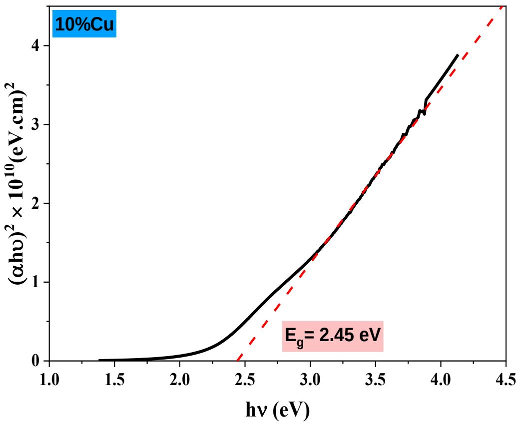

Fig. (6) Determination of optical band gap of CdO and Zn:Cu co-doped CdO thin films

The presence of deep energy states can confine electrons, resulting in a marginal drop in the energy necessary for absorption and thus a reduction in the optical bandgap. The Moss-Burstein effect has been identified as the underlying cause of the observed increase in the energy gap resulting from high-concentration doping with Zn [40]. The Moss-Burstein effect is characterized by the phenomenon of the absorption edge being displaced toward higher energy levels. The observed shift can be attributed to the filling of certain states next to the conduction band, which occurs when the concentration of electron carriers exceeds the density of available states. This phenomenon results in degenerating doping. In this phenomenon, once the concentration of electron carriers exceeds the density of states that are available states, all states found below the Fermi level become occupied. As a result, the excitation of electrons can solely occur within the conduction band, i.e., at energy levels surpassing the Fermi level. Consequently, the observed band gap can be expressed as the sum of the intrinsic band gap and the Moss-Burstein displacement [41]. This result aligns with the outcomes documented in the citation [42].

The use of Hall effect measurement is a helpful technique for introducing the fundamental electrical characteristics of metal oxide semiconducting materials, and hence assessing their appropriateness for certain applications [43]. Hall measurements were conducted at ambient temperature for thin films of CdO and Zn:Cu co-doped CdO deposited on glass substrates. The conductivity (σ), carrier concentration (n_H), and carrier mobility (μ_H) were figured out for each film sample, and the corresponding data are presented in table (2). The verification of the n-type conductivity of this system was set up through the observation of negative Hall coefficients in all thin layers. The occurrence of this phenomenon can be attributed to the existence of imperfections, including oxygen vacancies and/or intrinsic interstitial cadmium atoms, due to the strong likelihood of ionization associated with these defects. [44,45]. The electrons that are generated because of this process make a significant contribution to electrical conduction, hence causing CdO to show the characteristics of an n-type semiconductor. Based on the data presented in the table, the carrier concentration shows an upward trend as the percentage doping level increases. Conversely, the carrier concentration proves a downward trend as the percentage of Cu increases but experiences an upturn when the Cu content reaches 10%. Furthermore, the sample with a 10% Cu content exhibits the maximum level of conductivity.

The improvement in electrical properties observed for the co-doped CdO thin films can be attributed to the increase in carrier concentrations, mobilities, and conductivities, as well as the decrease in resistivity values. If Cu^{+2} and Zn^{+2} ions are replaced with Cd^{+2} ions or if Cu^{+2} and Zn^{+2} ions combine with O^{+2} ions, this improvement could occur. These techniques can enhance the carrier concentration of the deposited films by introducing an extra electron during every incorporation [46].

4. Conclusions

In conclusion, this research effectively produced CdO films doped with Zn and Cu using the sol-gel spin coating technique. The films show cubic crystalline structure. Significant changes in morphology and particle size were seen with Zn and Cu co-doping. Increasing Zn doping has raised the optical bandgap energy due to the Burstein-Moss effect, while increasing Cu doping lowered it. The n-type conductivity was confirmed in all films, with the highest conductivity saw at a 10% Cu doping level. These findings highlight the critical impact of dopant type and concentration on the CdO films' physical properties, especially the optical bandgap, pointing towards their potential in enhancing optoelectronic device technology.

Acknowledgements

This project received assistance from the Diyala University, College of Science.

References

[1] D. Sharma and R. Jha, “Transition metal (Co, Mn) co-doped ZnO nanoparticles: effect on structural and optical properties”, *J. Alloys Comp.*, 698 (2017) 532-538.

[2] P.B. Nair et al., “Structural, optical, photoluminescence and photocatalytic investigations on Fe doped TiO2 thin films”, *Thin Solid Films*, 550 (2014) 121-127.

[3] T. Jan, et al., “Structural, Raman and optical characteristics of Sn doped CuO nanostructures: a novel anticancer agent”, *Ceram. Int.*, 41(10) (2015) 13074-13079.

[4] N. Manjula, et al., “Enhancement in some physical properties of spray deposited CdO: Mn thin films through Zn doping towards optoelectronic applications”, *Optik*, 127(16) (2016) 6400-6406.

[5] R.N. Bulakhe and C.D. Lokhande, “Chemically deposited cubic structured CdO thin films: use in liquefied petroleum gas sensor”, *Sens. Actuat. B: Chem.*, 200 (2014) 245-250.

[6] M. Ramamurthy, M. Balaji and P. Thirunavukkarasu, “Characterization of jet nebulizer sprayed CdO thin films for solar cell application”, *Optik*, 127(8) (2016) 3809-3819.

[7] M. Soylu, A.A. Al-Ghamdi and F. Yakuphanoglu, “Transparent CdO/n-GaN (0001) heterojunction for optoelectronic applications”, *J. Phys. Chem. Solids*, 85 (2015) 26-33.

[8] M. Eskandari, V. Ahmadi and R. Ghahary, “Enhanced photovoltaic performance of a cadmium sulfide/cadmium selenide-sensitized solar cell using an aluminum-doped zinc oxide electrode”, *Ceram. Int.*, 41(2) (2015) 2373-2380.

[9] R.J. Deokate, et al., “Spray deposition of highly transparent fluorine doped cadmium oxide thin films”, *Appl. Surf. Sci.*, 254(7) (2008) 2187-2195.

[10] E. Gürbüz, R. Aydin and B. Şahin, “A study of the influences of transition metal (Mn, Ni) co-doping on the morphological, structural and optical properties of nanostructured CdO films”, *J. Mater. Sci.: Mater. Electron.*, 29 (2018) 1823-1831.

[11] Z. Ganjiani, F. Jamali-Sheini and R. Yousefi, “Electrochemical synthesis and physical properties of Sn-doped CdO nanostructures”, *Superlatt. Microstruct.*, 100 (2016) 988-996.

[12] P. Velusamy et al., “Characterization of spray pyrolytically deposited high mobility praseodymium doped CdO thin films”, *Ceram. Int.*, 42(11) (2016) 12675-12685.

[13] Z.A. Alahmed, et al., “Optical band gap controlling of nanostructure Mn doped CdO thin films prepared by sol–gel spin coating method”, *Optik*, 126(5) (2015) 575-577.

[14] S. Aydemir, et al., “Influence of Al-doping on microstructure and optical properties of sol–gel derived CdO thin films’, *Superlatt. Microstruct.*, 71 (2014) 72-81.

[15] N. Manjula and A.R. Balu, “Double doping (Mn+Cl) effects on the structural, morphological, photoluminescence, optoelectronic properties and antibacterial activity of CdO thin films”, *Optik*, 130 (2017) 464-472.

[16] S. Akın, et al., “Improvement of physical properties of CdO thin films by Au–Ag nanocluster codoping”, *J. Alloys Comp.*, 579 (2013) 272-278.

[17] R. Aydin and B. Şahin, “Comprehensive research on physical properties of Zn and M (M: Li, Na, K) double doped cadmium oxide (CdO) nanostructures using SILAR method”, *Ceram. Int.*, 43(12) (2017) 9285-9290.

[18] D.A. Lamb and S.J. C. Irvine, “A temperature dependant crystal orientation transition of cadmium oxide films deposited by metal organic chemical vapour deposition”, *J. Cryst. Growth*, 332(1) (2011) 17-20.

[19] B. Şahin, T. Taşköprü and F. Bayansal, “Bandgap variation of nanostructure tin doped CdO films via SILAR processing”, *Ceram. Int.*, 40(6) (2014) 8709-8714.

[20] R. Kumaravel et al., “Electrical, optical and structural properties of aluminum doped cadmium oxide thin films prepared by spray pyrolysis technique”, *Mater. Chem. Phys.*, 122(2-3) (2010) 444-448.

[21] B.J. Zheng et al., “Optical and electrical properties of Sn-doped CdO thin films obtained by pulse laser deposition”, *Vacuum*, 85(9) (2011) 861-865.

[22] B. Saha, S. Das and K.K. Chattopadhyay, “Electrical and optical properties of Al doped cadmium oxide thin films deposited by radio frequency magnetron sputtering”, *Sol. Ener. Mater. Sol. Cells*, 91(18) (2007) 1692-1697.

[23] R.R. Salunkhe, V.R. Shinde and C.D. Lokhande, “Liquefied petroleum gas (LPG) sensing properties of nanocrystalline CdO thin films prepared by chemical route: effect of molarities of precursor solution”, *Sens. Actuat. B: Chem.*, 133(1) (2008) 296-301.

[24] F. Yakuphanoglu, “Synthesis and electro-optic properties of nanosized-boron doped cadmium oxide thin films for solar cell applications”, *Sol. Ener.*, 85(11) (2011) 2704-2709.

[25] M. Thirumoorthi and J.T.J. Prakash, “A study of Tin doping effects on physical properties of CdO thin films prepared by sol–gel spin coating method”, *J. Asian Ceram. Soc.*, 4(1) (2016) 39-45.

[26] G. Cerveau, R.J. Corriu and E. Framery, “Sol–gel process – influence of ageing on the textural properties of organosilsesquioxane materials”, *J. Mater. Chem.*, 11(3) (2001) 713-717.

[27] M.A. Barakat, M. Shaban and A.M. El Sayed, “Structural, ultrasonic and spectroscopic studies of tin oxide thin films; effect of Ir and (Ni, Ir) double doping”, *Mater. Res. Exp.*, 5(6) (2018) 066407.

[28] A.A. Dakhel, “Optoelectronic properties of Eu- and H-codoped CdO films”, *Curr. Appl. Phys.*, 11(1) (2011) 11-15.

[29] R.J. Deokate, et al., “Structural, optical and electrical properties of chemically sprayed nanosized gallium doped CdO thin films”, *J. Alloys Comp.*, 496(1-2) (2010) 357-363.

[30] A.A. Dakhel, “Correlated transport and optical phenomena in Ga-doped CdO films”, *Sol. Ener.*, 82(6) (2008) 513-519.

[31] Y. Zhao et al., “The effect of Eu doping on microstructure, morphology and methanol-

sensing performance of highly ordered SnO_2 nanorods array", *Nanomater.*, 7(12) (2017) 410.

[32] I.S. Yahia et al., "Optical properties of Al-CdO nano-clusters thin films", Superlatt. Microstruct., 64 (2013) 178-184.

[33] N.K. Husien and J. Alzanganawee, "An investigation (Cd+Co) Co-Loading Impact on Physical Properties of Nano-Structured (CuO) Thin Films", *Acad. Sci. J.*, 1(1) (2023) 122-139.

[34] K.S. Mohammed et al., "An investigation of annealing and (Zn+Co) co-loading impact on certain physical features of nano-structured (CdO) thin films coated by a sol-gel spin coating process", *J. Ovonic Res.*, 17(5) (2021).

[35] R.D. Shannon, "Revised effective ionic radii and systematic studies of interatomic distances in halides and chalcogenides", *Acta Crystallog. A: Cryst. Phys. Diffract. Theor. Gen. Crystallog.*, 32(5) (1976) 751-767.

[36] C. Wang et al., "Structure, morphology and properties of Fe-doped ZnO films prepared by facing-target magnetron sputtering system", *Appl. Surf. Sci.*, 255(15) (2009) 6881-6887.

[37] A. Goktas et al., "Tuning of structural, optical and dielectric constants by various transition metal doping in ZnO: TM (TM= Mn, Co, Fe) nanostructured thin films: a comparative study", *Ceram. Int.*, 43(1) (2017) 704-713.

[38] P. Kumarn et al., "Nano porous hematite for solar hydrogen production", *J. Electrochem. Soc.*, 159(8) (2012) H685.

[39] B.A. Gozeh et al., "Zn-doped CdO effects on the optical, electrical and photoresponse properties of heterojunctions-based photodiodes", *J. Alloys Comp.*, 872 (2021)159624.

[40] N. Manjula et al., "Optoelectronic, magnetic and antibacterial properties of CdO thin films doubly doped with Mn (cationic) and F (anionic) ions", *J. Mater. Sci.: Mater. Electron.*, 28 (2017) 7615-7621.

[41] Z.M. Gibbs, A. LaLonde and G.J. Snyder, "Optical band gap and the Burstein–Moss effect in iodine doped PbTe using diffuse reflectance infrared Fourier transform spectroscopy", *New J. Phys.*, 15(7) (2013) 075020.

[42] I.S. Yahia et al., "Linear and nonlinear optical discussions of nanostructured Zn-doped CdO thin films", *Physica B: Cond. Matter*, 511 (2017) 54-60.

[43] S.A. Russell et al., "Surface transfer doping of diamond by MoO_3: A combined spectroscopic and Hall measurement study", *Appl. Phys. Lett.*, 103(20) (2013) 202112.

[44] S.J. Helen et al., "Transparent conducting Mo-doped CdO thin films by spray pyrolysis method for solar cell applications", *J. Electron. Mater.*, 47 (2018) 2439-2446.

[45] K. Sankarasubramanian et al., "Influence of substrate temperature on ethanol sensing properties of CdO thin films prepared by facile spray pyrolysis method", *J. Mater. Sci.: Mater. Electron.*, 26 (2015) 955-961.

[46] M. Anitha et al., "Influence of a novel co-doping (Zn+F) on the physical properties of nano structured (111) oriented CdO thin films applicable for window layer of solar cell", *Appl. Surf. Sci.*, 443 (2018) 55-67.

Table (1) Parameters of the CdO and Zn:Cu co-doped CdO thin films

Sample	2θ (deg)	FWHM (deg)	D (nm)	Lattice constant (a) (Å)	d-spacing (Å)	Strain (ε)	Dislocation density (δ) (nm^{-2})
CdO	33.0308	0.2430	35.6	4.6928	2.7097	0.001007	0.000789
10%Zn	33.1315	0.3493	24.8	4.6829	2.7017	0.001462	0.001626
7.5%Zn:2.5%Cu	33.0966	0.3143	27.5	4.6840	2.7045	0.001318	0.001322
5%Zn:5%Cu	33.1211	0.2396	36.1	4.6845	2.7025	0.001006	0.000767
2.5%Zn:7.5%Cu	33.1665	0.3143	27.5	4.6790	2.6989	0.001318	0.001322
10%Cu	33.2014	0.3492	24.8	4.6743	2.6962	0.001461	0.001626

Table (2) Carrier concentration, mobility, conductivity type of "CdO and Zn:Cu co-doped CdO thin films

Sample	$n\times10^{16}$ (cm^{-3})	μ_H ($cm^2/v.sec$)	σ_{RT} ($\Omega^{-1}.cm^{-1}$)	Type
CdO	-2.11	223	0.753	n-type
10%Zn	-31.40	75	3.75	n-type
7.5%Zn:2.5%Cu	-19.16	93	2.86	n-type
5%Zn:5%Cu	-13.02	110	0.61	n-type
2.5%Zn:7.5%Cu	-9.51	152	2.31	n-type
10%Cu	-30.82	127	6.26	n-type

Characterization of Nickel and Nickel Oxide Nanoparticles Prepared by Laser Ablation Technique: Effect of Laser Wavelength and Energy

Bushra M. Ghdhaib
Sahar N. Rashid

Department of Physics,
College of Science,
University of Tikrit,
Tikrit, IRAQ

Iraqi Journal of Applied Physics
Q4 Electronic, Optical and Magnetic Materials
best quartile
SJR 2022
0.19
powered by scimagojr.com

Pulsed laser ablation in liquids is a process that has many advantages over traditional methods used to prepare nanoparticles. A piece of pure, polished nickel metal was used to prepare nanoparticles using pulsed laser ablation technique in ethanol using Nd:YAG laser with three wavelengths (1064, 532, and 355nm) and three energies (50, 100, and 150mJ). This work focuses on evaluating the extent of the influence of some ablation parameters on the properties of prepared nanoparticles by characterizing them structurally and optically. The results showed the formation of both nickel nanoparticles and nickel oxide nanoparticles with spherical shapes and with an average diameter ranging between 11.35 and 76.6 nm. It was found that the oxidation rate increases when the shorter wavelength of the laser is used in the preparation. Absorbance increases with increasing laser energy, and the most appropriate wavelength and laser energy in preparation are 532nm and 150mJ. This technique has proven to be one of the easiest physical methods for preparing nanoparticles of metals and their oxides and is characterized by its speed and low cost.

Keywords: Laser ablation; Colloidal solutions; Nanoparticles; Nickel oxide
Received: 08 March 2024; **Revised:** 30 April 2024; **Accepted:** 07 May 2024

1. Introduction

One-step, top-down, easy, fast, economical, and environmentally friendly is, in short, the most important description of the pulsed laser ablation in liquid (PLAL) technique to prepare nanoparticles (NPs) [1-4]. One of the many advantages of this approach is the ability to control the shape, morphology, size, and properties of the produced NPs [5-7]. This control results from the control of various ablation parameters, such as laser energy, laser pulse width, repetition rate, wavelength, ablation time, and fluid height level above the target surface [8-11]. This technique depends on laser ablation, which has a high intensity to result in the interaction of the laser with the surface of the target material, thus producing a plasma plume immersed in the liquid. Special thermodynamic conditions arise when both pressure and temperature are high, which allows the production of NPs [11]. Figure (1) shows the mechanism of nanoparticle formation by laser ablation [12].

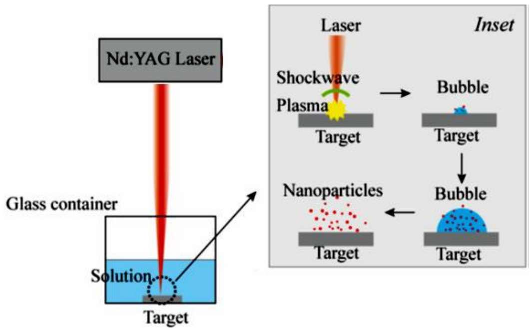

Fig. (1) Schematic diagram of PLAL process

Depending on the wavelength of the laser used, its energy works to oscillate the free electrons on the surface of the metal target collectively, where absorption and scattering occur. This mechanism is a result of the ability of metal nanoparticles to absorb visible light by creating a collective vibration of the conduction bands, which are in strong resonance with specific frequencies. This phenomenon is a unique feature of metallic NPs called surface plasmon resonance (SPR), which results in measurable changes in the NPs optically as the electromagnetic field in the surroundings is enhanced by plasmon excitation [5]. Among the many metal nanoparticles that are the subject of extensive research, nickel (Ni) NPs are distinguished for their wide applications resulting from their properties, the most important of which are extreme catalytic activity, superparamagnetic properties, and antibacterial effects [13-18]. In addition, nickel oxide NPs have received great attention in a variety of scientific fields because they have important physical, biological, and chemical properties [19-24].

This work aims to evaluate the effect of changing some laser parameters, namely energy, and wavelength, on the optical and structural properties of NPs prepared from a pure nickel piece using the pulsed laser ablation technique in a liquid medium, to enable control over the properties of the resulting nanoparticles.

2. Experimental Part

Nd:YAG laser, with wavelengths of 355, 532, and 1064 nm, energies of 50, 100, and 150 mJ, number of pulses of 500, and repetition rate of 3 Hz, was used to prepare three solutions of colloidal NPs in 3 ml of absolute ethanol utilizing a pure nickel metal piece with dimensions 10×10×1 mm, where the ethanol level was 1 cm high above the Ni target and the distance between the laser source and Ni target was 15 cm.

To evaluate the influence of energy and wavelength on the most important structural and optical characteristics of the prepared colloidal solutions containing the nanoparticles, the diagnosis of these properties was done using x-ray diffraction (XRD), the field-emission scanning electron microscopy (FE-SEM), the energy-dispersive x-ray spectroscopy (EDX), the Fourier-transform infrared (FTIR) spectroscopy, and UV-visible spectrophotometry. XRD was used to determine, in addition to the crystalline structure, the average sizes of the prepared nanoparticles using the Debye–Scherrer's equation [25]:

$$D = \frac{0.9\times\lambda}{\beta Cos\theta} \qquad (1)$$

where λ is the wavelength of the x-ray (1.54Å), θ is the angle of diffraction, and β is the full-width at half maximum (FWHM) of the diffraction peaks using different laser fluencies. FE-SEM was used to determine the morphology and average diameter of the prepared NPs, EDX was used to calculate the proportions of the components of the colloidal solutions, FTIR spectroscopy was used to determine the compositions of the resulting colloidal solutions and the active groups in them, and UV-visible spectrophotometry was used to record the absorption spectra of the prepared NPs and to calculate the optical conductivity (σ) using the equation (2) [26], and the energy gap using the Tauc's equation (3) [27]

$$\sigma = \frac{\alpha nc}{4\pi} \qquad (2)$$

$$\alpha h\upsilon = B(h\upsilon - E_g)^{\frac{1}{2}} \qquad (3)$$

where α is the absorption coefficient, c is the velocity of light, n is the refractive index, B is a constant, h is the Planck's constant, υ is the photon frequency, and E_g is the energy gap

3. Results and Discussion

XRD patterns of nano-colloidal solutions prepared by laser ablation at the three wavelengths at the highest preparation energy in this work (150 mJ) show the formation of cubic-phase Ni NPs according to JCPDS card no. 00-001-1260, and NiO NPs with two dominant phases were also formed. They are cubic for nickel oxide nanoparticles (NiO NPs) according to JCPDS card no. 47-1049 and hexagonal for nickel trioxide nanoparticles (Ni_2O_3 NPs) according to JCPDS card no. 00-01-0481, as in Fig. (2). The appearance of oxides and other additional peaks is due to the interactions between the extracted nickel and the surrounding liquid, in addition to the difference in molecular pressures in the preparation space due to laser energy, where the preparation process took place in the air. Table (1) summarizes the results of XRD analysis and shows that the average sizes of NPs calculated using Eq. (1) are 27.6, 26.5, and 29.84 nm, for the samples prepared at wavelengths of 1064, 532, and 355 nm, respectively. It turns out that using the wavelength of 532 nm led to the production of NPs with a smaller average size, meaning that using a shorter wavelength (532 nm) caused an increase in laser flux, which in turn caused a decrease in the average size of the resulting NPs, as in [9]. Continuing to increase the laser energy flux using the shorter wavelength (355 nm) of the laser, led to the NPs aggregation, which led to an increase in their average sizes as a result of an increase in the ablation rate.

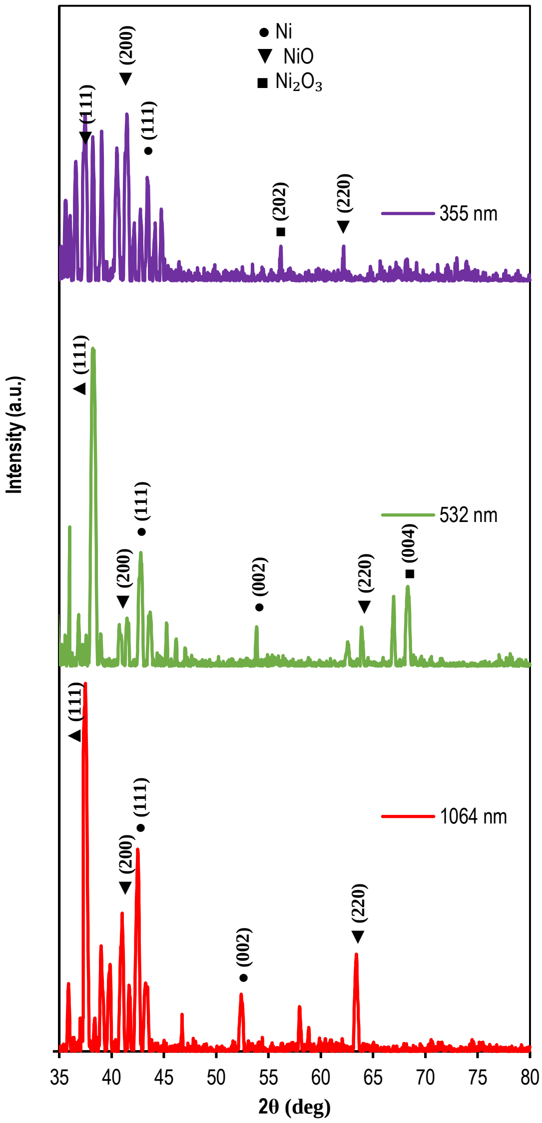

Fig. (2) XRD patterns of prepared NPs at 150 mJ

The FE-SEM analysis of nano-colloidal solutions prepared at the energy of 150 mJ, which is shown in figures (3), (4), and (5) using wavelengths of 1064, 532, and 355 nm, respectively, shows the average diameters and the morphology of the prepared samples, and at scales of 100 nm and 10 µm, where the average diameters of the prepared NPs are 76.6, 11.35, and 19.9 nm using wavelengths of 1064, 532, and 355 nm, respectively. The scale of 100 nm shows the average diameters of the prepared NPs, while the other scale (10 μm) shows its shape in addition to the resulting agglomerations, and this magnification image shows good contrast of the structure. This is consistent with what was stated in the results of the XRD analysis, where the average sizes of NPs were smaller when prepared using 532 nm of laser radiation.

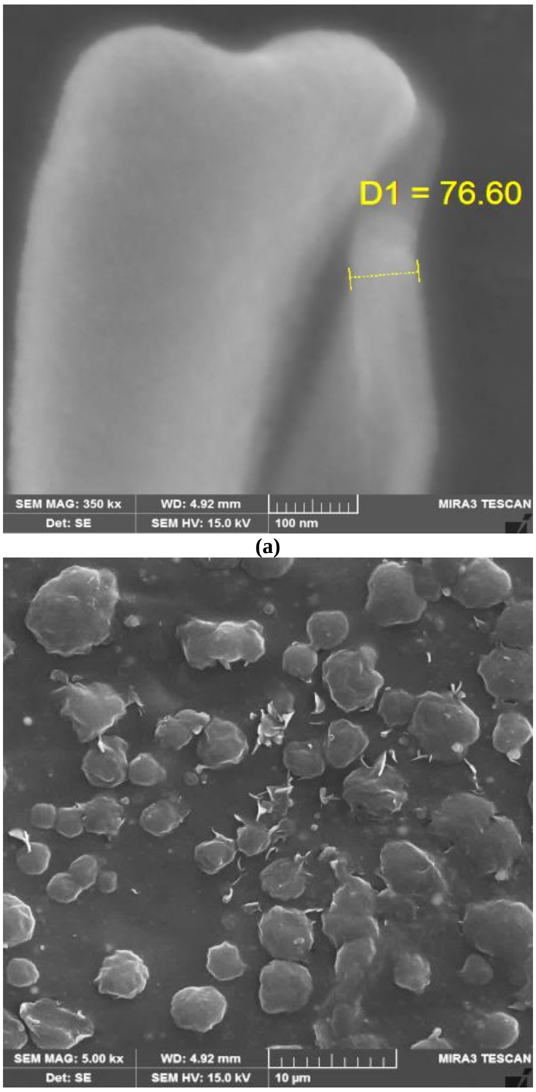

(a)

(b)

Fig. (3) FE-SEM images of prepared NPs using 1064nm with scale of (a) 100nm, (b) 10μm

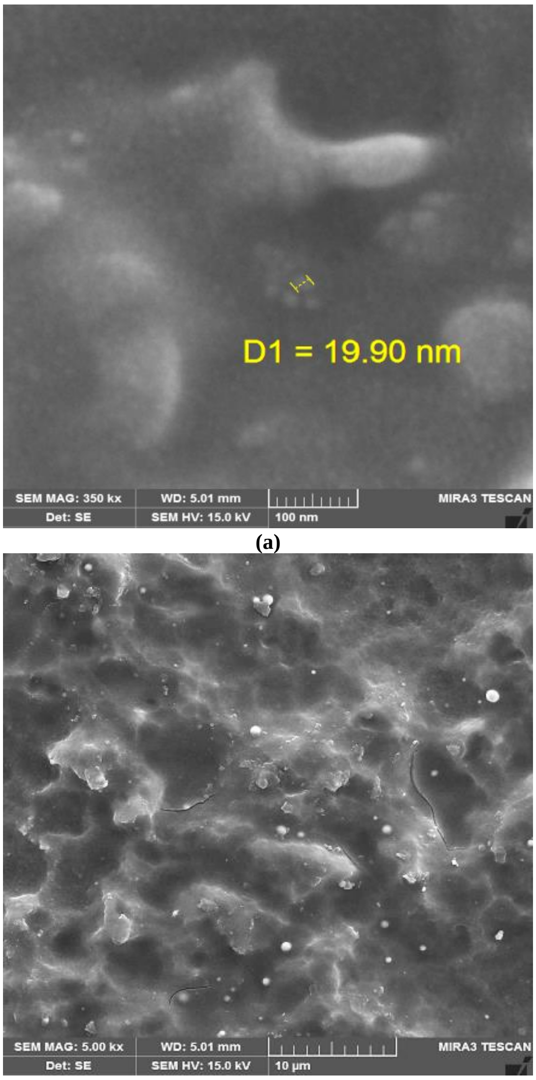

(a)

(b)

Fig. (4) FE-SEM images of prepared NPs using 532nm with scale of (a) 100nm, (b) 10μm

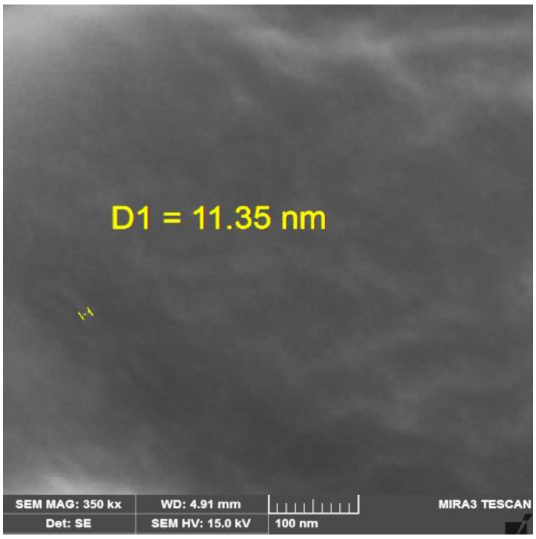

(a)

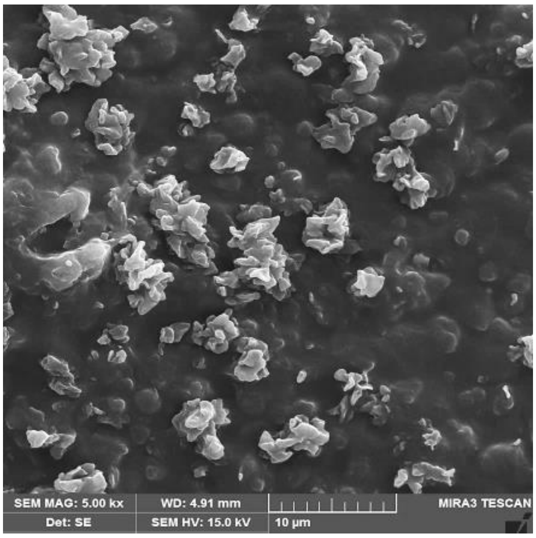

(b)

Fig. (5) FE-SEM images of prepared NPs using 355 nm with scale of (a) 100nm, (b) 10μm

The elemental compositions of the samples prepared using an energy of 150 mJ were analyzed. They showed an increase in oxidation rates consistent with what appeared in the results of XRD analysis, as in figures (6), (7) and (8), where the source of oxygen (O) in these figures is the oxidation resulting from the surrounding environment, as the ablation process did not take place in a vacuum, and it may result from the environment surrounding the EDX device itself, in addition to the fact that the preparation medium is ethanol which containing the oxygen element. The weight percentages, atomic percentages, and k-ratio of oxygen increased with laser fluence by decreasing the laser wavelength used to prepare the samples and were calculated based on the weight and atomic percentages and k-ratio of Ni as in table (2).

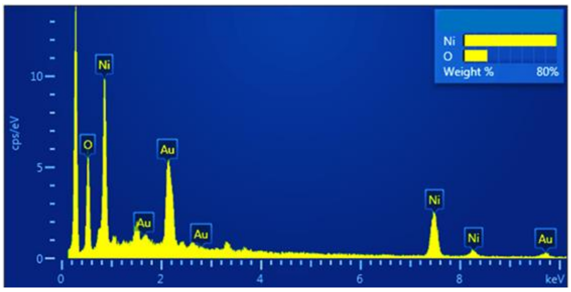

Fig. (6) EDX spectrum of NPs prepared using 1064 nm

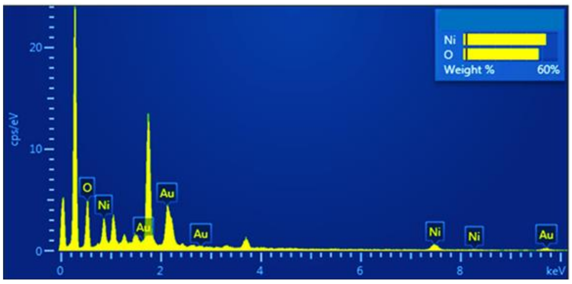

Fig. (7) EDX spectrum of NPs prepared using 532 nm

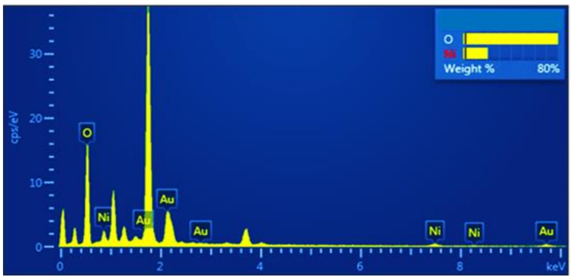

Fig. (8) EDX spectrum of NPs prepared using 355 nm

The results of FTIR measurements included an analysis of all samples prepared using wavelengths of 1064, 532, and 355 nm, as in figures (9), (10), and (11), respectively, from which the effective groups consisting of O-H, O-H-O, and C-O bonds are evident in all spectra representing samples prepared in ethanol. The occurrence of some slight shifts and differences in absorption intensity was noted as a result of the effect of laser parameters, and the effect of nickel NPs and its oxide, where the shapes show bending and stretching vibrations around 400 and 600 cm^{-1}, which are the result of Ni-O (which is the focus of this study). This result is consistent with [28] and [29].

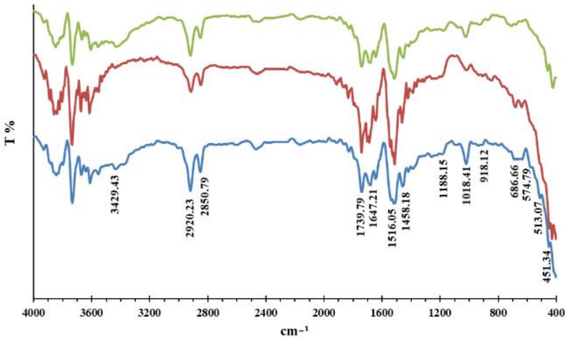

Fig. (9) FTIR spectrum of NPs prepared using 1064nm (Green 150mJ, Red 100mJ, Blue 50mJ)

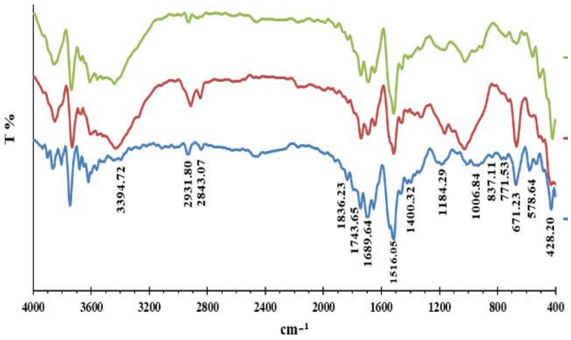

Fig. (10) FTIR spectrum of NPs prepared using 532nm (Green 150mJ, Red 100mJ, Blue 50mJ)

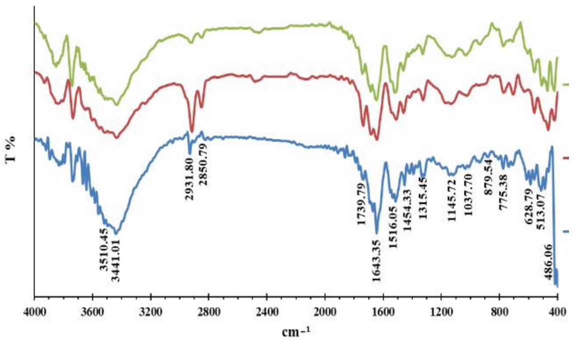

Fig. (11) FTIR spectrum of NPs prepared using 355nm (Green 150mJ, Red 100mJ, Blue 50mJ)

Figures (12), (13), and (14) represent the absorption and optical conductivity spectra, in addition to the energy gap, of the prepared NPs using wavelengths of 1064, 532, and 355 nm, respectively. These figures, in general, show that the absorbance increases with increasing laser energy for all wavelengths used, in addition to the broadening of the peak width. The appearance of these peaks representing SPR around the wavelength of 295 nm is attributed to the frequency of the incident light photons matching the frequency of the surface electrons of the NPs. This is attributed to the coloring of the resulting solution and growth in intensity with increasing laser fluence as a result of increasing the laser energy and thus increasing the concentration of NPs in the solution, which in turn means increasing the number of extracted NPs. This works to increase the absorbance as these NPs have the property of increasing the surface-to-volume ratio, so they are highly effective, and as a result, the absorbance increases. The results show that the optical conductivity of the prepared NPs peaks approximately in the SPR region, and its value is affected by changing the ablation parameters, as it increases with increasing preparation energy. Since the optical properties of materials, in general, depend on their structural properties, the optical energy gap of the prepared samples was calculated as a result of changing the composition of the samples, as the appearance of the metal oxide NPs detected in the XRD analysis of the prepared samples means the formation of an energy gap for them. Energy gap values were 3.9-3.89 eV, 3.42-3.38 eV, and 3.56-3.42 eV for NPs prepared using the wavelengths of 1064, 532, and 355 nm, respectively. It was observed that their values decrease when the laser energy is increased, that is, the conductivity of nanoparticles increased with the increase in their acquisition of the applied energy.

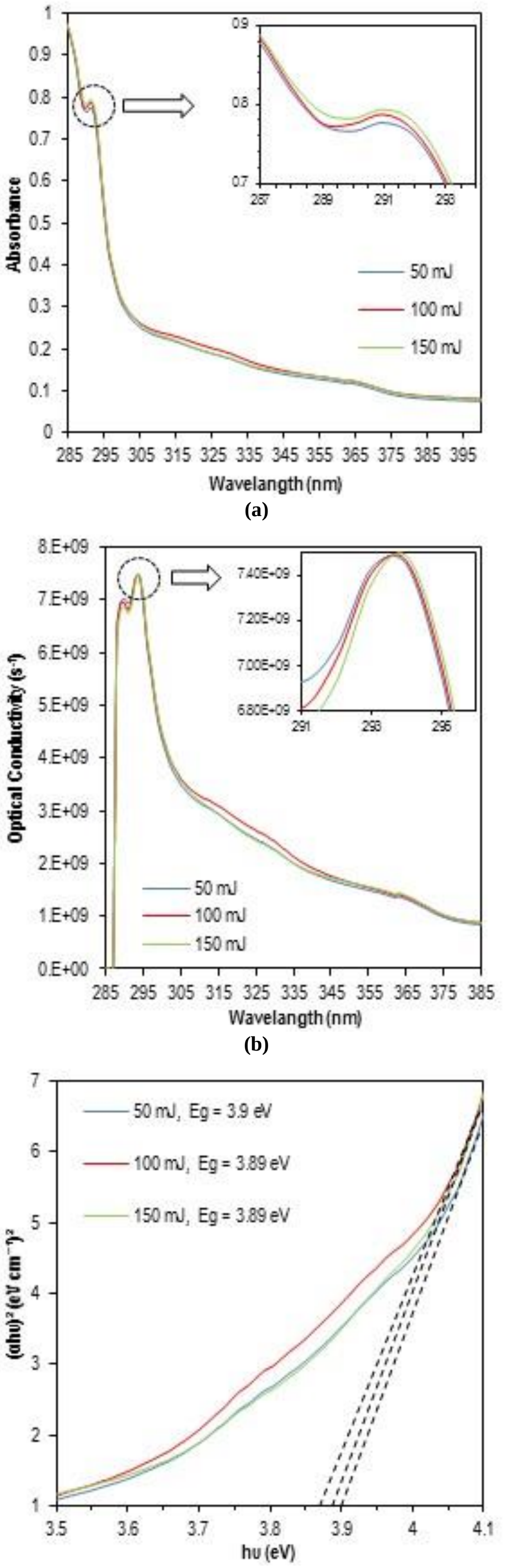

(a)

(b)

(c)

Fig. (12) UV-visible spectrophotometry analysis of prepared NPs at 1064nm (a) Absorbance, (b) Optical conductivity, and (c) Energy gap

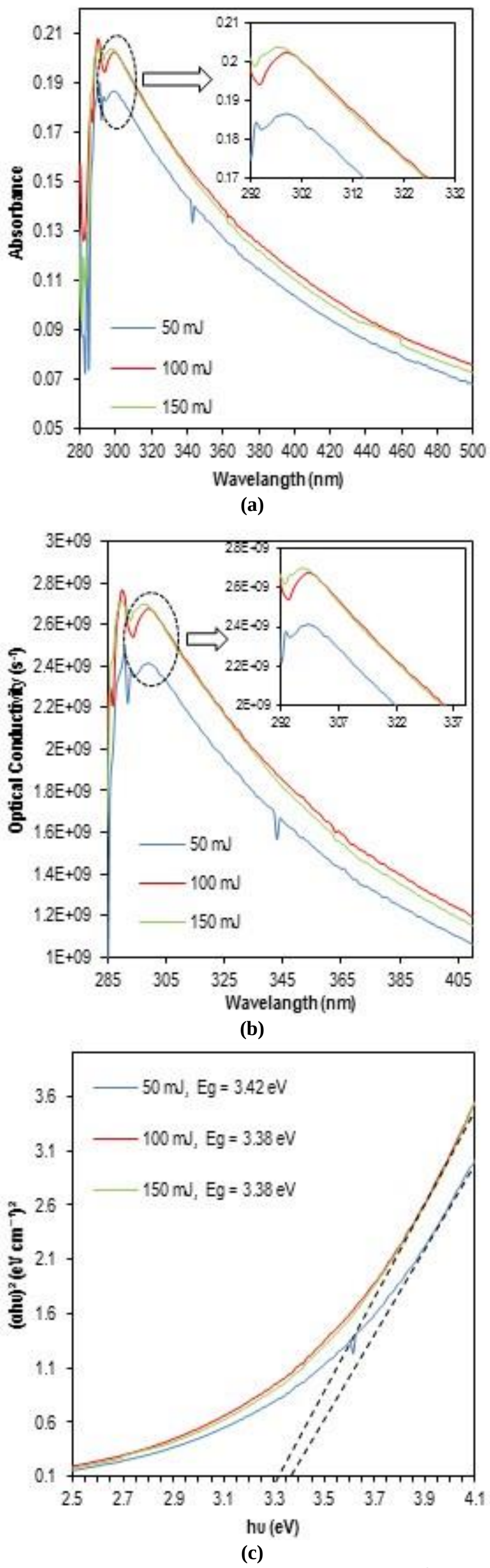

Fig. (13) UV-visible spectrophotometry analysis of prepared NPs at 532nm (a) Absorbance, (b) Optical conductivity, and (c) Energy gap

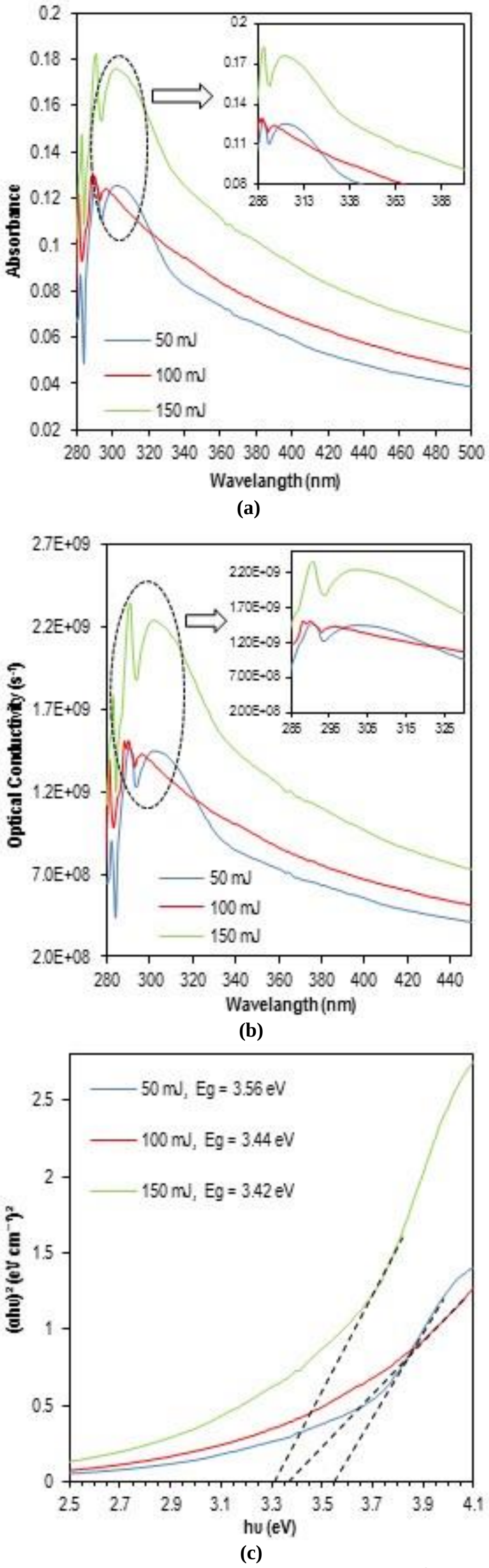

Fig. (14) UV-visible spectrophotometry analysis of prepared NPs at 355nm (a) Absorbance, (b) Optical conductivity, and (c) Energy gap

By analyzing the results of the optical properties, it becomes clear that the optimum wavelength for preparing nickel and nickel oxide NPs within the current working environment is 532nm, which resulted in obtaining smaller average sizes. This was observed in XRD and FE-SEM results.

4. Conclusion

PLAL technique has proven its ability to prepare NPs and its superiority over other techniques in terms of speed, ease, low cost, and the possibility of controlling the physical properties of the prepared NPs by controlling the ablation parameters. It was shown that shorter laser wavelength and higher laser energy used for the preparation of Ni and NiO NPs led to an increase in the oxidation rate and an increase in the concentration of the NPs and thus their aggregation. It was found that the most suitable laser wavelength and energy for the preparation in this study were 532 nm and 150 mJ, meaning that the second harmonic of Nd:YAG laser was the optimum, although the first and third harmonics of the same laser gave good results.

References

[1] K.S. Khashan et al., "Generation of NiO nanoparticles via pulsed laser ablation in deionised water and their antibacterial activity", *Appl. Phys. A*, 123 (2017) 1-10.

[2] V. Iacono et al., "Pulsed laser ablation production of Ni/NiO nanoelectrocatalysts for oxygen evolution reaction", *APL Energy*, 1 (2023) 1-8.

[3] K.A. Altammar, "A review on nanoparticles: characteristics, synthesis, applications, and challenges", *Front. Microbiol.*, 14 (2023) 1-20.

[4] N.A. Hussain, L.Y. Abbas and L.A. Latif, "Preparation of Nickel Oxide Microparticles by Pulsed Laser Ablation and Application to Gas Sensors", *Eng. Technol. J.*, 39(6) (2021) 1011-1018.

[5] S.N. Rashid et al., "Synthesized Zinc Nanoparticles via Pulsed Laser Ablation: Characterization and Antibacterial Activity", *Karbala Int. J. Mod. Sci.*, 8(3) (2022) 462-476.

[6] J. Kim et al., "The influence of laser wavelength and fluence on palladium nanoparticles produced by pulsed laser ablation in deionized water", *Solid State Sci.*, 37 (2014) 96-102.

[7] F. Seifikar et al., "One step synthesis of stable nanofluids of Cu, Ag, Au, Ni, Pd, and Pt in PEG using laser ablation in liquids method and study of their capability in solar-thermal conversion", *Sol. Ener.*, 246 (2022) 74-88.

[8] K.S. Khashan et al., "Influence of laser energy on the optoelectronic properties of NiO/Si heterojunction", *J. Phys. Conf. Ser.*, 1795 (2021) 1-6.

[9] M. Safa et al., "Characterizing nickel oxide nanostructures produced by laser ablation method: effects of laser fluence", *Appl. Phys. A*, 125 (2019) 1-9.

[10] A. Baladi and R. Mamoory, "Effect of Laser Wavelength and Ablation Time on Pulsed Laser Ablation Synthesis of Al Nanoparticles in Ethanol", *Int. J. Mod. Phys.: Conf. Ser.*, 5 (2012) 58-65.

[11] A.M. Mostafa and E.A. Mwafy, "The effect of laser fluence for enhancing the antibacterial activity of NiO nanoparticles by pulsed laser ablation in liquid media", *Enviro. Nanotech. Monitor. Manag.*, 14 (2020) 1-8.

[12] H. Huang et al., "Pulsed laser ablation of bulk target and particle products in liquid for nanomaterial fabrication", *AIP Adv.*, 9 (2019) 1-9.

[13] N.I.S. Yahaya et al., "Synthesis of nickel nanoparticles by pulsed laser ablation in different liquid media", *Int. Laser Technol. Opt. Symp.*, 2432 (2023) 1-9.

[14] C. Shalichah and A. Khumaeni, "Synthesis of nickel nanoparticles by pulse laser ablation method using Nd: YAG laser", *IOP J. Phys.: Conf. Ser.*, 1025 (2018) 1-4.

[15] N. Jaji et al., "Advanced nickel nanoparticles technology: From synthesis to applications", *Nanotech. Rev.*, 9 (2020) 1456-1480.

[16] W. Giurlani, M. Innocenti and A. Lavacchi, "X-ray Microanalysis of Precious Metal Thin Films: Thickness and Composition Determination", *Coatings*, 8(84) (2018) 1-12.

[17] M.R. Hassani et al., "Synthesis and Applications of Nickel Nanoparticles (NiNPs) - Comprehensive Review", *J. Ultra Chem.*, 19(1) (2023) 9-37.

[18] J. Wawrzyniak et al., "Laser-Assisted Synthesis and Oxygen Generation of Nickel Nanoparticles", *Materials*, 13 (2020) 1-13.

[19] M.G. Berhe and Y.T. Gebreslassie, "Biomedical Applications of Biosynthesized Nickel Oxide Nanoparticles", *Int. J. Nanomed.*, 18 (2023) 4229-4251.

[20] M. Aftab et al., "Effect of Molarity on the Structure, Optical Properties, and Surface Morphology of (002)-Oriented Ni_2O_3 Thin Films Deposited via Spray Pyrolysis", *Proc. Pakistan Acad. Sci.: A. Phys. Comput. Sci.*, 57(2) (2020) 51-74.

[21] M.K. Khalaf, F.J. Kadhim and O.A. Hammadi, "Fabrication of UV Photodetector from Nickel Oxide Nanoparticles Deposited on Silicon Substrate by Closed-Field Unbalanced Dual Magnetron Sputtering Techniques", *Opt. Quantum Electron.*, 47(12) (2015) 3805-3813.

[22] A.M. Hameed and M.A. Hameed, "Highly-Pure Nanostructured Metal Oxide Multilayer Structure Prepared by DC Reactive Magnetron Sputtering Technique", *Iraqi J. Appl. Phys.*, 18(4) (2022) 9-14.

[23] M.A. Hameed, S.H. Faisal, R.H. Turki, "Characterization of Multilayer Highly-Pure Metal Oxide Structures Prepared by DC Reactive Magnetron Sputtering Technique", *Iraqi J. Appl. Phys.*, 16(4) (2020) 25-30

[24] A.M. Hameed and M.A. Hameed, "Spectroscopic characteristics of highly pure metal oxide nanostructures prepared by DC reactive magnetron sputtering technique", *Emerg. Mater.*, 6 (2022) 627-633.

[25] L.E. Smart and E.A. Moore, **"Solid State Chemistry: An Introduction"**, 3rd ed., Taylor & Francis, (2005), p. 105.

[26] S.N. Rashid et al., "Evaluation of Laser Influence on Optical Properties of Magnesium Oxide Thin Films Prepared by Drop Casting Method", *Iraqi J. Appl. Phys.*, 19(2) (2023) 33-37.

[27] J. Singh, **"Optical Properties of Materials and Their Applications"**, 2nd ed., John Wiley & Sons Ltd. (2020), p. 69.

[28] K.S. Khashan et al., "Synthesis, characterization and antibacterial activity of colloidal NiO nanoparticles", *Pakistan J. Pharm. Sci.*, 29(2) (2016) 541-546.

[29] S.D. Khairnar and V.S. Shrivastava, "Facile synthesis of nickel oxide nanoparticles for the degradation of Methylene blue and Rhodamine B dye: a comparative study", *J. Taibah Univ. Sci.*, 13(1) (2019) 1108-1118.

Table (1) XRD analysis results of prepared NPs

λ (nm)	NPs	Phase	2θ (deg)	hkl	β (deg)	d (nm)	D (nm)	JCPDS Card No.
1064	NiO	Cubic	37.49	111	0.3	0.239609	27.95335	47-1049
	NiO	Cubic	42.49	200	0.4	0.212498	21.30059	47-1049
	Ni	Cubic	46.73	111	0.2	0.194157	43.25283	00-001-1260
	Ni	Cubic	52.39	002	0.4	0.174434	22.12533	00-001-1260
	NiO	Cubic	63.41	220	0.4	0.146514	23.33545	47-1049
532	NiO	Cubic	38.41	111	0.8	0.234079	10.51148	47-1049
	NiO	Cubic	42.79	200	0.5	0.211077	17.05789	47-1049
	Ni	Cubic	45.25	111	0.3	0.200157	28.67761	00-001-1260
	Ni	Cubic	53.78	002	0.2	0.170249	44.51959	00-001-1260
	NiO	Cubic	62.57	220	0.3	0.148278	30.9745	47-1049
	Ni_2O_3	Hexagonal	66.97	004	0.35	0.139564	27.2042	00-01-0481
355	NiO	Cubic	37.45	111	0.4	0.239856	20.96253	47-1049
	NiO	Cubic	43.39	200	0.15	0.208296	56.9773	47-1049
	Ni	Cubic	44.75	111	0.2	0.202277	42.93874	00-001-1260
	Ni_2O_3	Hexagonal	56.17	202	0.1	0.165099	12.82479	00-01-0481
	NiO	Cubic	62.17	220	0.1	0.148641	15.47332	47-1049

Table (2) EDX analysis results of prepared NPs

λ (nm)	Element	k-ratio	Weight (%)	Atomic (%)
1064	O	48.84	20.65	0.00515
	Ni	51.16	79.35	0.03938
532	O	76.95	47.64	0.00447
	Ni	23.05	52.36	0.00804
355	O	93.56	79.83	0.01501
	Ni	6.44	20.17	0.00481

IRAQI JOURNAL OF APPLIED PHYSICS Vol. 20, No. 3, July-September 2024, pp. 485-492

Enhanced Gas Sensing Performance of Plasma-Treated Tin-Zinc–Oxide Thin Films Deposited by Spray Pyrolysis

Amer A. Ramadhan [1]
Moahmmed M. Hameed [2]
Moahmmed O. Salman [3]
Eman M. Nasir [1]

[1] *Department of Physics, College of Science, University of Baghdad, Baghdad, IRAQ*
[2] *Ministry of Higher Education and Scientific Research, Baghdad, IRAQ*
[3] *Department of Medical Physics, College of Applied Sciences, University of Fallujah, Fallujah, IRAQ*

This study explores the impact of plasma treatment on the gas sensing capabilities of tin-zinc oxide (SZO) composite thin films, fabricated through spray pyrolysis. It investigates variations in Sn atomic ratios, ranging from 0.0 to 0.6. The study explores the effects of plasma etching, utilizing cold plasma induced by a plasma torch, on the morphological and electrical characteristics of the prepared SZO films. Findings, revealed by Field Emission Scanning Electron Microscopy (FE-SEM), illustrates a noteworthy porous structure with uniformly sized spherical nanoparticles. The introduction of plasma induces significant surface porosity, thereby enhancing gas sensing performance through the porous SZO layer. Testing against NO_2 gas indicates an optimum operating temperature of 150°C. These results emphasize the effectiveness of the plasma exposure method in significantly improving the efficiency of NO_2 gas sensing, marking a crucial advancement in sensor technology.

Keywords: Tin-zinc oxide; Gas sensing; Plasma treatment; Spray pyrolysis
Received: 12 February 2024; **Revised:** 05 May 2024; **Accepted:** 12 May 2024

1. Introduction

Gas sensors with high sensitivity across a wide range of gas concentrations are essential for various applications, including indoor safety and environmental monitoring [1,2]. Among the materials investigated for gas sensing applications, zinc oxide (ZnO) nanostructures have garnered considerable attention [3]. The utilization of porous thin film structures enhances their interaction with gas molecules due to their enlarged surface area, offering high sensitivity and improve selectivity to target gases. Altering porous structures in fabricated thin films through adjustments deposition parameter enhances the functionality of resulting devices [4]. Tin-zinc oxide (SnZnO) composite films possess distinct physical and chemical properties suitable for gas sensor applications, demonstrating sensitivity to various gases [5]. Spray pyrolysis stands out as a popular, cost-effective, and easily controllable technique for fabricating thin films, particularly metal oxides [6,7]. Nevertheless, defects in prepared SnZnO films may compromise gas sensing efficiency [8]. Researchers employ various post-deposition processing techniques to address these challenges and enhance sensor performance [9]. Among these techniques, plasma processing exhibits significant potential in improving gas sensing performance [10]. Plasma etching involves bombarding material surfaces with active ions, thereby altering surface structure parameters such as roughness and crystalline grain size, consequently impacting gas sensing properties [11,12].

Despite the potential benefits, limited studies have specifically investigated the effect of plasma treatment on SnZnO films synthesized via spray pyrolysis. Understanding the influence of plasma treatment on the gas sensing performance of SnZnO films is fundamental for modifying their properties to meet specific gas sensing application requirements [13]. Zinc stanate (Zn_2SnO_4) stands out as a significant ternary oxide in numerous applications [14]. Among its phases, Zn_2SnO_4 exhibits a unique crystal structure and chemical composition, be suitable for gas sensing applications, as evidenced in previous studies [15]. Zinc stanate thin films can be prepared using various techniques, including chemical vapor deposition and spray pyrolysis. Plasma treatment has the potential to modify the surface properties of the active layer for gas sensing by enhancing crystallinity, surface morphology, and gas adsorption capability [16]. In 2020, Zhang et al. investigated the doping effect of copper and iron on zinc Stanate and observed improved gas sensing performance towards specific target gases [15,17].

This paper aims to investigate the effect of plasma treatment on the gas sensing performance of SnZnO films prepared by spray pyrolysis. The changes in the structural, and morphological properties of the films after plasma etching and correlate them with the gas sensing response at different concentration ranges were investigated. This study provide a strategy for the design and optimization of gas sensing materials.

2. Experimental Part

Composite thin films of $(ZnO)_{1-x}(SnO_2)_x$ at various molar ratios were synthesized employing a spray pyrolysis technique. A 0.1 M aqueous solution comprising zinc chloride ($ZnCl_2$) and tin chloride $SnCl_2$ (sourced from Sigma-Aldrich) was prepared in distilled water using a magnetic stirrer. Prior to application, the solutions underwent filtration using filter paper. The thin films were deposited onto glass slides via spray deposition, with the substrate temperature maintained at 500°C. The spray nozzle was positioned 30cm above the substrates in a vertical configuration. Spraying was conducted at a rate of 1 mL/min using compressed air at 4 bar pressure. The thickness of the films, approximately 200nm, was determined using Angstrom TFProbe optical spectroscopic reflectometer. The crystalline structure of the prepared samples was analyzed using Shimadzu XRD-6000 X-ray Diffraction system. Surface morphology was assessed using a ZEISS Sigma field-emission scanning electron microscope.

To enhance the gas sensing properties of SZO thin films, a novel approach utilizing a plasma torch was employed. High alternating voltage operating at 10kV, and a controlled flow of argon were utilized. The deposited SZO thin films underwent plasma treatment at a distance of 2 cm from the plasma orifice for 3 minutes. The argon flow rate was adjusted to optimize the plasma treatment process to 1 SLM. This plasma treatment induced surface modifications.

The gas sensing efficiency of as-prepared and plasma-modified SZO samples was evaluated against NO_2 gas at different concentrations and operating temperatures of 50, 100, 150, and 200°C. Initially, the as-deposited samples were tested, followed by the plasma-treated samples to assess the effect of plasma etching on their performance. The change in electrical resistance was determined as the response of the fabricated gas sensors for each operating temperature within the gas concentration range of 2 to 100 ppm. The measurements were conducted in a controlled environment using a gas chamber with precise concentration control.

3. Results and Discussion

The structural properties of SZO thin films were investigated using x-ray diffraction. Figure (1) shows the diffraction patterns of SZO thin films deposited at different Sn molar ratios on glass substrates. These patterns reveal polycrystalline structures and distinctive phases depending on the Sn molar ratio for the started precursor. Specifically, when the Sn molar ratio was x=0.2, the diffraction pattern showed ZnO phase of hexagonal crystal (according to the ICDD card number 36-1451). This suggests successful incorporation of Sn atoms into the ZnO lattice without significant alteration to the host lattice structure at lower Sn ratios.

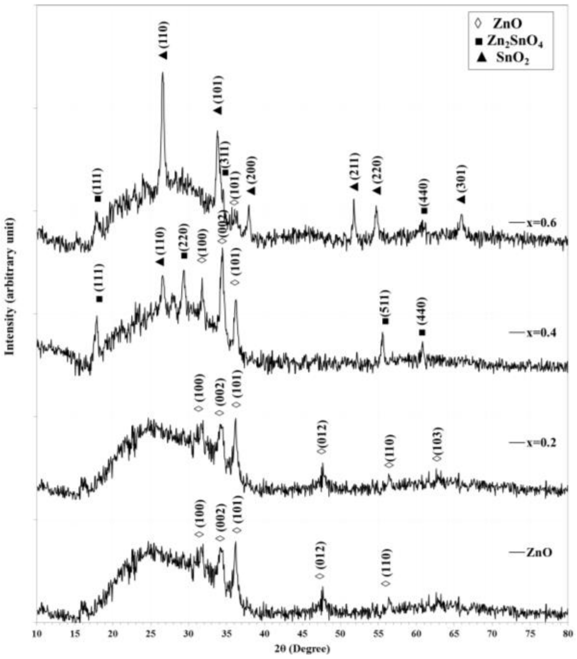

Fig. (1) XRD patterns for SZO thin films at different Sn:Zn atomic ratio

Increasing the Sn ratio to x=0.4, additional peaks corresponding to the Zn_2SnO_4 and SnO_2 phases (according to the ICDD card numbers 24-1470 and 41-1445, respectively) emerged alongside the ZnO diffraction lines. This observation aligns with the stoichiometric ratio required for the formation of Zn_2SnO_4 (Sn:Zn=1:2), indicating a complex composite structure with the coexistence of multiple phases within the thin film.

Further increase in the Sn ratio to x=0.6 led to enhanced crystallinity of the SnO_2 phase while reducing the intensity of the Zn_2SnO_4 phase. The prominent peaks of the SnO_2 phase, accompanied by smaller peaks corresponding to other phases, signify higher Sn content within the film. Consequently, the phase composition of the SZO thin film was observed to be highly influenced by the atomic ratio of Zn to Sn, with different compositions resulting in the formation of distinct phases.

These findings are consistent with previous research employing alternative techniques to achieve similar Zn:Sn ratios. For example, Kurz et al. utilized sol-gel spin coating at a Zn:Sn molar ratio of 32:68, leading to the formation of Zn_2SnO_4 [18]. Similarly, Sun et al. achieved Zn_2SnO_4 formation through solvothermal synthesis, employing a Zn:Sn molar ratio of 1:2 [19]. The reproducibility of Zn_2SnO_4 formation across different techniques and ratios supports the reliability of the observed phase composition in the SZO thin film system.

The phase diagram of the Zn-Sn-O system provides valuable insights into the composition-dependent behavior of this ternary oxide system. In order to explore the phase distribution and composition ranges within this system, a two-dimensional x-ray analysis was conducted utilizing

XPowder software, which shows the phase distribution within the Zn-Sn-O system. This analysis, as illustrated in Fig. (3), offers the point of phases variations. The dominant phase was ZnO at x=0.1. Interestingly, this phase remained predominant even at higher Sn content. This suggests that ZnO exhibits the highest stability compared to other phases within this system. At the composition range of x= 0.2 to 0.3, the XRD analysis showed the emergence of a new phase of Zn_2SnO_4. This phase, is attends within this range indicates a compositional preference for a specific zinc to tin ratio, around x=0.4. While, increasing the x ratio more than 0.4 makes the dominant phase is the SnO_2.

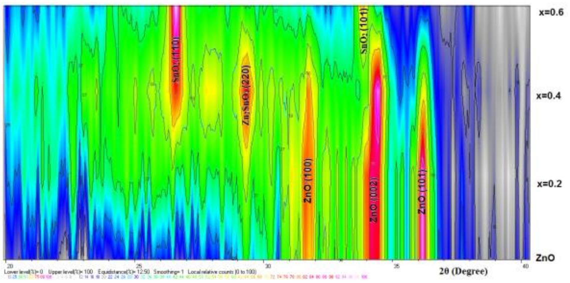

Fig. (2) 2D XRD analysis attained by XPowder software for Zn-Sn-O system with the Sn malar ratio

The FE-SEM was conducted to examine the surface morphology of the prepared thin films. Figure (3) displays morphological images of the ZnO and SZO composite thin films. The fabricated ZnO thin films constructed from spherical particles with a similar size around 100 nm diameter. These spherical nanoparticles were closely interconnected, contributing to the overall porous architecture. These characteristics are advantageous for gas sensing applications, as the performance of such sensors heavily relies on nanostructure shapes, surface-to-volume ratios, and the connectivity between adjacent nanoparticles [20]. The sample composed with 0.2 atomic ratio of Sn cause to decrease the porosity due to enhanced particle attachment. Increasing in the Sn ratio to 0.4 resulted in the presence of two distinct particle types. Larger particles appeared as Irregular rock-like shapes of diameter about 600 nm, alongside the smaller particles measuring around 100 nm, indicating the existence of two phases within the structure. Lastly, the sample prepared with 0.6 Sn ratio displayed particles of 200 nm diameter attached with nanoparticles forming whole structure. The porosity significantly reduced at this ratio.

Figure (4) shows the FE-SEM images of both ZnO and SZO composite thin films subsequent to plasma treatment. The ZnO film exhibited a uniformly distributed porous structure comprising spherical particles of approximately 100 nm in diameter. The plasma-treated samples exhibited noteworthy enhancements in porosity compared to the untreated SZO samples. The spherical nanoparticles exhibited close interconnection act as channels for electrical connection which is a significant affect the gas sensing mechanism. The alterations in surface and interfacial properties induced by plasma treatment facilitated gas adsorption, thereby leading to improved sensitivity towards target gases. Such attributes confer several advantages for gas sensing applications, as sensor performance is markedly influenced by the size and morphology of nanostructures, as well as the interconnectivity among adjacent nanoparticles [21]. The barrier height across the charge carriers within the interconnected channels is depending upon the formation of a depletion layer subsequent to electron extraction by adsorbed oxidized molecules on the sample surface. This phenomenon leads to alterations in the energy barrier across the channels relative to gas concentration. Consequently, this process effectively enhances the gas sensing performance [22].

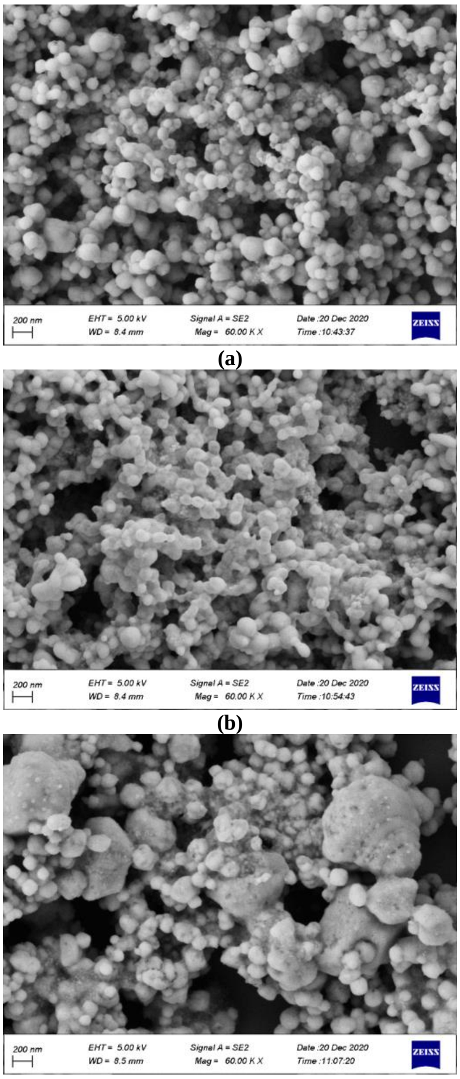

(a)

(b)

(c)

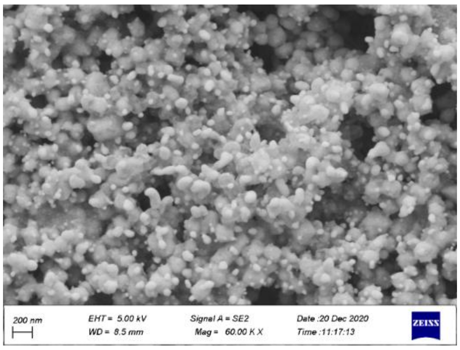

(d)

Fig. (3) Top view of FE-SEM images for ZnO layer (a) SZO composite thin films at x= 0.2 (b), x= 0.4 (c), and x=0.6 (d)

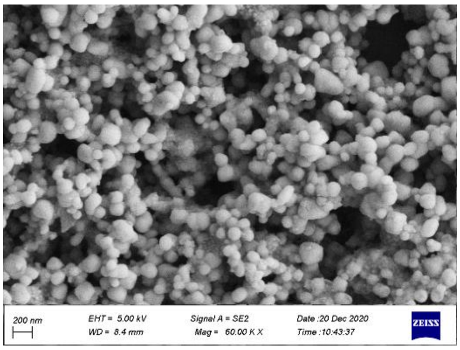

(a)

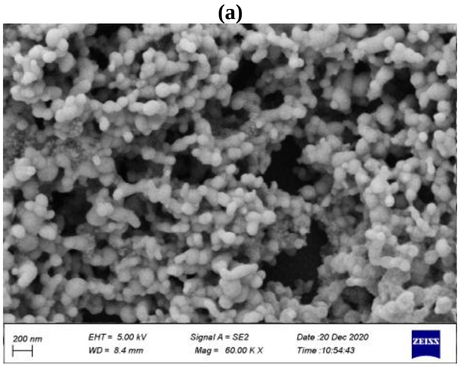

(b)

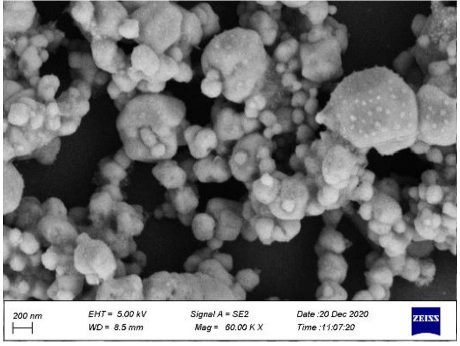

(c)

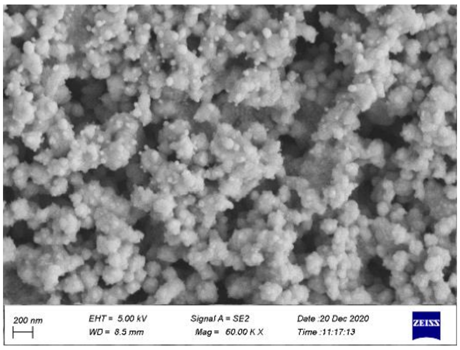

(d)

Fig. (4) The FE-SEM images for ZnO thin film after plasma treatment (a) SZO composite thin films at x=0.2 (b), x=0.4 (b), and x=0.6 (c)

Figures (5) depicts the variation of resistance for the as prepared SZO thin films, which was prepared under various tin ratio, while subjecting the samples to a 20 ppm NO_2 gas at 150°C working temperature. Across all samples, exposed to the gas resulted in an increase in resistance. This phenomenon can be explained by the extraction of a more electrons from material due to the oxidation reaction by the target gas. Gas adsorption led to a reduction in sample conductivity due to two main factors. Firstly, it caused a decrease in the charge carriers concentration, and secondly, it reduce the mobility of carriers by forming a surface depletion layer, which built a potential barrier across the charge carriers at the grain boundaries. The sensitivity various according to surface morphology, so the largest variation occurred for the x=0.2 sample. To enhance sensing behaviour, it is crucial to fine-tune the morphology of the sensing materials and establish well-defined channels of connection between the nanostructures. By optimizing these factors, gas sensing performance can be significantly improved [23].

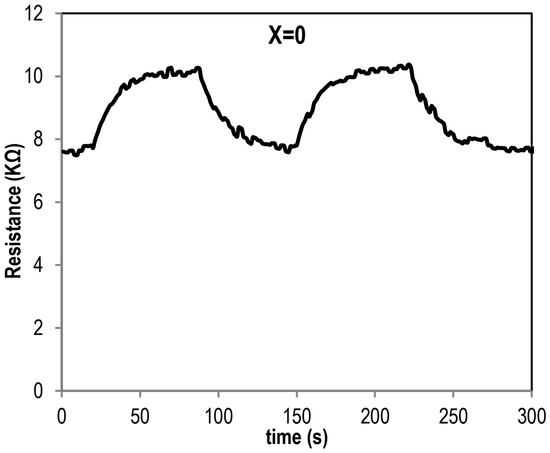

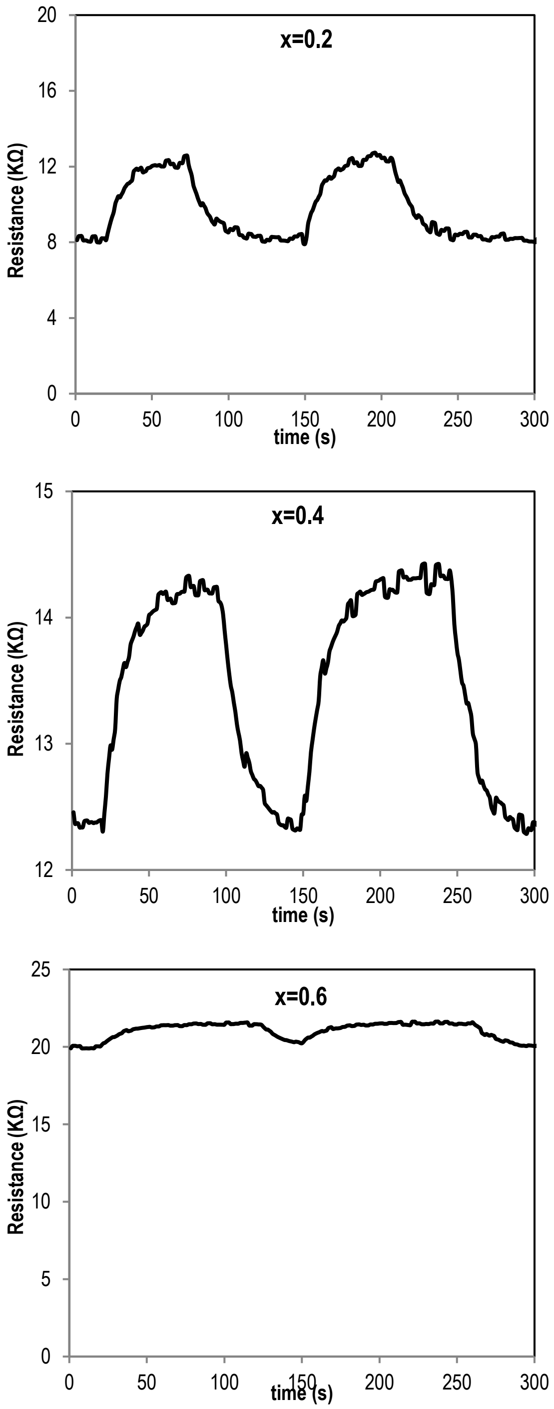

Fig. (5) Variation of resistance of the SZO-based sensor prepared at different x against 20 ppm NO_2 gas exposure at 150°C working temperature

Figures (6) displays the variation of resistance with time for sensor based on the plasma treated-SZO thin films prepared at different x against 20 ppm NO_2 gas at 150°C. The variation in resistance fluctuation improved after plasma exposure specially for the x=0.2 sample compared to the as prepared samples due to the variation in samples porosity, so increase the surface area that exposed to NO_2 gas.

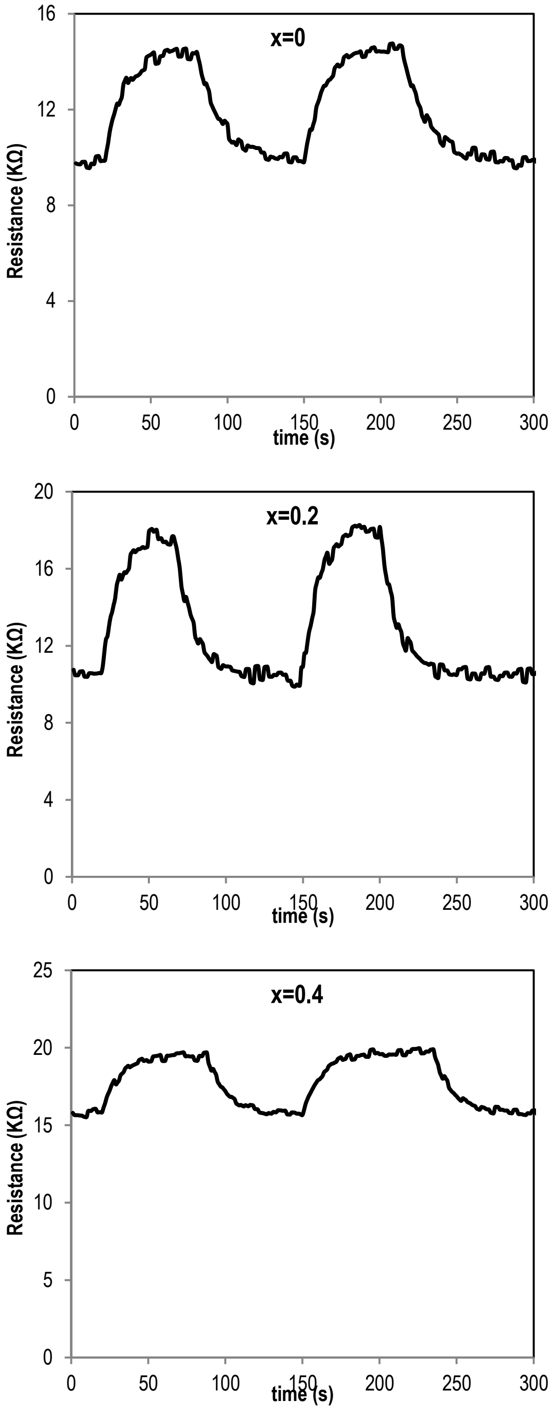

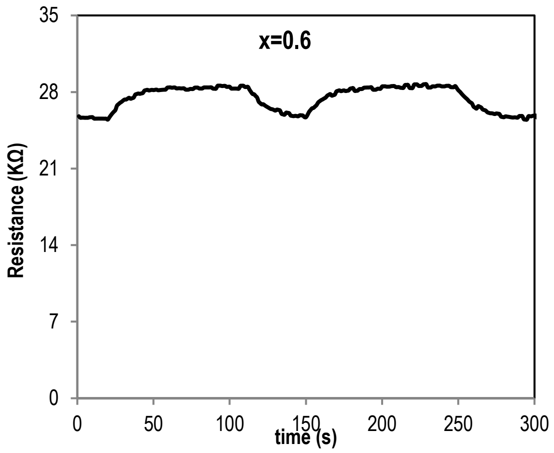

Fig. (6) Variation of resistance of the SZO-based sensor prepared at different x against 20 ppm NO_2 gas exposure at 150°C after plasma treatment

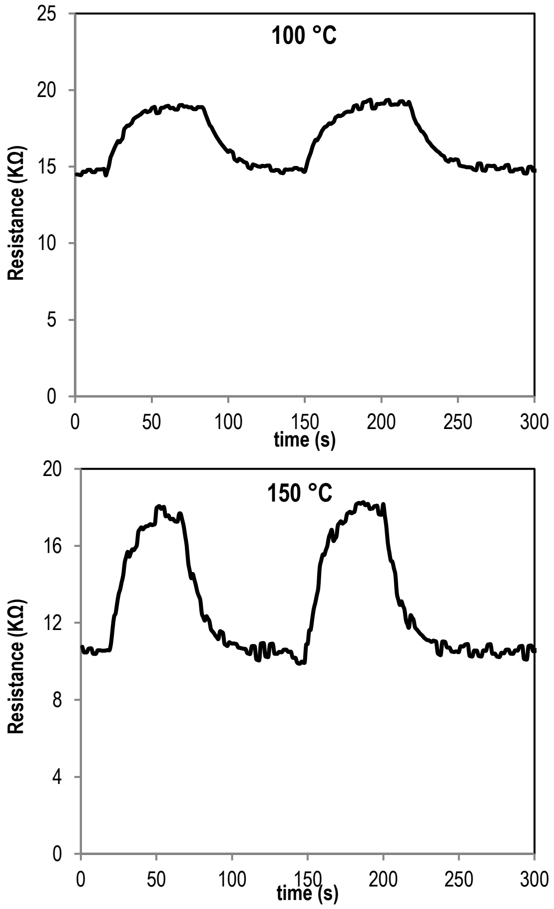

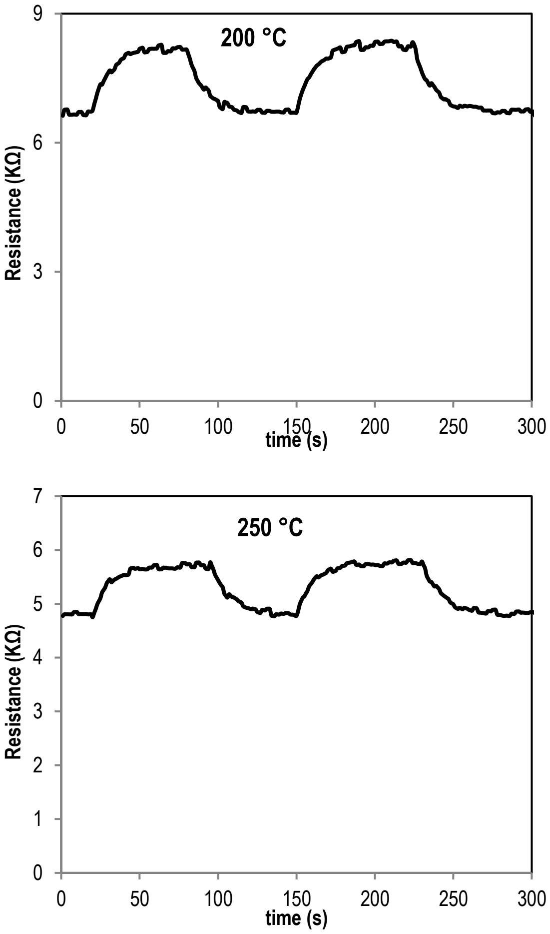

Fig. (7) Variation of resistance against 20 ppm NO_2 at different working temperatures for the SZO-based sensor at x=0.2 after plasma treatment

Figure (8a) illustrates a comparison between sensitivity before and after plasma treatment against 20 ppm NO_2 with the Sn ratio at 150°C operating temperature. The optimum sensitivity appeared for x=0.2, and the sensitivity improved after plasma treatment for all samples, but with different ratios, and the best enhancement was 1.4 folds for x=0.2. Figure (8b) illustrates the changes in gas sensitivity to 20 ppm NO_2 gas for x=0.2 following plasma treatment at different working temperatures. The highly dependence of sensitivity on the temperature due to variations in chemical response rates and gas desorption. The highest sensitivity is observed at an optimal temperature of 150°C. At lower temperatures, the sensitivity is constrained by the chemical response speed, while at higher temperatures, which is governed throughout the desorption of gas particles. A balance between these two processes is achieved at a moderate point, resulting in the sensor's optimal sensitivity value [24].

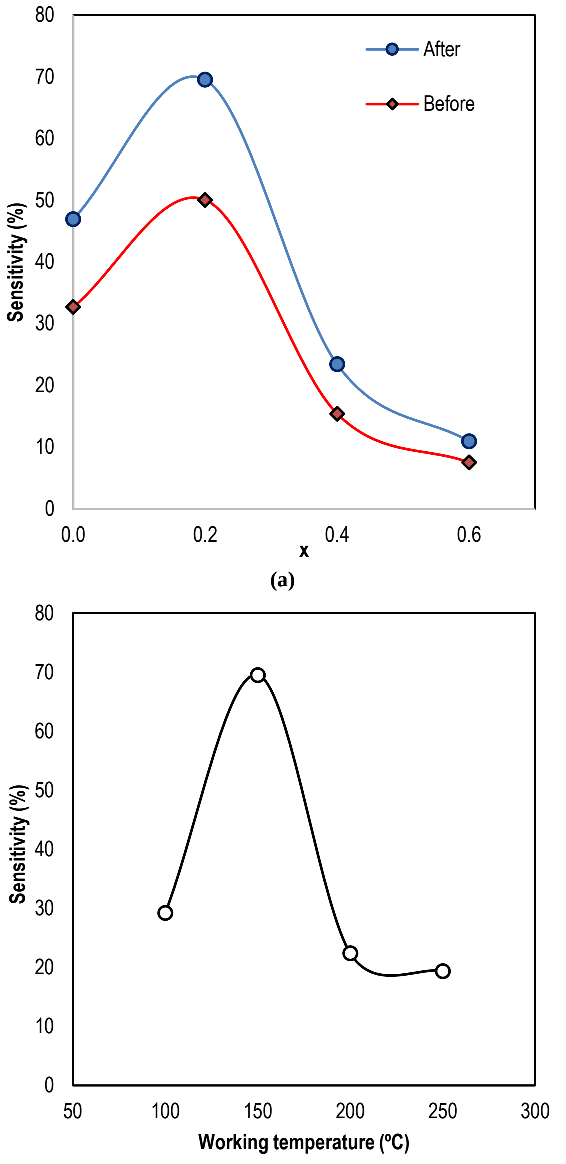

(a)

(b)

Fig. (8) Variation of sensitivity against 20 ppm NO_2 :(a) at 150°C against Sn ratio before and after plasma treatment, (b) for x=0.2 after plasma treatment with operating temperature

Figure (9) shows the sample response of sensor based on SZO with the optimum ratio of x=0.2 at 150°C against different gas concentrations. It seem that the response depend on gas concentration within the range of 5 to 40 ppm. The depletion layer thickness is influenced by the amount of adsorbed gas, resulting in an elevation of the energy barrier concerning gas concentration. Therefore, changes in sample resistance serve as an indicator of gas concentration [25].

Figure (10) shows the best exponent-curve fitting of variation of response for the SZO sample at x=0.2 after plasma treatment against the concentration of NO_2 (5-40 ppm) at 150°C operating temperature. The normalized fitting of gas sensitivity against gas concentration was $y = 0.6671x^{0.3263}$ with high fitting accuracy of $R^2=0.9533$.

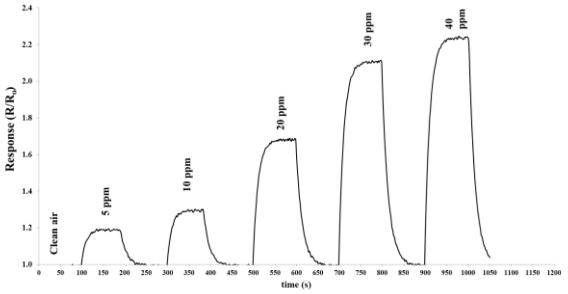

Fig. (9) The sensor response of SZO prepared at x=0.2 against different NO_2 gas concentrations at 150°C operating temperature

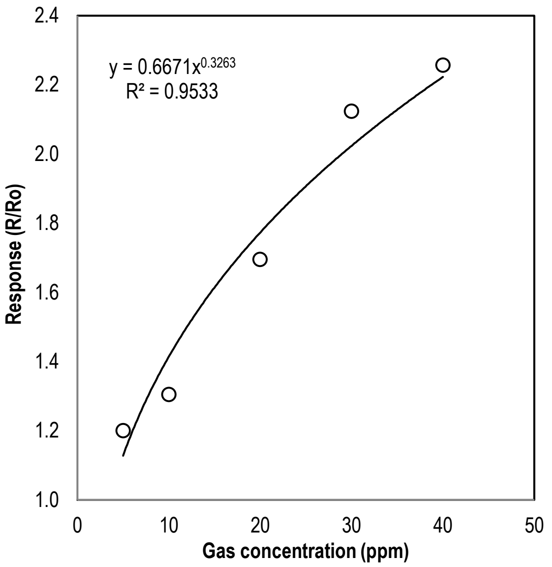

Fig. (10) The fitting of variation of response for the SZO sample at x=0.2 after plasma treatment with gas concentration at 150°C operating temperature

4. Conclusions

The investigation into composition-dependent of SZO nanocomposites thin films deposited via spray pyrolysis shows emergence of Zn_2SnO_4 at 0.4 Sn ratio. Plasma etching cause significant morphological changes in films, enhancing sensing capabilities. Improved sensitivity and response to NO_2 gas are observed across different concentrations and operating temperatures, notably peaking at 150 °C. Moreover, gas sensors based on SZO nanocomposites with x=0.4 exhibit enhanced sensitivity and response compared to others, underscoring the essential Sn ratio in determining gas sensing properties. These findings underscore the efficacy of plasma exposure in enhancing gas sensitivity of prepared SZO thin film toward NO_2 across various conditions.

References

[1] K. Anand et al., "Hydrogen sensor based on graphene/ZnO nanocomposite", *Sens. Actuat. B: Chem.*, 195 (2014) 409-415.

[2] M. Laurenti and V. Cauda, "Porous zinc oxide thin films: Synthesis approaches and applications", *Coatings*, 8(2) (2018) 67.

[3] W. Zhang et al., "Three-terminal nonvolatile memory photodetectors based on rationally

engineered heterostructured tin zinc oxide nanowires", *Curr. Appl. Phys.*, 48 (2023) 34-41.

[4] M.O. Salman, M.A. Kadhim and A.A. Khalefa, "CdO:SnO_2 Composite UV-Assisted Room Temperature Ozone Sensor", *Iraqi J. Sci.*, 64(3) (2023) 1190-1202.

[5] Z. Chen et al., "Performance improvement of tin-doped zinc oxide thin-film transistor by novel channel modulation layer of indium tin oxide/tin zinc oxide", *Jap. J. Appl. Phys.*, 54(4S) (2015) 04DF03.

[6] M. Thirumoorthi and J.T.J. Prakash, "Doping effects on physical properties of (101) oriented tin zinc oxide thin films prepared by nebulizer spray pyrolysis method", *Mater. Sci. Eng. B*, 248 (2019) 114402.

[7] P. Chesler et al., "Tin–Zinc oxide composite ceramics for selective CO sensing", *Ceram. Int.*, 42(15) (2016) 16677-16684.

[8] A. Ani et al., "Evaluation of spray pyrolysed In:ZnO nanostructures for CO gas sensing at low concentration", *J. Mater. Sci.: Mater. in Electron.*, 32(17) (2021) 22599-22616.

[9] L.H. Kathwate et al., "Ammonia gas sensing properties of Al doped ZnO thin films", *Sens. Actuat. A: Phys.*, 313 (2020) 112193.

[10] K. Hu et al., "Enhanced hydrogen gas sensing properties of Pd-doped SnO_2 nanofibres by Ar plasma treatment", *Ceram. Int.*, 46(2) (2020) 1609-1614.

[11] S. Sahoo et al., "A review on supercapacitors based on plasma enhanced chemical vapor deposited vertical graphene arrays", *J. Ener. Stor.*, 53 (2022) 105212.

[12] K. Hu et al., "Ar plasma treatment on ZnO–SnO_2 heterojunction nanofibers and its enhancement mechanism of hydrogen gas sensing", *Ceram. Int.*, 46(13) (2020) 21439-21447.

[13] S. Dabbabi et al., "Fabrication and Characterization of Sensitive Room Temperature NO_2 Gas Sensor Based on $ZnSnO_3$ Thin Film", *phys. stat. sol. (a)*, 216(16) (2019) 1900205.

[14] S. Dinesh et al., "Hydrothermal synthesis of zinc stannate (Zn_2SnO_4) nanoparticles and its application towards photocatalytic and antibacterial activity", *J. Mater. Sci.: Mater. Electron.*, 27(9) (2016) 9668-9675.

[15] Z. Lu et al., "Electrospun ZnO–SnO_2 Composite Nanofibers and Enhanced Sensing Properties to SF_6 Decomposition Byproduct H_2S", *Front. Chem.*, 6 (2018) in "Advanced Nanomaterials for Sensing Applications" Z. Wang, W. Zeng and Z. Li (ed.).

[16] A. Rovisco et al., "Microwave-Assisted Synthesis of Zn_2SnO_4 Nanostructures for Photodegradation of Rhodamine B under UV and Sunlight", *Nanomater.*, 12(12) (2022) 2119.

[17] L. Chen et al., "Regulation of intrinsic physicochemical properties of metal oxide nanomaterials for energy conversion and environmental detection applications", *J. Mater. Chem. A*, 8(34) (2020) 17326-17359.

[18] A. Kurz and M.A. Aegerter, "Novel transparent conducting sol-gel oxide coatings", *Thin Solid Films*, 516 (2008) 4513-4518.

[19] G. Sun, S. Zhang and Y. Li, "Solvothermal synthesis of Zn_2SnO_4 nanocrystals and their photocatalytic properties", *Int. J. Photoener.*, 2014 (2014) 25-29.

[20] P.H. Suman et al., "Comparative gas sensor response of SnO_2, SnO and Sn_3O_4 nanobelts to NO_2 and potential interferents", *Sens. Actuat. B: Chem.*, 208 (2015) 122-127.

[21] H. Du et al., "Investigation of gas sensing properties of SnO_2/In_2O_3 composite hetero-nanofibers treated by oxygen plasma", *Sens. Actuat. B: Chem.*, 206 (2015) 753-763.

[22] P. Feng et al., "Gas sensors based on semiconducting nanowire field-effect transistors", *Sensors*, 14(9) (2014) 17406-17429.

[23] Y.F. Sun, S.B. Liu and F.L. Meng, "Metal oxide nanostructures and their gas sensing properties: A review", *Sensors*, 12(3) (2012) 2610-2631.

[24] O.A. Fahad, H.S. Al-Jumaili and M.H. Suhail, "Studies on spray pyrolised nanostructured SnO_2 thin films for H_2 gas sensing application", *Adv. Enviro. Biol.*, 17(2) (2014) 125-141.

[25] A.A. Ramadhan, F.T. Ibrahim and E.M. Nasir, "The Preparing and Characterization of Nanocomposite (PTh/SWCNT) for NO_2 Gas Sensing", *J. Phys.: Conf. Ser.*, 1660 (2020) 012093.

IRAQI JOURNAL OF APPLIED PHYSICS Vol. 20, No. 3, July-September 2024, pp. 493-499

Firas J. Hameed
Isam M. Ibrahim

Department of Physics,
College of Science,
University of Baghdad,
Baghdad, IRAQ

Enhancement Cathode Electrode of PPy by GO to Applied for Supercapacitor

In this study, chemical oxidation was used to prepare polypyrrole (PPy) composites. Additionally, PPy has been treated with graphene oxide (GO) nanosheets that were produced and added in a certain ratio. The structural characteristics of the mixed polypyrrole and polypyrrole-graphene oxide were investigated. The nanocomposites were produced by adding GO to PPy in volume ratios of 10, 30, and 50%. The molecular structures of PPy, GO, and PPy-GO nanocomposites were determined. The formation of a network of polypyrrol nanofibers was confirmed. Nanocomposites were produced by doping PPy nanofibers with GO in various amounts (10%, 30%, and 50% volume ratios). According to the electrochemical experiments, the nanocomposites exhibit high pseudocapacitive activity.

Keywords: Polypyrrole (PPy); Structural properties; Supercapacitor; Capacitance
Received: 19 February 2024; **Revised:** 25 March 2024; **Accepted:** 01 April 2024

1. Introduction

Conducting polymers (CPs) exhibit the capacity to facilitate the conduction of charge current across the polymer network in electrochemical activities, given favorable conditions [1-3]. They may be used as templates because of their enormous surface area to volume ratio, long length, consistent diameter, large surface area, and low density [4,5]. Given its ease of mixing, strong conductivity, and environmental steadiness, PPy is one of the most widely used CPs [6]. The main requirement for PPy's electrical effects is bonding. Through catalytic activities that result in the process of combining various entities, such as cations, inorganic anions, natural compounds, and so forth, the expected outcome is an enhancement in the electrical conductivity of PPy [7]. The special qualities of CPs create new opportunities for mechanical operations, such as the ability to recharge batteries or create biochemical allergies. By means of the mechanism of countercharge accumulation and release brought on by redox reactions occurring in an electric field, CPs are able to store capacitance [8-12]. Researchers from all over the world are still looking closely at the introduction of electrostatic polymers. PPy is a highly specialized polymer due to its exceptional conductivity, significant storage capacity, environmental resilience, and strong chemical current [13,14]. Capacitors are commonly built by arranging a set of parallel plates that are separated by an insulating material. When voltage is introduced in series to the plates, the opposing sign's capacitive charge begins to accumulate. Although the supercapacitors have higher capacity (F), they have lower power values (mF) than these regular capacitors [15]. The research is motivated by the unique properties of conducting polymers, like Polypyrrole (PPy), which facilitate charge conduction in electrochemical activities. These polymers offer high surface area to volume ratio, strong conductivity, and environmental stability.

Aim of the work Preparation PPy nanofiber and nanocomposites from PPy with the addition of different concentrations of GO nanosheets, studying the structural characteristics for the prepared nanocomposites, to use it in electronic device (supercapacitor device application).

2-Experimental Part

The methodology defined by Yang [16] was used to construct the combination of polypyrrole nanostructure. The first stage involved evenly dispersing 0.818 g of methyl orange in 60 mL of distilled water. 2.237 g from ferric chloride were dispersed in a fluid solution including methyl orange while being stirred slowly at 80 rpm and submerged in an ice bath with the addition of 1 milliliters of pyrrole. What was mixed turned black and stirred continuously for 1 day. The precipitate underwent multiple ethanol and distilled water washes, filtering, and drying for 60 minutes.

To create a homogeneous, ready-to-use dispersion, a suitable amount of GO was dissolved in distilled water, added to PPy at volume ratios of 10, 30 and 50% then treated to ultrasonic waves for an hour.

The production of the PPy-GO as an electrode was done on a nickel foam (1x1 cm^2) substrate. Drop casting was used to deposit PPy-GO nanocomposite on nickel foam substrate in the ratios of 10%, 30%, and 50%, respectively. The generated sample (PPy-GO/nickel foam) was tested using cyclic voltammetry (CV), galvanostatic charge-discharge analysis (GCD), and electrochemical impedance spectroscopy (EIS). In a volume of 1 mL, a concentrated solution of sulphuric acid with a concentration of 100%. The electrode (PPy-GO) weighed 0.7 mg. The supercapacitor electrode sample is schematically shown in Fig. (1).

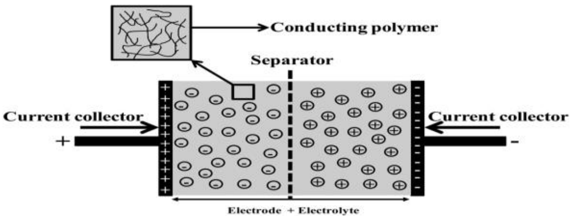

Fig. (1) A schematic of an electrochemical supercapacitor with electrodes made of a layer of conductive polymer

3-Results and Discussion

The x-ray diffraction (XRD) was employed to examine the structural characteristics of both polypyrrole (PPy) and the three different concentrations of the PPy-GO hybrid nanocomposite. XRD measurements were used to examine the composition of the composites. Figure (2) displays the PPy, PPy/GO composite's XRD patterns. The XRD pattern of pure polypyrrole (PPy) has a diffraction peak at 2θ=20.30°. This peak is characterized by poor intensity and broadness, suggesting the amorphous nature of the substance [17]. The peak intensity at 20.30° for the 10% GO composite has significantly increased and shifted to 20.80°. The increase in peak intensity may be attributed to the exfoliation of GO layers induced by ultrasonication [18].

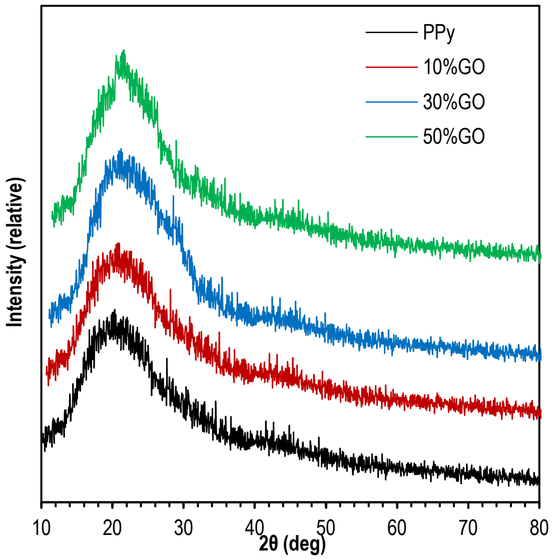

Fig. (2) XRD patterns of (a) GO, (b) PPy/GO composite and (c) Pure PPy and different percentages of PPy-GO

Polypyrrole-graphene oxide composite's active production has been confirmed using FTIR spectra. Figure (3) displays the spectra of several samples, including PPy, and PPy-GO by different percentages (10% GO, 30% GO and 50% GO). The measured signals at 3420 and 3150 cm^{-1} are attributed to PPy-GO, the hydroxyl group, and O-H bond stretching vibration [19]. The (C=O) carboxyl group is responsible for the signal at 1755 cm^{-1}. The peak at 1630 cm^{-1} is attributable to the stretching vibration of the (C-OH), the three peaks at 1090 cm^{-1}, 602 cm^{-1}, and 386 cm^{-1} are epoxide (C-O-C) [19,20]. The polypyrrole ring's N-H, C-C stretching vibration mode, and C-H deformation vibrations are each attributed to peaks in the PPy FTIR spectrum at 3630, 1540 and 1050 cm^{-1}, respectively [21,22]. The PPy-GO composite has a peak at 1090 cm^{-1}, which is a shift from the 1080 cm^{-1} peak observed in PPy-GO spectra. This shift is attributed to an interaction between PPy and GO, specifically involving the epoxide group. Additionally, the peaks at 1540 and 1680 cm^{-1} are connected to, respectively, carbonyl C=O and polypyrrole ring C=C stretching vibration. The peak previously located at 3420 cm^{-1} in PPy spectra has been shifted to 3379, 3370 and 3351 cm^{-1} at 10% GO, 30% GO, and 50% GO, respectively. This shift is a result of the interaction between PPy and GO, specifically the stretching vibration of N-H. Additionally, the peak at 3130 cm^{-1} has shifted to 3140, 3145 and 3150 cm^{-1} with different percentages of GO. This shift is attributed to the interaction between PPy and GO, specifically the stretching vibration of O-H [19,23,24].

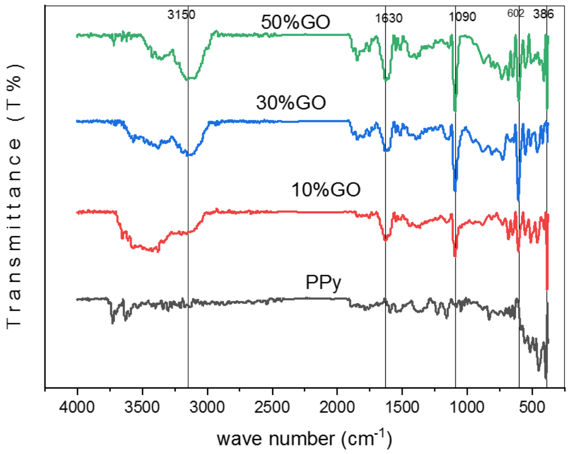

Fig. (3) FTIR spectra of PPy, 10% GO, 30% GO and 50% GO

As-made PPy and PPy-GO hybrid nanocomposite films were examined for surface morphology using the field emission scanning electron microscopy (FE-SEM) method, as shown in Fig. (4). The nanofiber shapes in the microstructure images of pure PPy in figures (4a) and (4b) are depicted at different magnifications of 350000X and 135000X, respectively. When PPy was chemically created in the method of chemical oxidation and the ice bath as previously described, it was discovered through the examination of the morphology of the material that the substance was nanofibers by the photographs.

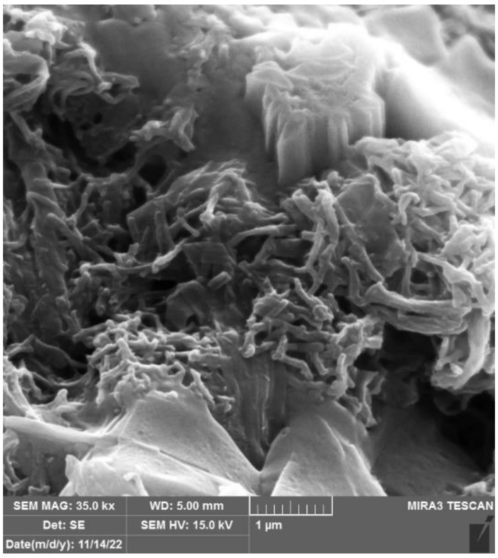

PPy

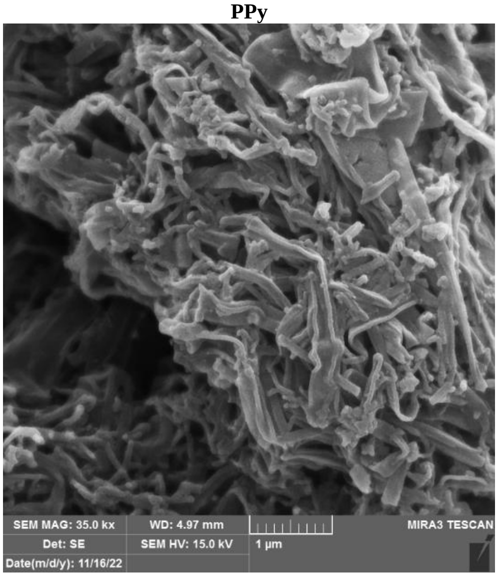

10% GO

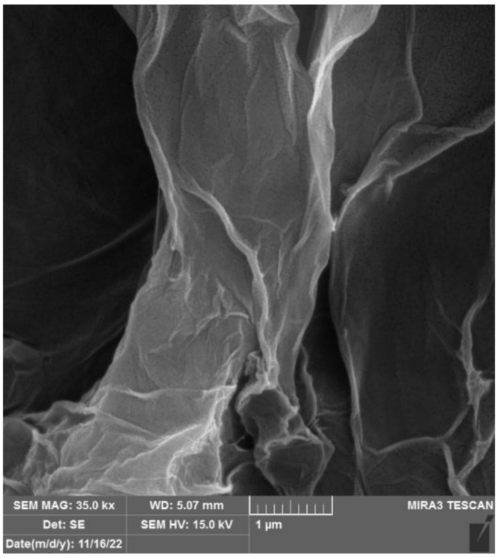

30% GO

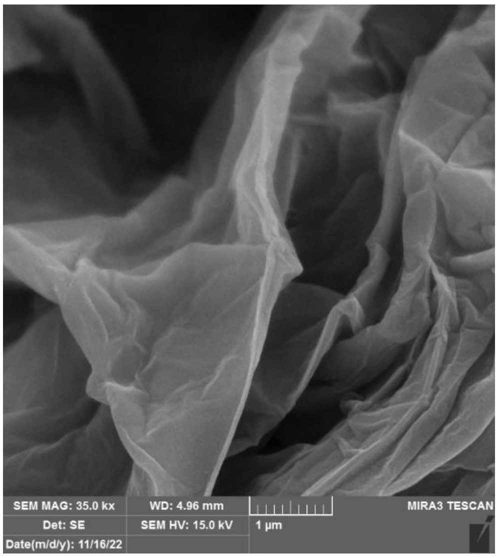

50% GO

(a)

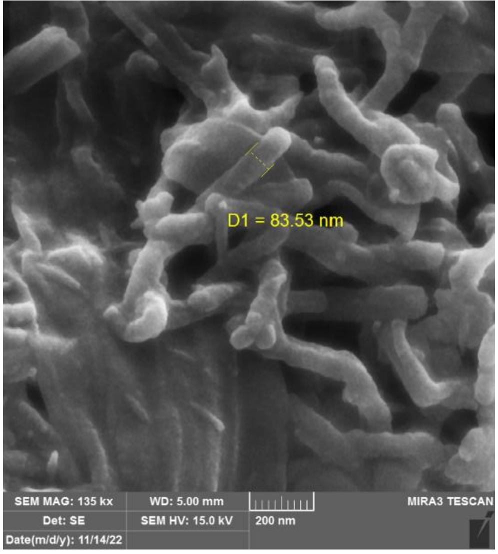

PPy

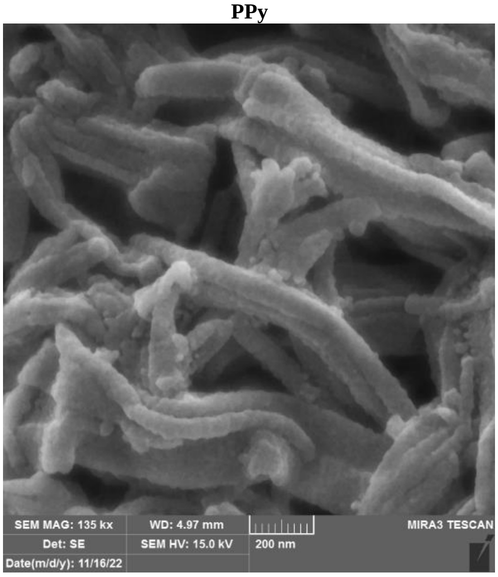

10% GO

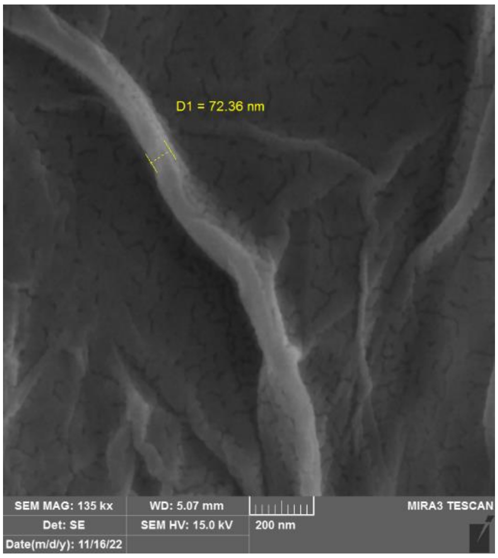

30% GO

50% GO

(b)

Fig. (4) FE-SEM images of PPy, 10% GO, 30% GO and 50% GO at (a) 35000X magnification, and (b) 135000X magnification

The shape of the PPy-GO nanocomposites, which displayed a homogeneity between PPy nanofibers and GO nanosheet morphology, is depicted in figures (4a) and (4b) at 10, 30 and 50% GO by different magnifications. The PPy constructed scaffold provides interconnected, 3D-conductive fibers/sheets in the matrix, with the majority of these nanofibers having widths between 50 and 100 nm. The PPy-GO hybrid nanocomposites exhibit the formation and aggregation of PPy fibers on the surface, due to the interactions between the fibers and GO sheets, as observed in the FE-SEM images. The outcomes of these images are nearly identical to those of the subsequent study [25,26].

Figure (5a-c) shows the results of the cyclic voltammetry examination of the PPy and PPy-GO films. We can see the anode and cathode peaks at (6.37, 8.72, 6.47, 8.67mA), (13.2, 16.4, 12.9, 16.9mA), and (19.1, 24.1, 19.9, 25.6mA), respectively, by repeatedly applying the scan rate (150, 100, 50mV). The materials exhibit electrochemical dynamism within the specified potential range, according to CV results. The electrochemical functions of both PPy and GO are incorporated into the PPy-GO combination film. The nanocomposites PPy-GO membrane has an apparent electrochemical activity observed when the voltage is set under a positive value of 0.6 V, as shown in Fig. (5). The anode electrode functions as the emitter of positive charges, The cathode electrode functions as the location where positive charge carriers are stored in the PPy and PPy-GO materials, During the discharge process, this mechanism operates. The cathode side turns black when CV forms, while the anode stays white. Unlike pure PPy, the Gaussian distribution seen in Fig. (5) highlights the notable importance of the electrochemical interaction within PPy-GO composites. The elucidation of this phenomenon may be achieved due to the synergistic effects of PPy and GO. The presence of two distinct and prominent redox peaks on each curve depicted in Fig. (5a-c) indicates the occurrence of a pseudo-capacitative characteristic in the supercapacitor. This feature is a result of the Faradaic redox reactions. The polyaniline-GO composite membrane was reported to have comparable characteristics [16,27].

Using GCD test, this electrochemical characteristic of the composite PPy-GO electrode were determined. In order to ensure optimal performance of the hybrid system, potential fluctuations for individual electrodes were recorded independently when a Ni-foam reference anode was introduced. With one and two stages for the negative and positive electrodes, respectively (protrusions present when charging and discharging), the potential variations are nearly slanting, identical to the CV data given in Fig. (5). This is due to redox reactions' possible dependent nature. A polymer that inserts anions, PPy is p-doped.

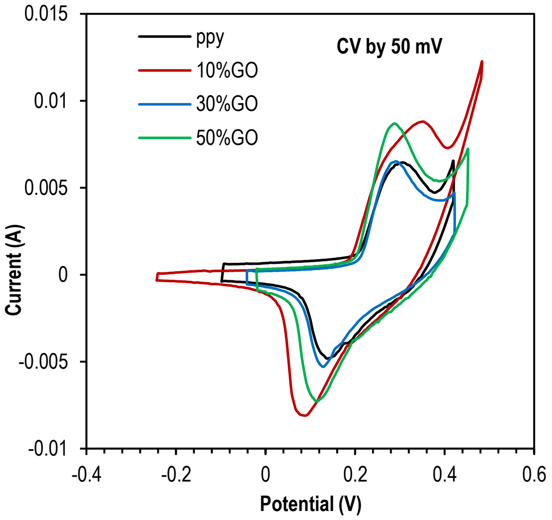

(a)

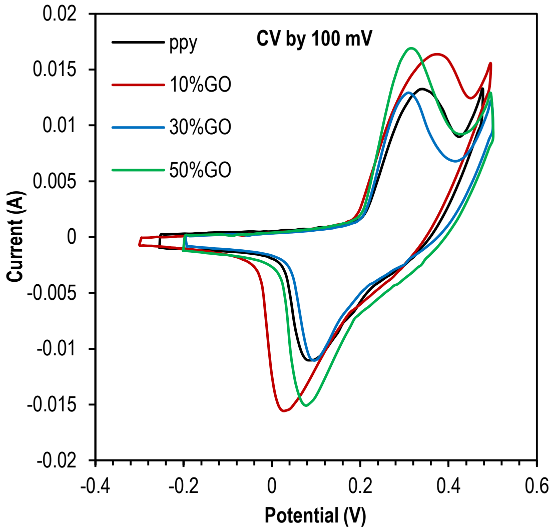

(b)

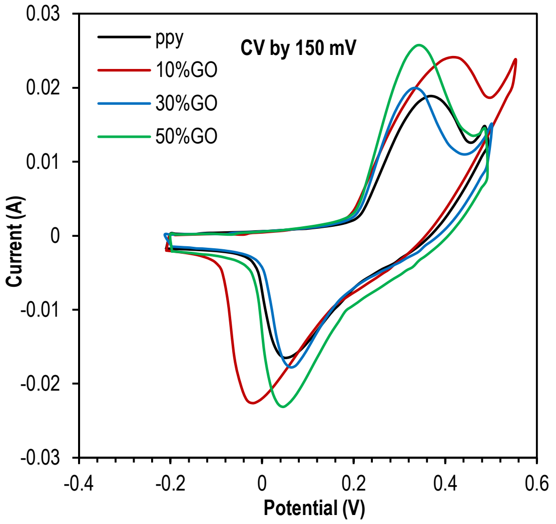

(c)

Fig. (5) C-V curves of PPy and PPy-GO nanocomposite with various GO concentrations at (a) 50 mV, (b) 100 mV, and (c) 150 mV

A polaron emerges as a consequence of the continuous movement of electrons within a neutral region of their quinoid structure chains causes a localized distortion of the positive charge. The PPy and PPy-GO electrodes exhibit reasonable performance over the typical potential ranges during the charge and discharge processes, as depicted in Fig. (6). Additionally, the PPy-GO hybrid composite electrode can function within the 0.2 V working potential window [28].

The following equation can be used to determine the specific capacitance from the CD curve. The specific capacitance (C) can be calculated using the formula $C=I\Delta t/m\Delta V$, where C represents the specific capacitance (in F/g), ΔV represents the potential window (V) (in this case, it is 0.2 V), I represents the discharge current (A) (in this case, it is 0.5 mA), Δt represents the discharge time (s) (5 s for pure PPy, 6 s for 10% GO, 5.7 s for 30% GO, and 4 s for 50% GO), and m represents the electrode's mass (PPY or PPY-GO) (g) (in this case, it is 0.1 mg) [16]. We were able to increase the capacity of pure PPy from 125 F/g to 142.5 F/g by adding 30% GO, and we were able to increase it to 150 F/g by adding up to 10% GO while the capacity decreased to 100 F/g at 50% GO. The higher capacitance observed may be attributed to the attractive forces between polypyrrol nanofibers and graphene oxide, leading to an increase in surface area. The oxidative polymerization process in PPy-GO nanocomposites and 1 M H_2SO_4 electrolysis achieved a maximum capacity value of 150 F/g [29].

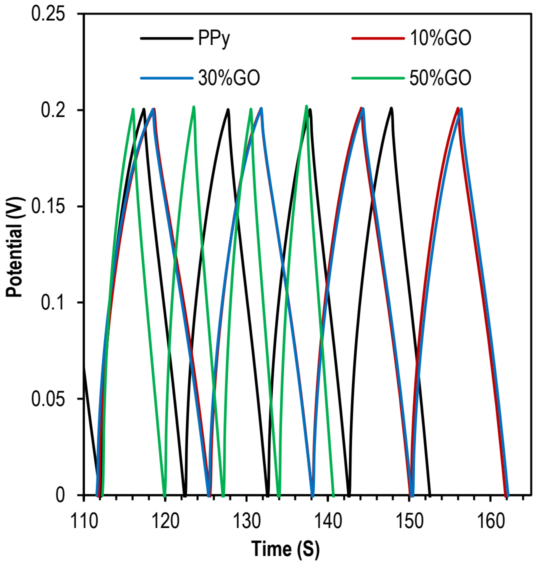

Fig. (6) GCD for pure PPy and PPy-GO at a different percentages

The Nyquist plot was examined by applying a sinusoidal AC voltage with an amplitude of 5 mV at the open circuit potential. The frequency range used for the test ranged from 1 Hz to 1000 kHz, as shown in Fig. (7). In order to get insight into the charge transfer behavior of the PPy/GO electrode material, an electrochemical impedance spectroscopy (EIS) plot was conducted on both PPy samples and PPy/GO composites (Fig. 7). The measurement of ohmic resistance can be obtained by determining the high-frequency intercept of the semicircle within the impedance.

At elevated frequencies, the diminutive semi-circle indicates a diminished transfer resistance of the charge accompanied by a less pronounced diffusion at lower frequencies. If the straight line showed a 45° angle in the low-frequency band, it suggests that the mechanism was affected by diffusion. Conversely, if the slope was 90°, it indicates that the behavior was purely capacitive. The impedance map displays a semi-circular pattern, indicating a highly efficient passage of electric charge. The aforementioned discovery provides additional evidence supporting the remarkable durability of the PPy/GO nanocomposite during electrochemical cycling. This material exhibits promising prospects as an electrode material for electrochemical supercapacitors [30] [31].

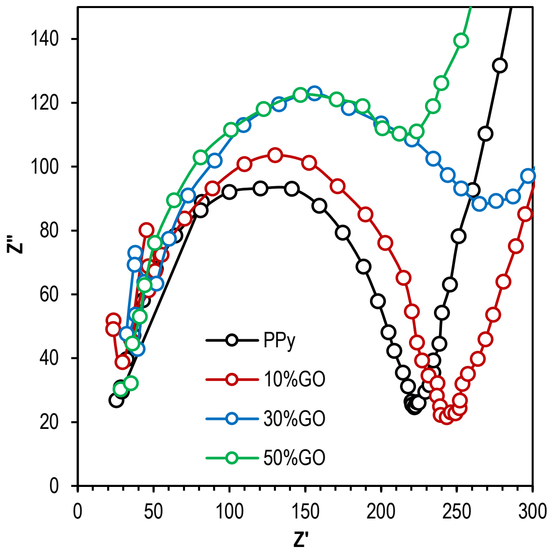

Fig. (7) The Nyquist plots obtained from the electrochemical impedance spectroscopy measurements conducted on the samples of PPy and PPy/GO

4. Conclusions

In summary, PPy nanofiber and nanocomposite of PPy/GO have been prepared by simple method. The composite film of PPy and GO is a good electrode material for electrochemical supercapacitor. The maximum capacitance values (153 F/g) that determined by GCD curves were obtained from PPy nanofibers doped with 30% GO, but for pure PPy the capacitance is very small compared to PPy doping with GO. Therefore, doping plays a very important role in improving the capacitance of supercapacitor.

References

[1] K. Dutta et al., "Enhancements of catalyst distribution and functioning upon utilization of conducting polymers as supporting matrices in DMFCs: a review", *Polym. Rev.*, 55(1) (2015) 1-56.

[2] P. Santhosh, A. Gopalan, and K.-P. Lee, "Gold nanoparticles dispersed polyaniline grafted multiwall carbon nanotubes as newer electrocatalysts: preparation and performances for methanol oxidation", *J. Catal.*, 238(1) (2006) 177-185.

[3] J. Ding et al., "Self-assembly of gold nanoparticles on gold core-induced polypyrrole nanohybrids for electrochemical sensor of dopamine", *Nano*, 10(8) (2015) 1550115.

[4] H.M. Hawy and I.M. Ali, "The role of Ag NPs in PVA electrospun NFs for ultra-high sensitivity photodetector", *Optik*, 262 (2022) 169263.

[5] A.J. Almusawe et al., "Linear optical properties of Bromocresol green dye doped Poly Methyl Methacrylate thin films", *Iraqi J. Sci.*, 59(1B) (2018) 299-306.

[6] N. Yasser, N.A. Ali and L.H. Sulaiman, "The Polymer optical fiber sensor side-pumped with polymer clad doped lasing compounds", *Iraqi J. Sci.*, 59(1B) (2018) 294-298.

[7] Z. Huang et al., "Selective deposition of conducting polymers on hydroxyl-terminated surfaces with printed monolayers of alkylsiloxanes as templates", *Langmuir*, 13(24) (1997) 6480-6484.

[8] J. Jang, "Conducting polymer nanomaterials and their applications," in Emissive Materials Nanomaterials, Springer (2006), pp. 189-260.

[9] A. Babakhanian et al., "Development of α-polyoxometalate–polypyrrole–Au nanoparticles modified sensor applied for detection of folic acid", *Biosens. Bioelectron.*, 60 (2014) 185-190.

[10] P. Novák et al., "Electrochemically active polymers for rechargeable batteries", *Chem. Rev.*, 97(1) (1997) 207-282.

[11] X. Lu et al., "A novel nanocomposites sensor for epinephrine detection in the presence of uric acids and ascorbic acids", *Electrochim. Acta*, 56(21) (2011) 7261-7266.

[12] Y.-Z. Long et al., "Recent advances in synthesis, physical properties and applications of conducting polymer nanotubes and nanofibers", *Prog. Polym. Sci.*, 36(10) (2011) 1415-1442.

[13] Q. Zhang, X. Zhou, and H. Yang, "Capacitance properties of composite electrodes prepared by electrochemical polymerization of pyrrole on carbon foam in aqueous solution", *J. Power Sources*, 125(1) (2004) 141-147.

[14] H. Kang and K.E. Geckeler, "Enhanced electrical conductivity of polypyrrole prepared by chemical oxidative polymerization: effect of the preparation technique and polymer additive", *Polymer*, 41(18) (2000) 6931-6934.

[15] C. Dulgerbaki and A.U. Oksuz, "Fabricating polypyrrole/tungsten oxide hybrid based electrochromic devices using different ionic liquids", *Polym. Adv. Technol.*, 27(1) (2016) 73-81.

[16] F.J. Hameed and I.M. Ibrahim, "Preparation of PPy-WO3 nano-composite for supercapacitor applications", *Iraqi J. Sci.*, 62(5) (2021) 1503-1512.

[17] A. Liu et al., "Electrochemical deposition of polypyrrole/sulfonated graphene composite films", *J. Phys. Chem. C*, 114(51) (2010) 22783-22789.

[18] C. Bora and S.K. Dolui, "Fabrication of polypyrrole/graphene oxide nanocomposites by liquid/liquid interfacial polymerization and evaluation of their optical, electrical and electrochemical properties", *Polymer*, 53(4) (2012) 923-932.

[19] M.A. Farea et al., "Carbon monoxide sensor based on polypyrrole–graphene oxide composite: a cost-effective approach", *Appl. Phys. A: Mater. Sci. Process.*, 127(9) (2021) 354014453.

[20] S. Yang et al., "Graphene nanosheets-polypyrrole hybrid material as a highly active catalyst support for formic acid electro-oxidation", *Nanoscale*, 3(8) (2011) 3277-3284.

[21] A. Singh and A. Chandra, "Graphite oxide/polypyrrole composite electrodes for achieving high energy density supercapacitors", *J. Appl. Electrochem.*, 43 (2013) 773--782.

[22] F.J. Hameed et al., "Enhancing Optical and Electrical Gas Sensing Properties of Polypyrrole Nanoplate by Dispersing Nano-Sized Tungsten Oxide", *ECS J. Solid State Sci. Technol.*, 10(10) (2021) 107001.

[23] A. Yussuf et al., "Synthesis and characterization of conductive polypyrrole: the influence of the oxidants and monomer on the electrical, thermal, and morphological properties", *Int. J. Polym. Sci.*, 2018 (2018) 4191747.

[24] K.V. Harpale, S.R. Bansode and M.A. More, "One-pot synthesis, characterization, and field emission investigations of composites of polypyrrole with graphene oxide, reduced graphene oxide, and graphene nanoribbons", *J. Appl. Polym. Sci.*, 134(32) (2017) 45170.

[25] C. Zhu et al., "Graphene oxide/polypyrrole nanocomposites: One-step electrochemical doping, coating and synergistic effect for energy storage", *J. Mater. Chem.*, 22(13) (2012) 6300-6306.

[26] L. Shahriary and A.a. Athawale, "Graphene Oxide Synthesized by using Modified Hummers Approach", *Int. J. Renew. Energy Environ. Eng.*, 2(1) (2014) 58-63.

[27] C. Dulgerbaki and A.U. Oksuz, "Fabricating polypyrrole/tungsten oxide hybrid based electrochromic devices using different ionic liquids", *Polym. Adv. Technol.*, 27(1) (2016) 73-81.

[28] Y. Yan et al., "Facile Synthesis of Polypyrrole Nanotubes and Their Supercapacitive Application", *Int. J. Electro. Sci.*, 12 (2017) 9320-9334.

[29] H.O.A. Kareem et al., "The significance of doping in enhancing polypyrrol nanofiber storage ability as a supercapacitor", *Dig. J. Nanomater. Biostruct.*, 16(2) (2021) 493-500.

[30] K. Amirazodi, M. Sharif and M. Bahrani, "Polypyrrole doped graphene oxide reinforced epoxy nanocomposite with advanced properties for coatings of mild steel", *J. Polym. Res.*, 26 (2019) 1-12.

[31] M. Ates and Y. Yuruk, "Facile preparation of reduced graphene oxide, polypyrrole, carbon black, and polyvinyl alcohol nanocomposite by electrospinning: a low-cost and sustainable approach for supercapacitor application", *Ionics*, 27(6) (2021) 2659-2672.

IRAQI JOURNAL OF APPLIED PHYSICS Vol. 20, No. 3, July-September 2024, pp. 500-504

We'am Sami

Department of Physics,
College of Education,
University of Al-Qadisiyah,
Qadisiyah, IRAQ

Physical and Magnetic Properties of $Ni_{1-x}Cd_xFe_2O_4$ Ferrites Synthesized by Glycine-Nitrate Auto-Combustion Process

In this work, magnetic spinel $Ni_{1-x}Cd_xFe_2O_4$ ferrites (where x = 0, 0.4, and 0.6) were synthesized through glycine-nitrate auto-combustion process. Physical and magnetic properties that reported through XRD analysis, surface morphology, FTIR analysis, and magnetic measurement confirmed the formation of spinel structure for all ferrites with secondary phase of CdO with the crystallite size decreases from 32.09nm to 20.59nm with the increase of Cd^{2+} ion content for x = 0.4. FE-SEM images show that pure Ni-ferrite nanoparticles possess agglomeration. With increasing cadmium content at x=0.6, the morphology of the particles slightly changes. The agglomeration slightly enhance and spherical nanoferrites formation. FTIR spectra present the slight shift of the higher absorption band to low wavenumber for (x=0.4 and 0.6), which confirms the formation of $Ni_{1-x}Cd_xFe_2O_4$ spinel structure. Results show that, saturation magnetization decreased as the Cd content increases.

Keywords: Spinel; ferrite; Glycine; Nanoparticles; Magnetic properties
Received: 15 February 2024; **Revised:** 02 May 2024; **Accepted:** 09 May 2024

1. Introduction

The preparation of the crystalline spinel ferrites in nano size plays a significant role in determining their physical properties at nano and sub-nano levels [1-3]. Ferrites are classified as ferromagnetic electro-ceramics that are consist of ferric oxide along with other metal with a general formula MFe_2O_4, where M is divalent metal ion such as Ni^{2+}, Cd^{2+} of the Ni-Cd ferrite [4,5]. The physical, chemical, and magnetic properties of ferrites in the nanosize regime are influenced by particle size [6,7]. The metal ions are distributed in two sub-lattices in spinel ferrites, namely the tetrahedral (A-site) and octahedral (B-site), based on the geometrical configuration of the oxygen nearest neighbors [8,9]. Nickel ferrite is one of the soft ferrite materials and due to ferrimagnetic properties and high electrochemical stability [1], it has several applications in technological fields such as photocatalytic degradation, biomedical efficiency, and cancer hyperthermia and information systems and data storage devices [10-13]. Nickel ferrite has a spinel ferrite with an inverse structure that is based on a face-centered cubic lattice of oxygen ions with an eight-unit unit cell, with all Ni ions occupy octahedral site and iron ions located in both tetrahedral and octahedral sites [14,15]. The various techniques to synthesis nickel ferrite were examined in a publication published in 2020. Co-precipitation, micro-emulsion method, solid-state [13], hydrothermal method, reactive sputtering, and sol-gel auto combustion method are the most commonly utilized methods [3,16]. When cadmium is added to nickel ferrite, a novel composite material with good magnetic properties is produced [17]. However, there hasn't been much research done on Ni-Cd ferrites nanoparticles thus far. Thus, in present work, we have reported synthesis of Ni-Cd ferrite nanoparticles using glycine-nitrate auto-combustion process.

2. Material and Methods

Nitrate salts of nickel ($Ni(NO_3)_2{\bullet}6H_2O$), cadmium ($Cd(NO_3)_2{\bullet}6H_2O$), and iron ($Fe(NO_3)_3{\bullet}9H_2O$) from HIMEDIA Co., India were used as raw materials. The following experimental steps were taken to synthesize $Ni_{1-x}Cd_xFe_2O_4$ ferrite samples, where x=0, 0.4 and 0.6, by glycine-nitrate auto-combustion process: (i) the required amount of nitrates was weighed separately with a molar ratio 1:2 for Ni-Cd:Fe, respectively and dissolved in a suitable quantity of de-ionized water, (ii) the solution was thoroughly mixed for 20 minutes by a magnetic stirrer at auto-combustion temperature 100°C, (iii) an amount of glycine was added to the nitrate solution as a fuel with G/N ratio of 0.33 without heat exchange. The self-sustaining combustion process was started in the system once the entire amount of water was vaporized, (iv) the product powder was washed via ethanol and distilled water for 4 times, dried at 80°C for 2 hours, and (vi) mortar was used to grind the resulting powder for 4 minutes to result in fine powder.

3. Results and Discussion

The as-synthesized ferrites were structurally characterized using Shimadzu X-ray diffractometer. The phase formation and structure analyses for all synthesized series samples are shown in Fig. (1). As compared with the standard pattern (00-054-0964) and (00-005-0674) of the Ni and Cd ferrites, respectively, the formation of phase cubic spinel structure is confirmed by prominent diffraction peaks (111), (220), (311), (222), (400), (422), (511), (440), (620), and (533).

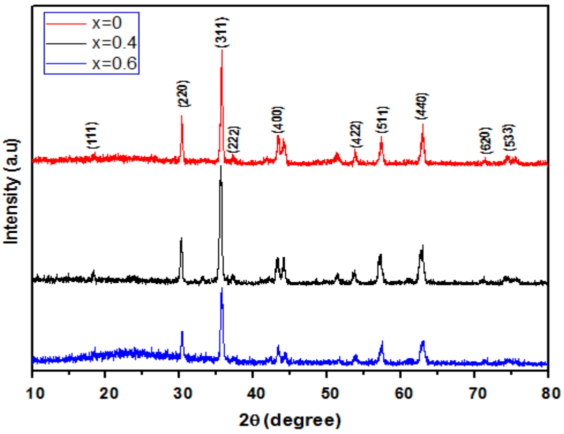

Fig. (1) XRD patterns of $Ni_{1-x}Cd_xFe_2O_4$ ferrite series samples

When Ni^{2+} ions are replaced by Cd^{2+} ions, there is a tiny shift to there is a tiny shift to high 2θ values. This suggests that indicates an decrease in lattice parameter, such shift indicates that this decrease in lattice parameter may be justified by the difference in ionic radius between Cd^{2+} (0.97Å), Ni^{2+} (0.69Å) ions and Fe^{3+} (0.49Å) [3,13] is the cause of the displacement. Furthermore, the small-sized nanoparticles in all samples were found to be responsible for the large bread width of the peaks in all patterns. Structure parameters such as crystallite size (*D*) and lattice constant (*a*) were calculated using the equations below from XRD line broadening of the highest peak (311) plane, as well as the distance between magnetic ions (hopping length) in A site (tetrahedral) and B site (octahedral) were calculated by using the complying relations (LA and LB) [14,15] and tabulated in table (1).

$$D = \frac{0.9\lambda}{\beta\ cos\theta} \qquad (1)$$

$$a = d\sqrt{(h^2 + k^2 + l^2)}\ \text{Å} \qquad (2)$$

$$n\,\lambda = 2\ d\ \sin\theta \qquad (3)$$

$$LA = \frac{a \times \sqrt{3}}{4},\ LB = \frac{a \times \sqrt{2}}{4} \qquad (4)$$

In Debye-Scherrer's relation (Eq. 1), λ indicates the x-ray wavelength (1.542Å), θ is the Bragg's diffraction angle corresponding to the most intense reflection plane (311), and β is the full-width at half maximum (FWHM). Bragg's law (Eq. 3) was used to determine the inter planer spacing (*d*)

From table (1), it is clear that the crystallite size decreases from 32.09 to 20.59 nm with the increase of Cd^{2+} ion content for x=0.4 but this decrease is not continuous as the crystallite size will increase at x=0.6, which can be illustrated as the distance between the magnetic ions (hopping length), which increases as Cd content increases. This behavior of hopping length with x is analogous with behavior of '*a*' with x, and may be attributed to the difference in the ionic radii of the constituent ions [16] where an ionic radius of Ni^{2+} ions is smaller than the ionic radius of Cd^{2+} ions [3]. This is consistent with Bakale et al. for Ni-Cd ferrite, and Reyes-Rodríguez et al. and W. Sami et al. for other spinel ferrites [17,18]. Furthermore, based on the earlier research [19], the crystallite size is related to the value of pH. However, crystallite size does not decrease continuously with an increase in Cd ions, and is related to the pH value. When the pH value is too high, there is a lot of gas emitted during combustion process, leading to a decrease in crystallite size. Literature state that the lattice constant and crystallite size are directly related. Increasing in crystallite size lead to decrease or increase in the lattice constant [20]. In the present work, for the decrease in the crystallite size at x=0.4, the lattice constant has increased to 8.3612Å.

The surface morphology for spinel $Ni_{1-x}Cd_xFe_2O_4$ nanoparticles was recorded using a TESCAN Mira3 field-emission scanning electron microscope (FE-SEM). The FE-SEM images of all as-synthesized ferrites are depicted in Fig. (2).

FE-SEM images show that pure Ni-ferrite nanoparticles agglomerate due to their magnetic nature and the binding of initial particles held together by weak surface interactions such as the Van der Waals force. The holes and apertures in the photographs can also be attributed to the release of a massive volume of gas formed by the combustion's decomposition. Similar observations were seen in other ferrites [21]. However, with increasing Cd content to x=0.6, the morphology of the particles slightly changes. The agglomeration slightly enhance and spherical ferrite nanoparticles are formed. The impact of substitution Ni^{2+} by Cd^{2+} on the microstructure of Ni-ferrite can be explained as follows: Cd^{2+} substitution enhances grain growth of Ni-ferrite as a reaction center by increasing bulk diffusion due to aberration and activation of crystal lattice caused by substituted Cd^{2+}. Similar observations were seen in Ref. [13] for Ni-Cd ferrite and Ref. [22] for Ni-Zn ferrite.

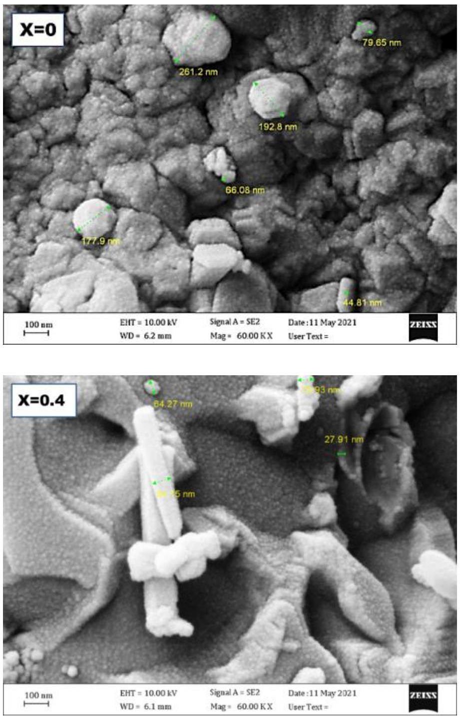

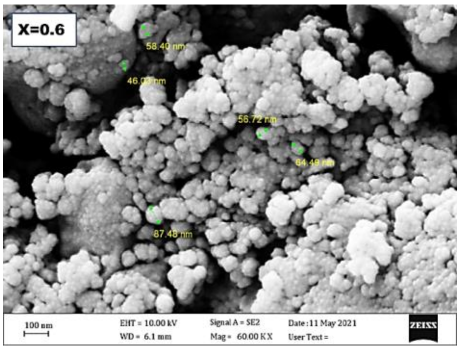

Fig. (2) FE-SEM images of the spinel $Ni_{1-x}Cd_x$ Fe_2O_4 ferrite series samples

To determine the chemical structure of the as-synthesis samples, the FTIR spectra were recorded using a Shimadzu 8400S FTIR spectrometer in the wavenumber range of 4000-450 cm^{-1}, as shown in Fig. (2).

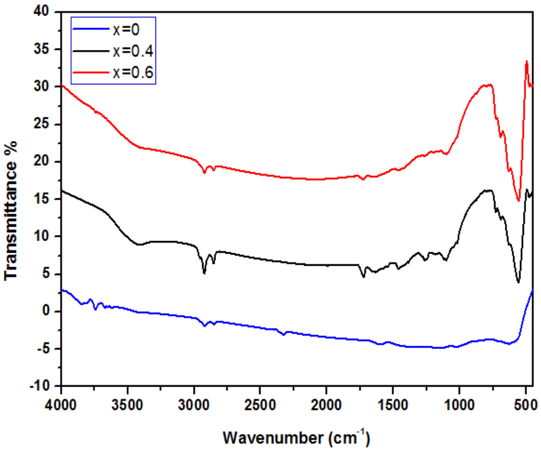

Fig. (3) FT-IR spectra of the spinel $Ni_{1-x}Cd_x$ Fe_2O_4 ferrite series samples

The spinel ferrite nanoparticles are known to have two FTIR-active bands, one is higher absorption band designated as υ_{Tet} and the other one is lower absorption band designated as υ_{Oct} in the range of 450-900 cm^{-1} [23]. In the present study, FT-IR spectra of all samples exhibit two intense peaks at 629 cm^{-1} (higher peak) and 459.70 cm^{-1} (lower peak) and correspond to the metal oxygen bonds. Higher and lower frequency bands are associated with oxygen-tetrahedral (Fe-O) and oxygen-octahedral (O-Fe-O) bending vibrations, respectively [14]. They are the characteristic peak of the spinel structure [24]. The significant Fe–O vibrational mode clearly showed that strong Cd doping occurred in $NiFe_2O_4$ spinel lattice. The hydroxyl group can be assigned to the wide band around 3400 cm^{-1}, while the in-plane and out-plane of O–H vibration can be assigned to the bands around 1630-1384 and 970-880 cm^{-1}, respectively. The remaining bands are most likely attributable to overtones or combinational frequencies. Similar variation was observed in Ref. [10]. The band positions (υ_{Tet}) and (υ_{Oct}) in the current ferrite system have been observed to change significantly as Ni^{2+} is replaced by Cd^{2+}. This could be related to the distribution of Cd^{2+} in the tetrahedral A-site, which replaces Fe^{3+} [13]. In the present series samples of $Ni_{1-x}Cd_xFe_2O_4$ ferrites the nickel divalent cations are stabilized in octahedral crystal field, while cadmium divalent cations are occupied tetrahedral sites due to the ability to form covalent connections involving sp3 hybrid orbitals. Higher and lower absorption band, as well as force constant for tetrahedral K_{Tet} and octahedral K_{Oct} of the series samples of $Ni_{1-x}Cd_xFe_2O_4$ ferrites are summarized in table (2). The force constant (k) was calculated using the following relation [25]:

$$k = 4\pi^2\upsilon^2c^2\mu \qquad (5)$$

where υ is the vibration frequency of the tetrahedral and octahedral sites, c is the light velocity, and μ is the reduced mass of the Fe^{3+} ion and the O^{2-} ions (2.065×10^{-23} g/mol)

Table (2) Tetrahedral and octahedral absorption band as well as force constants of the $Ni_{1-x}Cd_xFe_2O_4$ ferrite series samples

x	D (nm)	a (Å)	υ_{Tet} (cm^{-1})	υ_{Oct} (cm^{-1})	K_{Tet} $\times10^2$ N. m^{-1}	K_{Oct} $\times10^2$ N. m^{-1}
0	32.09	8.3321	629.00	-	2.87	-
0.4	20.59	8.3612	558.86	478.30	2.27	1.66
0.6	21.23	8.3303	476.71	459.70	1.65	1.53

Interestingly, the slight shift of the higher absorption band υ_{Tet} towards the lower wavenumbers is observed with an increase of Cd-substitution, which is attributed to decreased force constants and contraction of Fe^{3+}-O^{2-} bond lengths at both tetrahedral and octahedral sites, where force constants are directly related to the stretching and bending of chemical bonds [26]. These results are consistent with previously reported FTIR spectrum in Ref. [13].

The magnetic measurements are determined using a MDK vibrating sample magnetometer (VSM). Figure (4) shows the magnetic hysteresis loop for the mixed spinel $Ni_{1-x}Cd_xFe_2O_4$ ferrite at room temperature with applied external field of 15 kOe.

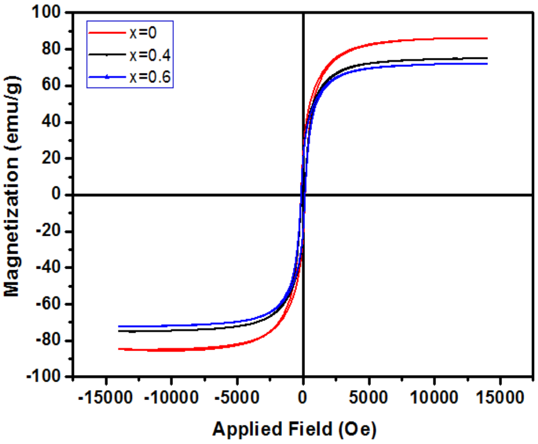

Fig. (4) Magnetization (emu/g) versus applied magnetic field (Oe) of $Ni_{1-x}Cd_xFe_2O_4$ ferrite at room temperature

As can be seen from both hysteresis curve and table (2), the Ni-Cd ferrites prepared in this work showed a S-shape hysteresis curve with high value of saturation magnetization and narrow loop that brought the low coercivity values. The saturation magnetization decreased as the Cd content is increased. In the present series of $Ni_{1-x}Cd_xFe_2O_4$ (where x=0, 0.4, and 0.6), magnetic nickel divalent cations are replaced by non-magnetic cadmium divalent cations and magnetic iron trivalent cations are replaced by non-magnetic cadmium divalent cations. As a result, the A-B interaction decreases in the system then the value of saturation magnetization decrease. Similar results were reported in Ref. [13].

Table (2) Magnetic measurements extracted from hysteresis loops of the spinel $Ni_{1-x}Cd_xFe_2O_4$ ferrite

Sample	x	Ms (emu/g)	Mr (emu/g)	Mr/Ms
$NiFe_2O_4$	0	86.04	29.15	0.338
$Ni_{0.6}Cd_{0.4}Fe_2O_4$	0.4	75.03	29.00	0.386
$Ni_{0.4}Cd_{0.6}Fe_2O_4$	0.6	72.31	28.00	0.387

4. Conclusion

In the present work, mixed spinel $Ni_{1-x}Cd_xFe_2O_4$ ferrite was synthesized using the glycine-nitrate auto-combustion process where x=0, 0.4, and 0.6. We found that the glycine-nitrate auto-combustion process has simplicity that is usually performed in solution media. Also, the lattice constant increases with increasing the Cd content at x=0.4 but this increase is not continuous as the lattice constant will be decrease at x=0.6. The $Ni_{1-x}Cd_xFe_2O_4$ ferrite showed soft ferrite with S-shape and pure nickel ferrite has higher saturation magnetization value but when nickel ions (Ni^{+2}) are replaced by cadmium ions (Cd^{+2}), a decrease in saturation magnetization has been exhibited.

References

[1] S. Sagadevan, Z.Z. Chowdhury and R.F. Rafique, “Preparation and Characterization of Nickel Ferrite Nanoparticles via Co-precipitation Method”, *Mater. Res.*, 21 (2018) 1-5.

[2] O.A. Hammadi and N.E. Naji, “Fabrication and Characterization of Polycrystalline Nickel Cobaltite Nanostructures Prepared by Plasma Sputtering as Gas Sensor”, *Phot. Sen.*, 8(1) (2018) 43-47.

[3] A. El-Mahdi and I. bin Selima, “Non-Equilibrium Plasma Assisted Combustion Kinetics”, Iraqi J. Mater., 2(3) (2023) 97-106.

[4] S. Iraqui, S.S. Kashyap and Md.H. Rashid, “$NiFe_2O_4$ Nanoparticles: An Efficient and Reusable Catalyst for The Selective Oxidation of Benzyl Alcohol to Benzaldehyde Under Mild Conditions”, *Nanoscale Adv.*, 2 (2020) 1-35.

[5] A.K. Nandanwar et al., “Effects of Ni^{2+}-Substitution on Structural, Magnetic and Electrical Properties of Cadmium Spinel Ferrite Nanoparticles via Chemical Route”, *Integ. Ferroelect.*, 203 (2019) 12-18.

[6] J. Jacob and M. Abdul Khadar, “Investigation of Mixed Spinel Structure of Nanostructured Nickel Ferrite”, *Conf. Ser.: J. Appl. Phys.*, 107 (2010) 1-10.

[7] A.J. Raheem and S.M. Raji, “Nickel Ferrite Nanostructures Prepared by DC Reactive Magnetron Sputtering”, Iraqi J. Appl. Phys. Lett., 7(2) (2024) 7-10.

[8] A. Samavati and A.F. Ismail, “Antibacterial Properties of Copper-Substituted Cobalt Ferrite Nanoparticles Synthesized by Co-Precipitation Method”, *Particuology*, 30 (2017) 1-6.

[9] J.O. Sattar, “Fabrication and Characterization of Nickel Cobaltite Nanostructures for Gas Sensing Applications”, Iraqi J. Appl. Phys. Lett., 7(2) (2024) 15-18.

[10] S. Hirthna et al., “Synthesis and Characterization of $NiFe_2O_4$ Nanoparticles for the Enhancement of Direct Sunlight Photocatalytic Degradation of Methyl Orange”, *J. Supercond. Novel Magnet.*, 31 (2018) 3315-3322.

[11] H.Q. Alijani et al., “Bimetallic Nickel-Ferrite Nanorod Particles: Greener Synthesis Using Rosemary and Its Biomedical Efficiency”, *Artif. Cells Nanomed. Biotech.*, 48 (2020) 242-251.

[12] D. Saykova et al., “Synthesis and Characterization of Core–Shell Magnetic Nanoparticles $NiFe_2O_4$@Au”, *metals*, 10 (2020) 1-13.

[13] C. Cherpin et al., “Study of The Solid-State Synthesis of Nickel Ferrite ($NiFe_2O_4$) by X-ray Diffraction (XRD), Scanning Electron Microscopy (SEM) and Raman Spectroscopy”, *Materials*, 14 (2021) 1-9.

[14] M. De, A. Mukherjee and H.S. Tewari, “Characterization of Cadmium Substituted Nickel Ferrites Prepared Using Auto-Combustion Technique”, *Process. Appl. Ceram.*, 9 (2015) 193-197.

[15] D. Guragain et al., “Effect of Terbium Ion Substitution in Inverse Spinel Nickel Ferrite: Structural and Magnetic Study”, *Magnetochem.*, 6 (2020) 1-14.

[16] J. Haman, “New Geometrical Arrangement to Prepare Nickel Ferrite Nanostructures on Glass Substrates Using DC Reactive Magnetron Sputtering”, Iraqi J. Sci. Ind. Res., 3(2) (2024) 42-46.

[17] K. Rafeekali and E.M. Muhammed, “Antibacterial Study of Cadmium Substituted Nickel Ferrite Nano Particles”, *Int. J. Eng. Res. General Sci.*, 3 (2015) 321-324.

[18] S.P. Jadhav et al., “Effect of Cadmium Substitution on Structural and Magnetic Properties of Nano Sized Nickel Ferrite”, *Chinese J. Chem. Phys.*, 23 (2010) 459-464.

[19] W.A. Farooq et al., “Structural, Optical and Electrical Properties of $Cu_{0.6}Co_xZn_{0.4-x}Fe_2O_4$

(x=0.0, 0.1, 0.2, 0.3, 0.4) Soft Ferrites", *Molecules*, 26 (2021) 1-10.

[20] P. Bakale et al., "Synthesis, Structural and Mechanical Properties of $Ni_{1-x}Cd_xFe_2O_4$ Ferrites (x=0.1, 0.2, 0.3, and 0.4)", *Int. J. Adv. Sci. Eng.*, 6 (2019) 1285-1290.

[21] B.H. Devmunde, P.S. Bhalerao and M.B. Solunke, "Structural Morphological and Infrared Properties of Cd^{2+} Substitutes Nickel Ferrite Particles", *J. Phys.: Conf. Ser.*, 1644 (2020) 1-8.

[22] P.Y. Reyes-Rodríguez et al., "Structural and Magnetic Properties of Mg-Zn Ferrites ($Mg_{1-x}Zn_xFe_2O_4$) Prepared by Sol-Gel Method", *J. Mag. Mag. Mater.*, 427 (2017) 268-271.

[23] W. Sami and Z.S. Sadeq, "Synthesis, Characterizations, and Magnetic Properties of Mixed Spinel $Mg_{1-x}Zn_xFe_2O_4$ Ferrites", *Iraqi J. Sci.*, 63 (2022) 997-1003.

[24] Q. Lin et al., "Magnetic and Mössbauer Spectroscopy Studies of Zinc-Substituted Cobalt Ferrites Prepared by the Sol-Gel Method", *Materials*, 11 (2018) 1-12.

[25] L.R. Nivedita et al., "Correlation Between Crystal Structure, Surface/Interface Microstructure, and Electrical Properties of Nanocrystalline Niobium Thin Films", *J. Nanomater.*, 10 (2020) 1-23.

[26] P.A. Udhaya, M. Meena and M.A.J. Queen, "Green Synthesis of $MgFe_2O_4$ Nanoparticles Using Albumen as Fuel and Their Physico-Chemical Properties", *Int. J. Sci. Res. Phys. Appl. Sci.*, 7 (2019) 71-74.

[27] S.B. Khan, S. Irfan and S.-L. Lee, "Influence of Zn^{+2} Doping on Ni-Based Nanoferrites ($Ni_{1-x}Zn_xFe_2O_4$)", *Nanomater.*, 9 (2019) 1-17.

[28] M.A. Ansari et al., "Synthesis and Characterization of Antibacterial Activity of Spinel Chromium-Substituted Copper Ferrite Nanoparticles for Biomedical Application", *J. Inorg. Organomet. Polym. Mater.*, 28 (2018) 2316-2327.

[29] W. Sami, and Z.S. Sadeq, "Synthesis and Study of Calcination Effect of Zinc Ferrite on the Structure and Morphology of Nanoparticles", *J. Phys. Conf. Ser.*, 1999 (2021) 1-10.

[30] C. Kumari et al., "Structural and Optical Properties of Nanosized Co Substituted Ni Ferrites by Coprecipitation Method", *Phase Trans. A Multinational J.*, 93 (2020) 207-216.

[31] A. Abbasi, "Structural and Spectroscopic Studies of Solvated Metal Ions", PhD thesis, Stockholm University (2005), 8.

Table (1) Crystallite size and lattice constant, and hopping length for A site (Tetrahedral) and B site (Octahedral) of the $Ni_{1-x}Cd_x Fe_2O_4$ ferrite series samples

As-synthesized powder samples	x	2θ (deg)	FWHM (deg)	d (Å)	Lattice Constant a (Å)	Crystallite Size D(nm)	hopping length	
							L_A	L_B
$NiFe_2O_4$	0	35.7113	0.25590	2.51223	8.3321	32.09	3.6077	2.9458
$Ni_{0.6}Cd_{0.4}Fe_2O_4$	0.4	35.5829	0.38450	2.52100	8.3612	20.59	3.6205	2.9561
$Ni_{0.4}Cd_{0..6}Fe_2O_4$	0.6	35.7191	0.37390	2.51170	8.3303	21.23	3.6071	2.9452

IRAQI JOURNAL OF APPLIED PHYSICS Vol. 20, No. 3, July-September 2024, pp. 505-510

Ahmed A. Ahmed [1]
Najat A. Dahham [1]
Ghazwan G. Ali [2]

[1] *Department of Physics, College of Science, University of Tikrit, Tikrit, IRAQ*
[2] *Department of Physics, College of Education for Pure Science, University of Mosul, Mosul, IRAQ*

Iraqi Journal of Applied Physics
Q4 Electronic, Optical and Magnetic Materials best quartile
SJR 2022 0.19
powered by scimagojr.com

Optical Properties of CuS/Porous Silicon Heterojunction

In the present work, monocrystalline porous silicon was fabricated using the photo-electrochemical etching technique and then copper sulfide (CuS) nanoparticles were deposited on a porous silicon substrate at 250°C using spray pyrolysis method at different concentrations of CuS (0.1, 0.3 and 0.5M). The physical properties of CuS/PSi/c-Si heterojunction were studied. The results of photoluminescence (PL) exhibited that the peak position of PL spectra was shifted to the longer wavelength or lower energy when the concentration of CuS was increased. On the other side, the energy gap of CuS decreased with increasing concentration. The values of energy gap are 2.7, 2.59, and 2.55 eV at 0.1, 0.3 and 0.5M, respectively. The properties of the CuS/PSi/n-Si structure were enhanced.

Keywords: Copper sulfide; Thin films; Porous silicon; Photoluminescence
Received: 04 April 2024; **Revised:** 25 April 2024; **Accepted:** 01 May 2024

1. Introduction

In recent years, many of papers have focused on nanostructured semiconductors, which have their unique structural properties. Copper sulfide (CuS) is a p-type semiconductor with direct energy gap of 1.6-2.7eV [1-4]. The composition of Cu_xS exists many stable phases. The composite Cu_2S, the copper-rich, the diorlite, dignite, and anilite, ending with the covellite (CuS) phase, which is rich in sulfur [5-7]. Copper sulfide thin films were deposited using many methods such as chemical bath deposition, sol-gel, chemical vapor deposition (CVD), chemical spray, and spin coating [8,9]. The thermochemical spray pyrolysis method is considered the most common among the chemical methods for preparing thin films. These methods are summarized by spraying a solution of the material from which the film is to be prepared onto hot bases at a specific temperature that depends on the type of material used, as a thermochemical reaction occurs between the atoms of the material and the hot base, and as a result of this reaction a thin membrane is formed [10,11]. Porous silicon (PSi) is a material with strong emissivity, showing effective illumination over a wide spectral range [12,13]. Many research works have focused on porous silicon and is based on optoelectronic techniques such as light-emitting diodes, wave vectors, and photovoltaic diodes [14,15]. The mixture between CuS thin film and PSi layer can provide an excellent homogenous of lattice constant [16-18].

The goal of this paper is to study the photoluminescence (PL) and UV-visible spectrophotometric properties of CuS/PSi hybrid junction. The influence of CuS deposited on the porous silicon substrate properties plays an important role to uniform porous surface.

2. Experimental Work

Figure (1a) exhibits a schematic diagram of the anodization etching method. In this work, there are two orientations; (100) and (111); of n-type silicon wafers are used with resistivity of 0.01-0.02 Ω.cm and the thickness of the silicon wafer is 505±12μm. The Si wafers were cleaned before the etching to remove any contamination on the surface.

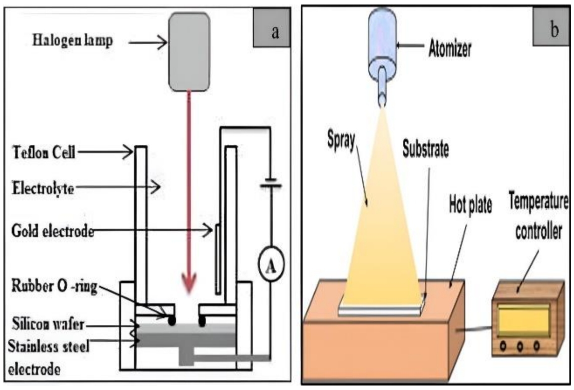

Fig. (1) (a) Diagram of adonization process, (b) diagram of chemical spray

The hydrofluoric acid (16 wt.%) contraction has been diluted by using an absolute ethanoic solution (99%) (C_2H_5OH) to minimize the hydrogen bubbles during the etching. Fixed current density was maintained at 15 mA/cm^2 and etching time of 5, 10 and 15 min were used. Additionally, a tungsten lamp of 100 mW/cm^2 intensity was carried out. The set-up consists of two electrodes, the first part is gold and is connected to the acid solution (HF), the second part is a stainless-steel put under the Si substrate. After that, CuS/PSi heterojunction was achieved by using spray pyrolysis process. We used aqueous solution of copper chloride and sodium sulfide (Na_2S) at various concentrations. We mixed first in distilled water (H_2O) and then sprayed on the substrate in order to obtain ions of copper and sulfide. The CuS nanoparticles were deposited on PSi substrate at 250°C using spray pyrolysis method at different concentrations of CuS (0.1, 0.3 and 0.5M). The spray rate was used at 25 mL/min. The distance between the nozzle and the sample were fixed about 30 cm and a k-type thermocouple was used as shown Fig. (1b) and table (1).

Table (1) Values of Concentration and weight used of preparation of CuS thin films

Concentration	0.1M	0.3M	0.5M
Weight(gm) $CuCl_2$	0.270	0.780	1.32
Weight(gm) Na_2S	0.129	0.452	0.77

3. Results and Discussion

The PL spectra shown in figures (2) and (3) are for CuS/Psi heterojunctions prepared at etching time of 15 min with fixed current density (15 mA/cm^2), concentration of HF (18%) and concentration of CuS (0.1M and 0.5M) with orientation (100) and (111). Obviously, the strong emission peaks of CuS/PSi at orientation (100) were observed at 577.5 nm, 535.3 nm and 546.4 nm (green region) corresponding to energies of 2.19 eV, 2.31 eV and 2.27 eV of pure PSi and concentration 0.1 and 0.5M respectively (Fig. 2).

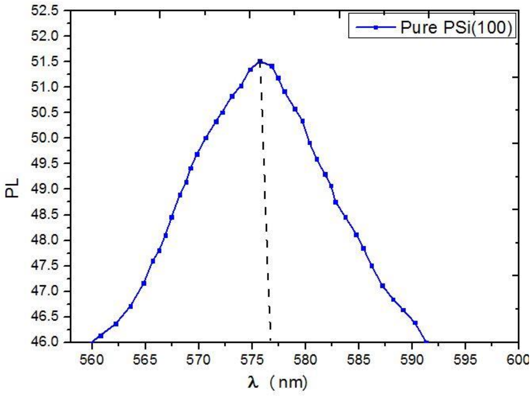

(a)

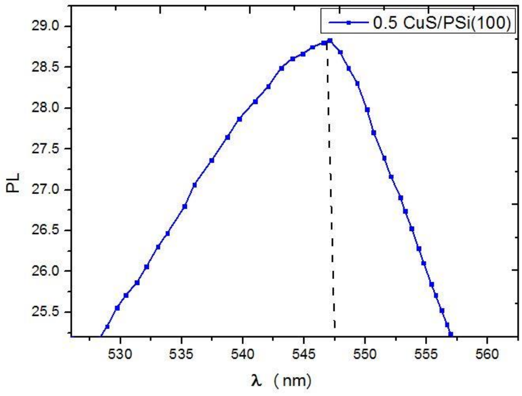

(b)

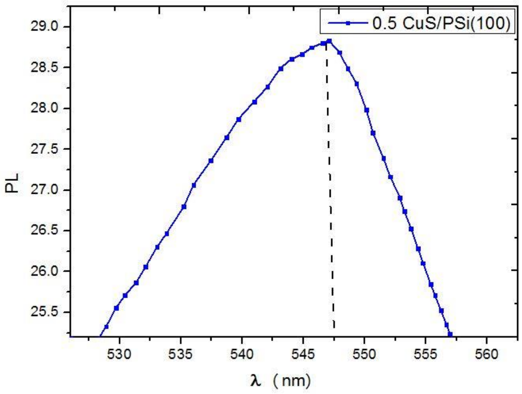

(c)

Fig. (2) PL spectra of CuS/PSi nanostructures fabricated at concentrations of (a) 0.1M, (b) 0.3M, (c) 0.5M of orientation (100)

In the same way, the PL emission peaks at orientation (111) were illustrated at 566.5 nm, 577.2 nm and 605.6 nm (green region) corresponding to energies of 2.15 eV, 2.14 eV and 2.04 eV of pure PSi and concentration 0.1 and 0.5M, respectively (Fig. 3) because of the carriers restricted (electron-hole) recombining in the PSi surface, and this is further supported by measurements of the particle sizes' statistical distribution [19-21]. The peak position was shifted to the long wavelength or lower energy with increasing concentration of CuS due to the density of state of PL and the absorbance of the carriers due to quantum confinement effects [22,23]. It can be seen the change in the peaks intensity due to the increasing of the number of smaller nanocrystallite sizes contributes to the PL since it generates more holes for further reactions as in tables (2) and (3). The silicon atoms near the crystallite's surface modify their bonds and dimension to adapt variations in the immediate environment, forming the recombination centers. The possibility of electron and hole recombination is a less dimension structure as the energy gap decreased with increasing concentration due to the confinement of PSi practical in a smaller dimension [24,25].

Table (2) Parameters of concentration, wavelength and energy gap at orientation (100)

Sample	Concentration (M)	Wavelength (nm)	E_g (eV)
(100) PSi	-	577.5	2.19
CuS/PSi	0.1	535.3	2.31
CuS/PSi	0.5	546.4	2.27

Table (3) Parameters of concentration, wavelength and energy gap at orientation (111)

sample	Concentration (M)	Wavelength (nm)	E_g (eV)
(111) PSi	-	566.5	2.15
CuS/PSi	0.1	577.2	2.14
CuS/PSi	0.5	605.6	2.04

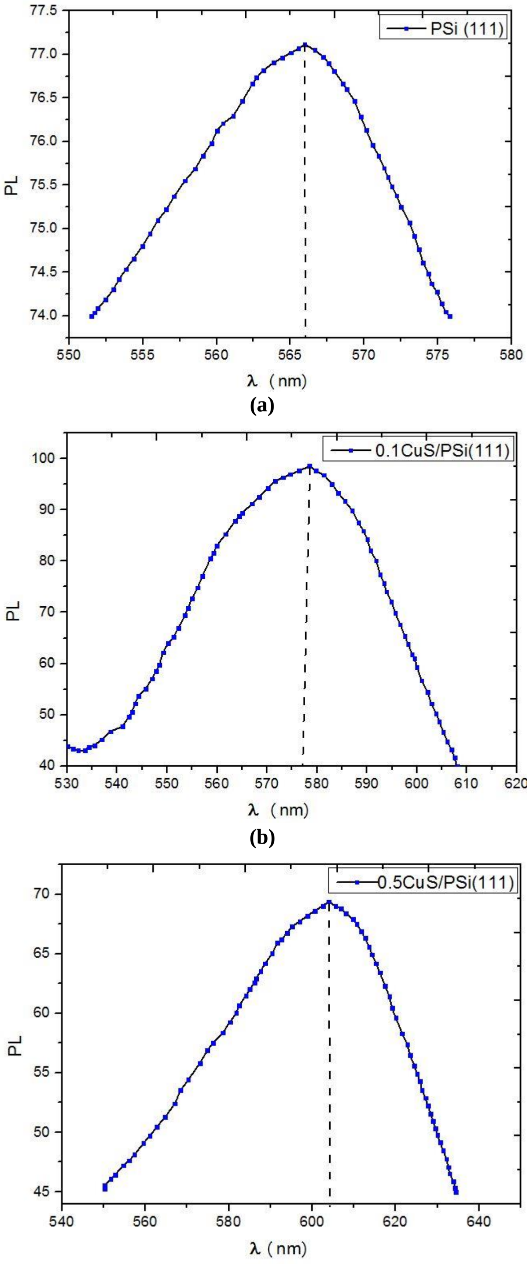

(a)

(b)

(c)

Fig. (3) PL spectra of CuS/PSi nanostructures fabricated at concentrations of (a) 0.1M, (b) 0.3M, (c) 0.5M of orientation (111)

The optical properties of the CuS nanostructures were characterized at concentrations 0.1, 0.3 and 0.5M using UV-visible spectrophotometer. The relationship between absorption spectra and wavelength are shown in Fig. (4a). The film's optical absorbance diminishes as wavelength increases. The findings show that for all samples, the absorbance of CuS thin films increased as concentration is increased. This could be because of the breaking of bonds on the CuS surface leading to a rise in absorption mechanisms, the trap-related electron-hole recombination has been observed. Increasing of concentration allows to formation defects. These defects are an interested component in optoelectronic devices and they play a critical role in the optical properties or color centers [26]. Figure (4b) illustrates the reflection spectra of CuS nanostructures at different concentrations. We can calculate the reflectance (R) using the following equation:

$$R = 1 - (T + A) \qquad (1)$$

where T is the transmittance, and A is the absorbance

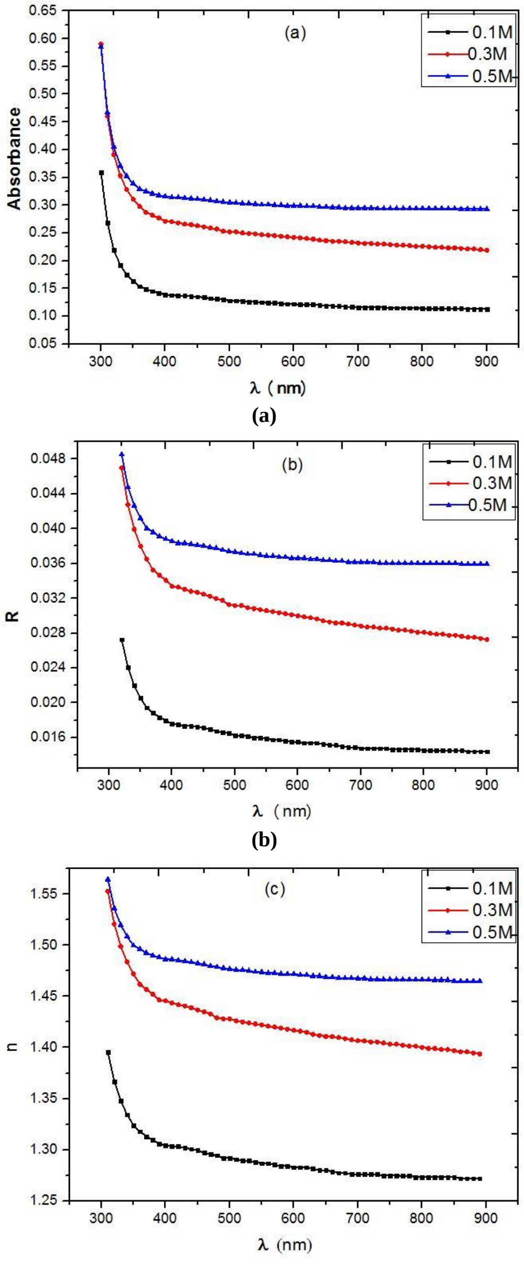

(a)

(b)

(c)

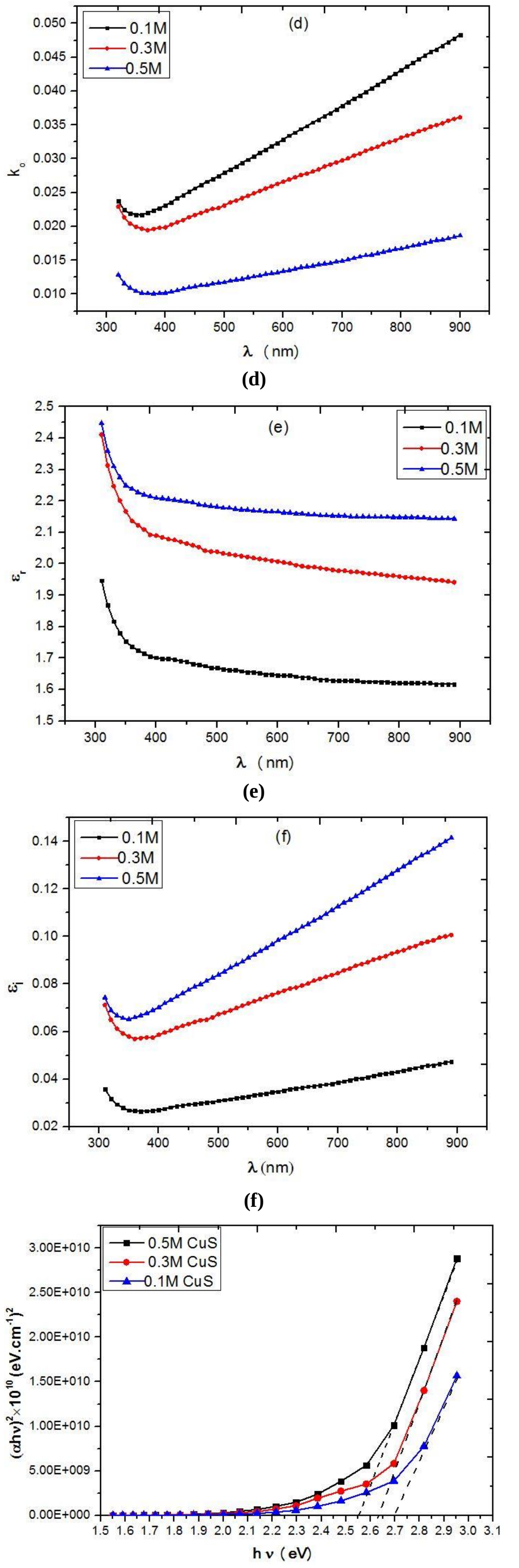

(d)

(e)

(f)

(g)

Fig. (4) (a) Absorbance, (b) Reflectance, (c) Refractive index, (d) Extinction coefficient, (e,f) real and imaginary parts, and (g) energy gap

It can be seen that reflectance and refractive index decrease when the wavelength increased in the visible region, and increase with increasing concentration because the incident photons have been absorbed in the CuS thin films as in Fig. (4c). In addition, the extinction coefficient (k_o), real part (ε_r), and imaginary part (ε_i) decreased with wavelength. Moreover, the values at concentration of 0.5M were larger than those of 0.1M and 0.3M, as shown Fig. (4d,e,f,g). Furthermore, the curves between $(\alpha h\nu)^2$ and photon energy for CuS thin films are studied. This behavior can be justifiable by producing additional energy states with enhancing concentration. Additionally, the interface band transition at localized states in the energy gap was observed. The majority of flaws are generated using the positioning vacancies of oxygen and alterations in crystal structure. We can the estimated the energy gap (E_g) by Tauc's formula:

$$(\alpha h\nu) = B\left(h\nu - E_g\right)^{r} \qquad (2)$$

where r takes value of 1/2 for the direct transition and 2 for the indirect transition, $h\nu$ is photon energy, B is constant, and α is the absorption coefficient

The results show that the optical energy gap decreases with concentration and its values are 2.7eV, 2.59eV, 2.55 eV for concentrations of 0.1M, 0.3M and 0.5M, respectively. This is in excellent agreement with the published data for CuS film deposited using alternative techniques [27-29].

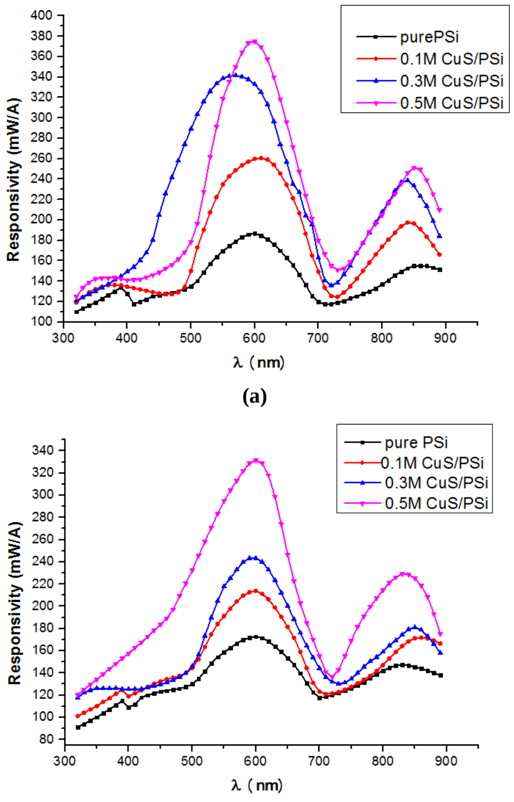

(a)

(b)

Fig. (5) Responsivity of CuS deposited on PSi substrates (a) (111) orientation, and (b) (100) orientation

The photosensitivity measurements of prepared CuS/PSi heterojunction showed the maximum value of the quantum efficiency in visible region was found to be 500-600nm. Additionally, the photodetector of CuS/PSi heterojunction samples at direction of (111) are upper than direction of (100) due to reconfiguration of structure as shown in figures (6-8). Furthermore, the fabrication of the CuS/PSi photodetector are effectively depends on fabrication requirements [30-32].

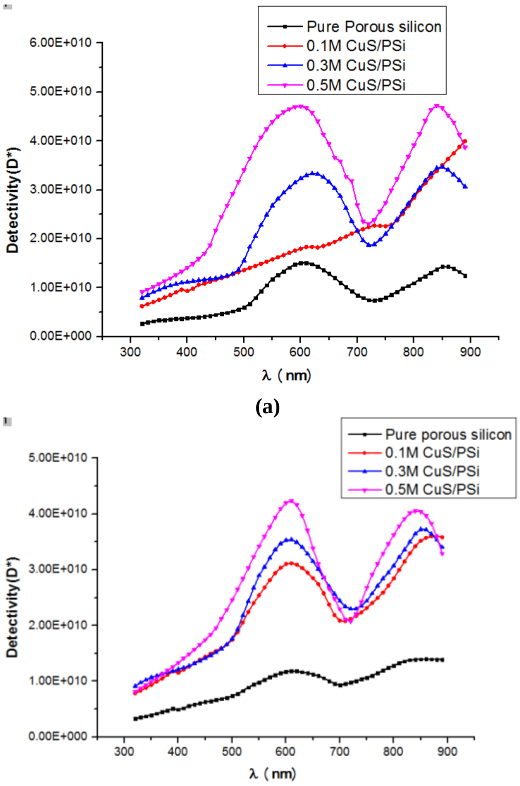

(a)

(b)

Fig. (6) Detectivity of CuS deposited on PSi (a) (111) orientation, and (b) (100) orientation

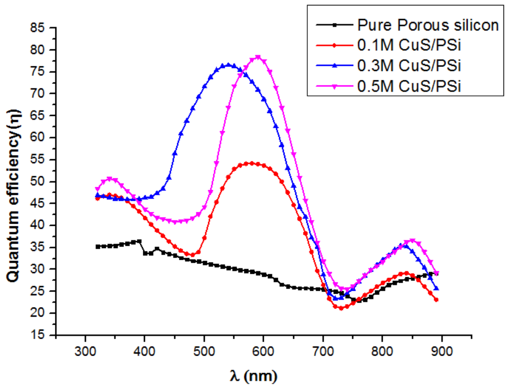

(a)

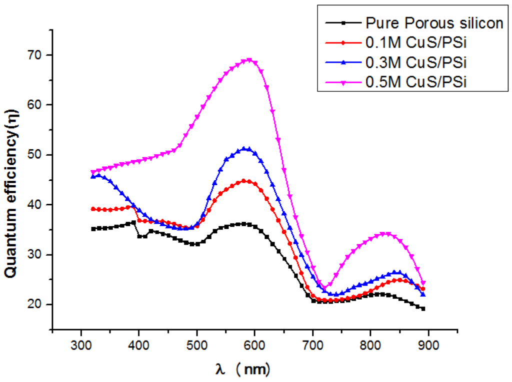

(b)

Fig. (8) Efficiency of CuS deposited on PSi (a) (111) orientation, and (b) (100) orientation

4. Conclusion

In summary, CuS nanostructures were successfully deposited on porous Si wafer using chemical spray method. The peak position of photoluminescence was shifted to the long wavelength or lower energy when the concentration of CuS was increased. The energy gap increases with increasing concentration of CuS. Consequently, the experimental circumstances can be used to control the size and shape of the final structures. In brief, the characteristics of CuS/PSi photodetectors are effectively dependent on fabrication requirements.

References

[1] Y. Sandhya and P. Kumar Bajpai, “Effect of substrate on CuS/PVA nanocomposite thin films deposited on glass and silicon substrate”, *Soft Nanosci. Lett.*, 8(2) (2018) 9-19.

[2] S.T. Kassim, H.A. Hadi and R.A. Ismail, “Fabrication and characterization of high photosensitivity CuS/porous silicon heterojunction photodetector”, *Optik*, 221(3) (2020) 3126-3140.

[3] S. Gunasekaran et al., “Photosensitive activity of fabricated core-shell composite nanostructured p-CuO@CuS/n-Si diode for photodetection applications”, *Sens. Actuat. A: Phys.*, 317 (2021) 112373.

[4] J. Zhang et al., “Excellent near-infrared response performance in p-CuS/n-Si heterojunction using a low-temperature solution method”, *Surf. Interfaces*, 26 (2021) 101430.

[5] R.A. Rasool et al., “The effect of epoxy layer supported by carbon, alumina and silica grains on the solar cell”, *Digest J. Nanomater. Biostruct.*, 14(3) (2019) 743-750.

[6] Y. Xu et al., “High-performance CuS/n-Si heterojunction photodetectors prepared by e-beam evaporation of Cu films as precursor layers”, *J. Alloys Comp.*, 884 (2021) 161121.

[7] A.K. Katiyar et al., “Optical photoresponse of CuS–n-Si radial heterojunction with Si nanocone arrays fabricated by chemical

etching", *Phys. Chem. Chem. Phys.*, 15(48) (2013) 20887-20893.

[8] B. Güzeldir, M. Sağlam and A.Y.T.U.N.Ç. Ateş, "Temperature Dependent Electrical Characteristics of Cu/CuS/n-Si/Au-Sb Structure Deposited by SILAR Method", *AIP Conf. Proc.*, 1400(1) (2011).

[9] H.I. Naşcu and V. Popescu, "CuS thin films obtained by spray pyrolysis", *Leonardo Electron. J. Pract. Technol.*, 4 (2004) 22-29.

[10] A.A. Sulaiman, G.G. Ali and A.I. Thanon, "Synthesis and study of ZnO thin films using CVD technique for waveguide sensor applications", *J. Nanostruct.*, 12(1) (2022) 1-11.

[11] S.-Y. Wang, W. Wang and Z.-H. Lu, "Asynchronous-pulse ultrasonic spray pyrolysis deposition of Cu_xS (x=1,2) thin films", *Mater. Sci. Eng. B*, 103(2) (2003) 184-188.

[12] G.G. Ali, M.A. Ahmed and A.A. Sulaiman, "Structural properties of AuNPs/PSi nanostructure", *Digest J. Nanomater. Biostruct.*, 17(2) (2022) 473-480.

[13] A.H. Mustafa, "The effect of doping in some physics properties of Cu_2S thin film prepared by spraying pyrolysis", MSc thesis, University of Technology (2006).

[14] L. Isac et al., "Copper sulfide (Cu_xS) thin films as possible p-type absorbers in 3D solar cells", *Energy Procedia*, 2(1) (2010) 71-78.

[15] T.A. Aswad, T.A. Abbas and G.G. Ali, "Effect of deposition time on optical properties of CuO thin film prepared by chemical bath deposition method", *Digest J. Nanomater. Biostruct.*, 16(3) (2021).

[16] P.V. Nho et al., "Preparation and characterization of low resistivity CuS films using spray pyrolysis", *Chalcogen. Lett.*, 9(10) (2012) 397-402.

[17] M. Adelifard, H. Eshghi and M.M. Bagheri Mohagheghi, "An investigation on substrate temperature and copper to sulphur molar ratios on optical and electrical properties of nanostructural CuS thin films prepared by spray pyrolysis method", *Appl. Surf. Sci.*, 258(15) (2012) 5733-5738.

[18] D. Shin et al., "Effect of RF power on the properties of sputtered-CuS thin films for photovoltaic applications", *Energies*, 13(3) (2020) 688.

[19] N.P. Huse et al., "An experimental and theoretical study on soft chemically grown CuS thin film for photosensor application", *Mater. Sci. Semicond. Process.*, 67 (2017) 62-68.

[20] Y.E. Firat et al., "Ultrasonic spray pyrolysis deposited copper sulphide thin films for solar cell applications", *Scanning*, 2017 (2017).

[21] J. Santamaria et al., "Sputtering process of Cu_2S in an Ar atmosphere", *Vacuum*, 37(5-6) (1987) 433-436.

[22] G.G. Ali, A.K.A. Sulaiman and I.B. Karomi, "The effect of the ZnO thickness layer on the porous silicon properties deposited by chemical vapor deposition", *AIP Conf. Proc.*, 2034(1) (2018).

[23] C. Naşcu et al., "Spray pyrolysis deposition of CuS thin films", *Mater. Lett.*, 32(2-3) (1997) 73-77.

[24] Y.Y. Kasim, G.G. Ali and M.H. Younus, "Irradiation Effects on the Sensitivity of ZnO Thin Films Synthesized on Glass Substrate by Sol-gel Method", *Iraqi J. Sci.*, (2021) 130-137.

[25] T. Çayır Taşdemirci, "Study of the physical properties of CuS thin films grown by SILAR method", *Opt. Quant. Electron.*, 51(7) (2019) 245.

[26] F.A. Sabah et al., "Influences of substrate type on the pH sensitivity of CuS thin films EGFET prepared by spray pyrolysis deposition", *Mater. Sci. Semicond. Process.*, 63 (2017) 269-278.

[27] G.G. Ali et al., "Properties of P-type porous silicon bombarded by neutrons", *Nucl. Instrum. Meth. Phys. Res. B: Beam Interact. Mater. Atoms*, 468 (2020) 23-27.

[28] A.K. Sahoo, P. Mohanta and A.S. Bhattacharyya, "Structural and optical properties of CuS thin films deposited by Thermal co-evaporation", *IOP Conf. Ser.: Mater. Sci. Eng.*, 73(1) (2015).

[29] G.G. Ali et al., "Study of porous silicon behavior via neutron irradiation: Fabrication and Characterization", *Res. in Phys.*, 14 (2019) 102466.

[30] D. Shin et al., "Effect of RF power on the properties of sputtered-CuS thin films for photovoltaic applications", *Energies*, 13(3) (2020) 688.

[31] J. Santos Cruz et al., "Optical and electrical properties of thin films of CuS nanodisks ensembles annealed in a vacuum and their photocatalytic activity", *Int. J. Photoener.*, 2013 (2013).

[32] R. Zeinodin, F. Jamali-Sheini and M. Cheraghizade, "Physical properties of Pb-doped CuS nanostructures for optoelectronic applications", *Mater. Sci. Semicond. Process.*, 123 (2021) 105501.

IRAQI JOURNAL OF APPLIED PHYSICS Vol. 20, No. 3, July-September 2024, pp. 511-516

Ali N. Munif
Firas J. Kadhim

Department of Physics,
College of Science,
University of Baghdad,
Baghdad, IRAQ

Investigation of Photocatalytic Activity of Anatase Titanium Dioxide Prepared by DC Reactive Magnetron Sputtering for Air Pollutants Degradation

In the present work, Titanium dioxide nanostructure were prepared by dc closed-field unbalanced reactive magnetron sputtering system using different values of Ar:O_2 gas mixing ratios. The magnetron sputtering system's operation parameters were optimized to prepare TiO_2 nanostructures as thin films with optical and structural homogeneity. The X-ray diffraction patterns and UV-visible spectroscopy show that the prepared films contain an anatase structure and an optical energy band gap of 3.2 eV. The production of Ti–O bonds has been confirmed by Fourier-transform infrared spectroscopy. The TiO_2 particles in the deposited films had an average size of 47.44 nm. TiO_2 as active photocatalyst material is employed in the field of air purification through using methane gas as an organic pollutant. The material's photocatalytic activity was evaluated by test the deterioration of polluted gas in the presence of a xenon lamp using an appropriate gas sensor (MQ2 gas sensor).

Keywords: Titanium dioxide; Nanostructures; Photocatalysis; Air purification
Received: 27 February 2024; **Revised:** 25 March 2024; **Accepted:** 01 April 2024

1. Introduction

One of the world's problems is air pollution. It harms the environment and human health. Reducing these pollutants requires practical treatment methods and efficient technologies [1]. Photocatalytic oxidation is considered an ideal air purification technology because it can use sunlight (or artificial light) under ambient conditions to breakdown various air pollutants into non-toxic or less harmful forms [2]. A photocatalytic pollution treatment method was discovered using nano-TiO_2 materials [3,4]. After Honda and Fujishima discovered light-induced water decomposition on TiO_2 electrodes [5], the photocatalytic process began to be widely studied, especially for air and water polluted treatment. These studies focus on the photocatalytic activity of TiO_2 nanoparticles under ultraviolet (UV) light (λ<387nm), which accounts for only a small fraction (3-5%) of solar radiation [6]. Titanium dioxide (TiO_2) nanoparticles have got significant interest because of their distinct characteristics. Given its exceptional characteristics like non-toxicity, high photocatalytic activity, chemical stability, and suitability for use as a coating, photocatalytic properties offer a promising solution to address the existing issues with indoor air quality and building air purification systems [7-11]. A TiO_2 thin film deposited on a substrate is environmentally friendly and known as the most promising photocatalyst among all semiconductor photocatalysts [12,13]. The photocatalytic activity is related to the average nanocrystalline size, specific surface area of pure TiO_2, phases involved and crystallinity [14-19]. TiO_2 appears in three different polymorphs: anatase, rutile, and brookite. Anatase TiO_2 is the most active form of TiO_2 than rutile, and rutile is the most stable primary form [20-23]. TiO_2 can be prepared using a variety of deposition techniques including pulsed laser deposition (PLD), sputtering, sol-gel process, spray pyrolysis, chemical vapor deposition (CVD), electrophoretic deposition, etc. [24-27]. These nanoparticles were prepared using the magnetron sputtering technique to ensure high homogeneity, purity, and control over the structural phase of the deposited film by controlling the gas mixing ratio [28-31].

2. Experimental Part

In this work, nanostructured titanium dioxide films were deposited on glass substrates using dc reactive magnetron sputtering. The optimum operation and preparation conditions were selected to be discharge voltage of 3 kV, discharge current of 50 mA, the inter-electrode distance of 4 cm, Ar:O_2 gas mixing ratio of 50:50, and deposition time of 3 hours. More details on the sputtering system and optimum operation conditions can be found elsewhere [32-35]. The structural characteristics of the prepared samples were carried out on the nanopowders extracted from the thin film samples in order to avoid the contribution of the glass substrate on which the thin film was deposited. These nanopowders were extracted by the conjunctional freezing-assisted ultrasonic extraction method [36,37].

The system used to evaluate the effectiveness of gas purification consists of a cylindrical chamber with a diameter of 6 cm and a length of 30 cm. There is a gas injection port in this chamber. The xenon lamp inside the chamber is arranged along its length with its axis parallel to the cylinder's axis as shown in Fig. (1). The xenon lamp is operated with 6 W power and generates light spectrum centered at 300 nm. The chamber includes a MQ2 sensor. The interior wall of the cylinder is covered with glass slides on which the TiO_2 films were deposited. These slides cover an area of about 200 cm^2 in total. The deposited slides were placed three centimeters away from the xenon lamp. The gas concentration in parts per million (ppm) is displayed on a display screen via an Arduino card that has been pre-programmed and attached to the sensor. The displayed concentration is calibrated based on the type of gas being analyzed. This entire system is connected to a personal computer for real-time data recording during the examination, as depicted in Fig. (1). The gas concentration was continually measured and recorded within the closed chamber at one-second intervals during this test. The gas testing process included pumping the test gas into the chamber at a constant rate. In the first test, measurements were taken without injecting the gas. In the second test, gas pumping occurred without the use of the xenon lamp. In the third test, we introduced the xenon lamp while the pollutant gas was present to evaluate the photocatalytic effect on the tested gases inside the chamber. All recorded data was saved on the computer for subsequent analysis.

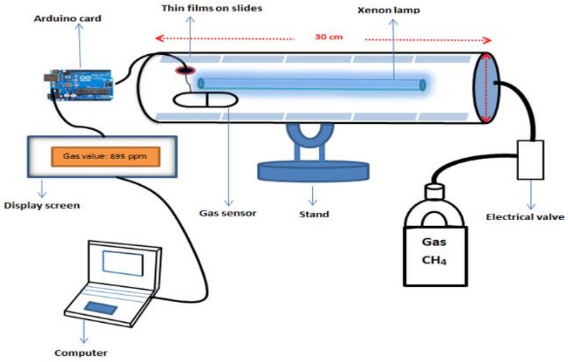

Fig. (1) Schematic diagram of the experimental system used for testing photocatalytic activity in air pollutants degradation

3. Results and Discussion

The structural characteristics bonds of TiO_2 films were determined through FTIR measurement using Shimadzu 8400S FTIR equipment. The Ti-O stretching vibration band appeared at approximately 447 and 667 cm^{-1}, and the Ti-O-Ti bonds in the TiO_2 lattice are responsible for the peak at 408.91 cm^{-1} [20, 21]. There are no peaks belonging to pollutions or contaminants, therefore, the samples can be categorized as highly pure. The absorption bands at approximately 3450 and 1620 cm^{-1} are caused by the stretching and bending vibrations, respectively, of the OH group in atmospheric water molecules [38-40].

The crystal structure of titanium dioxide samples was examined using a Shimadzu x-ray diffractometer using a Cu-K source (1.54Å). Figure (3) illustrates the XRD pattern of a TiO_2 thin film sample that was synthesized with a 50:50 gas mixing ratio and deposited time of three hours employing a heat sink under the substrate. This sample was selected as the optimum one among all others. According to JCPDS card no. 21-1272 (anatase TiO_2), nine different peaks may be seen in this figure, all of which are allocated to the anatase crystalline phase of TiO_2. In order to produce such nanostructures with highly-pure structural phases, dc reactive magnetron sputtering is advantageous, as demonstrated by the results, which exhibited no peaks belonging to the rutile phase in the synthesized sample.

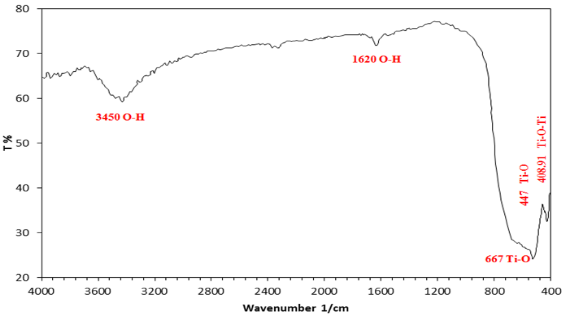

Fig. (2) FTIR spectrum of TiO_2 sample prepared at inter-electrode distance of 4 cm and using Ar:O_2 gas mixture of 50:50 after deposition time of 3 hours

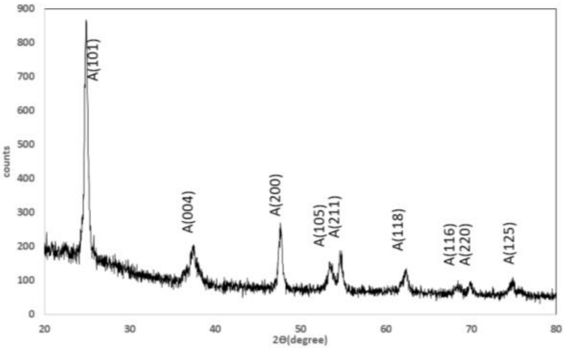

Fig. (3) XRD pattern for single-phase (anatase) TiO_2 sample prepared using gas mixing ratio of 50:50 after deposition time of 3 hours with heat sink under the substrate

The UV-visible spectroscopy was used to record and investigate the absorption spectra of TiO_2 film samples in the spectral region 300-800 nm using different gas mixing ratios as shown in Fig. (4). They exhibit considerable absorption to wavelengths shorter than 300 nm, peaking at approximately 312 nm. At 400 nm, the absorbance reaches its minimum and then rapidly decreases before gradually increasing at longer wavelengths. In the visible wavelength range of 400-700 nm, these films can be regarded as transparent. Consequently, the energy band gap of these samples can be determined using the following formula:

$$\alpha = \frac{A(h\nu - E_g)^n}{h\nu} \qquad (1)$$

where n is dependent on the type of transitions, A is a constant, and E_g is the optical energy band gap

The particle size of the prepared samples was ascertained using the FE-SEM. Figure (6) shows the image of the optimum TiO_2 sample, in which the nanoparticles are seen in irregular shapes and sizes and with average particle size of 47.44 nm. These particles aggregate and indicate good connectivity as they are held together by weak forces arising from the van der Waals force which leads to an electrostatic effects through the residual charge of the structure [41,42].

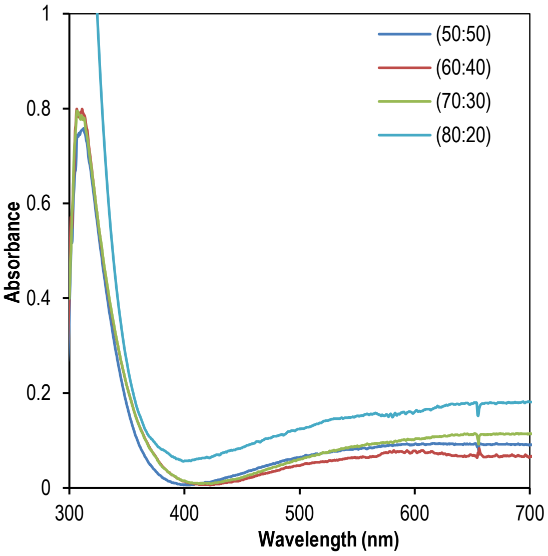

Fig. (4) Absorption spectra of TiO_2 thin films prepared using different Ar:O_2 gas mixing ratios

Figure (5) shows the determination of energy band gap for titanium dioxide thin films prepared using gas mixing ratios of (80:20), (70:30), (60:40) and (50:50) to be 3.24, 3.17, 3.16 and 3.2 eV, respectively. The optimum gas mixing ratio was (50:50) and thus energy band gap was determined to be 3.2 eV for single phase of anatase TiO_2.

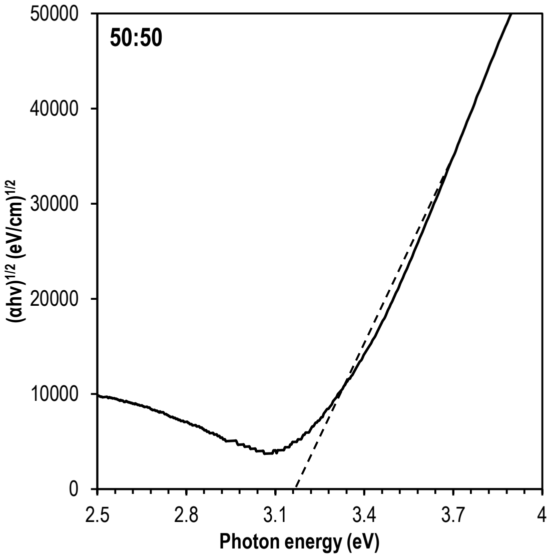

(a)

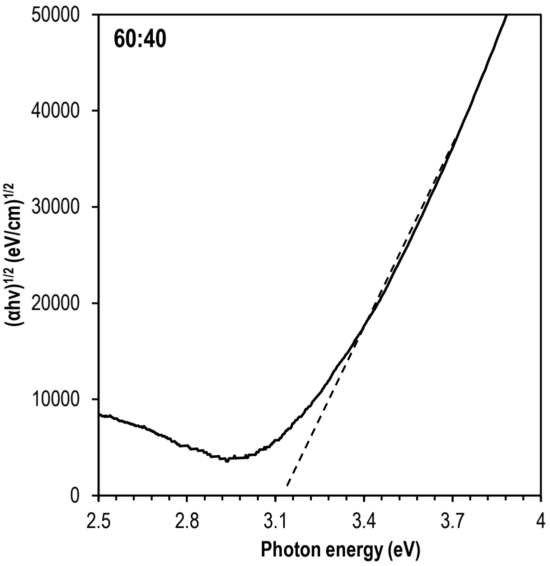

(b)

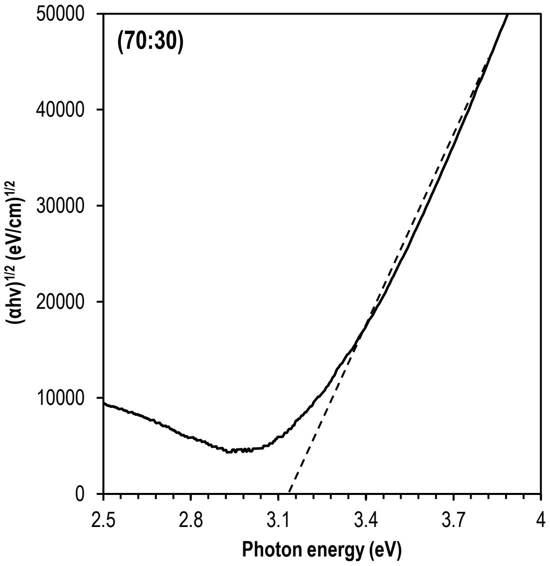

(c)

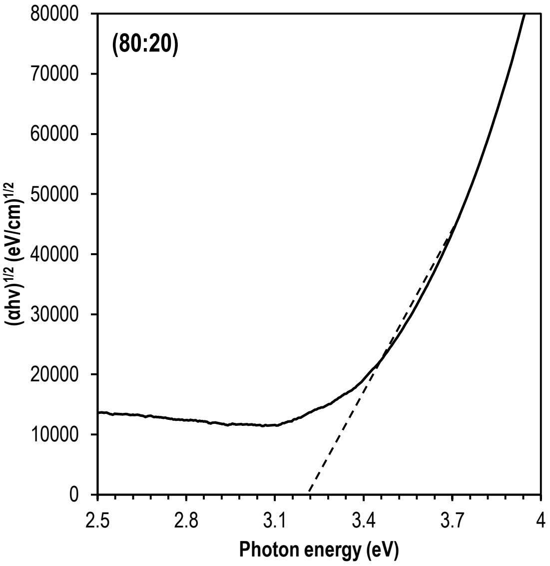

(d)

Fig. (5) Determination of energy band gap (E_g) for TiO_2 thin films prepared using different Ar:O_2 gas mixing ratios

The energy-dispersive x-ray (EDX) spectrum of the optimum sample was recorded and analyzed as shown in Fig. (7). This spectrum revealed the presence of titanium and oxygen in the thin layers and thus the formation of TiO_2 thin films was confirmed. With Ti and O present in the final sample, the weight ratios of Ti and O were 72.1% and 24.7%, respectively. The presence of 3.2% carbon is resulted from fixing the sample inside the EDX instrument.

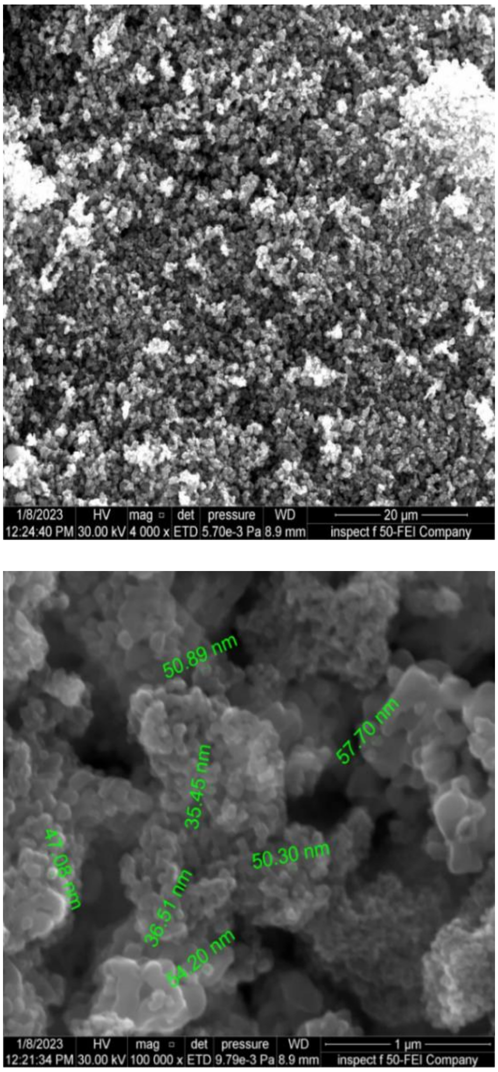

Fig. (6) FE-SEM images of the nanostructured anatase TiO_2 sample prepared using Ar:O_2 gas mixing ratio of 50:50, inter-electrode distance of 4 cm, and deposition time of 3 hours

The prepared nanostructured titanium dioxide thin films prepared were evaluated for their effectiveness in degradation of methane gas, which is a flammable, non-toxic, colorless, tasteless, and odorless gas. We measured the change in gas concentration over time in a sealed chamber containing static air, both before and after methane gas was added. The interaction between the gas and thin film deposited on glass substrate was monitored with and without the use of a xenon lamp. Initially, a steady gas concentration of 20 ppm was recorded in the static air representing the normal level of organic gases before adding methane. Upon pumping methane gas into the chamber and the xenon lamp was off, the gas concentration stayed mostly stable at approximately 898 ppm. On the other hand, the gas concentration progressively decreased upon switching the xenon lamp on and reached an almost constant value of 130 ppm over time period of 34 minutes as shown in Fig. (8).

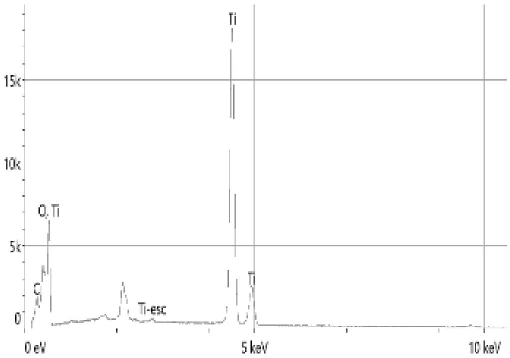

Element	Atomic %	Weight %
C	8.0	3.2
O	46.6	24.7
Ti	45.4	72.1

Fig. (7) EDX results for the nanostructured anatase TiO_2 sample prepared using Ar:O_2 gas mixing ratio of 50:50, inter-electrode distance of 4 cm, and deposition time of 3 hours

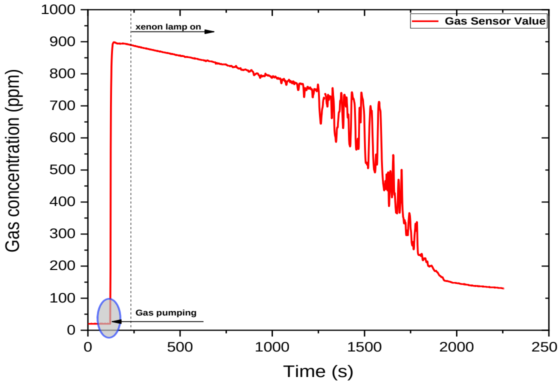

Fig. (8) Air purification test against methane gas based on photocatalytic effect of TiO_2 thin films prepared by dc reactive magnetron sputtering

4. Conclusion

In this study, nanostructured TiO_2 thin films – known as the optimum photocatalyst – were prepared by dc reactive magnetron sputtering technique and the energy band gap of these samples was determined to be 3.2eV, which belongs to the anatase phase of TiO_2. The prepared thin films are described by their optical and structural homogeneity. The prepared samples were tested in the field of air purification when irradiated by a xenon lamp. The results showed the high effectiveness of the prepared samples in air purification within a period of 34 min.

References

[1] F. He, W. Jeon and W. Choi, “Photocatalytic air purification mimicking the self-cleaning process of the atmosphere”, *Nat. Commun.*, 12 (2021) 2528.

[2] B.S. Weon, F. He and W. Choi, “Status and challenges in photocatalytic nanotechnology for cleaning air polluted with volatile organic compounds: visible light utilization and catalyst deactivation”, *Environ. Sci. Nano*, 6 (2019) 3185-3214.

[3] M.R. Hoffmann et al., “Environmental Applications of Semiconductor Photocatalysis”, *Chem. Rev.*, 95(1) (1995) 69-96.

[4] A. Fujishima, T.N. Rao and D.A. Tryk, “Titanium dioxide photocatalysis”, *J. Photochem. Photobio. C: Photochem. Rev.*, 1(1) (2000) 1-21.

[5] A. Fujishima and K. Honda, “Electrochemical Photolysis of Water at a Semiconductor Electrode”, *Nature*, 238 (1972) 37-38.

[6] T. Tachikawa, M. Fujitsuka and T. Majima, “Mechanistic Insight into the TiO_2 Photocatalytic Reactions: Design of New Photocatalysts”, *J. Phys. Chem. C*, 111(14) (2007) 5259-5275.

[7] N.H. Hashim, F.J. Kadhim and Z.S. Abdulsattar, “Characterization of Electrochromism and Photoelectrochromism of N-Doped TiO_2 and Co_3O_4 Thin Films Prepared by DC Reactive Magnetron Sputtering: Comparative Study”, *Iraqi J. Appl. Phys.*, 19(1) (2023) 5-12.

[8] M.A. Nima and F.J. Kadhim, “Photocatalytic Performance of Mixed and Single Phases of Titanium Dioxide Nanoparticles on Growth of Fusarium Oxysporum Fungal”, *Iraqi J. Appl. Phys.*, 17(4) (2021) 9-14.

[9] O.A. Hammadi et al., “Photocatalytic Activity of Nitrogen-Doped Titanium Dioxide Nanostructures Synthesized by DC Reactive Magnetron Sputtering Technique”, *Nonl. Opt. Quantum Opt.*, 51(1-2) (2019) 67-78.

[10] E.A. Al-Oubidy and F.J. Al-Maliki, “Photocatalytic activity of anatase titanium dioxide nanostructures prepared by reactive magnetron sputtering technique”, *Opt. Quantum Electron.*, 51(1-2) (2019) 23.

[11] Z.H. Zaidan et al., “Effect of Structural Phase on Photocatalytic Activity of Titanium Dioxide Nanoparticles”, *Iraqi J. Appl. Phys.*, 19(3A) (2023) 55-58.

[12] E.A. Al-Oubidy and F.J. Al-Maliki, “Effect of Gas Mixing Ratio on Energy Band Gap of Mixed-Phase Titanium Dioxide Nanostructures Prepared by Reactive Magnetron Sputtering Technique”, *Iraqi J. Appl. Phys.*, 14(4) (2018) 19-23.

[13] R.A.H. Hassan and F.T. Ibrahim, “Preparation and Characterization of Anatase Titanium Dioxide Nanostructures as Smart and Self-Cleaned Surfaces”, *Iraqi J. Appl. Phys.*, 16(4) (2020) 13-18.

[14] K.V. Baiju et al., “Photocatalytic activity of Sol-Gel-Derived nanocrystalline Titania”, *J. Phys. Chem. C*, 111(21) (2007) 7612-7622.

[15] M. Riazian, “Electrical properties, and enhancement of photocatalytic activity of TiO_2 nanorods doped with SiO_2”, *S. Afr. J. Chem.*, 70 (2017) 189-199.

[16] E.A. Ajaj, Z.R. Musleem and B.M. Al-Shabander, “Preparation of TiO_2 nanorods by Sol-Gel template method and measured its photo-catalytic activity for degradation of methyl orange”, *Iraqi J. Phys.*, 13(26) (2015) 171-177.

[17] S.S. Al-Awadi et al., “Optical and Structural Properties of Titanium Dioxide Papered by DC Magneton-Sputtering as a NO_2 Gas Sensor”, *Iraqi J. Sci.*, 61(10) (2020) 2562-2569.

[18] F.J. Al-Maliki, O.A. Hammadi and E.A. Al-Oubidy, “Optimization of Rutile/Anatase Ratio in Titanium Dioxide Nanostructures prepared by DC Magnetron Sputtering Technique”, *Iraqi J. Sci.*, 60 (2019) 91-98.

[19] F.J. Al-Maliki and E.A. Al-Oubidy, “Effect of gas mixing ratio on structural characteristics of titanium dioxide nanostructures synthesized by DC reactive magnetron sputtering”, *Physica B: Cond. Matter*, 555 (2019) 18-20

[20] F.J. Al Maliki and M.A. Al Rubaiy, “Synthesis and study the concentration effect on the photocatalytic activity of titania nanoparticles as antibactria using reactive magnetron sputtering technique”, *Opt. Quantum Electron.*, 54 (2022) 377.

[21] F.J. Kadhim, O.A. Hammadi and E.A. Al-Oubidy, “Optimization of Rutile/Anatase Ratio in Titanium Dioxide Nanostructures prepared by DC Magnetron Sputtering Technique”, *Iraqi J. Sci.*, 60 (2019) 91-98.

[22] Z.H. Zaidan et al., “Using Banana Peels for Green Synthesis of Mixed-Phase Titanium Dioxide Nanopowders”, *Iraqi J. Appl. Phys.*, 18(4) (2022) 27-30.

[23] D.M. Challoob, M.Y. Khdiar and O.A. Hammadi, “Highly-Pure Titanium Dioxide nanopowders Synthesized by EcoFriendly Solvothermal Method”, *Iraqi J. Appl. Phys.*, 20(2B) (2024) 381-386.

[24] R. Hippler et al., “Deposition of cobalt oxide films by reactive pulsed magnetron sputtering”, *Surf. Coat. Technol.*, 405 (2021) 126590.

[25] O.A. Hammadi and N.E. Naji, “Fabrication and Characterization of Polycrystalline Nickel Cobaltite Nanostructures Prepared by Plasma Sputtering as Gas Sensor”, *Phot. Sen.*, 8(1) (2018) 43-47.

[26] R.O. Abdulsada and T.A.A. Hassan, “Synthesis of TiO_2 Thin Films Nanoparticles with Different

Layers using Simple Sol-Gel Method", *Iraqi J. Sci.*, 62(11) (2021) 4425-4429.

[27] M.B. Al-Taee and B.M. Alshabander, "Photocatalytic Degradation of Methyl blue by TiO_2 Nanoparticles Incorporated in Cement", *Iraqi J. Phys.*, 21(1) (2023) 10-20.

[28] N. H. Hashim, F. J. Kadhim, "Structural and Optical Characteristics of Co_3O_4 Nanostructures Prepared by DC Reactive Magnetron Sputtering", *Iraqi J. Appl. Phys.*, 18(4) (2022) 31-36.

[29] M.A. Hameed, S.H. Faisal, R.H. Turki, "Characterization of Multilayer Highly-Pure Metal Oxide Structures Prepared by DC Reactive Magnetron Sputtering Technique", *Iraqi J. Appl. Phys.*, 16(4) (2020) 25-30

[30] R.A.H. Hassan and F.T. Ibrahim, "Preparation and Characterization of Ni-doped TiO_2 Nanostructures for Surface Cleaning Applications", *Iraqi J. Appl. Phys.*, 17(1) (2021) 3-8.

[31] Z.H. Zaidan et al., "Effect of Preparation Method on Crystalline Structure of Titanium Dioxide Nanoparticles", *Iraqi J. Appl. Phys. Lett.*, 6(2) (2023) 11-14.

[32] O.A. Hammadi et al., "Operation Characteristics of a Closed-Field Unbalanced Dual-Magnetrons Plasma Sputtering System", *Bulg. J. Phys.*, 41(1) (2014) 24-33.

[33] O.A. Hammadi et al., "Employment of Magnetron to Enhance Langmuir Probe Characteristics of Argon Glow Discharge Plasma in Sputtering System", *Iraqi J. Appl. Phys.*, 12(4) (2016) 19-28.

[34] A.M. Hameed and M.A. Hameed, "Highly-Pure Nanostructured Metal Oxide Multilayer Structure Prepared by DC Reactive Magnetron Sputtering Technique", *Iraqi J. Appl. Phys.*, 18(4) (2022) 9-14.

[35] A.M. Hameed and M.A. Hameed, "Spectroscopic characteristics of highly pure metal oxide nanostructures prepared by DC reactive magnetron sputtering technique", *Emerg. Mater.*, 6 (2022) 627-633.

[36] O.A. Hammadi, "Production of Nanopowders from Physical Vapor Deposited Films on Nonmetallic Substrates by Conjunctional Freezing-Assisted Ultrasonic Extraction Method", *Proc. IMechE, Part N, J. Nanomater. Nanoeng. Nanosys.*, 232(4) (2018) 135-140.

[37] O.A. Hammadi, "Effects of Extraction Parameters on Particle Size of Titanium Dioxide Nanopowders Prepared by Physical Vapor Deposition Technique", *Plasmonics*, 15(6) (2020) 1747-1754.

[38] J. Mohan, "Organic spectroscopy principles and applications", 2nd ed., Narosha Publishing House Pvt. Ltd, New Delhi, 28–95, 2009.

[39] R.A. Aziz and I. Sopyan, "Synthesis of TiO_2-SiO_2 powder and thin film photocatalysts of sol-gel method", Int. J. Chem., Vol. 48, pp. 951-957, 2009

[40] F.J. Al-Maliki, O.A. Hammadi and N. Muthesher, "Photocatalytic activity of TiO_2/SiO_2 nanocomposites synthesized by reactive magnetron sputtering technique", *J. Nanophot.*, 16(2) (2022) 026005.

[41] F.J. Al-Maliki and N.H. Al-Lamey, "Synthesis of Tb-doped titanium dioxide nanostructures by sol–gel method for environmental photocatalysis applications", *J. Sol-Gel Sci. Technol.*, 81(1) (2017) 276-283.

[42] Y. Zhao et al., "Synthesis and optical properties of TiO_2 nanoparticles", *Mater. Lett.*, 61(1) (2007) 79-83.

Mohammed H. Al-Dharob [1]
Ammar A. Hamad [2]
Ahmed Y. Qasim [3]
Omar A. Abdulrazzaq [4]
Ahmed A. Alwan [4]

[1] *Al-Karkh University of Science, Baghdad, IRAQ*
[2] *Ministry of Industry and Minerals, Scientific Advisory Office, Baghdad, IRAQ*
[3] *Corporation of Research and Industrial Development, Baghdad, IRAQ*
[4] *Renewable Energy and Environment Research Center, Corporation of Research and Industrial Development, Baghdad, IRAQ*

Investigating the Potential of Al_2O_3 Nanocomposites for Innovative Self-cooling Photovoltaic Technology

In this research, we investigate the use of a passive radiative self-cooling layer made of an Al_2O_3 nanocomposite on the backside of a compact 10W PV module. The coating, composed of Al_2O_3 nanoparticles (with a particle size of 30nm) blended with $Na_2SiO_3.9H_2O$ in a specific ratio, forms a ceramic glue applied to the module's rear surface in both horizontal and vertical directions using a standard paintbrush. The experiments were carried out in the 50°C ambient temperature of Baghdad summer. The results indicate a significant decrease in the temperature of the PV module in hot weather, reducing from 63°C to 58°C with the application of the nanocomposite layer. Additionally, the nanocomposite coating improves key performance parameters, such as open circuit voltage, short circuit current, voltage at maximum power, and current at maximum power. This enhancement results in a notable 10% increase in PV module power output, from 6.58W before coating to 7.22W after coating. The observed temperature reduction is attributed to the high emissivity of the ceramic layer, measured at 0.96 using a Fluke thermal camera. Extrapolating these findings to a larger scale, calculations for a 500W coated panel show a substantial power increase of 50W in hot weather conditions. Moreover, the annual energy gain is estimated to be 87kWh, with an impressive payback time of 1.5 years. Additionally, there is a noteworthy environmental impact, with a yearly reduction of 60kg of CO_2 emissions.

Keywords: Al_2O_3 NPs; Self-cooling; Passive radiation; Photovoltaic module
Received: 06 February 2024; **Revised:** 28 March 2024; **Accepted:** 03 April 2024

1. Introduction

Despite decades of progress since the first silicon solar cell, the inherent limitations of the p-n junction architecture, as defined by the Shockley limit, constrain its maximum power output per area [1,2]. The theoretical efficiency limit of a single-junction silicon cell hovers around 33%, due to the inability to efficiently utilize all captured sunlight. This limitation arises from unabsorbed low-energy photons and thermal losses from high-energy photon absorption. In addition to the intrinsic limitations of silicon photovoltaic (PV) cell efficiency, environmental conditions contribute to additional efficiency losses, including cloud cover, dust, and temperature. The first two factors lead to a reduction in irradiance and subsequently a drop in PV module power, while the last one predominantly affects the PV voltage [3]. In extremely hot countries such as Iraq, the PV efficiency may decrease to as low as 30% of its original value. To address these challenges, a high emissivity surface can be utilized as a heat sink layer for PV panels. Inorganic metal oxide nanomaterials, previously employed in Passive Daytime Radiative Cooling Systems, offer a solution due to their high rate of infrared emission [4,5]. Previous studies have recorded a sub-ambient cooling of 2.8°C for surface cooling using a mixture of Al_2O_3, SiO_2, and Si_3N_4 nanoparticles [6]. Ongoing research efforts continue to explore various cooling methods for PV modules [7-10].

This paper presents the first attempt to deposit a high emissivity layer on the rear side of a PV module, serving as an infrared passive radiative self-cooling layer. Aluminum oxide nanoparticles blended with sodium metasilicate were chosen as the passive cooling layer in this novel approach.

Burch's equation, derived from the Shockley model of the diode, provides a tool for examining the influence of irradiance and temperature on the open-circuit voltage (V_{OC}) and short-circuit current (J_{SC}) [11].

$$I_{SC} = [I_{SCr} + K_I(T_{Panel} - T_r)]\frac{G}{G_r} \tag{1}$$

$$V_{OC} = V_{OCr} + K_V(T_{Panel} - T_r) \tag{2}$$

where T_r is the ambient temperature (standard about 25°C), T_{Panel} is the real panel's temperature, I_{SCr} & V_{OCr} are short circuit current and open circuit voltage at the standard conditions (1000W/m^2, temperature of 25°C) respectively, K_I & K_V are the temperature coefficients respectively, G_r is the standard irradiance (1000W/m^2), and G is the real irradiance

Equation (1) reveals that the short circuit current (I_{SC}) is contingent on both temperature and irradiance, establishing a direct correlation with both T and G. In contrast, equation (2) illustrates that the open circuit voltage (V_{OC}) remains unaffected by irradiance, displaying a linear relationship solely with temperature. The source of V_{OC} lies in the built-in potential at the junction, determined by doping concentration and junction properties, with irradiance exerting no influence on these characteristics.

Essentially, as per Varshni's empirical Eq. (3), an elevated temperature induces a reduction in the silicon bandgap, resulting in an upsurge in the saturation current, commonly known as leakage current, in accordance with Shockley's model Eq. (4) [12]

$$E_g(T) = E_g(0) - \frac{\alpha T^2}{T+\beta} \quad (3)$$

$$I_S = AT^3 \exp\left(-\frac{E_g}{nkT}\right) \quad (4)$$

where $E_g(0)$ denotes the silicon bandgap at zero Kelvin, while α and β are material-specific parameters. I_S represents the saturation current (leakage current), A is the Shockley constant for silicon, E_g is the bandgap of silicon at the given temperature, n is the ideality factor of the diode, k is the Boltzmann constant, and T is the temperature in Kelvin

The open circuit voltage (V_{OC}) is logarithmically linked to the saturation current (I_S) through the following equation [13]:

$$V_{OC} = \frac{kT}{q}\ln\left[\frac{I_{SC}}{I_S}\right] \quad (5)$$

With an increase in temperature, both I_{SC} and I_S will rise, with IS (leakage current) dominating in Eq. (4). Specifically, I_S doubles in magnitude for every 10°C temperature increase. Consequently, the logarithmic component of Eq. (5) experiences a significant reduction, leading to a notable decrease in V_{OC}. Consequently, the PV power output is diminished.

The decrease in power in a PV module due to temperature is governed by the module's temperature coefficient, typically around 0.45% per degree Celsius [14]. This coefficient reflects the rate at which power decreases after the Standard Test Conditions (STC) temperature of 25°C. The power drop can be estimated using the following equation:

$$\text{Power Drop (\%)} = (T - 25) \times \text{Temp. Coef.} \quad (6)$$

where T is the PV panel temperature (which is different from the ambient temperature). The PV panel temperature is higher than the ambient temperature by about 20°C because the PV module is a good absorber and the passing current during operation heats the panel. Homer method can be used to estimate the panel's temperature compared to ambient temperature as follows [3]:

The constant A is calculated from:

$$A = (\text{NOCT} - 20)/G \quad (7)$$

where NOCT is Nominal Operating Cell Temperature, G is the radiation in W/m^2. The constant B is calculated from:

$$B = 1 - (\text{Eff.}/0.9) \quad (8)$$

where Eff. is the power conversion efficiency. The panel temperature then is calculated from:

$$\textit{Panel Temp.} = \textit{Ambient Temp} + (\textit{Radiation} \times A \times B) \quad (9)$$

As an example of the Homer method, consider a PV module with a maximum power of 250W operating at an ambient temperature of 50°C. According to equations (7-9), the PV panel temperature will be 69°C, which is 20°C higher than the ambient temperature. As per Eq. (6), the power drop will be 20W, representing an 8% decrease from the STC initial value. When extrapolating this ratio to a large-scale PV system, such a power loss becomes significant. For instance, a 1MW PV system could lose 80kW of its STC energy when operating at 50°C. In extremely hot countries like Iraq, where ambient temperatures can reach as high as 70°C in June and July, corresponding to the peak electricity demand, the PV system may experience a power loss of about 25 to 30% of its STC value.

Numerous attempts have been made to mitigate the impact of temperature on PV module performance, with water-based cooling and air-based cooling being among them [15]. However, these solutions are often not economically feasible for large-scale systems. Nanomaterials, extensively studied across various applications, including PV cells, have been employed as antireflection layers, absorbent layers, and superhydrophobic layers [3]. Some nanomaterial blends exhibit an emissivity near unity. Emissivity, defined as the effectiveness of a material's surface in emitting thermal radiation, follows the Stefan-Boltzmann law, ranging from 0 (non-emitting surface) to 1 (perfect-emitting surface or a perfect black body) [16]

$$E = \sigma T^4 \quad (10)$$

where σ is the Stefan-Boltzmann constant and equals 5.67×10^{-8} W/m^2.K^4. According to this equation, a perfect black body emits 448W/m^2. This is the highest ever emissivity that any surface can emit.

2. Experimental Procedure

2.1. Materials Characterization

Aluminum oxide nanoparticles (Al_2O_3 NPs) with α-phase were procured from Changsha Santech Company, boasting a purity level of 99.99%. This material presents as a fine white powder. To ensure its quality, the powder underwent characterization using a Scanning Electron Microscope (SEM) of the Quattro S type. Emissivity measurements were conducted employing a Fluke thermal camera. The emissivity was determined by measuring the surface temperature of the layer with a Fluke Ti125 thermal camera and a thermocouple. The Fluke SmartView Software facilitated recalibration of the emissivity to align the temperature measured by the thermal camera with the temperature recorded by the thermocouple.

2.2. PV Module Characterization

In this study, a small PV module with a nominal power of 10W was employed. The module underwent testing under Standard Test Conditions (STC) and Normal Operating Cell Temperature (NOCT) conditions, facilitated by the Keyland Photovoltaic Sun Light Simulator and Solar 4000 PV Analyzer, respectively. NOCT conditions refer to the module parameters evaluated at 50°C and 800W/m^2. Figure (1) provides a visual representation of the sun simulator utilized in the measurements. The outcomes of the module parameters are detailed in table (1).

Fig. (1) The Keyland Photovoltaic Sun Light Simulator used for STC test

2.3. Solution Preparation and Module Painting

To prepare the solution, 1mg of Al_2O_3 NPs was added to 100ml of sodium metasilicate ($Na_2SiO_3.9H_2O$). The mixture underwent blending using an ultrasonic probe sonicator with a water jacket for 5 minutes. It is important to note that an extended sonication time could lead to overheating and solidification of the solution, while a shorter duration might result in a nonhomogeneous solution. The result was a thick, homogeneous solution with a milky color, as depicted in Fig. (2).

For the application of the back coating, a regular paintbrush was utilized on the rear side of the PV panel. The process involved the application of two layers: the first layer was painted in the horizontal direction, followed by a one-hour waiting period to allow the layer to dry. Subsequently, a second layer was applied over the first one, this time in the vertical direction. This sequential application resulted in an approximately 5mm micrometer thickness of the back coating layer on the substrate of the solar modules. The coated layer was left to dry completely overnight.

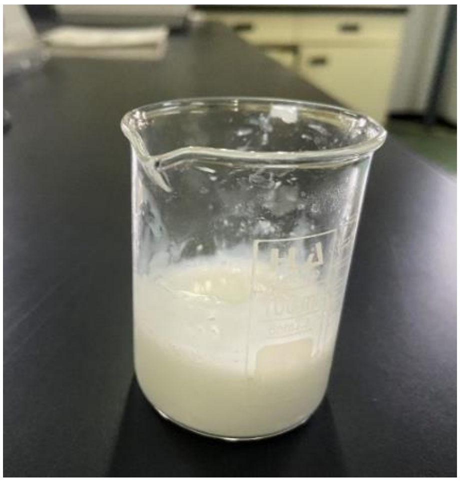

Fig. (2) The solution of the paint after 5 min probe sonicating

Figure (3) visually represents the PV module both before and after the coating process. The total rear area of the PV module is $0.25m^2$, and the coating was applied to nearly the entire area, with only a small portion near the edges left uncoated.

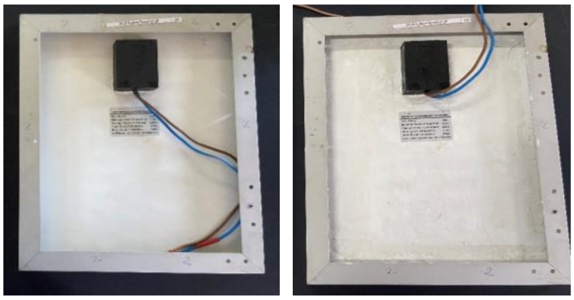

Module before Coating **Module after Coating**

Fig. (3) Rear side of the panel before and after coating with Al_2O_3 NPs

3. Results and Discussion

Figure (4) depicts the influence of average ambient temperature on both the PV output power and the surface temperature of the PV panel over the course of a year. The data presented pertains to a 250W (STC) PV panel and was gathered in Baghdad throughout the year 2018. As evident from the figure, the surface temperature of the PV panel consistently exceeds the ambient temperature, aligning with the previously mentioned Eq. (9). The decline in power as temperature rises is in accordance with the findings of Eq. (6).

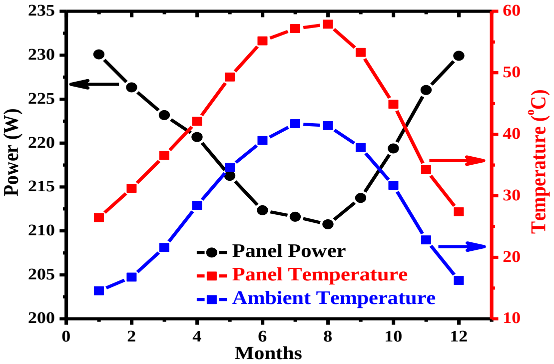

Fig. (4) The variation of PV module power with ambient over one year in Baghdad city

The SEM image of the Al_2O_3:Na_2SiO_3 blend is presented in Fig. (5a), revealing a matrix of sodium metasilicate adorned with Al_2O_3 nanoparticles. Pinholes are evident in the image, attributed to the non-homogeneity of the coated layer. Figure (5b) zooms in on the Al_2O_3 nanoparticles, showing a diverse particle size distribution ranging from 30nm to 50nm. Notably, a few particles exceed 50nm, while others are below 30nm.

For a more detailed examination of the specimens' morphological features, SEM images of native Al_2O_3 nanoparticles and modified Al_2O_3 nanoparticles were acquired (Fig. 5). The modified Al_2O_3 nanoparticles exhibit a homogeneous dispersion, as depicted in Fig. (5a), while apparent agglomeration is observed in the image of native Al_2O_3 nanoparticles (Fig. 5b). This observation suggests that chemical or physical bonding occurs between the polarity bonds of KH-560 and hydroxide groups. The macromolecular chains grafted onto the surface of Al_2O_3 nanoparticles induce mutual exclusion and steric hindrance effects, reducing the surface free energy and effectively controlling agglomeration. These findings emphasize the crucial role of KH-560 in achieving the dispersion of Al_2O_3 nanoparticles [17].

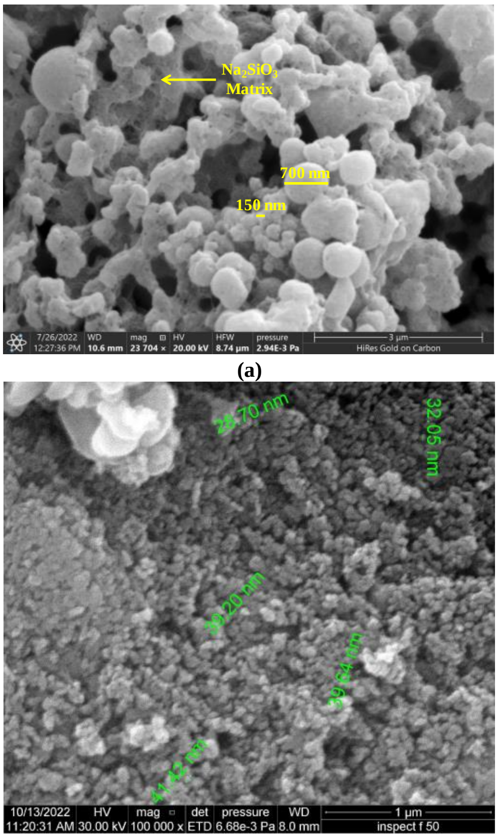

(a)

(b)

Fig. (5) SEM images of (a) Al_2O_3: Na_2SiO_3, and (b) Al_2O_3 nanoparticles

On August 30, 2021, at 12:00 PM, two PV modules were tested after being exposed to direct sunlight for one hour to allow their temperature to equalize with the ambient conditions. At the time of testing, the solar radiation and ambient temperature were 837 W/m^2 and 53°C, respectively. The uncoated rear surface of one module registered a temperature of 63°C, while the rear side of the module coated with Al_2O_3 nanoparticles exhibited a surface temperature of 58°C. This signifies a notable 5°C temperature reduction, attributed to passive cooling facilitated by the infrared emission from the nanoparticle layer induced by lattice vibration [10]. The nanoparticles absorb heat from the silicon bulk and reemit it as infrared radiation continuously, leading to the PV panel reaching an equilibrium temperature lower than that of a conventional panel. Additional contributing factors include the white color of the coating, which prevents back heating from albedo, and the increase in mass due to the layer's weight.

To calculate emissivity, a Fluke thermal camera was employed. Figure (6) displays the thermal images of the panel before and after coating. At an emissivity of 1 (perfect black body), the camera read 53.6°C, whereas for the uncoated panel, it was 58.1°C. Emissivity was determined by using a thermocouple to measure the temperature at the same surface point. The emissivity value was adjusted using SmartView Software until the temperature matched that measured by the thermocouple. At this point, the emissivity was found to be 0.96, a remarkably high value even exceeding that of black paint. This high emissivity accounts for the reduction in panel temperature compared to the uncoated counterpart. In comparison to other cooling methods, such as using phase change material as passive cooling for PV panels, which demonstrates a power increase of about 5.23% under similar conditions [18], the Al_2O_3 nanoparticle coating shows promising effectiveness.

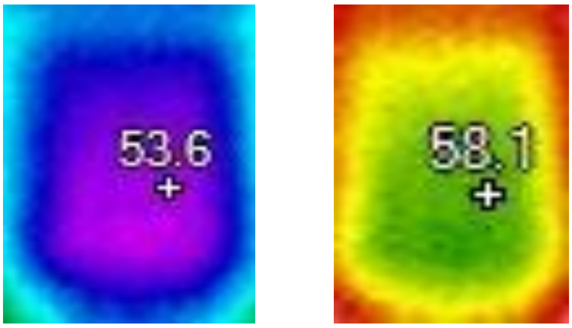

Temperature before Calibration

Temperature after Calibration

Fig. (6) Thermal image taken by Fluke thermal camera

The IV curves of the PV panel under different conditions are presented in Fig. (7). An initial test at room temperature (RT) was conducted for comparison purposes. As depicted in the figure, the PV panel coated with Al_2O_3 nanoparticles demonstrates improved values for V_{OC} and Pm in comparison to the uncoated PV panel. However, I_{SC} shows no significant effect, as temperature predominantly influences voltage rather than current, as discussed in Eq. 5 and the subsequent paragraph. The results of the PV parameters are summarized in table (2). Notably, the coated PV panel shows a 10% increase in maximum power (P_m). This outcome holds considerable significance when considering the potential application of this technique to large-scale PV systems.

Table (2) highlights the increase in V_{OC}, V_m, I_{SC}, and I_m for the passive cooling nanocomposite paint applied to solar panels. To enhance the visibility of the results from table (2), a feasibility analysis was conducted for a 500W PV panel, as depicted in table (3). The table reveals that each coated panel can yield an additional 50W of power. This translates to an annual energy gain of 87kWh and a reduction of 60kg of CO_2 emissions per year. With a coating cost of $12 per module, the payback period for this investment is a mere 1.5 years. This underscores the economic viability and potential environmental benefits of implementing the coating on solar panels.

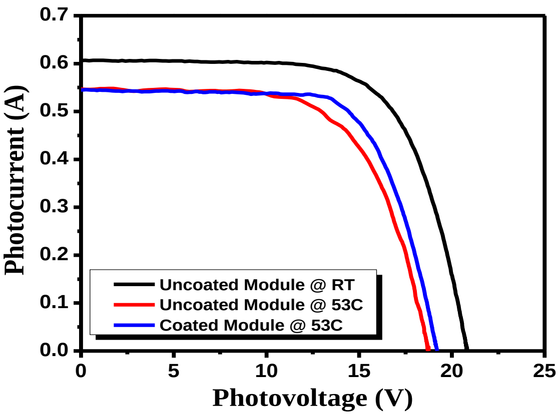

Fig. (7) The forth quadrant IV curves under illumination

Table (3) Feasibility estimation on 500W PV panel coated with Al_2O_3 NPs

Power Difference	50W
Panel Area	$2m^2$
Energy Gain in One Year	87kWh
Paint Cost	$12
Electricity Bill Price	120 ID/kWh
Yearly Profit	$7.5
Payback Time	1.5 Year
CO_2 Avoided per Year	60kg

4. Conclusions

Passive radiative self-cooling systems employing nanoparticles, such as Al_2O_3 NPs, emerge as a practical and economical solution for enhancing the efficiency of PV cooling systems when compared to conventional solar modules. In contrast to alternative methods, such as water cooling, this approach stands out as a self-cooling technique that eliminates the need for water or energy-consuming components like pumps or wipers. The method proves highly effective, inducing a substantial reduction in PV module temperature. Its efficiency and simplicity make it a promising avenue for improving the performance of solar panels.

Acknowledgment

The Corporation of Research and Industrial Development is thankful for the logistic support provided.

References

[1] D.M. Chapin, C.S. Fuller and G.L. Pearson, “A new silicon p-n junction photocell for converting solar radiation into electrical power, *J. Appl. Phys.*, 25(5) (1954) 676–677.

[2] W. Shockley and H.J. Queisser, “Detailed Balance Limit of Efficiency of p-n Junction Solar Cells,” *J. Appl. Phys.*, 32(3) (1961) 510–519.

[3] S.K. Abdulridha, S.A. Tuma and O.A. Abdulrazzaq, “Study of the Partial Shading Effect on the Performance of Silicon PV Panels String,” *J. Appl. Sci. Nanotechnol.*, 1(1) (2021) 32–42.

[4] F. Moreno et al., “Evaluating the efficiency of utilizing selectively optimized metamaterial nanostructures for passive radiative cooling of5t5 satellites and components,” *PAM Rev. Energy Sci. Technol.*, 6 (2019) 110–123.

[5] Y. Zou et al., “Al_2O_3/reduced graphene oxide double-layer radiative coating for efficient heat dissipation,” *Mater. Des.*, 157 (2018) 130–140.

[6] R. Harahap and S. Suherman, “Active versus passive cooling system in increasing solar panel output,” Procedia Environmental Science, *Eng. Manag.*, 8(1) (2021) 157-166.

[7] S. Wu and C. Xiong, “Passive Cooling Technology for Photovoltaic Panels for Domestic Houses,” *Int. J. Low-Carbon Technol.*, 9(2) (2013) 118-126.

[8] E. Kozak-Jagieła, P. Cisek and P. Ocłoń, "Cooling techniques for PV panels: A review", *Scientiae Radices*, 2 (2023) 47-68.

[9] A.M. Elbreki et al., “Experimental and economic analysis of passive cooling PV module using fins and planar reflector", *Case Studies Therm. Eng.*, 23 (2021) 100801.

[10] D. Chae et al., “Spectrally Selective Nanoparticle Mixture Coating for Passive Daytime Radiative Cooling,” *ACS Appl. Mater. Interfaces*, 13(18) (2021) 21119–21126.

[11] M. Arnaout, W. Salameh and A. Assi, “Impact of solar radiation and temperature levels on the variation of the series and shunt resistors in photovoltaic modules", *Int. J. Res. Eng. Technol.*, 5(3) (2016) 295-301.

[12] S.M. Sze and K.K. Ng, **"Physics of Semiconductor Devices"**, 3rd ed., John Wiley & Sons, Inc. (2007).

[13] M. Rudan, **"Physics of Semiconductor Devices"**, 3rd ed., John Wiley & Sons, Inc. (2015).

[14] A. Descoeudres et al., “Silicon Heterojunction Solar Cells: Towards Low-cost High-Efficiency Industrial Devices and Application to Low-concentration PV,” *Energy Procedia*, 77 (2015) 508–514.

[15] Y.M. Irwan et al., “Indoor Test Performance of PV Panel through Water Cooling Method,” *Energy Procedia*, 79 (2015) 604–611.

[16] K. Tang et al., “A Thermal Radiation Modulation Platform by Emissivity Engineering with Graded Metal–Insulator Transition,” *Adv. Mater.*, 32(36) (2020) 1907071.

[17] T. Luo et al., "Study of Surface Modification of Al_2O_3 Nanoparticles with KH-560", *Asian J. Chem.*, 25(12) (2013) 6777-6779.

[18] A. Al Miaari and H. Muhammad Ali, "Technical method in passive cooling for photovoltaic panels using phase change material", *Case Studies Therm. Eng.*, 49 (2023) 103283.

Table (1) PV module parameters of the used panel

Condition	V_{OC} (V)	I_{SC} (A)	V_m (V)	I_m (A)	P_m (W)	Effic. (%)	FF	Rad. (W/m^2)	Temp. (°C)
STC	21.38	0.52	17.43	0.47	8.16	3.2	0.73	1000	25
NOCT	18.89	0.49	12.96	0.32	4.20	1.6	0.45	800	50

Table (2) The PV parameters of the PV module before and after coating

Condition	V_{OC} (V)	I_{SC} (A)	V_m (V)	I_m (A)	P_m (W)	Effic. (%)	FF	Rad. (W/m^2)	Amb. Tem. (°C)	Surf. Tem. (°C)
Reference @ 35°C	20.83	0.60	16.04	0.53	8.57	3.4	0.68	870	35	35
Before Coating	18.65	0.54	14.21	0.45	6.39	2.5	0.62	837	53	63
After Coating	19.20	0.54	14.35	0.50	7.22	2.8	0.69	837	53	58

Hamsa N. Naser
Rafea T. Ahmed
Jinan A. Abd
Nada A. Mohammed

Department of Laser Physics,
Faculty of Science for Women,
University of Babylon,
Babil, IRAQ

Silver Nanoparticles Effects on Methyl Orange Dye Photocatalysis for Environmental Applications

Silver nanoparticles (AgNPs) were synthesized by one of the most popular technique of pulsed laser ablation in liquids (PLAL) for photodegradation of methyl orange dye. To investigate the surface morphology of the nanoparticles, x-ray diffraction (XRD) and field-emission scanning electron microscopy (FE-SEM) were used. Their results indicated that silver particles have sizes within nanoscale range. While UV spectrophotometer was used to examine the optical characteristics at regular time intervals (30, 60, 90 and 120 min). The UV results of the prepared materials showed that the best absorbance has been obtained for the concertation of $3\text{x}10^{-4}$ mol of dye which has been measured to be ~489nm. Results denoted that the dye degradation efficiency of AgNPs increased as the concentration of Ag increased in the dye solution to be 81% at the ablated time of Ag that equals to 3 mins. This work enhances the reduction of environmental pollution through this technology that can be environmentally friendly.

Keywords: Dye removal; Laser ablation; Silver nanoparticles; Photodegradation
Received: 06 February 2024; **Revised:** 28 March 2024; **Accepted:** 03 April 2024

1. Introduction

In the recent years, rapid development has made nanotechnology research integral to metal nanoparticles. Generally, nanoparticles have a diameter of 1–100 nm with unique properties and they can be described by their massive surface-to-volume ratios in electronic attributes and quantum effects [1]. The distinctive properties of nanoparticles such as high surface area, electrical, magnetic and/or optical properties, high reactivity, morphological and considerable porosity turn them into valuable materials in adsorption, catalysis, sensing and optic-electronic applications [1,2] as well as bring new options in numerous fields: pharmaceutical, agriculture, text, engineering, etc. [3].

Noble-metal nanomaterials with, among others, a bottom-up approach with discrete morphologies such as spheres, cubes, stars and wires; versatility in synthesis; and low cost demonstrate remarkable physical/ chemical properties allowing unique interactions with the ecosystem [4,5]. This is particularly purely made inorganic nanoparticles including gold, silver and copper that have distinctive photothermal and optical characteristics in absorbing a broad area of visible spectrum in the electromagnetic radiation. Gold (Au) and silver (Ag) nanoparticles have magnified the properties of optoelectronic stability and biocompatibility [6]. Silver nanoparticles (AgNPs) hold good antibacterial properties making them useful materials in different fields products for industrial purposes. This includes biomaterials, therapeutics, catalysis, photocatalysis, sensing and dye-sensitized solar cells [7].

Based on that, one of the most successful utilization of (AgNPs) against water/wastewater treatment that pollutants with organic materials and heavy metals. AgNPs works as plasmonic sensors for photocatalysts. This encourages the degradation (oxidation) of dyes and pesticides, amplifying the environmental functions [8,9].

Generally, Methyl orange (MO) is utilized as a coloring agent in many areas. Although, it is a low-toxic agent, it could have toxic effects and slow decomposition upon disintegration when discharged into water bodies leading to some health risks [9,10]. Therefore, Methyl orange (MO) degradation methods need to be investigated. In order to remove colors, adsorption has been used due to different benefits including adaptability and fast action. Accordingly, sorbents showed well- defined, large and also well accepted area. In the current work, silver nanoparticles (AgNPs) have been synthesized by pulsed laser ablation methods (PLAL) in liquids as photodegradation catalysts of Methyl orange (MO) dye and the degradation efficiency of silver nanoparticles (AgNPs) were studied.

2. Experimental Part

To prepare a solution of methyl orange dye with a concentration of 3×10^{-4}, 5×10^{-4} and 7×10^{-4} mol, a 0.00376 g of the dye powder was dissolved in a volume of 10 cm^3 of distilled water according to the relationship:

$$M.W = (M_m \times C \times V)/1000 \qquad (1)$$

where M_m is the weight of the dye (g), C is the concentration to be prepared (mol), V is the volume of solvent (cm^3), and M.W is the molecular weight of the dye used (g/mol)

The different concentrations of dye have been obtained using dilution relationship:

$$C_1V_1 = C_2V_2 \qquad (2)$$

An immersed pellet of silver has been ablated in 5 ml of distilled water by Nd:YAG laser (1064nm, 80mJ and 5Hz). When the laser pulses strike the silver surface, a plume will be generated with a strong vibration wave that spreads in all directions within the impact area. This plume emits light and noise, forming a visible plume of silver particles that are adsorbed of the surface of the metal and dispersed in all directions within the liquid. It was noted that the color of the solution changes as the nanoparticles concentration increased due to increment of the number of pulses per minutes (for the chosen concertation $3x10^{-4}$ mol, the ablated time was applied for 1, 2, 3 and 4 mins). Figure (1) shows the process of laser ablation of silver nanomaterial and figure (2) displays the samples that used for degradation applications by exposing them to UV source through (30, 60, 90 and 120 min) using $3x10^{-4}$ mol concentration of dye with ablated time 1, 2 and 3 minutes of Ag nanoparticles.

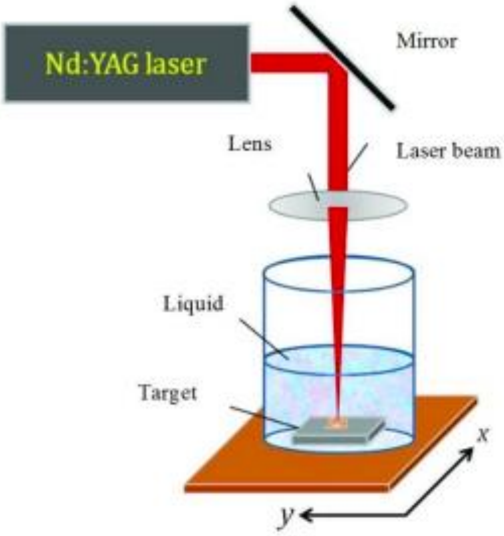

Fig. (1) The pulse laser ablation process

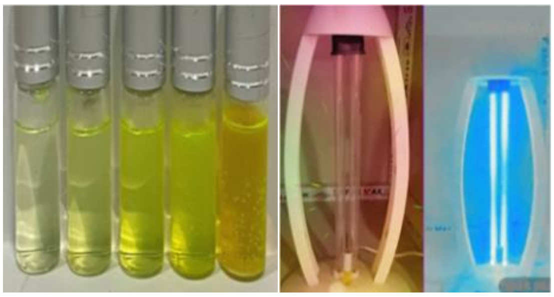

Fig. (2) The samples before and after exposure to UV radiation

3. Results and Discussion

The XRD and FE-SEM tests have been utilized to determine the size of silver particles. Figure (3) presents the XRD pattern, which indicates that the prepared particles are silver nanoparticles and have polycrystalline of face-centered cubic (FCC) structure with notable peaks at 2θ = 37°, 42.5°, 64° and 77° belong to (111), (200), (220) and (311) planes corresponding to (JCPDS File No. 04-0783) [11].

The crystallite size (D) of the silver particles has been calculated using Scherrer's formula, equation (3) [12].

$$D = \frac{0.9\,.\lambda}{\beta\cos\theta} \qquad (3)$$

The calculated crystallite size (D) of preferred orientation along (200) plane indicates that the crystallite size is within the nanoscale and is about (13.24 nm) which is very close to the value of other research [11].

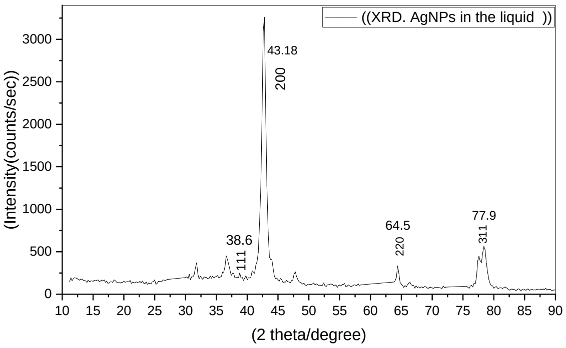

Fig. (3) XRD pattern of silver nanoparticles

FE-SEM images shown in figures (4) and (5) specify that the range of particles sizes smaller than 50 nm according to the device scale. The images show a light emitting and semi-spherical shape of silver nanoparticles. Most metals, including Ag, have FCC structures and grow from nucleation into twinned and multiply twinned particles with surfaces bordered. Ag nanoparticles tend to agglomerate due to the high surface energy and high surface tension of the ultrafine nanoparticles, which may account for the observation of some larger nanoparticles. Catalytic activity, a crucial feature of the produced Ag NPs, is enhanced by their small particle size and wide surface area [13].

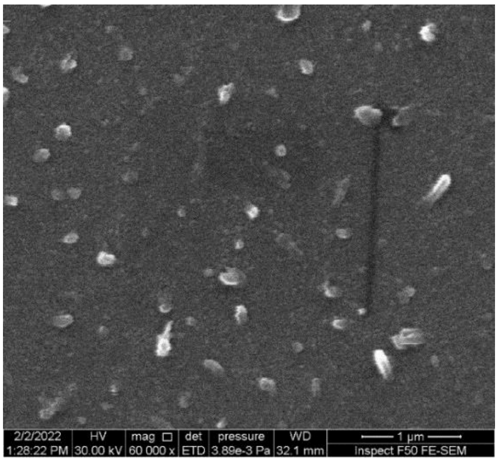

Fig. (4) FE-SEM examination of silver nanoparticles with dimensions of 1μm

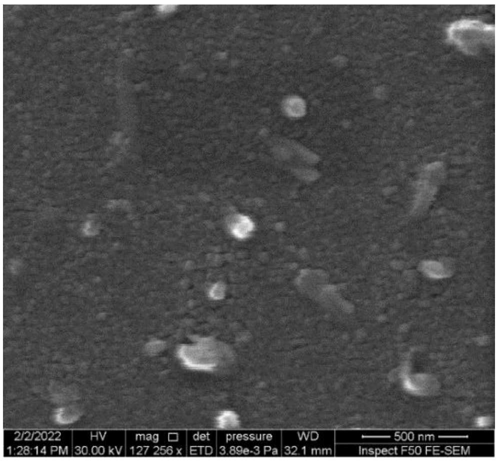

Fig. (5) FE-SEM image of silver nanoparticles with dimensions of 0.5µm

The absorption spectrum as a function of wavelength for methyl orange without and with the prepared Ag nanomaterial were measured using a UV-visible spectrophotometer as shown in figures (6) and (7), respectively. Figure (6) indicates that the absorbance spectrum of dye lies in the range of ~489nm) and figure (7) shows the spectrum of Ag particles lies in the range of ~403nm. The nanomaterial prepared at different times and with constant energy showed that the peak of the absorption spectrum increases with increasing the time-related to the number of pulses directed at the target. This increment contributes to increasing the occurrence of induced defects, and this result is consistent with previous results of other research [13,14].

The transmittance curve for all samples shows an opposite behavior to the absorbance (Fig. 8), as the curve begins to increase at the wavelength of 350 nm and then tends to saturate at wavelengths longer than 550nm, as the transmittance increases with increasing wavelength. These results about transmittance versus wavelength are similar to research [10]. It is also noted that the transmittance decreases with increasing time for the laser pulses directed at the target.

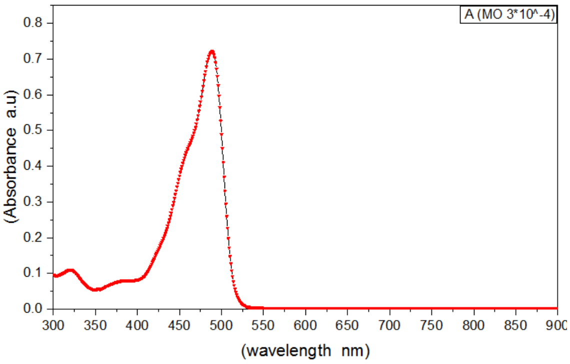

Fig. (6) The absorbance as a function of wavelength of methyl orange dye without Ag nanoparticles

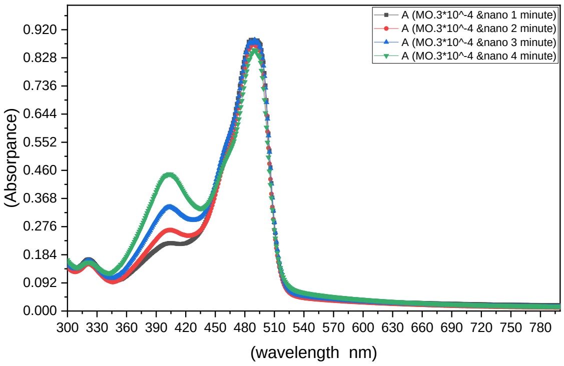

Fig. (7) The absorbance as a function of wavelength of methyl orange dye with Ag nanoparticles

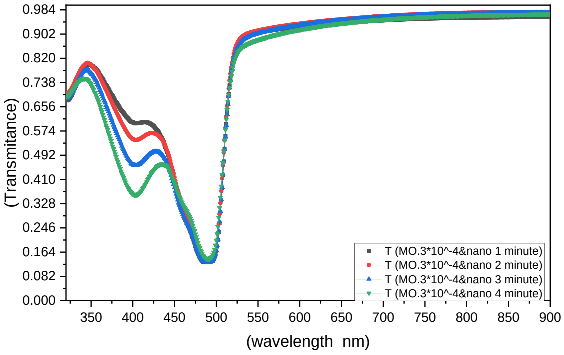

Fig. (8) The transmittance as a function of wavelength of methyl orange dye with Ag nanoparticles

The linear absorption coefficient with wavelength for both the dye and the silver nanoparticles has been calculated using the following equation [1]:

$$\alpha = 2.303\ A/d \qquad (4)$$

The absorption coefficients of all concentrations $\alpha > 10^6$ cm^{-1}, as shown in Fig. (9). This result indicates a close relationship between increasing absorption with increasing energy of the incident photon, and this result was noted by other researchers [10,14,15] that this is due to the increased probability of electronic transfer between valence levels to the conduction band with increasing energy of the incident photon. The value of the absorption coefficient is high and increases with increasing ablated time, as can be seen from Fig. (9), and this behavior was monitored by other research [10,16].

The extinction coefficient was found from the relationship [10]:

$$K = \alpha\ \lambda / 4\ \pi \qquad (5)$$

The extinction coefficient changes as a function of the wavelength, as shown in Fig. (10). It is clearly that in the ultraviolet region and at low concentrations, the extinction coefficient has low values and increases with increasing Ag nanoparticles concentration. In the visible region, the extinction coefficient is the highest possible due to the high absorption in this region.

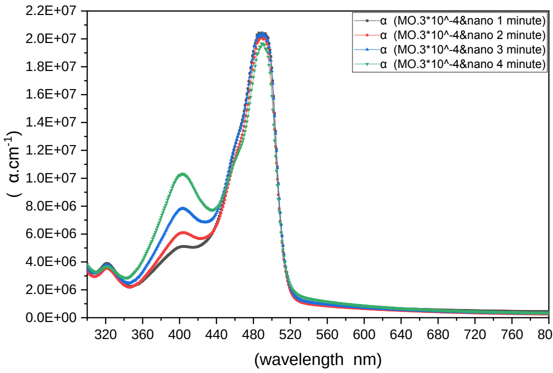

Fig. (9) The absorption coefficient (α) as a function of wavelength of methyl orange dye with Ag nanoparticles

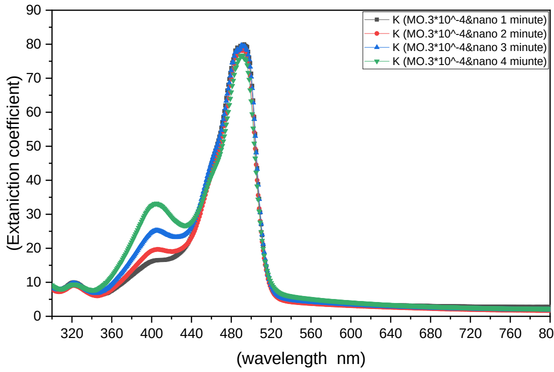

Fig. (10) The extinction coefficient as a function of wavelength of methyl orange dye with Ag nanoparticles

The refractive index has been calculated for the methyl orange dye and Ag nanomaterial. Figure (11) shows the refractive index values as a function of wavelengths within range of 350-500nm. It can be seen that the refractive index increases in the (UV) region. It extends to the visible region, as the concentration of the dye and Ag nanoparticles increase with increasing the time represented by the number of pulses, the value of the refractive index increases as a result of the stacking process that occurs within the crystalline structure. There is also a main reason, which is the increase in reflectivity at the expense of absorbance and optical transmittance**.**

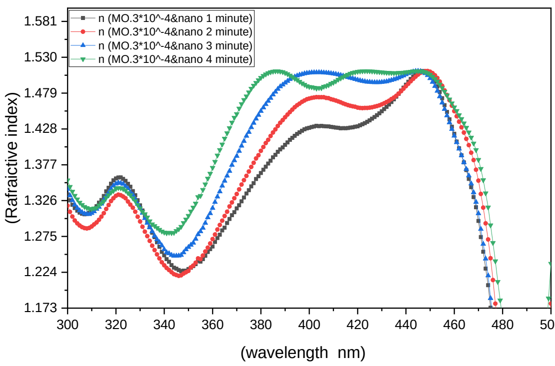

Fig. (11) The refractive index as a function of wavelength of methyl orange dye with Ag nanoparticles

Figure (12) represents the absorption spectrum of methyl orange (MO) dye, where the best concentration of the dye was taken through the absorption spectrum at a concentration of $3x10^{-4}$ mol mixed with different concentrations of Ag nanoparticles for 1, 2 and 3 min ablated time. Figures (12a), (12b) and (12c) represent the absorption spectrum of every concentration of Ag nanoparticles in the MO dye as a catalytic by exposing the samples to UV source through 30, 60, 90 and 120 min. It was observed that the absorption of Ag nanoparticles overlapped with the absorption of the dye at the range of 490 nm, as shown in the figure. The best degradation of dye concentration has been achieved at concentration of Ag nanoparticles of 3 min at 120 min of exposing time due to the adsorption of the dye by the silver nanomaterial which possesses a very high mobility.

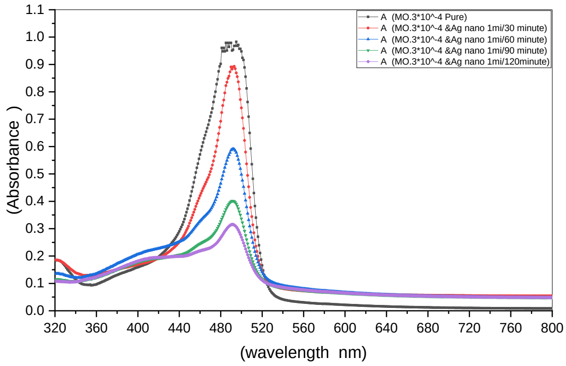

(a) 1 min

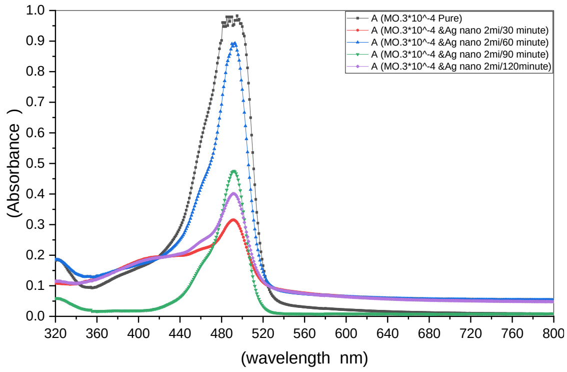

(b) 2 min

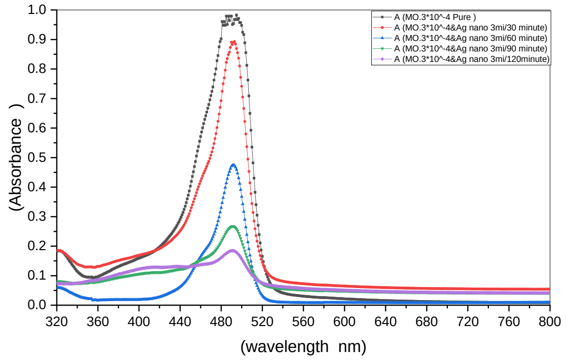

(c) 3min

Fig. (12) The absorbance and wavelength of methyl orange dye and silver nanoparticles after irradiation with UV source for different times

The heat was generated as a result of the absorption of UV light and the response of UV light at different times of Ag nanoparticles due to its plasmonic response, give an indication that Ag nanoparticles are good photocatalyst for degradation applications. This behavior has been observed by Yingying Sha and his group [17] as well as Sini Kuriakose and her group [18].

The ratios of A_t/A_0 for all sample have been tabulated in table (1) and drawn versus irradiation time in Fig. (13). The ratio for all concentrations specify that the photogradation process of dye by Ag nanoparticles increases with increasing of Ag concentration and exposing time to UV light.

Table (1) A_t/A_0 of samples during the irradiation time of ultraviolet source

Intensity of UV	1 minute	2 minute	3 minute
Time (min)	A_t/A_0		
0	1	1	1
30	0.642	0.673	0.793
60	0.543	0.595	0.707
90	0.378	0.452	0.502
120	0.081	0.094	0.133

To calculate the degradation efficiency of Ag nanoparticles (η), the following equation can be used

$$\eta = A_0 - A_t/A_0 \times 100\% \qquad (6)$$

A_0 is the absorbance at T= 0, A_t is the absorbance at T=T

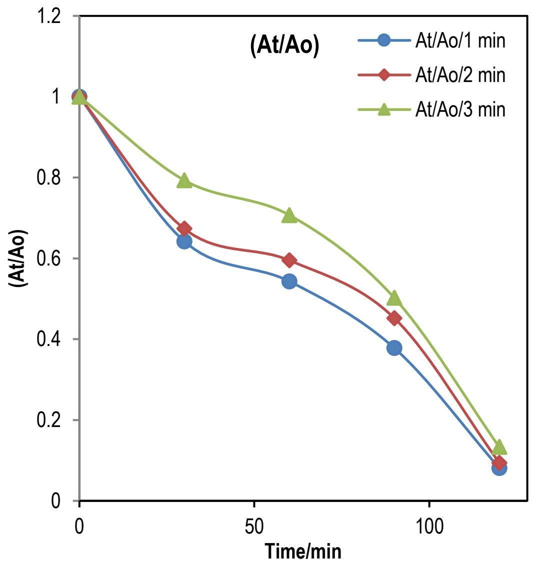

Fig. (13) The ratios of A_t/A_0 of methyl orange dye and silver nanoparticles as a function of irradiation time

Figure (14) is shown the efficiency values for all samples. From this figure, it can be noticed that the efficiency degradation increases up to 81% as the concentration of Ag nanoparticles increasing and the exposing time of every concentration to the UV source increasing.

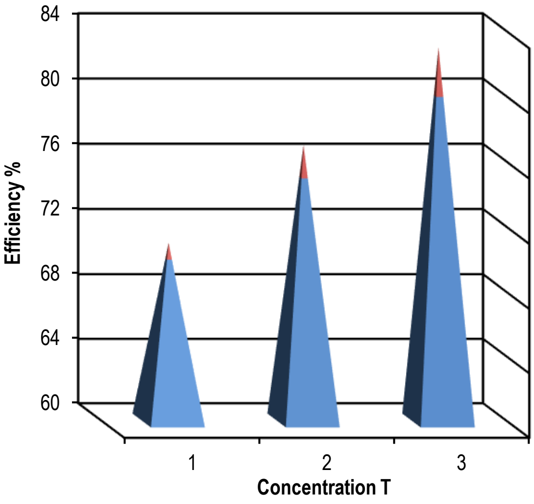

Fig. (14) The degradation efficiency of Ag nanoparticles with different concentrations

4. Conclusions

By studying the effectiveness of the photocatalyst of methyl orange dye and silver nanomaterial, we noticed that the catalytic process was very rapid, as the silver nanomaterial is characterized by strong and rapid absorption of ultraviolet rays for different periods, as the increase in the number of nanoparticles of small dimensions present in its structure, which makes it capable to break down toxic organic pollutants, in addition to the occurrence of the surface plasmon phenomenon, which occurs in noble elements such as silver, and the adsorption process, which has a significant impact on the process of removing organic pollutants and maintaining a clean environment. Nanoparticles of Ag have been successfully synthesized by laser ablation in liquids and used as catalysts. The results obtained show that the methyl orange dye degradation increases as the concentration of the nanoparticles increasing. The results indicate that Ag nanoparticles have the best degradation efficiency of (MO) dye at 120 mins of exposing time to UV source, which is about 81% at 3 mins of ablated time, while the degradation efficiency of 69 % and 75% at 1 and 2 mins of ablated time, respectively.

References

[1] G. Palani et al., “Silver Nanoparticles for Waste Water Management”, *Molecules*, 28 (2023) 3520.

[2] A. Callegari, D. Tonti and M. Chergui, “Photochemically Grown Silver Nanoparticles with Wavelength-Controlled Size and Shape”, *Nano Lett.*, 3 (2003) 1565-1568.

[3] V.K. Sharma and M. Feng, “Water depollution using metal-organic frameworks-catalyzed advanced oxidation processes: A review”, *J. Hazard. Mater.*, 372 (2019) 3-16.

[4] G.M. Nair, T. Sajini and B. Mathew, “Advanced green approaches for metal and metal oxide nanoparticles synthesis and their environmental

applications", *Talanta Open*, 5 (2021) 100080.

[5] L.S. Nair and C.T. Laurencin, "Silver nanoparticles: Synthesis and therapeutic applications", *J. Biomed. Nanotechnol.*, 3 (2007) 301-316.

[6] M. Kedzierska et al., "The Synthesis Methodology of PEGylated Fe_3O_4@Ag Nanoparticles Supported by Their Physicochemical Evaluation", *Molecules,* 26 (2021) 1744.

[7] W. Florkiewicz et al., "Investigation on Green Synthesis, Biocompatibility, and Antibacterial Activity of Silver Nanoparticles Prepared Using Cistus incanus", *Materials*, 14 (2021) 5028.

[8] M. Kedzierska et al., "The Synthesis Methodology and Characterization of Nano gold-Coated Fe_3O_4 Magnetic Nanoparticles", *Materials,* 15 (2022) 3383.

[9] F.H. Hussein, "Photochemical treatments of textile industries wastewater", *Asain J. Chem.*, 24(12) (2012) 5427-5434.

[10] H. Ibrahim, J.A. Abd and A.J.K. Algidsawi, "Fe_2O_3@SiO_2 Nanoparticles: Synthesis and characterization for photodegradation applications", *HIV Nursing*, 23(3) (2023) 1347-1351.

[11] B.K. Mehta et al., "Green synthesis of silver nanoparticles and their characterization by XRD", *J. Phys.: Conf. Ser.*, 836 (2017) 012050.

[12] J.A. Abd and W.M. Mohammed, "Indium oxide: Synthesis and characterization for future industrial applications", *AIP Conf. Proc.*, 2123 (2019) 020010.

[13] N. Nikolay et al., "Laser-assisted fabrication of gold nanoparticle-composed structures embedded in borosilicate glass", *Beilstein J. Nanotech.*, 8 (2017) 2454-2463.

[14] M.M. Al-Mousawi, A. Al-Nafiey and G. Al-Dahesh, "Studying the effect of the number of laser pulses on the structure, morphology, and optical properties for a thin film of GO-Ag nanocomposites", *J. Phys.: Conf. Ser.*, 1 (2021) 1999.

[15] K.M. Reza, A.S.W. Kurny and F. Gulshan, "Parameters affecting the photocatalytic degradation of dyes using TiO_2: A review", *Appl. Water Sci.*, 7 (2017) 1569-1578.

[16] B. Dabirvaziri et al., "A simple and effective synthesis of magnetic γ-Fe_2O_3@SiO_2@TiO_2–Ag microspheres as a recyclable photocatalyst: dye degradation and antibacterial potential", *J. Enviro. Health Sci. Eng.*, 17(2) (2019) 949-960.

[17] Y. Sha et al., "Rapid degradation of azo dye methyl orange using hollow cobalt nanoparticles", *Chemosphere,* 144 (2016) 1530-1535.

[18] S. Kuriakose et al., "Facile synthesis of Ag–ZnO hybrid nano spindles for highly efficient photocatalytic degradation of methyl orange", *Phys. Chem. Chem. Phys.*, 16(33) (2014) 17560 - 17568.

Effect of Magnetic Field on Self-focusing and Stimulated Raman Scattering of q-Gaussian Laser Beam in Plasma

Ahmed S. Ahmed
Hyder A. Salih
Khaleel I. Hassoon

Department of Applied Sciences, University of Technology, Baghdad, IRAQ

This paper delves into relativistic q-Gaussian laser beam self-focusing effects on stimulated Raman scattering (SRS) in magnetized plasma. Analytical solutions for nonlinear coupled wave equations defined by pump and electron plasma wave (EPW) for scattered waves were obtained using variational theory. We ran a numerical analysis on the resulting equations to determine how the laser and plasma properties affect the pump beam dynamics and the intensity of the scattered waves. The pump beam's self-focusing action greatly affects the dispersed wave's strength. Our research also shows that the stimulated Raman scattering effect increases as the self-focusing impact increases. The stimulated Raman scattering yield was analyzed with respect to several parameters, such as plasma density, q-value, and the influence of the magnetic field. The main effect is that when q increases, so do the SRS fluctuations; similarly, as plasma density and magnetic field concentration rise, the SRS fluctuations rise too. We can see that the pump beam's self-focusing significantly affects the plasma's reflectivity of SRS since the reflectivity decreases with rising q-value, density, and magnetic field values.

Keywords: Self-focusing; q-Gaussian; Stimulated Raman scattering; Magnetized plasma
Received: 14 March 2024; **Revised:** 25 April 2024; **Accepted:** 02 May 2024

1. Introduction

Stimulated Raman forward scattering (SRS) [1-6] is an important nonlinear process in the laser–plasma accelerator and fast igniter fusion scheme. In light scattering, electrons are the primary agents as a beam moves from one medium to another. The mobility of the nuclei is another factor that may affect the scattering of light [7]. This leads to Raman and Brillouin scattering, which occurs when the frequency of the propagating light varies in a manner that depends on the mobility of the nuclei. These values are the optical and acoustic phonon frequencies of Raman and Brillouin scattering, respectively [8]. If the intensity of the light beam that is passing is too high, the light that was originally scattered might induce more scattering of the light that is passing, ultimately resulting in a large rise in the intensity of the dispersed light [9]. This particular sort of scattering is referred to as stimulated scattering, and it occurs when light that was first dispersed boosts later scattering effects. There are both theoretical and practical uses for Raman scattering, making it an intriguing issue in nonlinear optics [10-12]. In 1962, when investigating ruby laser Q-switching with a nitrobenzene Kerr cell, Woodbury and Ng [11,12] discovered the stimulated Raman effect. The Kerr cell was found to be emitting strong infrared light.

The physics of stimulated Raman scattering in plasmas can be illustrated by considering the effect of laser beam with powerful energy (E_0) on a plasma that has fluctuations in its density along the $\vec{k}_0$ direction of the incident beam. These density fluctuations result from the propagation of EPW in the plasma. When the laser beam meets the plasma, it causes the electrons to vibrate due to the beam's electric field, generating a transverse current (J_T). If the wave vectors and frequencies are identical, the incident current creates a scattered wave with strength (E_S). The scattered wave interacts with the incident laser beam, causing changes in wave pressure. These changes in wave pressure move electrons from high to low-pressure areas. This increases the disturbance in density, enhancing the initial density fluctuations associated with the EPW, i.e., strengthening the plasma wave. This reactive process results in stimulated Raman scattering or instability [13,14].

SRS is a coherent Raman scattering phenomenon that gives up to 10^7 times amplification compared to spontaneous Raman scattering. It occurs when energy is transferred from a high-energy beam (pump beam) to a low-energy beam (probe beam) [15,16].

Numerous fields, including particle acceleration and laser-induced fusion, actively investigate ways to couple high-power laser beams with plasma more effectively. Stimulated Brillouin scattering (SBS), self-focusing, filamentation, two-plasmon decay, stimulated Raman scattering (SRS), and other instabilities are introduced into the laser-plasma interaction process [17-19]. Stimulated Raman Scattering (SRS) in the context of ICF is a phenomenon in which the incident laser, upon resonance with the fundamental mode of the plasma, decays into an electromagnetic wave (EW) and EPW. Scattering could occur in either of the three ways: (1) Backscattering, where the scattered EW traverses back and combines with the incoming laser, further driving the EPW resulting in the growth of its amplitude, increasing its scattering efficiency of the plasma (as the EPW denotes the natural fundamental mode of the plasma). This unstable feedback loop thus created causes SRS to grow exponentially, decreasing the effective energy deposition on the fusion fuel. Also, the scattered beams affect the illumination symmetry, which not only interferes with the efficient coupling of laser energy, but also induces tremendous growth in hydrodynamic instabilities. (2) Forward scattering, where the laser is scattered in the forward direction, resulting in formation of supra-thermal electrons of energies >10keV, causing preheat of the fusion fuel. (3) Side-scattering, where the SRS convects away from the source, inducing disturbances at farther regions in space [19-21]. Singh and Sharma [21] conducted a study on the stimulation of excitation of EPW in the presence of a laser beam with blank intensity at the centre. The concentration of hollow Gaussian beam (HGB), EPW stimulation, and back reflection of HGBs were explored. These results appear to find applications in the field of laser-induced fusion schemes, especially when higher modes are present in the laser beam. Gupta et al. [22] analyzed the reference system for lasers with elliptical q-Gaussian distribution in uniaxially inhomogeneous plasmas. The effect of laser beam self-focusing on the power of the scattered wave has been explored in detailed manner. Walia et al [23] discovered the existence of a self-focusing beam in stimulated Raman scattering (SRS) in collisional plasmas. In this context, nonlinear collisions arise as a result of nonuniform heating, which leads to carrier redistribution. The plasma density profile is adjusted in a direction perpendicular to the main beam axis. Ahmed and his colleagues [24] studied the occurrence of polarized radiation emission (SRS) when a q-Gaussian laser beam propagates through a non-magnetized plasma. The study showed that increasing the q value led to an increase in SRS throughput, as well as an increase in laser beam intensity and plasma density. The results also showed that the value of the integrated reflection was affected by the increase in the value of q, as its value increased with an increase in q and the growth rate.

Many researchers have studied self-focusing [25-28] and its effect on the stimulated Raman scattering, but few have studied its effect on the stimulated Raman scattering for q-Gaussian laser. This study used the paraxial approach method, which gave results different in some aspects from the previous work.

The current study thoroughly investigates the SRS of a q-Gaussian laser beam in magnetized plasma. Relativistic nonlinearity and its role in the creation of plasma waves are examined in the Section II. The analytical and numerical investigation of the relativistic self-focusing of a q-Gaussian laser beam is carried out in Section III. Section IV of the study examines and discusses the impact of relativistic nonlinearity and diffraction processes on the beamwidth parameters of both the pump and scattered beams and their effects on SRS. Finally, section V presents the conclusions.

2. Nonlinear permittivity tensor

Consider a uniform plasma of equilibrium electron density (n_0^0), immersed in a magnetic field $\vec{B}_0 \| \hat{y}$. An intense laser beam propagates through it along $\hat{z}$ direction,

$$\vec{E} = \vec{A} e^{-i(\omega t - kz)} \tag{1}$$

where $\vec{A} = \hat{x} A_x + \hat{z} A_z$

The response of plasma electrons is governed by the relativistic equation of motion,

$$m \frac{\partial}{\partial t}(\gamma_0 \vec{v}) + m \cdot \vec{\nabla}(\gamma_0 \vec{v}) = -e\vec{E} - \frac{e}{c} \vec{v} \times \vec{B}_0 \tag{2}$$

Where *m* is the rest mass, -*e* is the electronic charge, *c* is the speed of light in a vacuum, and γ_0 is the Lorentz factor where gives by:

$$\gamma_0 = (1 + \frac{e^2 E_0^2}{m^2 \omega^2 c^2})^{1/2} \tag{3}$$

For ω frequency response this equation reduces to

$$-i\omega\gamma_0 \vec{v} = -\frac{e\vec{E}}{m} + \vec{v} \times \vec{\omega}_{co}$$

giving

$$\vec{v} = -\frac{e(i\omega\vec{E} + \vec{E} \times \vec{\omega}_{c0}/\gamma_0)}{m\gamma_0(\omega^2 - \omega_{c0}^2/{\gamma_0}^2)} \tag{4}$$

where $\vec{\omega}_{c0} = \frac{e\vec{B}_0}{mc}$ and $\gamma \cong 1 + |v|^2/4c^2$

The permittivity tensor that it is composed of the following components [28]:

$$\varepsilon_{xx} = 1 - \frac{\omega_p^2}{(\omega^2 - \omega_c^2)} \tag{5}$$

$$\varepsilon_{xx} = \varepsilon_{yy} \tag{6}$$

$$\varepsilon_{xy} = i \frac{\omega_p^2}{\omega} \left(\frac{\omega_c}{\omega^2 - \omega_c^2} \right) \tag{7}$$

$$\varepsilon_{yx} = -i \frac{\omega_p^2}{\omega} \left(\frac{\omega_c}{\omega^2 - \omega_c^2} \right) \tag{8}$$

The intensity-dependent dielectric constant of the plasma is given by:

$$\varepsilon = \varepsilon_0 + \phi(E_z E_z^*) \tag{9}$$

where

$$\phi = \frac{\omega_{p0}^2}{\omega^2} \left(1 - \frac{1}{\left(1 + \frac{e^2 E_0^2}{m^2 \omega^2 c^2}\right)^{1/2}} \right) \tag{10}$$

The effective non-linear permittivity may be determined by using the following formula:

$$\varepsilon = \varepsilon_f + \beta \frac{r^2}{r_0^2} \tag{11}$$

where the values of ε_f and β are given by the following relationships:

$$\varepsilon_f = 1 - \frac{\omega_{\mathrm{po}}^2}{\omega^2} \left[1 + \frac{\alpha A_{00}^2}{f^2} \right]^{-\frac{1}{2}} \tag{12}$$

$$\beta = -\frac{\omega_{\mathrm{po}}^2}{\gamma \omega^2} \left[\frac{\omega_{\mathrm{co}}^2}{\omega^2} + \frac{\alpha A_{00}^2}{2\gamma^2 f^4} \right] \tag{13}$$

3. Relativistic Self-focusing

We study the possibility of propagating a high-energy q-Gaussian laser beam within a collisionless plasma, along the z-direction. The initial intensity distribution of the beam is determined by [28]:

$$E_0 E_0^* = A_{00}^2 \left[1 + \frac{r^2}{q{r_0}^2} \right]^{-q} \tag{14}$$

The wave equation is the prevailing equation that governs the electric field of a laser beam in a plasma [28]:

$$\nabla^2 \mathrm{E}_0 - \nabla\left(\nabla \cdot \vec{E}_0\right) + \frac{\omega_0^2}{c^2} \widehat{\varepsilon_0} \cdot \vec{E}_0) = 0 \qquad (15)$$

The symbol $\widehat{\varepsilon_0}$ is the permittivity tensor. When an electric field is given by:

$$\vec{E}_0 = \vec{A}(x,y,z) \exp\{i(\omega_0 t - k_0 z)\} \qquad (16)$$

$\vec{A}(x,y,z)$ represents the laser beam's amplitude field which a function of (x,y,z). Continuing with this assumption, $\vec{A}(x,y,z)$ might vary as:

$$\vec{A}(x,y,z) = \vec{A}_0 \ \exp\{-ik_0 S_0(x,y,z)\} \qquad (17)$$

For a q-Gaussian beam $\vec{A}_0$ and S_0 are defined as follows:

$$A_0^2(r,z) = \frac{A_{00}^2}{f^2(z)}\left[1 + \frac{r^2}{\mathrm{q} r_0^2 f^2(z)}\right]^{-q} \qquad (18)$$

$$S_0 = \frac{1}{2} r^2 \frac{1}{f}\frac{df}{dz} + \Phi_0(\mathrm{z}) \qquad (19)$$

In this context, f stands for the beam width and r_0 is the spot size parameter. After dividing the real and imaginary parts of the resultant formula, the following set of equations is formed by inserting Eq. (18) into Eq. (15). Additionally, in Eq. (15), the actual part is:

$$2\frac{\partial S}{\partial z} + \left(\frac{\partial S}{\partial r}\right)^2 = \frac{1}{k^2 A_{20}}\left(\frac{\partial^2 A_{20}}{\partial r^2} + \frac{1}{r}\frac{\partial A_{20}}{\partial r}\right) + \frac{\omega^2 \varepsilon}{c^2 k^2} \quad (20)$$

The equation controlling the bandwidth parameter f is obtained using Eqs. (4) and (7) in Eq. (6). In addition, the r^2 coefficient equation is used on both sides of the derived formula:

$$\frac{d^2 f}{d\zeta^2} = \frac{1}{f^3}\left(\frac{q+2}{q}\right) + \frac{\omega^2 r_0^2}{c^2}\left(-\frac{\omega_{p0}^2}{\gamma\omega^2}\left[\frac{\omega_{c0}^2}{\omega^2} + \frac{\alpha \mathrm{A}_{00}^2}{2\gamma^2 f^4}\right]\right) f \quad (21)$$

The fourth-order Runge-Kutta method was used to solve Eq. (21), which describes the laser and plasma parameters at variable levels. The problem is that an analytical solution is not possible. The vacuum wavelength of the laser beam is determined as 1.053 µm, and the original laser radius is r_0 = 10 µm due to the intensity of the laser beam (I=10^{18} W/cm^2).

Figure (1) shows, for different values of the q-parameter, the changes in the laser beamwidth parameter f concerning the normalized propagation distance ξ. For instance, self-focusing becomes more effective as q increased.

Figures (2) and (3) show how f changes with ζ, where figure (2) shows the relation when q=10 for four different values of $\omega_{\mathrm{p}0}^2/\omega^2$. From the figure, we see that increasing $\omega_{\mathrm{p}0}^2/\omega^2$ leads to improved self-focusing, which reduces the self-focusing length. We also note that increasing the plasma density increases the power and speed of self-focusing.

Figure (3) shows how the beamwidth parameter changes with propagation distance for the parameters $\omega_{\mathrm{p}0}^2/\omega^2 = 0.02$ and $\alpha A_{00}^2 = 1.2$ and $q = 10$. When the laser beam is stronger, the self-focus increases. In this case, the self-focus length decreases with the propagation distance due to the increasing value of the magnetic field. When the magnetic field is stronger, the self-focusing length becomes shorter than the previous form. The focus effect also becomes more intense.

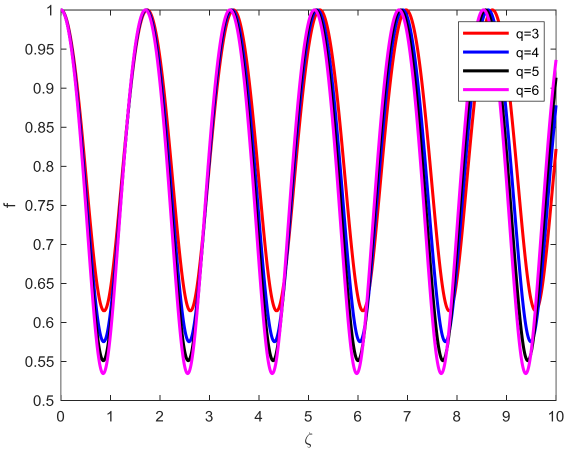

Fig. (1) Effect of the q value on the graph between of the beam width of the laser beam with propagating distance through the plasma for the fixed value of the $\boldsymbol{\omega_{p0}^2/\omega^2 = 0.02, \omega_{c0}^2/\omega^2 = 0.3 \ and \ \alpha A_{00}^2 = 1.2}$

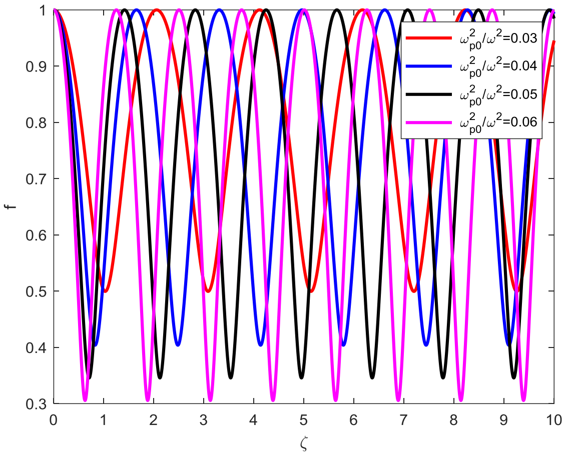

Fig. (2) Effect of the plasma density on the graph between of the beam width of the laser beam with propagating distance through the plasma for the fixed value of the $\boldsymbol{q = 10, \omega_{c0}^2/\omega^2 = 0.3 \ and \ \alpha A_{00}^2 = 1.2}$

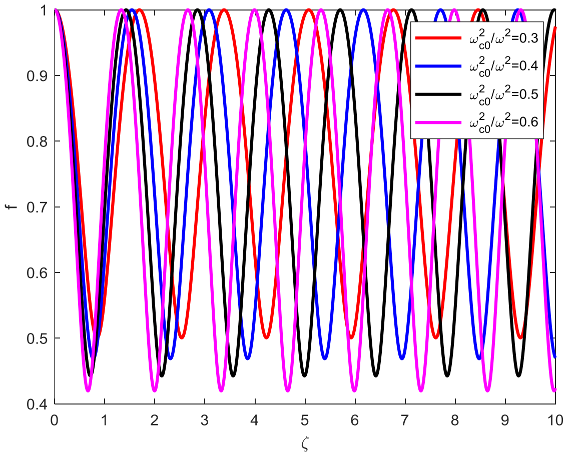

Fig. (3) Effect of the magnetic field on the graph between of the beam width of the laser beam with propagating distance through the plasma for the fixed value of the $\boldsymbol{q = 10, \omega_{p0}^2/\omega^2 = 0.02 \ and \ \alpha A_{00}^2 = 1.2}$

4. Stimulated Raman Scattering

In plasma, electron waves arise with frequencies (ω) and wavenumbers (k). When these waves interact with a powerful laser beam, SRS waves are emitted with frequencies (ω_s) and wavenumbers (k_s), which can be represented by the relations $\omega_s = \omega - \omega_0$ and $k_s = k - k_0$. Nonlinear interactions between the SRS wave and the laser wave led to attenuation of the laser wave.

The relations $\omega_s = \omega - \omega_0$ and $k_s = k - k_0$ may be used to express the frequencies ω_s and wavenumbers k_s of the SRS waves that are produced when these waves come into contact with a strong laser beam. Laser wave attenuation results from nonlinear interactions between SRS and laser waves. The travelling and consumed lasers are described by the wave equations with the following frequencies (ω_d) and wavenumbers (k_d):

$$\nabla^2 \vec{E}_d + \frac{\omega_d^2}{c^2}\left(1 - \frac{\omega_{p0}^2}{\gamma\omega_d^2}\right)\vec{E}_d + \frac{ie^2\omega_p^2 k|\vec{E}_s\vec{E}_s^*|\vec{E}_d}{16\Gamma_e m_0^2\gamma^3 c^2\omega_d\omega_s^2} = 0 \quad (22)$$

and

$$\nabla^2 \vec{E}_s + \frac{\omega_s^2}{c^2}\left(1 - \frac{\omega_p^2}{\gamma\omega_s^2}\right)\vec{E}_s + \frac{ie^2\omega_p^2 k^2|\vec{E}_d\vec{E}_d^*|\vec{E}_s}{16\Gamma_e m_0^2\gamma^3 c^2\omega_s\omega_d^2} = 0 \quad (23)$$

where

$$\vec{E}_d = \vec{E}_{d0}\exp(i\{\omega_d t - k_d[z + S_d]\})) \quad (24)$$

$$\vec{E}_s = \vec{E}_{s0}\exp(i\{\omega_s t - k_s[z' + S_s]\})) \quad (25)$$

In this equation, Γ_e is the damping coefficient and the other variables have the same usual meaning.

After entering these values into Eqs. (24) and (25) into Eq. (22), and by separating the real and imaginary parts, we obtain a set of related equations. The equation gives us:

$$2\frac{\partial S_d}{\partial z} + \left(\frac{\partial S_d}{\partial r}\right)^2 = \frac{\omega_d^2\varepsilon_d}{c^2k_d^2} + \frac{1}{k_d^2E_{d0}}\left(\frac{\partial^2 E_{d0}}{\partial r^2} + \frac{1}{r}\frac{\partial E_{d0}}{\partial r}\right) \quad (26)$$

where

$$E_{d00}^2(r,z) = \frac{E_{d20}^2}{\mathrm{f}_\mathrm{d}^2(z)}\left[1 + \frac{r^2}{\mathrm{qr}_0^2\mathrm{f}_\mathrm{d}^2(z)}\right]^{-q} e^{-2l_d z} \quad (27)$$

$$S_{d0} = \frac{1}{2}r^2\frac{1}{f_d}\frac{df_d}{dz} + \Phi_d(\mathrm{z}) \quad (28)$$

$$E_{s00}^2(r,z) = \frac{E_{s20}^2}{\mathrm{f}_s^2(z)}\left[1 + \frac{r^2}{\mathrm{qr}_0^2\mathrm{f}_s^2(z)}\right]^{-q} e^{-2l_s z'} \quad (29)$$

By substituting Equations 27 and 28 into Equation 26, one gets the following equation:

$$\frac{d^2 f_d}{d\xi^2} = \frac{q^2}{k^2 f_d^3(r^2/f_d^2 + \mathrm{qr}_0^2)^2} + \frac{\alpha E_{d20}^2\omega_p^2}{c^2 f_d^3 k^2 \mathrm{r}_0^2}e^{-2l_d z} \quad (30)$$

where f_d and E_{d0} represnts beam width and real function of depletion laser beam, respectively

Additionally, the variation of E_{S0} is presumed to be:

$$E_{s0} = E_{s00}\exp\{-ik_sS_s\} \quad (31)$$

By similar way to get Eq. (31) and assuming that:

$$S_{s0} = \frac{1}{2}r^2\frac{1}{f_s}\frac{df_s}{dz} + \Phi_s(\mathrm{z}') \quad (32)$$

and, by separating into real part and imaginary part, one gets the real part as:

$$2\frac{\partial S_s}{\partial z'} + \left(\frac{\partial S_s}{\partial r}\right)^2 = \frac{\omega_s^2\varepsilon_s}{c^2k_s^2} + \frac{1}{k_s^2E_{s0}}\left(\frac{\partial^2 E_{s0}}{\partial r^2} + \frac{1}{r}\frac{\partial E_{s0}}{\partial r}\right) \quad (33)$$

Substituting Eqs. (29-32) into Eq. (33), and by equating the coefficients of the variable r^2 on the two equation sides, one gets the subsequent equation:

$$\frac{d^2 f_s}{d\xi'^2} = \frac{1}{{f_s}^3}\left(\frac{q+2}{q}\right) + \frac{\omega^2 r_0^2}{c^2}\left(-\frac{\omega_{p0}^2}{\gamma\omega^2}\left[\frac{\omega_{\mathrm{c}0}^2}{\omega^2} + \frac{\alpha\mathrm{A}_{00}^2}{2\gamma^2\mathrm{f}_s^4}\right]\right) f_s e^{-2l_s z'} \quad (34)$$

where

$$l_s = \frac{-e^2\omega_p^2k^2|E_{d0}|_{r=0}^2}{32m_0^2\gamma_0^3\Gamma_e c\omega_s^2\omega_d^2\varepsilon_s^{\frac{1}{2}}} \quad (35)$$

The function A_d is a complex function that is dependent on spatial variables. Additionally, it is assumed that the variation of A_d is:

$$E_{d0} = E_{d00}\exp\{-ik_dS_d\} \quad (36)$$

Equation (35) was also solved using numerical methods. Figure (4) shows the relationship between the stimulated Raman scattering and the beamwidth when the q values are changed. It is observed that when q values are less than 3, defocus occurs.

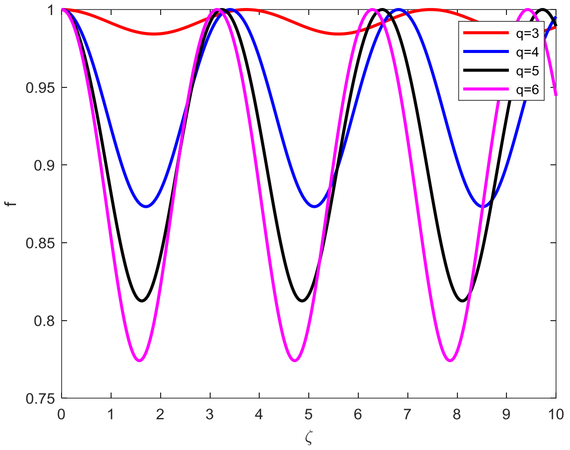

Fig. (4) Effect of the q value on the beam width parameter of the laser beam propagating through the plasma for the fixed value of the $\omega_{p0}^2/\omega^2 = 0.02, \omega_{c0}^2/\omega^2 = 0.3$ *and* $\alpha A_{00}^2 = 1.2$

Figures (5) shows how the plasma density and magnetic field affects the SRS back scattered of the laser beam. We note that the self-focusing range SRS back scattered of the laser beam improves as the plasma density and magnetic field increases. In Fig. (6), because the laser beam experiences a lower refractive index in the deeper parts of the plasma when the magnetic field is applied, and it helps increase the focus range of the laser beam.

The integrated reflectivity is the ratio between integrated of scatter power to integrated of input power:

$$R = \frac{E_{S20}^2}{A_{00}^2}\frac{r_{s0}}{r_0}e^{-l_s\zeta} \quad (37)$$

By using Eq. (37), as shown in figures (7-9), the integrated reflection with distance ξ. In Fig. (7), maximum back reflection occurs when the central laser beam is aligned with the centers of the q-Gaussian beam. It was also observed that the reflectivity decreases as the value of q in the array increases, because the density of q-Gaussian decreases as the beam size increases.

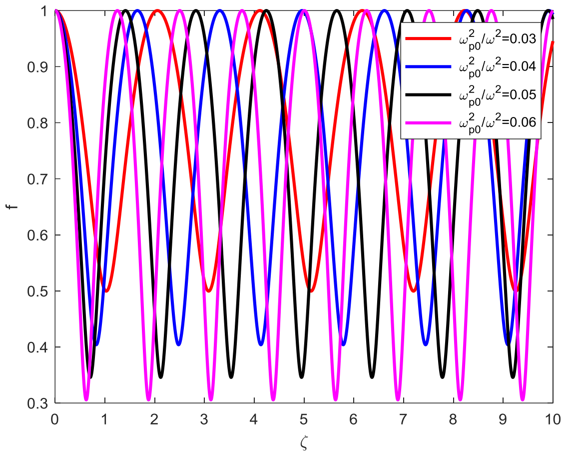

Fig. (5) Effect of the plasma density on the graph between back SRS and the beam width of the laser beam propagating through the plasma for the fixed value of the $q = 10, \omega_{c0}^2/\omega^2 = 0.3$ and $\alpha A_{00}^2 = 1.2$

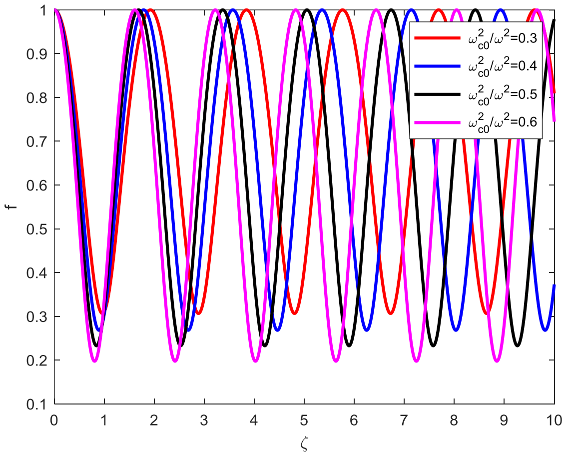

Fig. (6) Effect of the magnetic field on the graph between back SRS and the beam width of the laser beam propagating through the plasma for the fixed value of $q = 10, \omega_{p0}^2/\omega^2 = 0.02$ and $\alpha A_{00}^2 = 1.2$

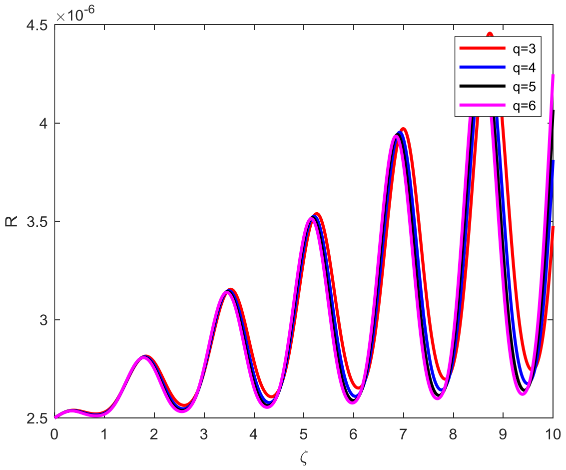

Fig. (7) Effect of the q-value on the evolution of the stimulated Raman reflectivity of the plasma for the fixed value of the $\omega_{p0}^2/\omega^2 = 0.02, \omega_{c0}^2/\omega^2 = 0.3$ and $\alpha A_{00}^2 = 1.2$

Figure (8) shows how reflectivity is affected by increasing plasma density. It can be seen that the reflectivity decreases as the density increases. This is because the plasma becomes more self-concentrated as the rate of change of the plasma density increases. Figure (9) shows the effect of increasing magnetic field on reflectivity. It is shown that the reflectivity decreases with increasing magnetic field. This is because the self-focusing length becomes shorter as the magnetic field strength increases.

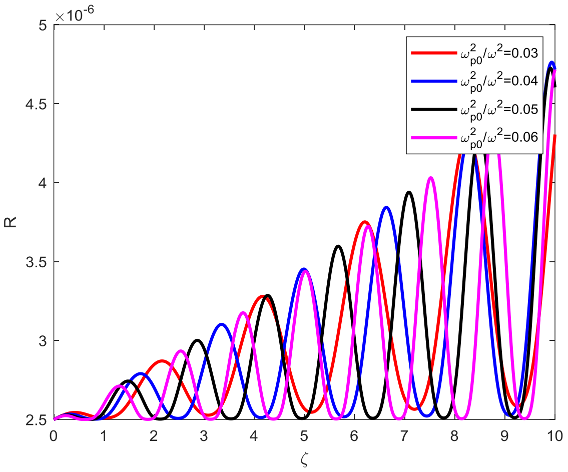

Fig. (8) Effect of the plasma density on the evolution of the stimulated Raman reflectivity of the plasma for the fixed value of the $q = 10, \omega_{c0}^2/\omega^2 = 0.3$ and $\alpha A_{00}^2 = 1$.

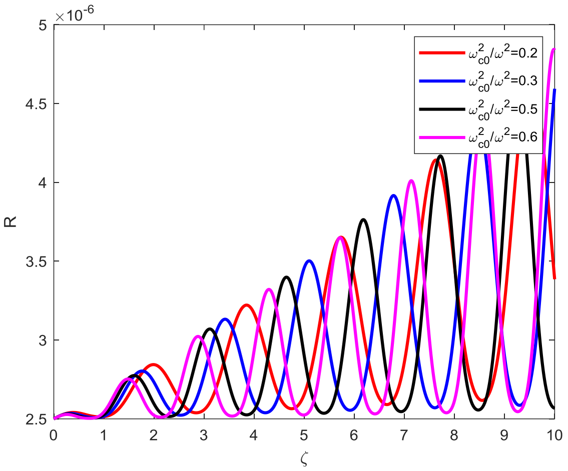

Fig. (9) Effect of the magnetic field on the evolution of the stimulated Raman reflectivity of the plasma for the fixed value of the $q = 10, \omega_{p0}^2/\omega^2 = 0.02$ and $\alpha A_{00}^2 = 1.2$

5. Conclusions

This study addresses the case of SRS when a q-Gaussian laser beam passes through a magnetized plasma. We can say that the relative self-focus of the scattered beam decreases a lot when the laser beam is close to the ideal Gaussian shape. In addition, the focus length becomes shorter because the scattered energy is proportionally reduced. When q, plasma density and magnetic field increase, the fluctuations in the SRS also increase and improve. The reflectivity of SRS is also affected by increasing the q value, plasma density, and magnetic field, as it decreases as these parameters increase.

References

[1] H.A. Salih, V.K. Tripathi and M. Rafat, "Stimulated Raman scattering of the beat wave of counter-propagating lasers", *Phys. Plasmas*, 11(2) (2004) 747-750

[2] V. Sajal and V.K. Tripathi, "Stimulated Raman scattering of a laser beam in a plasma with azimuthal magnetic field", *Phys. Plasmas*, 11(9) (2004) 4206-4212.

[3] H.A. Salih et al., "Stimulated Raman scattering of relativistic laser beam in plasmas", *Phys. Plasmas*, 12(4) (2005) 042302.

[4] K.I. Hassoon, H.A. Salih and V.K. Tripathi, "Stimulated Raman forward scattering of a laser in a plasma with transverse magnetic field", *Physica Scripta*, 80(6) (2009) 065501.

[5] V. Sajal, D. Dahiya and V. K.Tripathi, "Stimulated forward Raman scattering of a laser in a magnetized plasma", *Phys. Plasmas*, 14(3) (2007) 032109.

[6] V. Sajal et al., "Stimulated Raman backward scattering of a laser beam in a magnetized plasma", *Opt. Commun.*, 285(16) (2012) 3563-3566.

[7] E. Woodbury and W. Ng, "Ruby laser operation in the near IR", *Proc. IRE*, 50(11) (1962) 2347-2348.

[8] J.C. White, "Stimulated raman scattering," *Topics Appl. Phys, Tunable lasers*, (2005) 115-207.

[9] F. Palombo and D. Fioretto, "Brillouin light scattering: applications in biomedical sciences", *Chem. Rev.*, 119(13) (2019) 7833-7847.

[10] N. Gupta, S. Kumar and S. Bhardwaj, "Stimulated Raman scattering of self-focused elliptical q-Gaussian laser beam in plasma with axial density ramp: effect of ponderomotive force", *J. Opt.*, 51(4) (2022) 819-833.

[11] D. Biskamp and H. Welter, "Stimulated Raman scattering from plasmas irradiated by normally and obliquely incident laser light", *Phys. Rev. Lett.*, 34(6) (1975) 312.

[12] D. Polli et al., "Broadband coherent Raman scattering microscopy", *Laser Photon. Rev.*, 12(9) (2018) 1800020.

[13] T. Ito, Y. Obara and K. Misawa, "Single-beam phase-modulated stimulated Raman scattering microscopy with spectrally focused detection", *J. Opt. Soc. Amer. B*, 34(5) (2017) 1004-1015.

[14] L. Torrisi et al., "Self-focusing effect in Au-target induced by high power pulsed laser at PALS", *Laser Part. Beams*, 26(3) (2008) 379-387.

[15] A.A. Andreev et al., "X-ray spectroscopy observation of fast ions generation in plasma produced by short low-contrast laser pulse irradiation of solid targets", *Laser Part. Beams*, 25(2) (2007) 267-275.

[16] J. Kline et al., "Investigation of stimulated Raman scattering using a short-pulse diffraction limited laser beam near the instability threshold", *Laser Part. Beams*, 27(438) (2009) 185-190.

[17] S.K.K. Sivamalini et al., "Stimulated Raman scattering in inertial confinement fusion-A review", *AIP Conf. Proc.*, 2800(1) (2023) 020285.

[18] L. Baiwen, "The Complexities on Ultra-Intense Laser Interaction with Plasmas", (2004).

[19] R.J. Focia, "Investigation and characterization of single hot spot laser-plasma interactions", PhD thesis, Massachusetts Institute of Technology (2001).

[20] H.H. Ma et al., "Simulations of laser plasma instabilities using a particle-mesh method", *Plasma Phys. Control. Fusion*, 63(9) (2021) 095005.

[21] R.K. Singh and R. Sharma, "Stimulated Raman backscattering of filamented hollow Gaussian beams", *Laser Part. Beams*, 31(3) (2013) 387-394.

[22] N. Gupta, S. Kumar and S.B. Bhardwaj, "Effect of Self Focusing on Stimulated Raman Scattering of Elliptical q-Gaussian Laser Beam in Underdense Plasma with Axial Density Ramp", *Nonl. Opt. Quant. Opt.*, 58 (2023) 99-126.

[23] K. Walia and T. Singh, "The Influence of self-focused laser beam on Stimulated Raman Scattering process in Collisional Plasma", *Commun. Theor. Phys.*, 75(12) (2023) 1572-9494.

[24] A.S. Ahmed et al., "Stimulated Raman Scattering of Q-Gaussian Laser Beam in an Unmagnetized Plasma", *J. Appl. Sci. Nanotech.*, 3(4) (2023) 10-19.

[25] A.S. Ahmed, H.A. Salih and K.I. Hassoon, "Relativistic Self-Focusing of a q-Gaussian Laser Beam in Plasma by the Influence of Magnetic Field", *Brazilian J. Phys.*, 53(4) (2023) 112.

[26] A.S. Ahmed, H.A. Salih and K.I. Hassoon, "q-Gaussian laser beam for second-harmonic generation from unmagnetized plasma", *J. Opt.*, 53 (2024) 1328-1335.

[27] H.A. Salih, K.I. Hassoon and R.A. Khamis, "Investigating some parameters of q-Gaussian laser beam in plasma", *Phys. Plasmas*, 29(2) (2022) 023103.

[28] K.I. Hassoon, A.K. Sharma and R.A. Khamis, "Relativistic laser self-focusing in a plasma with transverse magnetic field", *Physica Scripta*, 81(2) (2010) 025505.

Azhaar A. Ali [1]
Malik H. Kheder [2]
Rajaa A. Basheer [2]

[1] *Department of Fuel and Energy, College of Oil and Gas Techniques Engineering, North Technical University, Kirkuk, IRAQ*
[2] *Department of Physics, College of Education for Pure Sciences, University of Al-Hamdaniya, Al-Hamdaniya, IRAQ*

Environmental Radioactive Contamination Assessment in the Water Samples of Nineveh Province

Naturally occurring radioactive and poisonous heavy metals, radium, and uranium with liquid and solid meals and collect in the, liver, kidneys, and bones while radon collect in the lung, where these metals can cause cancer. The obtained mean radon concentrations in tap and private well waters were 0.0430 and 0.1317 Bq.l^{-1} respectively. Total intake uranium is dependent mostly on the uranium content in the consumed water. The mean uranium concentrations in tap and private well waters were 8.8406 and 27.076 µg l^{-1}, whereas these values were below of 30 µg.l^{-1} the limit according to guidelines of WHO. This indicates that the risk of increased uranium intake from drinking tap water is almost very low. The excess cancer risk is 0.1222 and 0.3745 x10^{-4} indicates that the probability of 12 and 37 per million people will die by uranium intake from water which is very low so the studied area is safe.

Keywords: Radioactive pollution; Uranium; Well waters; Excess cancer risk
Received: 04 April 2024; **Revised:** 21 April 2024; **Accepted:** 28 April 2024

1. Introduction

The uranium is a heavy and radioactive metal is found in the natural world. While most sources believe that radioactive decay has a detrimental biological impact [1-3], some sources assert that low radiation has a beneficial influence on living processes [4]. In comparison to the parent material, the soil natural background values for uranium range from 0.79 to 11 mg kg^{-1} [5]. Leaching from the natural deposits or from anthropogenic activities like nuclear power, mining, the disposal of the medical waste and industrial, and the use of phosphate fertilizers in agriculture can all result in elevated uranium concentrations in environmental compartments [6-11]. Inhalation, ingestion, or skin contact by humans or animals exposed to uranium compounds may result in harmful health effects. Although skin contact with uranium poses a special risk to those employed in the uranium industry, ingestion and inhalation are likely routes of infection for larger segments of the populace residing in uranium-polluted areas. Uranium is ingested by drinking water and by way of food chains that include crops, animal products, and animal feed. The sensitivity of mammals to Uranium is especially strong [12]. After entering the body, uranium is moved to the extracellular fluids and then to other organs via the blood. Uranyl, in its soluble state, is carried and combines with anions and proteins to form complexes. The uranium is tends to build up in body, primarily in the bones, liver, kidneys, and spleen. Radiological and chemical dangers are associated with exposure to uranium. Given that uranium contributes only slightly to the total amount of radioactivity in the environment, it is undoubtedly a negligible cause for concern [13]. After uranium is absorbed by organism and integrated into its bones and tissues, this evaluation must be reevaluated. Cancer is the most notable harm that comes with low and medium exposure levels [14]. Uranium contaminations pose a significant risk to kidney health due to their peak concentrations during the excretion process. These risks are associated with the binding of uranium to organic molecules. The amount of uranium that is accumulated in the body is directly correlated with the amount of uranium that is inhaled in solid and liquid food. The amount of uranium that accumulates increases with age in an individual. This suggests that the likelihood of suffering harm from uranium usually rises with exposure duration and, consequently, and the limit of 30 µg l^{-1} according to WHO guidelines [15]. Keeping the daily uranium intake as low as feasible is necessary to minimize the risk of contracting uranium-related hazards, given that the ingestion of uranium cannot be prevented and there is no the lower limits for harmful effects from the uranium [16]. The quality of the drinking water is one of the constants in human existence household taps are connected to clearly defined private wells or public suppliers.

It was believed that the main factor impacting people' was the amount of uranium in drinking water. The research effort detailed here aimed to investigate the effects of different sources of water on metropolitan populations.

2. Experimental Part

Samples were taken from both private wells and the tap water. Very seldom is well water utilized for human consumption; instead, it is used to irrigate gardens. In the event that the water supply from the water works fails, the various water of wells have been examined to provide an indication of the water supply quality in a restricted region as in (Fig. 1).

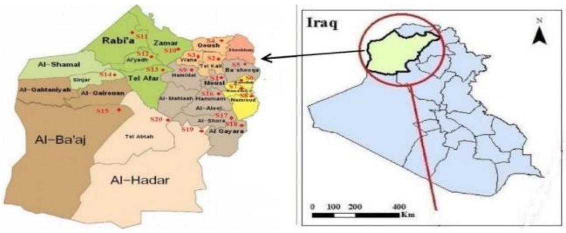

Fig. (1) The site map of samples

Measurements of the CR-39 detector are made using a plastic can radon dosimeter (7 cm in diameter and 10 cm in length). The detector is put on the bottom of the dosimeter cover and is used to measure the concentration of radon in the samples, shown in (Fig. 2). Samples with a volume of 115.4 ml and a height of 3 cm were placed in the dosimeter; the distance from the water samples to the surface of detector was 7 cm. Samples were filled and kept in the plastic can for duration of 60 days. Following a 60-day exposure period, the detectors were taken out of the dosimeter and etched chemically in a 6.25N solution of NaOH at 70°C for seven hours. Utilizing a 400x optical microscope, the tracks were counted.

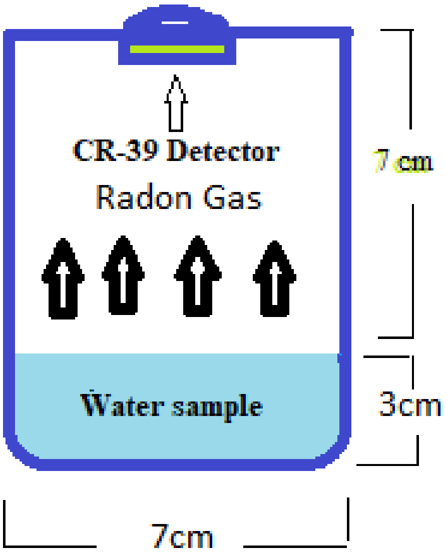

Fig. (2) The dosimeter

The radon concentration in the air volume within the container, as determined from the equation [17]

$$C_{Rn=}\rho[KT]^{-1} \quad (1)$$

K= 0.05916 Tr/cm^2.d/Bq/m^3; is the radon dosimeter utilized in this study's CR-39 detector calibration factor; ρ is the density of tracks; T is exposure period [18]

Radon concentrations in water samples determined using the formula [19]

$$C_S = \lambda_{Rn}C_{Rn}HT[l]^{-1} \quad (2)$$

where C_S is the radon concentration in water samples (Bq/m^3), C_{Rn} is the radon concentration in air space (Bq/m^3), and λ_{Rn} is the radon constant of decay (0.1814 day^{-1}), the T stands for exposure time (60 days), H is for height of air gap in the plastic can (7 cm), and l stands for sample thickness (3 cm)

The uranium contents were calculated by the secular activity equilibrium between the uranium and its daughters, and the concentration of radon measured with using the CR-39 detector. Activity of radon A_{Rn} in sample may calculated thanks to the correlation between C_{Rn} and the amount of radon in the sample [20]

$$A_{Rn} = C_{Rn}V \quad (3)$$

The sample volume is (V=πr^{2}L) = 115.4 X 10^{-6} m^3 = 115.4 mL, its thickness is l = 0.03 m, and its radon dosimeter radius is r = 0.035 m

$$\lambda_{Rn}N_{Rn} = A_{Rn} \quad (4)$$

The equation of the equilibrium between the uranium with its daughter (the uranium activity equals the activity of radon) was used to compute the uranium atoms number (N_U) in samples [21].

$$\lambda_U N_U = \lambda_{Rn}N_{Rn} \quad (5)$$

In this case, the uranium decay constant is λ_U = 4.883X10^{-18}s^{-1}. The uranium atom number N_U was then used to compute the uranium weight in samples using the equation

$$W_U = \frac{N_U a_U}{N_{avo.}} \quad (6)$$

where W_U is measured in micrograms (µg), N_{avo}= (6.02X10^{23}atom/Mol) is number of Avogadro, a_U is uranium mass number 238. Uranium content, determined by [22]

$$C_U = \frac{W_U}{W_S} \quad (7)$$

C_U represents the uranium concentration in (µg/L) units, with Ws equal to 115.4 mL.

Calculating excess risk of cancer: radiological risk evaluation, radioactive risk based on the specific activity (activity per unit of weight) or activity concentration of radiation. In the case of uranium equation (7) is used to compute Ac, or uranium activity concentration in (BqL^{-1}) unit, in the form

$$Ac = \lambda_U N_{avo.}[At_U]^{-1}C_U \quad (8)$$

The increased risk of cancer due to uranium in water, as determined by the provided method of [23].

$$ECR = AcR \quad (9)$$

According to BqL^{-1}, R is a risk factor, and ECR is the excess cancer risk. The factor of risk R associated with the ingestion of uranium via water is determined by multiplying the per capita activity intake (I) by the uranium risk coefficient (r) (1.19×10^{-9}) Bq^{-1} for death. Where (I) for uranium computed as the product of daily water consumption of 4.05 L day^{-1} and life expectancy of 63.7 years, or 23250 days [24]. The factor of the risk value R= r×I=1.19×10^{-9} $Bq^{-1}\times94162.5$ L=1.12×10^{-4} LBq^{-1} when I = 4.05 $Lday^{-1}\times23250$ day=94162.5 L.

3. Results and Discussion

Results of the water samples collected the various study locations are listed in table (1). Table (1) includes information on the concentration of radon in water samples C_{Rn} in units of Bq/L, the concentrations of uranium in the samples of water C_U in (µg/L), and the exceed cancer risk ECR. In tap and well water samples from the Nineveh Province, concentration levels of radon gas range from 0.0236 to 0.0607Bq/L for tap water, and 0.0708 to 0.1517 Bq/L in well water, due to variations in geological characteristics, the amount of radon in the samples of water varied from one place to another. Every detected concentration of radon in the samples of water was below the safe internationally recommended concentration limit, indicating that long-term exposure to high amounts of danger does not have a negative impact on health. The permissible limit of radon in drinking water for humans, as suggested by the agencies of health and environmental protection, is 4–40 Bq/L [25], the maximum radon contamination level in the drinking water, from to the US Environmental Protection Agency, is 11 Bq/L. The measurements results of radon in the drinking samples of water that were collected are safe. Results showed that, on average, the concentrations of uranium in units of µg/L, which averaged 8.8406 µg/L and 27.076 µg/L for tap and well water respectively, shown in (Fig 3), were generally lower than the standard level rate of uranium concentrations in the drinking water, which was set at 30 µg/L according to WHO guidelines, still not dangerous. Surface waters are mostly supplied by precipitation, which explains why their uranium level is lower than that of mineral waters [26]. Deeper layers of the earth's crust are home to many heavy minerals that contain radioactive nuclides; granite rocks, in particular, often have uranium concentrations of less than 1%. As a result, uranium concentrations in lower-depth water are anticipated to be higher than in surface water [27]. Water from very deep depths loses radioactivity when it rises to the earth's surface because of a mechanism Yoshida et al. [28]. Simplified, this procedure utilizes a mechanism similar to that seen in chromatography, whereby heavy molecules remain behind lighter ones in a stream passing down a column. Nevertheless, in an attempt to boost a source's yield, boosting the flow through a column weakens the separation process and therefore increases the amount of heavier radionuclides transferred to the surface. This is comparable to forcing mineral water through a pump.

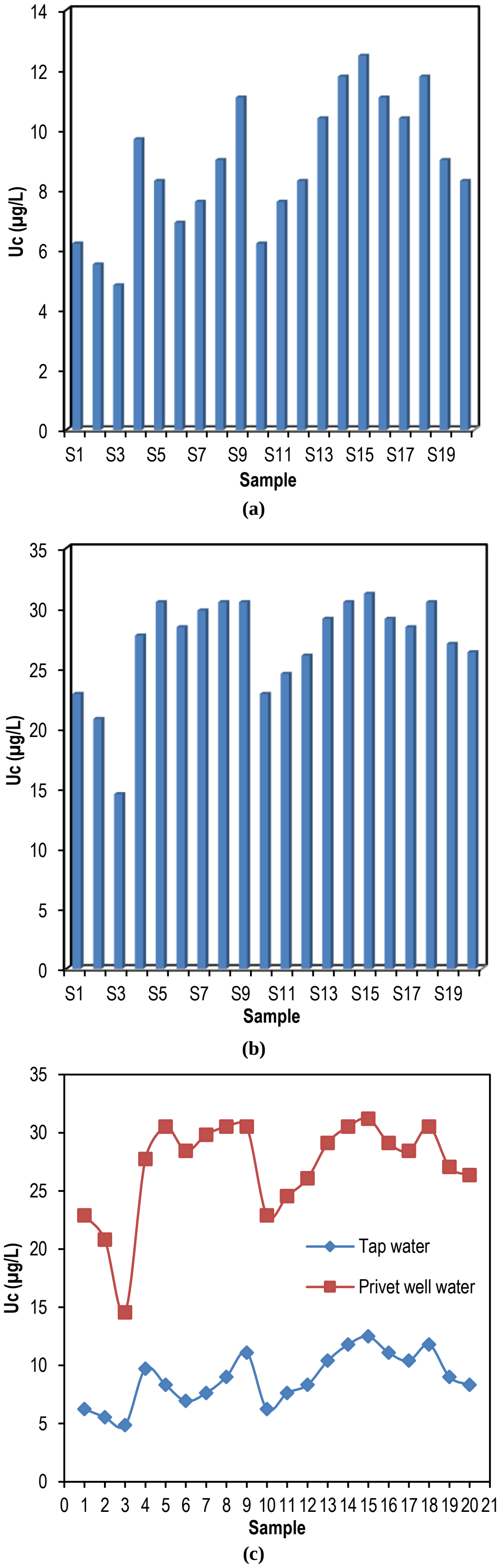

Fig. (3) Uranium concentrations: a. in tap water samples, b. in well water samples, c. the comparison between tap and well waters

With the mean value 0.1222 x10^{-4}, 0.3745 x10^{-4} for tap and well water indicates that the probability of 12 and 37 per million people will die by uranium intake from water which is very low so the studied area is safe. The water in these places poses a risk of cancer to 12 and 37 per million residents. Although there is no risk to human life, the high incidence of uranium availability in particular areas poses a risk to public safety and health. Similar to high-level radon exposure, significant health impacts associated with uranium have been seen; no treatment is necessary.

4. Conclusion

High radiation content water is one of the study area's causes of public health risks. The findings might be used to determine the background levels of uranium and radon in tap and well water, as well as to determine the uranium's impacts on cancer risk (ECR). The mean radon concentrations in tap and well waters were 0.0430 and 0.1317 Bq l^{-1} respectively. The mean uranium concentrations in tap and private well waters were 8.8406 and 27.076 µg l^{-1}, whereas these values were below the limit of 30 µg l^{-1} according to WHO guidelines. This indicates that the risk of increased uranium intake from drinking tap water is almost very low. The excess cancer risk is 0.1222 and 0.3745 x10^{-4} meaning that the water in these places poses a cancer risk to 12 and 37 out of every million residents for tap and well water respectively, by uranium intake from water which is very low so the studied area is safe.

References

[1] D. Banks et al., “Radioelement (U, Th, Rn) concentrations in Norwegian bedrock groundwaters”, *Envir. Geol.*, 25 (1995) 165-180.

[2] BEIR III, **"The effects on populations of exposure to low levels of ionizing radiation: 1980"**, Washington: National Academic Press (1980) p. 524.

[3] BEIR V, **"Health effects of exposure to low levels of ionizing radiation"**, Washington: National Academic Press (1990) p. 421.

[4] T.D. Luckey, **"Radiation hormesis",** Boca Raton: CRC Press (1991) p. 306.

[5] A. Kabata-Pendias and H. Pendias, **"Trace elements in soils and plants",** Boca Raton: CRC Press (2001) p. 413.

[6] M. Azouazi et al., “Natural radioactivity in phosphates, phosphogypsum and natural waters in Morocco”, *J. Enviro. Radioact.*, 54 (2001) 231-242.

[7] D. Barisic, S. Lulic and P. Miletic, “Radium and uranium in phosphate fertilizers and their impact on the radioactivity of waters”, *Water Res.*, 26 (1992) 607-611.

[8] F. Conceicao and D.M. Bonotto, “Anthropogenic influences on the uranium concentration in waters of the Corumbatai river basin (SP)", *Brazil. Revista Brasilieira de Geosciències*, 30(3) (2000) 555-557.

[9] F.T. Conceicao, and D.M. Bonotto, "Use of U-isotope disequilibrium to evaluate the weathering rate and fertilizer-derived uranium in Sao Paulo state", *Brazil. Enviro. Geol*, 44 (2003) 408-418.

[10] R.F. Spalding, and W.M. Sackett, "Uranium in runoff from the Gulf of Mexico: distributive province: anomalous concentrations", *Science*, 175(4022) (1972) 629-631.

[11] S. Kratz and E. Schnug, **"Rock phosphates and P fertilizers as sources of U contamination in agricultural soils"**, Heidelberg: Springer (Berlin, 2006) pp. 57-68.

[12] R.J. Fellows et al., **“Dynamics and transformations of radionuclides in soils and ecosystem health., Wis : SSSA, 386 p"**, *Soil Sci. Soc. Am. Spec. Publ.*, 52 (1998) 85-112.

[13] W.E. Falck and D. Wymer, **"Uranium in phosphate fertilizer production”,** in Merkel BJ, Hasche-Berger, A (eds), “Uranium in the environment: mining impact and consequences", Heidelberg: Springer (Berlin, 2006) pp. 57-68, pp. 857-865.

[14] P. Linsalata, "Uranium and thorium decay series radionuclides in human and animal food chains: a review", *J. Enviro. Qual.*, 23 (1994) 633-642.

[15] WHO, **"Uranium in drinking-water, background document for development of WHO Guidelines for Drinking-water Quality"**, World Health Organization (2004).

[16] ATSDR, **"Agency for Toxic Substances and Disease Registry Public health statement for uranium"**, World Health Organization (1999) CAS# 7440-61-1.

[17] B. Al-bataina et al., “Radon measurements in different types of natural waters in Jordan”, *Rad. Measur.*, 28(1-6) (1997) 591-94.

[18] M.H. Kheder et al., “Radioactivity concentrations in barley and wheat crops in Nineveh plain region in Iraq”, *Int. J. Nucl. Ener. Sci. Technol.*, 14(1) (2020) 50-60.

[19] M.H. Kheder, H.N. Azeez and F.M. Al-Jomaily, "Alpha emitters radioactivity concentrations in some cosmetics used in Iraq using LR-115 detector ", *J. Eureka: Phys. Eng.*, (2) (2020) 65-70.

[20] H. Cember and T.E. Johnson, **"Introduction to health physics"**, 4th ed., McGraw-Hill (2009).

[21] M.H. Kheder, "Radium and Uranium Concentrations in Some Fruits and Vegetables Cultivated in Nineveh Governorate, Iraq", *Iraqi J. Appl. Phys.*, 19(3B) (2023) 15-19.

[22] M.H. Kheder, H.N. Azeez and M.A. Al-Jubbori, "Measurement of Uranium and Radon Concentrations in Wells Water Samples of Some Farms near the Mosul City in Iraq", *Iraqi J. Appl. Phys.*, 19(3B) (2023) 3-8.

[23] M.H. Kheder et al., "Radon and uranium concentration in ground water of Nineveh plain region in Iraq", *J. Phys.: Conf. Ser.*, 1234(1) (2019).
[24] EPA, **"National primary drinking water regulations, radionuclides, final rule"**, United States environmental protection agency (Washington DC), (2000).
[25] S. Mittal, A. Rani and R. Mehra, "Estimation of radon concentration in soil and groundwater samples of northern rajasthan", *Indian J. Rad. Res. Appl. Sci.*, 9 (2016) 125-30.
[26] R. Gellermann and W. Stolz, "Uran in Wässern", *Z Umweltchem Ökotox*, 9 (1997) 87-92.
[27] L. Casas et al., "The role of pH and carbonate on the solubility of UO_2 and uranite under normally reducing conditions", *Geochim Cosmochim Acta*, 62 (1998) 2223-2231.
[28] H. Yoshida, K. Kodama and K. Ota, "Role of microscopic flow-paths on nuclide migration in sedimentary rocks: a case study from the Tono uranium deposit", *Centr. Japan. Radiochim Acta*, 66(7) (1994) 505-511.

Table (1) The radon concentrations, and the annual effective dose, uranium activity concentrations, and the exceed cancer risk

No	Location	Tap water			Privet well water		
		C_{Rn} (Bq/L)	C_U (μg/L)	ECR x 10^{-4}	C_{Rn} (Bq/L)	C_U (μg/L)	ECR x 10^{-4}
S1	Mosul	0.0303	6.2404	0.0863	0.1112	22.881	0.3164
S2	Telkaif	0.0269	5.5470	0.0767	0.1011	20.801	0.2877
S3	Wana	0.0236	4.8536	0.0671	0.0708	14.561	0.2014
S4	Al-Qoush	0.0472	9.7073	0.1342	0.1349	27.735	0.3836
S5	Ba'sheeqa	0.0404	8.3206	0.1150	0.1483	30.508	0.4219
S6	Bartellah	0.0337	6.9338	0.0959	0.1382	28.428	0.3932
S7	Al-Hamdaniya	0.0370	7.6272	0.1055	0.1450	29.815	0.4124
S8	Al-Namroud	0.0438	9.0139	0.1246	0.1483	30.508	0.4219
S9	Al-Hamidat	0.0539	11.094	0.1534	0.1483	30.508	0.4219
S10	Zummar	0.0303	6.2404	0.0863	0.1112	22.881	0.3164
S11	Rabia'a	0.0370	7.6272	0.1055	0.1194	24.552	0.3396
S12	Al-Iyadiah	0.0404	8.3206	0.1150	0.1268	26.071	0.3606
S13	Talla'far	0.0505	10.400	0.1438	0.1416	29.122	0.4028
S14	Sinjar	0.0573	11.787	0.1630	0.1483	30.508	0.4219
S15	Al-Ba'aj	0.0607	12.480	0.1726	0.1517	31.202	0.4315
S16	Hammam Al-Aleel	0.0539	11.094	0.1534	0.1416	29.122	0.4028
S17	Al-Shora	0.0505	10.400	0.1438	0.1382	28.428	0.3932
S18	Al-Qayara	0.0573	11.787	0.1630	0.1483	30.508	0.4219
S19	Al-Hadar	0.0438	9.0139	0.1246	0.1315	27.041	0.3740
S20	Telabtah	0.0404	8.3206	0.1150	0.1281	26.348	0.3644
	Min	**0.0236**	**15.254**	**0.2109**	**0.0708**	**45.763**	**0.6329**
	Max	**0.0607**	**39.225**	**0.5425**	**0.1517**	**98.064**	**1.3564**
	Mean	**0.0430**	**8.8406**	**0.1222**	**0.1317**	**27.076**	**0.3745**

IRAQI JOURNAL OF APPLIED PHYSICS Vol. 20, No. 3, July-September 2024, pp. 540-544

Effect of Material Irradiated Type and Spot Size on Spot Center Temperature of a Diode-Pumped Solid State Laser

Ragheed M. Ibrahim
Musab S. Mohammed

Department of Physics,
College of Education for
Pure Science,
University of Mosul,
Mosul, IRAQ

This article presents an experimental study of measuring the temperature of the center spot of DPSS green laser, which emits a light beam with a center wavelength of (532 nm), and its changing with the laser spot dimensions and the type of material. The optical properties of this laser were studied, for example, the threshold current value was determined to be 62mA at room temperature. The results showed that the temperature of the center of the spot decreases logarithmically with increasing laser spot size. Moreover, by studying the spectral power distribution with the laser spot dimensions, it is observed that the density of the power spectral distribution drops in an inverse exponential function with increasing spot size. Finally, the results showed that the temperature of the of the spot center increases as the density of the power spectral distribution increasing.

Keywords: Temperature distribution; Nd:YVO_4 laser; Thermal lensing; Laser Beam
Received: 24 March 2024; **Revised:** 15 May 2024; **Accepted:** 22 May 2024

1. Introduction

The significant development in solid-state laser technology over the past several years has been the result of numerous technical developments across many different fields, correspondingly increasing interest in using semiconductor diode lasers to excite solid-state lasers made of materials impregnated with transparent rare earth ions [1-3]. Laser diode-pumped solid state is commonly called DPSS laser. The resultant diode pumped laser has much better spectrum and spatial properties than the laser diode itself, these lasers' benefits include their high efficiency, long lifespan, stability, small design, and superb beam quality [4]. In numerous scientific uses, high power DPSS lasers have taken the role of ion lasers and flash lamp pumped lasers, and now they are considerably used in green and other color laser pointers. The DPSS lasers is widespread used several field such as information technology, science, industry, as well as in the military [5]. Because of its exceptional qualities, namely a high absorption coefficient and a wide absorption bandwidth at the pumping wavelength, as well as a large stimulated emission cross section at the laser wavelength, the Nd:YVO_4 crystal has gained the most interest among the several laser crystals suited for DPSL [2]. Additionally, by coupling the diode-pumped Nd:YVO_4 crystals with NLO crystals (LBO, BBO, or KTP), the resultant frequency can be changed from near infrared to green, blue, or even ultraviolet light [6]. Laser is used as a heat source in many industrial applications such as cutting, perforating, welding, annealing, etc. [7-9], and medical applications such as surgical operations, skin disease therapy, eye treatment, etc. [10,11]. This requires determining the amount of heat produced in the material as a result of the laser beam’s absorption. Thus, in order to make the best and most efficient use of lasers in a variety of applications, several theoretical and practical research have attempted to understand the heat distribution in the laser beam and the factors controlling it. For instance, many of the studies focused on the analysis of the impact of various laser parameters on temperature distributions across workpiece employing finite element model [7,12]. An important element in the stability and part quality of the laser beam melting process is temperature fields, which have been studied through numerically and experimentally in references [13,14]. In reference [15], the influence of uniform and Gaussian heat flux distribution in various beam diameters, power and velocity on bending angle was simulated for two types of lasers including Nd:YAG and CO_2 lasers. Many studies have attempted to understand how heat is distributed across in biological tissues when using lasers for medical therapy in order to reduce tissue damage brought on by excessive heat. Most of these studies have focused on the effects of several factors, including time of exposure, power, wavelength, spot size, on the temperature distribution in skin tissues and the thermal response of skin tissues when exposed to a laser source, using finite element technique numerical computations [11,16,17].

Measuring the laser spot size is not as easy as it may seem at first glance, especially if we want our measurements to be accurate and decisive. There are two meanings associated with the term "laser spot size". In the first, the diameter of the laser beam when it leaves the laser device or is in an area far from the laser is meant, and in the second, the size of the spot on the focal plane while focusing with the lens. It is important to distinguish two cases because the measurement method is different. The laser beam's diameter varies continuously as it propagates along its optical path. The following formula determines the beam's radius along the propagation z-axis for a Gaussian beam [21].

$$w(z) = w_o\sqrt{1 + (\frac{\lambda Z_R}{\pi w_o^2})^2} \qquad (1)$$

where w_o represents the beam radius and Z_R represents the Rayleigh length, which is given in the form of

$$z_R = \frac{\pi w_o^2}{\lambda} \qquad (2)$$

The waist value of the Gaussian beam focused using a lens with focal length *f*, see Fig. (1), is given as [21]

$$w_f = \frac{\lambda f}{\pi w_o} \qquad (3)$$

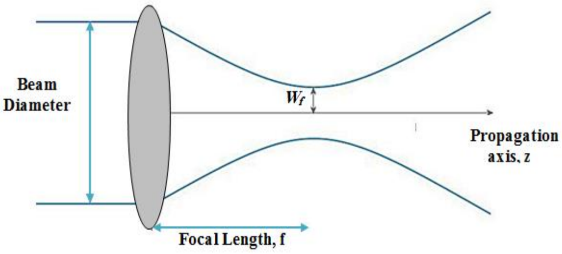

Fig. (1) A lens with a focal length *f* is used to focus the light beam

Therefore, the size of the focal point could be quite tiny, and in this case the beam size will vary very quickly along the axis of dissemination. Since determining the focal plane of a laser beam requires a high degree of accuracy in the location of the sensor's image plane and a method for altering this position, measuring the focused spot size of a laser beam is almost an art in and of itself. To calculate the magnitude of the laser spot size, there are three general definitions known for the diameter of the laser beam represented by FWHM, $1/e^2$, D4σ.

The FWHM is measured at the midpoint of the maximum value (also called the beam width at mid-power) from the beam intensity distribution curve along the pre-determined axis of propagation passing through the center of the beam, this is often the point with the highest level of intensity. FWHM corresponds to the distance between the two points closest to the peak that contains 50% of the maximum beam intensity [22]. Some people prefer to use other ratios of the maximum intensity of the beam to determine its width, and the common ratio 13.5% leads us to define the diameter of the beam as $1\backslash e^2$ of the maximum intensity, this approximation results from simplifying the equation that describes the radial distribution of the Gaussian beam. Since the definitions of both $1\backslash e^2$ and FWHM are computed from the distribution of intensity along one axis, therefore it does not consider the general appearance of the beam and thus the exact size of the laser light spot. The D4σ is the most often used definition for laser beam widths. In essence, the diameter (D4σ) is equal to four times of the standard deviation of the laser beams main axis' intensity distribution. It is computed using the laser beam's second kind of intensity distribution form [22].

The spectral power distribution (SPD) is given by the following relationship:

$$M = \lambda = \frac{P}{A\Delta\lambda} \quad W/m^3 \qquad (4)$$

where P is the radiant flux power and A is the area of the spot

Study of SPD is crucial for applications in optical sensing systems where optical properties such as transmittance, reflectivity, and absorption are important. As well as the sensor's response to the wavelength of the incident light [23].

This work aims to quantify the spot center temperature of a diode-pumped solid-state (DPSS) laser experimentally, considering both the type of irradiated materials and its spot size.

2. Experimental Part

The laser used in this study is a DPSS emitting a green light at 532 nm. Figure (2) depicts the main components of a microchip laser, which primarily consists of an Nd:YVO_4 crystal acting as the active medium which is optically pumped using a laser diode with a wavelength of 808 nm. The emitted wavelength (1064 nm) is passed through a KTP crystal, which is used as a frequency doubling medium, efficiently converting into a highly visible green. The primary axes of KTP and Nd:YVO_4 crystals are rotated by 45° toward one another for effective frequency doubling, because KTP exhibits an interaction of type II [18]. Despite the crystals are coated in a way that only allows green light (532 nm) to emerge from the cavity, the resultant green light still has some traces of 1064 nm. Therefore, the infrared filter is used to prevents 808 nm and 1064 nm light from exiting the laser [19,20].

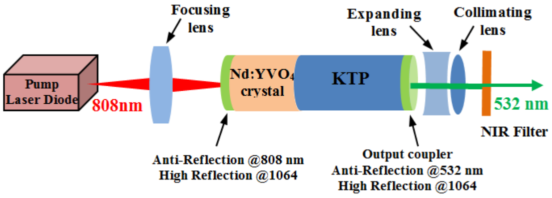

Fig. (2) DPSS green laser structure

Figure (3) depicts the schematic diagram of experimental system used for determining the temperature of the spot center of the DPSS laser. The wavelength of the DPSS laser (532nm) displays a spectral line of up to Δλ=30nm and an output optical output power of up to 180mW.

A precision thermal sensor with a resolution of ±0.1°C was used to monitor the temperature at the center of the laser light as a function of spot size with black and white backgrounds, because the color of the screen is of great importance in the issue of heat absorption or reflection The current was manually adjusted using a laser injection current controller providing a maximum current of 250 mA with a resolution of ±0.1 mA. An AS-M890A multimeter was used to measure the current. The laser spot size was measured by scanning the laser spot penetrating a small aperture in both the horizontal and vertical directions. The spot size was determined precisely through the precise variation of the vertical and horizontal scanning that was within a millimeter.

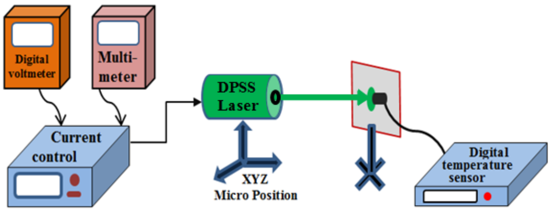

Fig. (3) Schematic diagram of the experimental setup

3. Results and Discussion

Figure (4) shows the photoelectric characteristics of a DPSSFD laser for the relationship between the output optical power from the laser versus the injection current. It is noted that the threshold current (which can be found from the intersection of the extension of the curve in the linear region with the current axis) is equal to 62mA. The stimulated emission occurs above this current. Therefore, the laser must be operated with a current higher than 62mA to ensure that the laser operates normally.

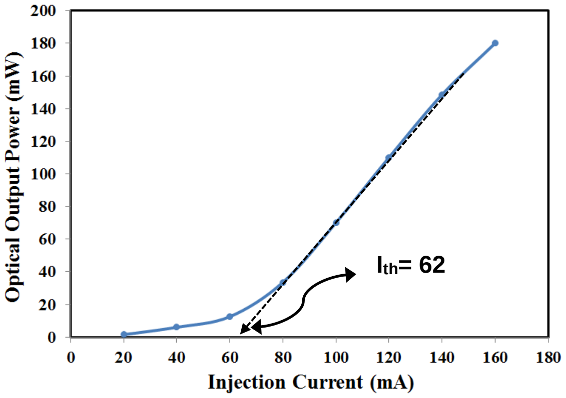

Fig. (4) Optical output power versus injection current of DPSS Laser

After operating the laser with a constant current of 75 mA and at an almost constant temperature while changing the spot size of the laser, the temperature of the spot center was measured in two cases of the screen on which the laser spot is incident.

The first is a white screen and the second is a black screen in order to compare the heat generated in the two cases of black and white. Figure (5) shows the relationship between the laser spot dimensions and the heat generated in the center of the spot. It is found that the temperature of the center of the spot decreases with the increase in the size of the spot. Moreover, in the cases of the white screen and the black screen, the equation of change for both cases is shown in the figure, as the amount of change in the temperature of the center of the laser spot with the spot size. The change is -14.625°C/m^2 for a black screen, while the change for a white screen is -11.636°C/m^2. The reason for the difference in temperatures is due to the high absorbency and emissivity nature of the black surface. The reason for taking two completely different colors in terms of absorbance of the screen on which the laser spot falls is to take into account other objects that differ between black and white in the case of treating these objects or cells optically to choose the average temperature of the center of the spot for the laser in treating these contrasting objects.

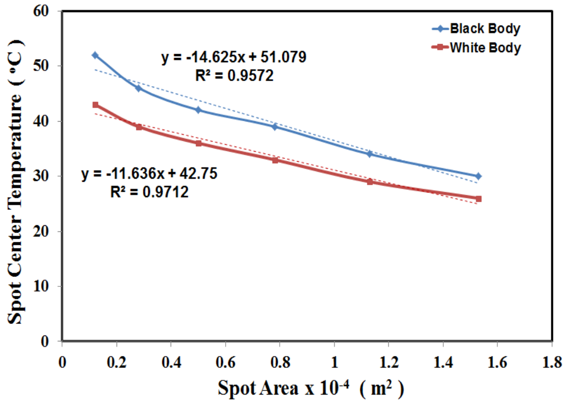

Fig. (5) Variation of spot center temperature with the spot area

Figure (6) represents the relationship between the average temperature extracted for the two curves in Fig. (5) versus the spot size of the laser. The equation of change for the curve is given by the following formula:

$$T_{avg} = -7.466\, ln(A) + 32.704 \qquad (5)$$

where T_{avg} represent the average spot center temperature, and *A* is the spot area

Through this relationship, it is possible to find the temperature of the center of the laser spot at any size. For example, if we have a sample of living cells with a number of 100,000 cells and the average diameter of one cell is 10 μm, the total area of this sample will be approximately 100 mm^2, or 10^{-4} m^2. Therefore, when a laser spot with a size of 10^{-4} m^2 is shined, the temperature of the sample will It will rise to about 40°C, and it can be increased by increasing the injection current of the laser.

Figure (7) represents the relationship between the spectral power distribution (SPD) versus the average temperature of the laser spot center. It can be seen that there is a non-linear increase in (SPD) with the increase in the temperature of the spot center, and when the spectral density of the laser spot rises to reach the value 275 GW/m^3, the average temperature of the center of the laser spot reaches to 47°C. The reason for this is that if the size of the laser spot is small, it leads to an increase in the number of photons per unit area and thus an increase in the temperature of the area on which the photons strike. Figure (8) represents the relationship between the spectral power distribution (SPD) versus the spot size of the laser. It is noted from this curve that (SPD) decreases when the laser spot size increasing. The change equation can be written as:

$$SPD = 33.249A^{-1.001} \qquad (6)$$

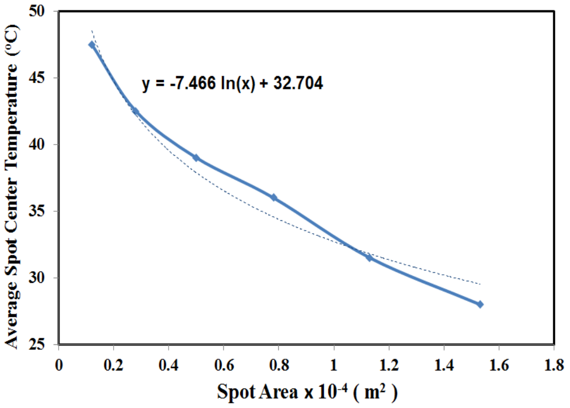

Fig. (6) Variation of average spot center temperature with the spot area

Finally, the results of this work could be used for medical and life applications in studying the effect of the temperature of the laser spot on the performance of bacteria, living cells, and enzymes.

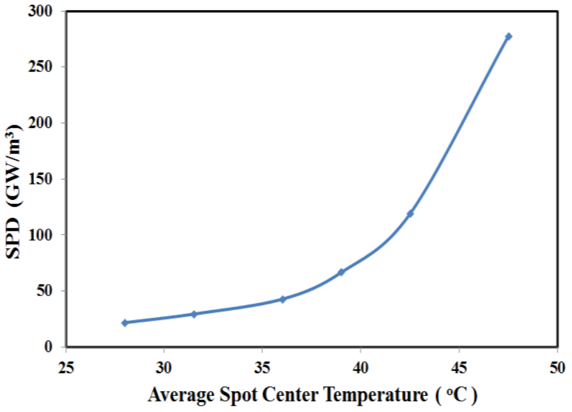

Fig. (7) Variation of spectral power distribution with the average spot center temperature

4. Conclusions

The following conclusions can be obtained from this work: For the DPSSFD green laser, the laser spot dimensions can be controlled by controlling the distance of the lens from the laser light exit. By studying the temperature of the center of the laser spot, we found that the temperature of the center of the spot decreases logarithmically with increasing laser spot size. We also found that by studying the spectral power distribution with the laser spot dimensions, the density of the power spectral distribution exponential decreases with increasing spot size, Finally, it was found that the temperature of the center of the spot increases when the density of the power spectral distribution increasing.

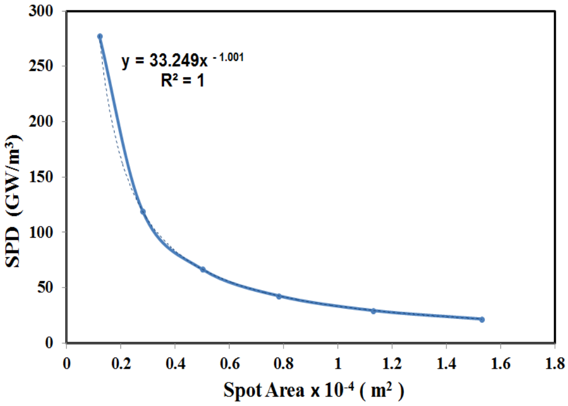

Fig. (8) Variation of spectral power distribution with the spot area

References

[1] B. Davarcioglu, “An Overview of Diode Pumped Solid State (DPSS) Lasers”, *Int. Arch. Appl. Sci. Technol.*, 1(2) (2010) 1-12.

[2] V.J. Pinto Robledo et al., “Experimental study of the dynamics of a diode-pumped Nd:YVO_4 laser under periodic modulation of losses”, *Rev. Mex. Fis. E*, 58 (2012) 150-155.

[3] R.M. Ibrahim et al., “Temperature-dependency performance of InGaAsP semiconductor laser amplifiers”, *Dig. J. Nanomater. Biostruct.*, 16(2) (2021) 385-392.

[4] L. Shang et al., “A Nd:YVO_4/LBO Intracavity Frequency Doubling Laser Pumped by a Diode-Laser”, *Adv. in Comp. Sci. Res.*, 94 (2019) 112-114, *Int. Conf. on Big Data Electron. Commun. Eng. (BDECE 2019).*

[5] S. Li et al., “Thermal effect investigation and passively Q-switched laser performance of composite Nd:YVO_4 crystals”, *Opt. Laser Technol.*, 68 (2015) 146-150.

[6] C. Jung et al., “Linearly-polarized Nd:YVO_4/KTP microchip green laser”, *Opt. Exp.*, 17(22) (2009) 19611-19616.

[7] A. Joshi, et al., “A Study of Temperature Distribution for Laser Assisted Machining of Ti6Al4V Alloy”, *Proced. Eng.*, 97 (2014) 1466-1473.

[8] T. Bergsa et al., “Optimized Temperature Distribution for Laser Hardening with Freeform Mirrors”, *Lasers in Manufact. Conf. (LiM)*, 24-27 June 2019, 1-7.

[9] M. Kubiak et al., “Research on Yb:YAG Laser Beam Power Distribution Used in Hybrid Processes”, *Acta Physica Polonica*, 139(5) (2021) 598-601.

[10] B. Sheeba and P. Myvizhi, “Application of laser in medical field”, *Int. J. Pure Appl. Math.*, 119(12) (2018) 3983-3990.

[11] P. Wongchadakul et al., “Simulation of temperature distribution in different human skin types exposed to laser irradiation with different wavelengths and laser irradiation intensities”, *Songklanakarin J. Sci. Technol.*, 41(3) (2019) 529-538.

[12] F. Njihia1 et al., “Analysis of Temperature Distribution in Laser Assisted Metal Polymer (LAMP) Joining”, *J. Sustain. Res. Eng.*, 4(1) (2017) 1-11.

[13] J. Schilp et al., “Investigations on Temperature fields during laser beam melting by means of process monitoring and multiscale process modeling”, *Adv. Mech. Eng.*, 6 (2014), doi: 10.1155/2014/217584.

[14] H. Ding et al., “Study on Three-Dimensional Temperature Field Induced by Laser Irradiation with Different Intensity Distribution”, *Adv. Intellig. Sys. Res.*, 168 (2019) 64-68.

[15] M. Riahia et al., “Experimental and numerical study of heat flux distribution in laser forming of bi-layer sheets”, *J. Comput. Appl. Res. Mech. Eng.*, 4(1) (2014) 67-79.

[16] K.M. Shurrab and M.S. El-Daher, “Simulation and Study of Temperature Distribution in Living Biological Tissues under Laser Irradiation”, *J. Lasers Med. Sci.*, 5(3) (2014) 135-139.

[17] K. Chen et al., “Simulation of temperature distribution in skin under laser irradiation with different wavelengths”, *Int. J. Light Electron Opt.*, 125 (2014) 1676-1679.

[18] E. Garmire, “Nonlinear optics in daily life”, *Opt. Exp.*, 21(25) (2013) 30532-30544.

[19] A.S. Elsafty et al., “Spectral characteristics of a microchip Nd:YVO_4 laser”, J. Opt, 52 (2023) 1717-1723.

[20] J. Galang et al., “A green laser pointer hazard”, *Int. Laser Safety Conf.*, (2011) 296-300.

[21] M. Safuan Mat Yeng et al., “The Determination of Laser Spot Size of an Optical Tweezers by Stuck Bead Method”, *J. Sci. Technol.*, 9(3) (2017) 70-74.

[22] H.J. Eichler et al., **“Laser Physics and Applications”**, Springer-Verlag (Berlin, 2004).

[23] O. Svelto, **“Principles of Lasers”**, 5th ed., Springer Science + Business Media (2010).

Effectiveness of Nuclear Track Detectors irradiation by Laser on Recording Concentration and Track Diameter of Alpha Particles Emitted from Radon

Malik H. Kheder

Department of Physics,
College of Education for
Pure Sciences,
University of AL-Hamdaniya,
AL-Hamdaniya 41006, IRAQ

Iraqi Journal of Applied Physics
Q4 Electronic, Optical and Magnetic Materials
best quartile
SJR 2022
0.19
powered by scimagojr.com

The effects of laser irradiation on the registration properties of nuclear solid state track detectors were examined. Two different kinds of lasers were used, along with three detectors. The findings demonstrated that the quantity of radon gas-produced tracks increased with irradiation time, peaking at 8 minutes increasing about 25%, suggesting that bonds in the detector broke and free radicals were created. The recording of tracks was then varied by the detector solidification due to recombination between the free radicals and other molecules, finally falling to a value near the initial value. In addition suggesting that laser power matters more than wavelength.

Keywords: Laser irradiation; Alpha particles; Track diameter; CR-39 detector
Received: 06 February 2024; **Revised:** 28 March 2024; **Accepted:** 03 April 2024

1. Introduction

The domains of application for nuclear track detectors have grown and increased due to their affordability, accuracy, and ability to preserve antiques. They are also simple to operate and do not require a power source. In uranium exploration, radiation protection in nuclear power plants, optical applications, and radiation protection dosimetry, the CR-39 detector is utilized as a simple charged particle monitor [1-4]. One of the most significant uses for them is radon gas concentration measurement to estimate the ensuing pollution to the environment [5]. Radiation is divided into two sorts based on its impact on matter: ionizing radiation and non-ionizing radiation. Ionizing radiation includes cosmic rays and x-rays, whereas non-ionizing radiation includes ultraviolet light, radiant heat, radio waves, and microwaves. Non-ionizing radiation has a longer wavelength, which results in a lower frequency and energy. Ionizing radiation has a shorter wavelength, a higher frequency, and a higher energy. Both non-ionizing and ionizing radiation can harm organisms and affect the natural environment [6]. Several research have lately investigated the impact of the laser on the polymeric detector to investigate the sensitivity increase [7-9]. The laser's interaction with polymeric detectors is influenced by factors such as wavelengths, pulse duration, pulse repetition rate, power density, energy density of the coherent beam, and ambient conditions, which are broadly classified as thermal and non-thermal [10]. Low-ionizing laser radiation can cause the polymer molecules in plastic track detectors to either cut or cross-link, which would speed up the etching process overall [11]. One of the organic reagents, CR-39 is a polymeric substance composed of small repeating units called monomers that are bonded together. Asra defeated her O-H, the CN-85 and LR-115 detectors utilizing cellulosic reagents. Due to the fact that the polymeric reagent is made up of tiny units that are joined by some that have an O-H covalent link that is easily broken when exposed to radiation, small polymeric chains with ends are produced [12]. Unlike other active chemicals, free radicals can interact with one another. These molecules become irritated and ionized due to the effect of radiation on the polymer. This stored effect, which breaks the links between them and damages the polymer material without dissipating under normal circumstances, is called the latent effect. Ionizing radiation-damaged areas are more able to interact with alkaline solutions, like sodium hydroxide, than intact areas. Consequently, the irradiated areas are swiftly penetrated by the chemical solution, leading to an increasing effect. When examined under a microscope, the latent effect of ionizing radiation may be observed, and its depth and diameter increase with scraping time [13]. Radiation either dissolves the polymer into free radicals or free radicals and ions, or causes dissolution, which includes reactions that break the chemical bonds between atoms in the polymer's main chains, resulting in a loss of structural strength, ductility, or flexibility, and a decrease in molecular weight [14-16]. A higher percentage of chemical processes and products involve free radicals. The polymers that emerge from these reactions might have tangled, branching, or linear forms. Alternately, harden it. If the free radicals are able to travel and restore fusion with other roots or with the main chain, this will lead to entanglement. The molecular chains are linked to one another by cross-linking, creating a complex network structure at the end, and this entwining increases the molecular weight, strength, and hardness of the reagent. When the polycarbonate surface was exposed to a laser, this resulted in both hardening and softening at power. The stability of the polymer is determined by the strength of the interatomic connection, and laser free ions have a comparatively limited lifetime [17-20].

The objective of the current investigation is to ascertain how laser radiation affects the detector's capacity to record alpha particle traces released by radon gas, as well as the diameter of those traces. Nuclear track solid state detectors, which can record tracks (damage places) and its width using ImageJ software after acquiring images from an optical microscope, were utilized to acquire results and information helpful in explaining some of the events that occur in polymers when exposed to laser.

2. Experimental Part

The nuclear track detector was exposed to a laser before being placed in a plastic container "Can technique" used as a dosimeter to measure the number of alpha particle tracks emitted from radon gas, in order to study the effect of lasers on the number and diameters of tracks resulting from radon gas exposure ImageJ software was used. The detectors CR-39, CN-85, and LR-115 were used, and the exposure lasers were:

1- (He-Ne) laser beam, is a type of gas laser, that irradiates with powers (5 mW) for (5 min), the distance between the source and the detectors is (0, 4, 8, 12, and 16 cm) and the wavelength is 632.8 nm as in Fig. (1a).

2- A laser diode beam that emits (250 mW) of light (5 min). The wavelength of 405 nm and the distance between the source and the detectors are (0, 4, 8, 12, and 16 cm) as in Fig. (1b).

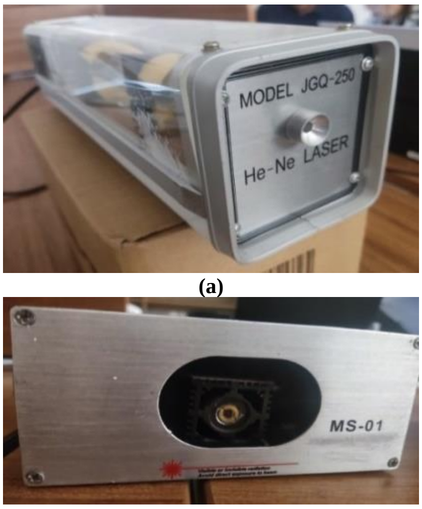

(a)

(b)

Fig. (1) The laser sources used in this work (a) He-Ne laser, and (b) Diode laser

To measure the number of tracks and their diameter, passive type detectors using the "Can technique" were used with detector film as alpha track detectors. Each detector piece was 1cm^2, fixed in the top of a sealed can and identified by a number or code, a hole on the bottom cover of 1.5 cm diameter covered with 2.5 x 1.5 cm^2 of sponge piece with a thickness of 1cm to prevent impurities, as shown in Fig. (2). Dosimeters were placed 50 cm away from the walls, windows, and sunlight, at a height of 2.00-2.25 m. For 60 days, dosimeters were placed in a room. After 60 days, the detectors were removed and etched at normality 6.25 N of NaOH in a water bath at heat 70°C tracks revealed. The detectors were then washed and dried, and the number of tracks was counted using ImageJ software, as well as the track diameter. The ImageJ software then calculates the average area of the tracks.

$$A = \pi r^2 \qquad (1)$$

The mean radius can be calculated from the area by the relation

$$r = \sqrt{(A/\pi)} \qquad (2)$$

Then the diameter calculated by the equation.

$$d = 2r \qquad (3)$$

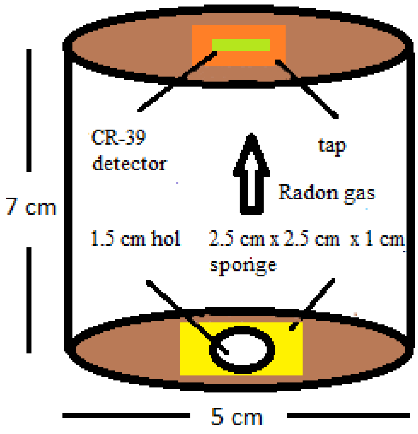

Fig. (2) Radon monitor technique "Dosimeter"

3. Results and Discussion

The obtained results from detectors of measured tracks number of alpha particles emitted from radon gas are listed in table (1). The calculated track diameters are listed in table (2).

Table (1) Track numbers from the three types of detectors for both lasers used in this work

Irradiation time (min)	Laser Diode			He-Ne Laser		
	CR-39 Tr.cm^{-2}	CN-85 Tr.cm^{-2}	LR-115 Tr.cm^{-2}	CR-39 Tr.cm^{-2}	CN-85 Tr.cm^{-2}	LR-115 Tr.cm^{-2}
0	159	120	140	159	120	140
4	181	136	161	174	134	156
8	201	152	175	193	150	169
12	176	133	155	168	131	151
16	165	125	143	161	123	141

Table (2) Track diameters from the three types of detectors for both lasers used in this work

Irradiation time (min)	Laser Diode			He-Ne Laser		
	CR-39 µm	CN-85 µm	LR-115 µm	CR-39 µm	CN-85 µm	LR-115 µm
0	28.10	27.18	27.64	28.10	27.18	27.64
4	32.32	31.72	29.86	31.31	31.72	29.43
8	35.69	34.23	33.85	35.15	33.85	33.48
12	31.52	31.52	32.51	30.90	29.86	32.12
16	29.86	29.86	28.99	29.64	28.55	28.32

The outcomes are shown in table (1). It shows that as the laser irradiation time increases for both types of lasers, the number of tracks increases for all detectors up to the maximum value of the number of tracks at the 8-minute mark. After that, the number of tracks starts to decrease as the laser irradiation time increases until it reaches its lowest value at the 16-minute mark, which is almost equal to the number of original tracks without irradiation. This result implies that weakly ionizing laser radiation applied to the plastic path detectors may enhance polymer cross-linking, resulting in the breaking and conversion of long chain molecules into shorter ones. As radon outperforms O-H because it is composed of tiny, tightly spaced repeating units known as monomers, which are easily damaged by radiation. Different active compounds known as free radicals can interact with other molecules or with each other. Crosslinking is produced when the irradiation time is extended, allowing free radicals to reunite with the main chain or additional radicals. Ultimately, as the irradiation period rose, the number of traces and their diameter decreased as a result of the polycarbonate surface being exposed to the laser, which also induced particle and free radical re-adhesion and surface particle interlocking and hardening. The radiation that hits the polymer irritates and ionizes it. This causes the bonds between them to break and the chemical bonds between the atoms in the polymer's major chains to break. The polymer then disintegrates into free radicals and loses its structural strength and flexibility, as well as reducing its weight. Ions and roots The final products of these transformations are polymers with linear, branching, or cross-linked structures because free radicals participate in a larger proportion of chemical processes. This explains why the number of traces and their diameter grow with irradiation time. Crosslinking is produced by letting free radicals roam around and recombine with other radicals or the main chain over an extended period of irradiation. The resulting intricate network structure reinforces, hardens, and raises the molecular weight of the detector. The number of traces and the diameter of the traces decreased as the irradiation time increased, the number of traces produced by radon gas at room temperature for the detectors, when the polycarbonate surface was exposed to the laser because the surface particles interlocked and hardened as well as the particles and free radicals re-adhered to each other. The number of traces increased during laser diode irradiation for CR-39, reaching a maximum value of 201 traces at an 8-minute irradiation time, or a 26.41 percent increase. This indicates the maximum amount of bond disintegration and free radical formation that was possible. Following this, the number of traces started to decrease, approaching the beginning of the irradiation due to recombination between the free radicals and the remaining molecules. This led to an increase in detector solidification and a decrease in trace recording.

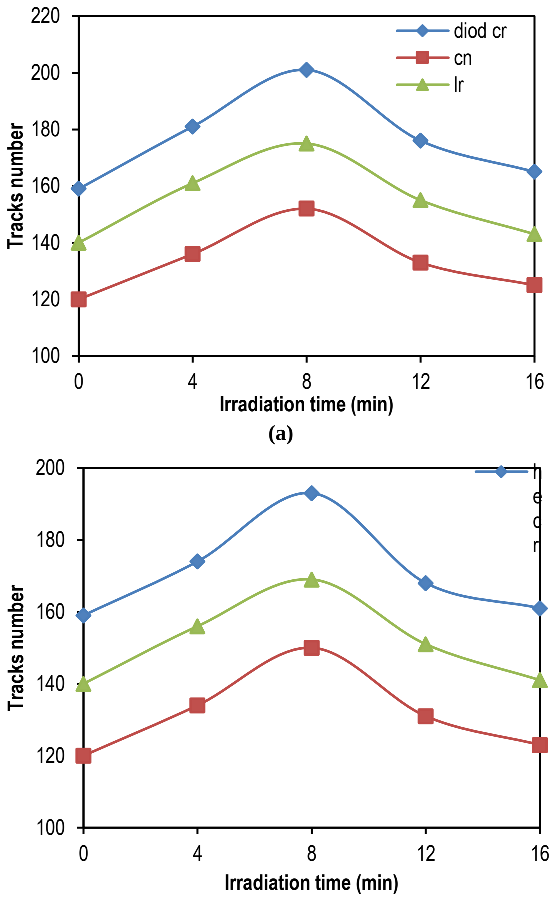

(a)

(b)

Fig. (3) Number of tracks comparison of the detector response among the three detector types for laser irradiation (a. Diode laser, b. He-Ne laser)

As there will be no more rise in the quantity of traces, radiation should be stopped. In contrast, the CN-85 detector showed a 26.66% increase, while the LR-115 showed a 25% increase. He-Ne laser irradiation resulted in increases of 21.38% for CR-39, 25 percentage for CN-85, and 20.71% for the LR-115 detector. The response to a laser diode is higher than that of a He-Ne laser for all detectors. The radon gas in the detectors produced a track diameter of 28.10 µm without laser irradiation. The track diameter rose with increasing irradiation duration, peaking at 35.69 µm during an 8 min irradiation time, or a 27.01% increase. Whereas the rise was 25.93% for the CN-85 detector and 22.46% for the LR-115 detector. There was a 25.08% rise for CR-39, a 24.54% increase for CN-85, and a 21.12% increase for an LR-115 detector when exposed to He-Ne laser radiation. The correlation between the two lasers' effects on the detectors is as follows: for the CR-39 detector, the laser diode's irradiation has an effect 5.03% greater than that of the He-Ne laser; for the CN-85 detector, the effect is 1.66 percent greater than that of the He-Ne laser; and for the LR-115 detector, the effect is 4.29% greater than that of the He-Ne laser. According to these findings, the CR-39 detector responds more quickly than the LR-115 detector, and both detectors are significantly bigger than the CN-85 for the laser kinds that were utilized. There is a difference of 42 tracks between the minimum and maximum number of track registrations of the CR-39 detector between the two lasers on the detectors (Fig. 3a: laser diode), which is more than the 35 tracks of the LR-115 detector and the 32 tracks of the CN-85 detector. As with CR-39 being higher than LR-115 and both being higher than CR-85 detector, the comparison for (Fig. 3b: He-Ne laser) displays the same difference.

4. Conclusion

The detectors exposed to the laser led to an increase in track density and track diameter. When it comes to track registration, diameter, and types of employed lasers, the CR-39 and LR-115 detectors perform better than the CN-85. Additionally, both detectors are substantially larger. The response of all detectors to the laser diode (power 250 mW, wavelength 405 nm) is larger than the response to the He-Ne laser (power 5 mW, wavelength 632.8 nm), suggesting that the laser power has a greater effect on the detector response than the wavelength.

References

[1] S.A. Durrani and R.K. Bull, "**Solid state nuclear track detection: Principles, methods and applications**", Pergamon Press (Oxford, 1987).

[2] M.H. Kheder, "Radon and uranium concentration in ground water of nineveh plain region in Iraq", *IOP Conf. Series: J. Phys. Conf. Ser.*, 1234 (2019) 012033.

[3] M.H. Kheder, "Alpha Emitters Radioactivity Concentrations in Some Cosmetics Used in Iraq Using LR-115 Detector", *EUREKA Phys. Eng.*, 2 (2020) 65-70.

[4] M.H. Kheder, "Radioactivity concentrations in barley and wheat crops in Nineveh plain region in Iraq", *Int. J. Nucl. Ener. Sci. Technol.*, 14(1) (2020) 50-60.

[5] H.N. Azeez, "Radon Concentration Measurement in Ainkawa Region Using Solid State Nuclear Track Detector", *Iraqi J. Sci.*, 59(1C) (2018) 482-488.

[6] J. Ford. "**Radiation, people and the environment (INIS-XA--703)**", (IAEA) International Atomic Energy Agency, Division of Public Information, Vienna (Austria) (2004).

[7] J. Zhou and H.H. Cui, "Sensitivity enhancement of PETP track detector by UV radiation", *Int. J. Rad. Appl. Instrum. D. Nucl. Tracks Rad. Measur.*, 15 (1988) 163-165.

[8] G. Hussain, "Influence of ultraviolet radiation on the nuclear track recording properties of CR-39 polycarbonate detectors", *Int. J. Appl. Rad. Isotop.*, 33(7) (1982) 517-519.

[9] C.F. Wong and P. Hoberg, "A comparison of the effects of UV radiation on CR-39 and Lexan plastic irradiated by alpha particles", *Nucl. Instrum. Meth. Phys. Res.*, 203 (1982) 443-449.

[10] B. Jaleha, "KrF laser irradiation effects on nuclear track recording properties of polycarbonate", *Rad. Measur.*, 38(2) (2004) 173-183.

[11] S. Prasher and S. Singh, "The effect of infrared radiation on etching characteristics of CR-39 plastic track recorder", *Rad. Measur.*, 36 (2003) 105-106.

[12] K.C. Tse, "Photo-degradation of PADC by UV radiation at various wavelengths", *Polym. Degrad. Stabil.*, 91 (2006) 2380-2388.

[13] S.A. Mohammed Saleh, "Radioactivity of Some Soils in the University of Tikrit, Iraq, college of Education for Girls using Solid-State Nuclear Track Detector type CR-39", *Iraqi J. Sci.*, 60 (2019) 2015-2021.

[14] J.M. Najim, "Generation of dye (Rhodamine B) laser by optical pumping and study its effect on solid-state nuclear track detector Cr-39", *AIP Conf. Proc.*, 2372 (2021) 110010.

[15] S.H. AL-Niaemi, "Effect of Electromagnetic Radiation on the Properties of Nuclear Track Detector CR-39 and Building of Electrochemical Etching System", PhD thesis, University of Mosul, Iraq (1998).

[16] K.F. Chan, "The Studies of CR-39 and Colorless LR-115 Solid-State Nuclear Detectors (SSNTDs) for Alpha-Particle Radiobiological Experiments", Msc thesis, City University of Hong Kong, China (2007).

[17] F. Abu-Jarad, "Effects of ultraviolet light, solar radiation, XeCl laser and Xenon arc lamp on the nuclear track recording properties of CR-39", *Int. J. Rad. Appl. Instrum. D: Nucl. Tracks Rad. Measur.*, 20 (1992) 531-541.

[18] C.C. Tse, "Investigation of the Effects of UV Irradiation on the Etching Behavior of CR-39 Solid State Nuclear Track", Msc thesis, City University of Hong Kong, China (2007).

[19] F.M. Ng, "Surface effect of ultraviolet radiation on electrochemically etched alpha-particle tracks in PADC", *Rad. Measur.*, 43 (2008) S102-S105.

[20] K.C. Tse, "Effects of UVC irradiation on alpha-particle track parameters in CR-39", *Rad. Measur.*, 43 (2008) S98-S101.

IRAQI JOURNAL OF APPLIED PHYSICS Vol. 20, No. 3, July-September 2024, pp. 549-552

Iman H. Hadi [1]
Doaa Sulaiman [1]
Ban A. Bader [2]

[1] *Department of Applied Science, University of Technology, Baghdad, IRAQ*
[2] *Department of Physics, College of Education, University of Al–Hamdaniya, Nineveh, IRAQ*

Synthesis of Zinc Nanoparticles on Various Substrates Using Direct Current Sputtering Method

Zinc (Zn) thin films were deposited on silicon and glass substrates using DC sputtering. The crystal structure and morphology of the films were characterized by X-ray diffraction (XRD) and field-emission scanning electron microscopy (FESEM), respectively. XRD analysis revealed a dominant Zn (002) peak, indicating a wurtzite crystal structure. FESEM images confirmed a uniform distribution of grains with a granular surface morphology. The grain size of the Zn thin films increased with longer sputtering times on both substrates. Scherrer's equation was employed to calculate the grain size from the XRD patterns. Notably, the Zn thin film deposited on the n-type Si substrate for 10 minutes exhibited the most uniform morphology among all samples. The best result was the formation of ZnNPs on silicon substrate at 5 minute where the particle size was at a peak 9 nm.

Keywords: Nanoparticles; Physical vapor deposition; DC sputtering; Metal NPs/Si
Received: 04 April 2024; **Revised:** 25 April 2024; **Accepted:** 01 May 2024

1. Introduction

Nanomaterials (1-100nm) exhibit distinct characteristics compared to the same material in bulk form to enable them to be used in different fields such as medicine, electronics, energy and environment [1]. Advancements in nanotechnology allow for the complete alteration of chemical as well as physical properties, along with nanoparticles surface-to-volume ratios [2]. This field enables the production of a diverse array of nanoparticles with unique spatial characteristics, facilitating their utilization across various applications and scientific research domains [3]. Zinc nanoparticles (ZnNPs) could be categorized based on the chemical structure into metallic, metal oxides, and semiconductor nanoparticles, zinc metal nanoparticles are good conductors and zinc semiconductors can be used for solar cell applications [4]. Various methods offer control over the structure and size of nanoparticles. While all methods can yield satisfactory nanoparticles, continuous improvement in procedures is essential for enhancing production efficiency and yield, particularly for industrial and commercial applications [5-7]. Deposition of metal thin films onto different substrates, including glass and silicon can be achieved using many techniques such as molecular beam epitaxy, [8], electroplating [9], spray pyrolysis [10], Pulsed Laser Ablation [11], physical vapor deposition (VPD) [12], magnetron, ion beam and DC sputtering [13]. This work aimed to investigate the structural characteristics and surface morphology of zinc thin films placed on two distinct substrates: glass and Si n-type.

2. Experimental Part

Figure (1) illustrates the home-made dc sputtering system schematic diagram. Two types of substrates (glass and n-type Si (111)) were inserted on the anode inside the deposition chamber, Si with resistivity ranging from 5 to 40 Ω.cm and a thickness of 0.45 mm. The dimensions of these substrates were 1x1 cm, after a cleaning process they have being subjected to ethanol in a digital ultrasonic cleaner for fifteen minutes.

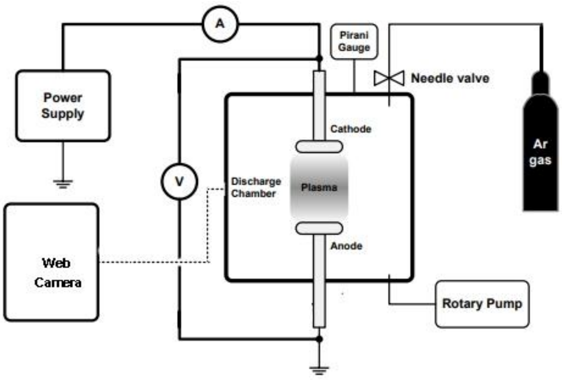

Fig. (1) Schematic diagram of DC sputtering system

A zinc target with 5cm diameter and a 5mm thickness was placed on the sputtering chamber's cathode. Using glow discharge, argon gas in the deposition chamber has been used to create plasma at a flow velocity of 500 sccm and a maximum pressure of 1.5 mbar. The tube discharged to a vacuum below 10^{-2} Torr using a rotary pump and a discharge current of 15 mA. Deposition times of 5 and 10 min were used to achieve various Zn thin film thicknesses, and 30 min were used for the analysis of x-ray diffraction (XRD) patterns obtained using a Phillips Xpert x-ray diffractometer (λ=1.54056Å). A MIRA3 TESCAN field-emission scanning electron microscope (FE-SEM) was used to introduce the structural properties of the prepared thin films.

3. Results and Discussion

The XRD patterns are presented in Fig. (2) in the scanning range of 10°-80°. For zinc thin films on glass substrates, the XRD peak is observed at approximately $2\theta=36°$ along the (002) plane. Conversely, for zinc thin films on n-type Si substrates, peaks appear at angles approximately 38°, 54°, and 75° corresponding to the (002), (102), and (004) planes, respectively. Figure (2b) displays the polycrystalline and hexagonal wurtzite structures of the prepared thin films [14]. According to this figure, it's clear that all thin films have maximum intensity along the (002) plane which is the preferred plane for the growth of Zn thin films. Figure (2) clearly shows the influence of substrate type on the XRD pattern of Zn thin film. Thin film growth on Si n-type substrate has larger grain size than that of film deposited on glass substrate. The thin film parameters derived from the XRD results are summarized in table (1).

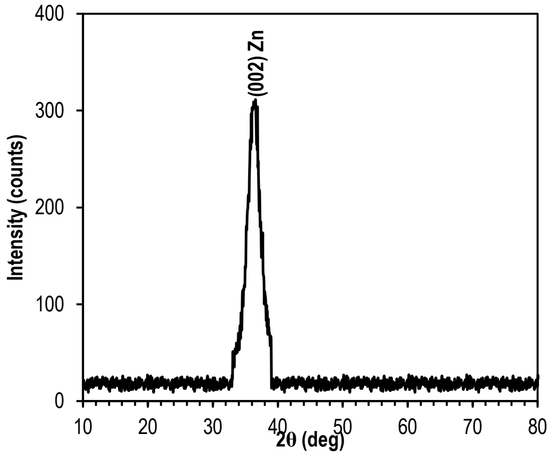

(a)

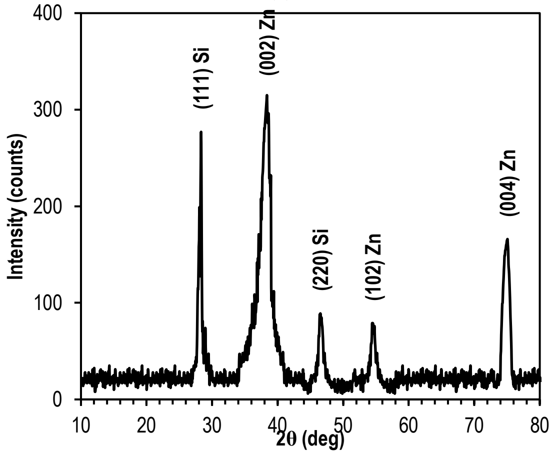

(b)

Fig. (2) XRD patterns of Zn nanoparticles on (a) glass, (b) Si (n-type)

Scherrer's equation has been utilized to obtain the grain size (x) within zinc thin film as

$$x = K.\frac{\lambda}{\beta.cos\theta} \qquad (1)$$

In this equation, the average grain shape factor represented by K (0.9), the x-ray wavelength (0.154056nm) denoted by λ, the full-width at half maximum (FWHM) of the peak diffraction signified by β in rad, and the diffraction peak angle represented by θ. Equation (2) emphasizes an inverse relationship between the grain size of nanoparticles and the FWHM of the diffraction peak. As the grain size increases, there will be sharpness in the diffraction peak.

Table (1) Zinc thin film parameters obtained from XRD measurements

Substrate type	(hkl)	2θ (deg)	FWHM (β) (rad)	x (nm) =0.9λ/βcosθ	$\delta=1/x^2$ (cm^{-2})
Glass	(002)	36.025	0.046	3.16	1.00E+13
Si n-type	(002)	38.275	0.035	4.23	5.59E+12
	(102)	54.425	0.011	14.64	4.67E+11
	(004)	74.725	0.017	10.06	9.88E+11

The density of dislocation (δ), indicating the dislocation length per unit volume of the crystal, could be calculated using the equation below:

$$\delta= 1/x^2 \qquad (2)$$

Surface morphology was studied depending on FE-SEM results. Figure (3) depicts a consistent and distinguishable granular surface morphology characterized by an identical distribution of the ZnNPs synthesized in this investigation. The nanoparticles exhibit uniform dispersion across the entirety of the substrate's surface. However, for samples prepared after 10 minutes of sputtering, the surfaces of both glass and silicon (Si) could not be observed.

Figure (4) illustrates the energy-dispersive x-ray (EDX) spectroscopy analysis of zinc nanoparticles synthesized after different sputtering times on different substrates. These data indicate that the EDX spectra of elements is largely similar with differing element weights according to the variation in sputtering time. Specifically, for ZnNPs deposited on glass substrates, about 23.6% and 30.2% of the total weight zinc consisted in the resulted nanoparticles after 5 and 10 minutes, respectively. Conversely, for ZnNPs deposited on n-type Si substrates, about 27.6% and 34.8% of the weight was attributed to zinc.

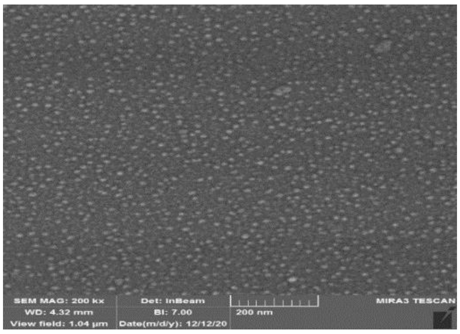

(a)

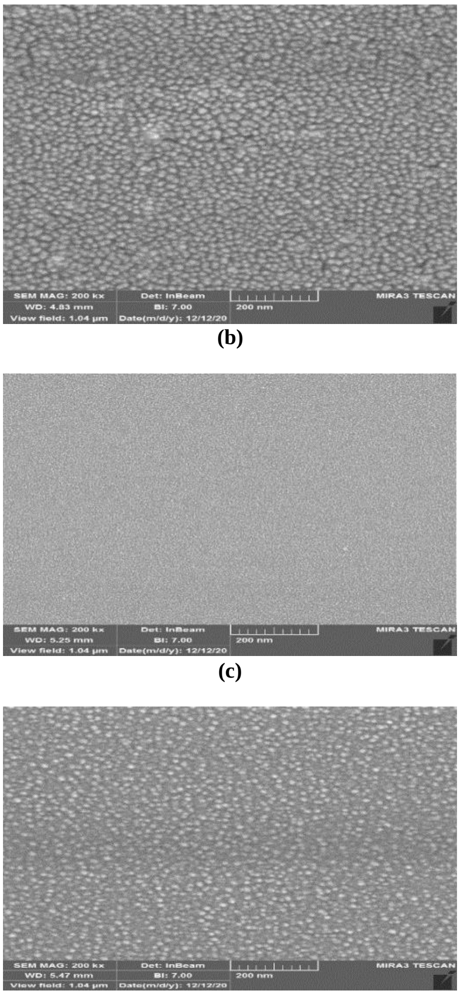

(b)

(c)

(d)

Fig. (3) SEM images of Zn nanoparticles (a), (b) glass (c), (d) Si (n-type) at 5 and 10 minutes, respectively

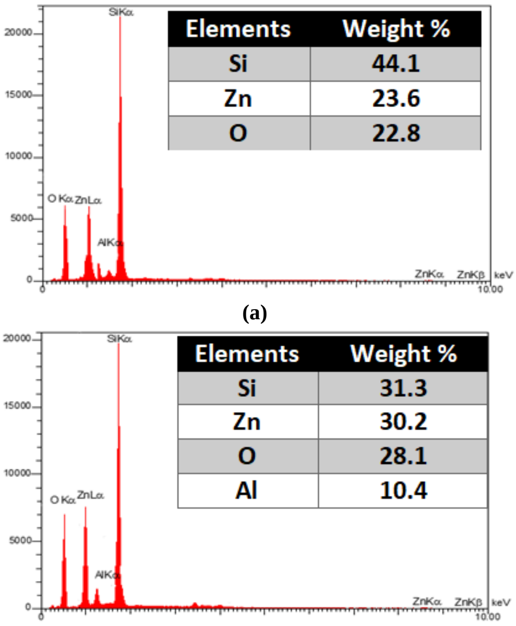

Elements	Weight %
Si	44.1
Zn	23.6
O	22.8

(a)

Elements	Weight %
Si	31.3
Zn	30.2
O	28.1
Al	10.4

(b)

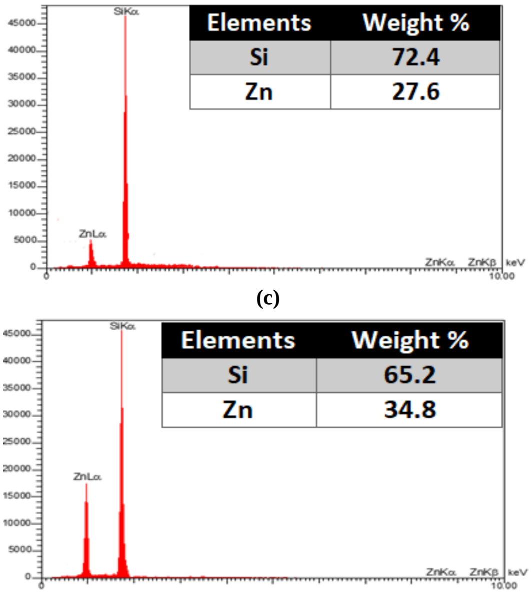

Elements	Weight %
Si	72.4
Zn	27.6

(c)

Elements	Weight %
Si	65.2
Zn	34.8

(d)

Fig. (4) EDX results at 5 and 10 minutes of (a), (b) Zn NPs on glass and (c), (d) Zn NPs on Si (n-type)

The histogram of zinc deposition on glass at 5 minutes (Fig. 5a) reveals a range of 2-18 nm, with a peak at 11 nm. Extending the deposition time to 10 minutes (Fig. 5b) leads to ZnNPs ranging from 6 to 28 nm, with a peak at 13 nm. On silicon substrate at 5 minutes (Fig. 5c), ZnNPs sizes vary from 2 to 11 nm, with a peak at 9 nm. At 10 minutes (Fig. 5d), ZnNPs sizes range from 4 to 19 nm, with a peak at 10 nm.

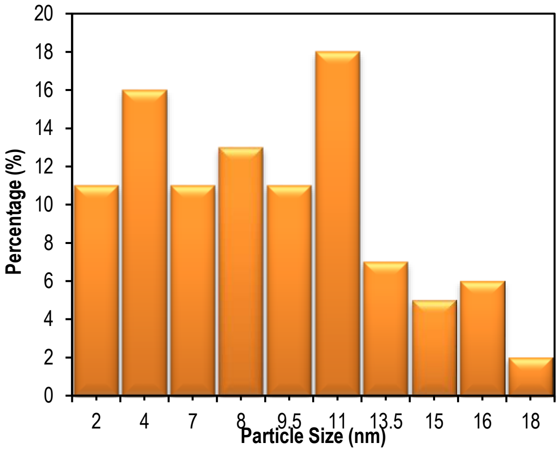

(a)

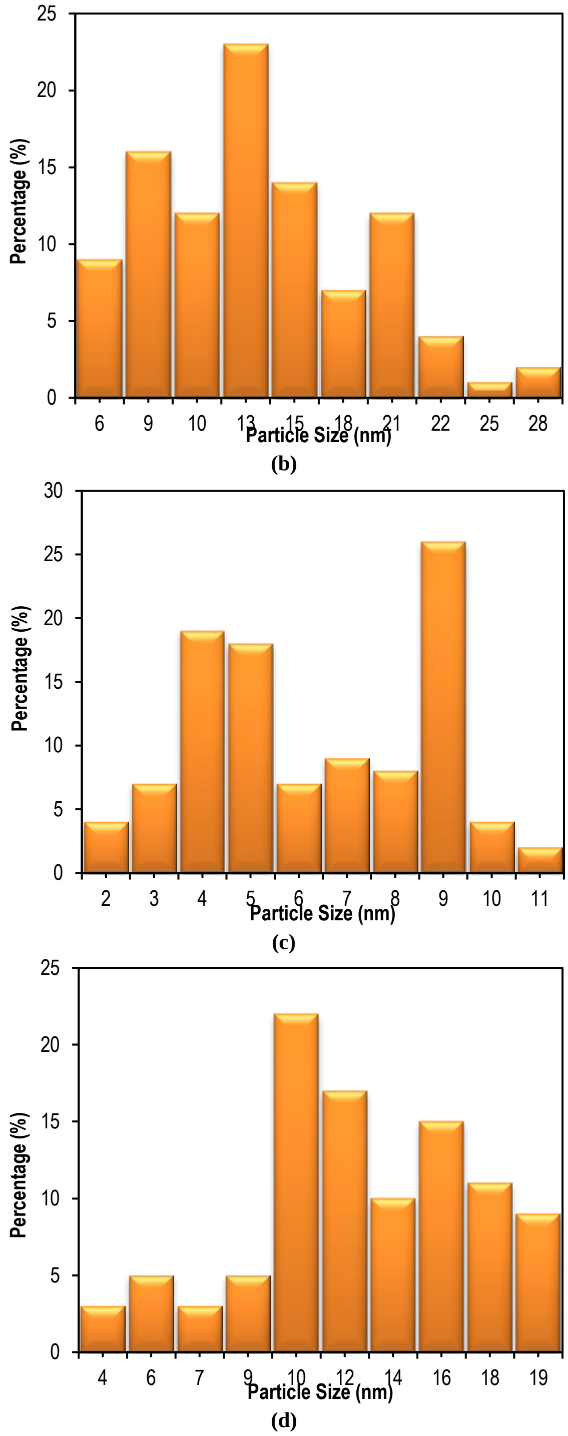

Fig. (5) Histogram at 5 and 10 minutes of (a), (b) Zn NPs on glass and (c), (d) Zn NPs on Si (n-type)

4. Conclusion

This study examines the influence of substrate type and sputtering time on Zn thin film deposition using dc sputtering. The results show a positive correlation between sputtering time and Zn thin film thickness. The successful formation of Zn with a wurtzite structure on both n-Si (111) and glass substrates was confirmed. The ZnNPs deposited on the n-type Si substrate had a larger grain size those deposited on glass. When Zn thin films are deposited on Si or glass substrates, a granular surface forms. The produced thin films have a standard orientation along the (002) plane and a polycrystalline nature with a hexagonal wurtzite structure.

References

[1] A.T. Saleh, "Nanomaterials: Classification, Properties, and Environmental toxicities", *J. Enviro. Technol. Innov.*, 20 (2020) 101067.

[2] P. Szczyglewska, A. Feliczak-Guzik and I. Nowak, "Nanotechnology–General Aspects: A Chemical Reduction Approach to the Synthesis of Nanoparticles", *Molecules*, 28 (2023) 4932.

[3] M. Mohammed et al., "Accurate Synthesis and Performance of SERS Sensing of Au/Ag Nanocomposites Site-Deposited on Apple Surfaces", *Plasmonics*, 18 (2023) 1-6.

[4] I. Khan, K. Saeed and I. Khan, "Nanoparticles: Properties, applications and toxicities", *Arab. J. Chem.*, 12 (2019) 908-931.

[5] G. Dutta and A. Sugumaran, "Bioengineered zinc oxide nanoparticles: Chemical, green, biological fabrication methods and its potential biomedical applications", *J. Drug Deliv. Sci. Technol.*, 66 *(*2021) 1773-2247.

[6] I.H. Hadi, K.I. Hassoon and M.F. Jawad, "Well-modifying the optical properties of bare Si solar cell by incorporating CuNPs", *Opt. Quant. Electron.*, 54 (2022) 629.

[7] K. Altammar, "A review on nanoparticles: characteristics, synthesis, applications, and challenges", *Front. Microbiol.*, 14 (2023)1155622.

[8] H. Mohamed, "Properties and applications of quantum dot heterostructures grown by molecular beam epitaxy", *Nanoscale Res. Lett.*, 1 (2006) 32-45.

[9] Q. Chen, "Electrodeposition of epitaxial metal thin films on silicon for energy conversion and flexible electronics", PhD thesis, Missouri University of Science and Technology (2019).

[10] P. Dainius and G. Ludwig, "Thin Film Deposition Using Spray Pyrolysis", *J. Electroceram.*, 14 (2005) 103-111.

[11] B.A. Bader et al., "Photodetector Based on Titanium Oxide Nanoparticles Produced via Pulsed Laser Ablation", *Adv. Cond. Matter Phys.*, 2022 (2022) 8066167.

[12] S. Doaa, M. Alwan and K. Walid, "Enhanced pesticides' limit of detection using bimetallic alloys nanoparticles", *J. Mater. Sci. Mater. Electron.*, 32 (2021) 18689-18698.

[13] I.H. Hadi, K.I. Hassoon and M.F. Jawad, "Characterization of Copper Nanostructures Prepared by DC Sputtering on Various Substrates", 1st Samarra Int. Conf., AIP Conf. Proc., 2394 (2022) 090015.

[14] J. Bhavana et al., "Effect of zinc acetate concentration on structural, optical and electrical properties of ZnO thin films deposited by electrostatic spray on ITO substrate", *J. Electrochem. Soc.*, 159 (2012) 716-721.

Uranium Concentrations Investigation in the chicken and their parts samples Using CR-39 detector in Nineveh Province, Iraq

Hanaa N. Azeez [1]
Azhaar A. Ali [2]
Malik H. Kheder [1]

[1] *Department of Physics, College of Education for Pure Sciences, University of Al-Hamdaniya, Al-Hamdaniya, IRAQ*
[2] *Department of Fuel and Energy, College of Oil and Gas Techniques Engineering, North Technical University, Kirkuk, IRAQ*

Chicken meat producers in Nineveh Province are in great demand for both organic and inorganic feeds that promote faster growth in chickens. Concerns over the quality of chicken meat and the potential for cancer and other biological consequences of radiation on consumers of chicken products are brought up by competition in the chicken producing industry. This study focused to determining the uranium concentrations in chicken meat and bones. Radiological risk parameters need to be determined in order to check the health risks to consumers of chicken products. The obtained mean radon concentrations were 44. 9565 Bq.m^{-3} which is below the world limit level of 100 Bq.m^{-3}. The mean uranium concentrations in were 8.53243 µg Kg^{-1}. The mean uranium activity concentrations value is 1.0529 Bq kg^{-1} which it's below the world average of 35 Bq kg^{-1}. The results indicates that the risk of increased uranium intake from chicken meat is almost very low so the studied area is safe.

Keywords: Radon concentration; Chicken; Chicken bones; Uranium concentration
Received: 04 April 2024; **Revised:** 21 April 2024; **Accepted:** 28 April 2024

1. Introduction

One of the staple foods for human consumption is considered to be chicken meat worldwide [1]. Understanding uranium products' dispersion and toxicity to humans and animals is beneficial, as there is an increase in uranium products that can be eaten or inhaled that contain uranium oxides [2,3] and its capacity to infiltrate the food chain for humans. One of the main ways that uranium enters the food chain and contaminates animals is by eating it in their food, water, or soil [4]. Water tainted with uranium is the primary factor affecting the amount of uranium activity in chicken meat [5]. A combination of organic and inorganic substances are used to make chicken feed [6], instead of naturally occurring technologically enhanced radioactive materials (TENORMs), which could increase the amount of radionuclides in chicken feed, meat, and bones [7]. Plants are more likely to absorb radionuclides when fertilizers and agrochemicals are used in farming, which creates a pathway for radiation exposure to plants, chicken feed, and chicken products [8,9]. Phosphate fertilizers and other inorganic materials include TENORM, while organic substances contain NORM [10,11]. Chicken is exposed to radioactive elements by the NORM and TENORM components. Moreover, living things are put in danger when NORM is present in the environment at activity concentrations above the radiological reference limits set by the United Nations Scientific Committee on the Effects of Atomic Radiation (UNSCEAR) [12]. Due to the widespread distribution of radioactivity in the earth's environment, the planet is constantly exposed to radiation, primarily from man-made and natural sources [13,14]. The natural radioactivity of uranium and its offspring exposes people to biological consequences of radiation and cancer [15]. Roughly, 30% of cancer cases worldwide are caused by nutrition [16]. Urbanization and dietary changes have been identified as the main drivers of the general increase in cancer risk. As a result, dietary changes in lifestyle might cause the percentage to grow or decline [17].

The goal of this study was to measure the amounts of uranium and radon in typical chicken parts including meat and bones.

2. Experimental Part

Samples of fresh chicken flesh were collected from farms, after which the birds were slaughtered, feathered out, and given a water bath. For bone samples, fresh chicken meat pieces were boiled for 1 hour at 100°C to separate the bones from meat. Each sample of chicken was oven dried meat at 100°C for 2 hours, and bones at 200°C for 1 hour. After cooling, each sample was grinded into powder, and sieved. Each sample of feeds, meat and bones was then put in plastic can. The measurements of the CR-39 detector are made using a plastic can radon dosimeter (7 cm in diameter and 10 cm in length). The detector is put on the bottom of the dosimeter cover and is used to measure the radon concentration of the samples, as shown in (Fig. 1).

Samples with a volume of 115.4x10^{-6} m^3 and a height of 3 cm were placed in the dosimeter; the distance from the samples and the detector surface was 7 cm. The samples were kept in the plastic can for duration of 60 days exposure period. The detectors were taken out of the dosimeter and etched chemically in a 6.25N of NaOH solution at 70°C for seven hours. Utilizing a 400X optical microscope, the tracks were counted.

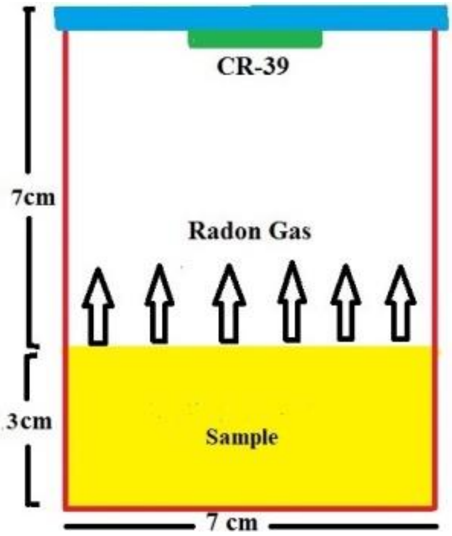

Fig. (1) The radon dosimeter

The radon concentration in the air volume within the container, as determined by the equation [18].

$$C_{Rn=}\rho[KT]^{-1} \quad (1)$$

where T is the exposure period, ρ is the track density, K (=0.05916 Tr/cm^2.d/Bq/m^3) is the radon dosimeter utilized in this study's CR-39 detector calibration factor [19]

Radon concentrations in samples determined using the formula [20]

$$C_S = \lambda_{Rn} C_{Rn} HT[l]^{-1} \quad (2)$$

where C_{Rn} is the air space radon concentration (Bq/m^3), C_S is the samples radon concentration (Bq/m^3), and λ_{Rn} is the radon decay constant (0.1814 day^{-1}), T stands for exposure time (60 days), H is for height of air gap in the plastic can (7 cm), and l stands for sample thickness (3 cm)

The uranium contents were calculated from the secular activity equilibrium of uranium and its daughters and the concentration of radon measured with the CR-39 detector. The activity of radon A_{Rn} in the sample may be calculated thanks to the correlation between C_{Rn} and the amount of radon in the sample [21].

$$A_{Rn} = C_{Rn} V \quad (3)$$

The volume of samples is ($V=\pi r^2 L$) =115.4X10^{-6} m^3, its thickness is 0.03 m, and its radon dosimeter radius is 0.035 m.

$$\lambda_{Rn} N_{Rn} = A_{Rn} \quad (4)$$

The equation of the equilibrium of uranium with its daughter (the uranium activity equals the radon activity) was used to compute the number of atoms of uranium (N_U) in the samples [22].

$$\lambda_U N_U = \lambda_{Rn} N_{Rn} \quad (5)$$

In this case, the uranium decay constant is λ_U (=4.883x$10^{-18}s^{-1}$). The uranium atom number N_U was then used to compute the uranium weight in samples using the equation

$$W_U = \frac{N_U a_U}{N_{avo.}} \quad (6)$$

where W_U is measured in micrograms (µg), N_{avo} (6.02x10^{23} atom/Mol) is the number of Avogadro, and a_U is the uranium mass number 238. Uranium content is determined by [23]

$$C_U = \frac{W_U}{W_S} \quad (7)$$

Here, C_U represents the uranium concentration in (µg/g or ppm) units, and W_S equal to 125g

Uranium activity concentration is determined in unit of Bq/kg, in the form

$$Ac = \lambda_U N_{avo.}[At_U]^{-1} C_U \quad (8)$$

3. Results and Discussion

The study's average value of five farms' samples are listed in table (1). That includes the concentration of radon in samples C_{Rn} in units of Bq.m^{-3}, uranium concentrations in the samples C_U in ppm, and the uranium concentrations in the samples C_U in µg/kg and uranium activity concentration A_C in Bq/kg (Fig. 2).

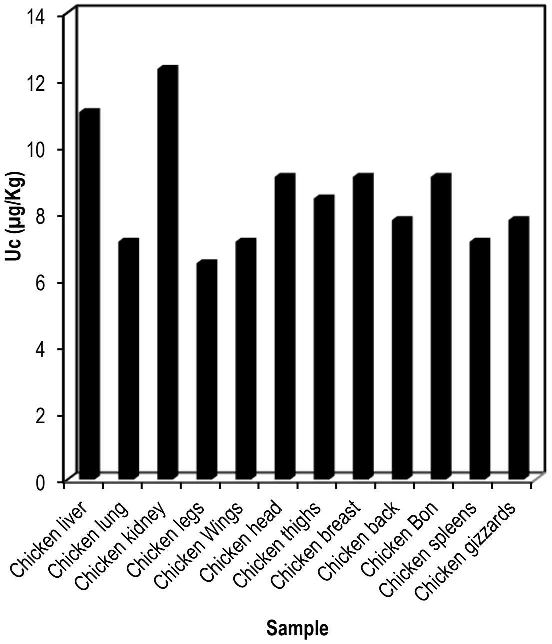

Fig. (2) Uranium concentrations (µg/kg) in the samples

The uranium content of chicken liver and kidney is higher than that of other chicken organs were the values are 12.312, and 11.0165 µg/kg respectively. Radionuclides from consuming water and other inorganic additives could be the cause of this. The chicken legs' low level of uranium content its value was 6.480 µg/kg. The mean uranium activity concentrations value is 1.0529 Bq/kg which it's below the world average of 35 Bq/kg [12]. Uranium can be readily absorbed by plants that are also used to raise chickens. Plant absorption is more influenced by the concentration of radionuclides in soil solutions than by their total concentrations [24]. The industrial methods used to make feeds and other human activities may be the cause of the high concentration of uranium found in feeds [25]. The findings demonstrated that eating chicken posed no dangers in the area under investigation.

4. Conclusion

Measuring uranium activity and concentration in chicken meat, bone, and other sections has been done. All of the samples were safe for ingestion by humans since their uranium activity contents were below the global average limit. According to the findings, eating chicken poses no dangers in the area under investigation.

References

[1] M.B. Allabaksh et al., "Assessment of Heavy Metal Content of Hen Eggs In The Surroundings of Uranium Mining Area, India Annals", *Food Sci. Technol.*, 14(2) (2013) 344-349.

[2] K.M. Muhannad, "Risk Assessment Related to Contamination of Terrestrial Food Chains by Atmospherically Deposited Lead particles", *Al-Mustansiriyiah J. Sci.*, 21(3) (2010) 103-116.

[3] N.H. Rasheed, "The Spatial Distribution for The Radiation Pollution in Iraq", *J. Res. Diyala Human.*, 57 (2013) 729-763.

[4] International Atomic Energy Agency (IAEA), **"Handbook of Parameter Values for the Prediction of Radionuclide Transfer in Terrestrial and Freshwater Environments"**, Tech. Rep. Ser., 472 (2010) 194.

[5] M. Jeambrun et al., "Study on Transfers of Uranium, Thorium and Decay Products from Grain, Water and Soil to Chicken Meat and Egg Contents", *J. Enviro. Monit.*, 14 (2012) 2170-2180.

[6] I. Mabe et al., "Supplementation of a Corn-soybean Meal Diet with Manganese, Copper, and Zinc from Organic or Inorganic Sources Improves Eggshell Quality in Aged Laying Hens", *Poultry Sci.*, 82 (2003) 1903-1913.

[7] Jr. Kennedy, **"Naturally occurring radioactive material (NORM V): Proceedings of An International Symposium"**, Sevilla, Spain (2007).

[8] A.A. Alao, "Assessment of NORM Containing Food Crops or Stuffs in OML 58 & OML 61 within the Niger Delta Region of Nigeria", in 1st Int. Technol. Edu. Enviro. Conf., 104 (2011).

[9] IAEA, "Naturally Occurring Radioactive Material (NORM VIII)", Proc. Int. Symp., Rio de Janeiro, Brazil (2016). Published by The International Atomic Energy Agency (2018).

[10] M. Atipo, O. Olarinoye and B. Awojoyogbe, "Comparative Analysis of NORM Concentration in Mineral Soils and Tailings from a Tin-mine in Nigeria", *Enviro. Earth Sci.*, 79 (2020) 1-17.

[11] B. Heaton and J. Lambley, "TENORM in the Oil, Gas and Mineral Mining Industry", *Appl. Rad. Isotop.*, 46 (1995) 577-581.

[12] United Nations Scientific Committee on the Effects of Atomic Radiation (UNSCEAR), **"Sources and Effects of Ionizing Radiation"**, *Technical Reports*, (2000).

[13] United Nations Scientific Committee on the Effects of Atomic Radiation (UNSCEAR), *Technical Reports*, (2008).

[14] V. Habakwiha, B. Orur and W. Tumps Ireeta, "Estimation of Radiological Effects from Consumption of milk from Volcanic Areas of Kisoro, South-western Uganda", *J. Rad. Nucl. Appl.*, 8(1) (2023) 81-91.

[15] W. Aguko, R. Kinyua and R. Ongeri, "Radiation Exposure Levels Associated with Gold Mining in Sakwa Wagusu Area, Bondo District, Kenya", *J. Phys. Sci. Innov.*, 5(1) (2013) 59-74.

[16] T.J. Key et al., "Diet, Nutrition and the Prevention of Cancer", *Pub. Health Nutr.*, 7 (2004)187-200.

[17] P. Bukirwa et al., "Trends in the Incidence of Cancer in Kampala, Uganda, 1991 to 2015", *Int. J. Cancer*, 148 (2021) 2129-2138.

[18] B. Al-bataina et al., "Radon measurements in different types of natural waters in Jordan", *Rad. Measur.*, 28(1-6) (1997) 591-94.

[19] M.H. Kheder et al., "Radioactivity concentrations in barley and wheat crops in Nineveh plain region in Iraq", *Int. J. Nucl. Ener. Sci. Technol.*, 14(1) (2020) 50-60.

[20] M.H. Kheder, H.N. Azeez and F.M. Al-Jomaily, "Alpha emitters radioactivity concentrations in some cosmetics used in Iraq using LR-115 detector", *J. Eureka Phys. Eng.*, 2 (2020) 65-70.

[21] H. Cember and T.E. Johnson, "**Introduction to health physics**", 4th ed., McGraw-Hill (2009).

[22] M.H. Kheder, "Radium and Uranium Concentrations in Some Fruits and Vegetables Cultivated in Nineveh Governorate, Iraq", *Iraqi J. Appl. Phys.*, 19(3B) (2023) 15-19.

[23] M.H. Kheder, H.N. Azeez and M.A. Al-Jubbori, “Measurement of Uranium and Radon Concentrations in Wells Water Samples of Some Farms near the Mosul City in Iraq”, *Iraqi J. Appl. Phys.*, 19(3B) (2023) 3-8.

[24] S. Sheppard, and W. Evenden, “Critical Compilation and Review of Plant/Soil Concentration Ratios for Uranium, Thorium and Lead”, *J. Enviro. Radioact.*, 8 (1988) 255-285.

[25] D. Cicchella et al., **“Natural Radioactive elements U, Th and K in European Soil; in Chemistry of Europe's Agricultural Soils”**, C. Reimann, M. Birke, A. Demetriades, P. Filzmoser and P. O'Connor (eds.) (2014).

Table (1) The radon concentrations, uranium concentrations in ppm, and in µg/Kg.

No	**Sample**	**C_{Rn} (Bq.m^{-3})**	**C_U (ppm)**	**C_U (µg/Kg)**	**A_C BqKg^{-1}**
S1	Chicken liver	58.04524	0.011017	11.01656	1.360546
S2	Chicken lung	37.55869	0.007128	7.128365	0.880353
S3	Chicken kidney	64.87409	0.012313	12.31263	1.52061
S4	Chicken legs	34.14426	0.00648	6.480332	0.800321
S5	Chicken Wings	37.55869	0.007128	7.128365	0.880353
S6	Chicken head	47.80196	0.009072	9.072464	1.120449
S7	Chicken thighs	44.38754	0.008424	8.424431	1.040417
S8	Chicken breast	47.80196	0.009072	9.072464	1.120449
S9	Chicken back	40.97311	0.007776	7.776398	0.960385
S10	Chicken Bon	47.80196	0.009072	9.072464	1.120449
S11	Chicken spleens	37.55869	0.007128	7.128365	0.880353
S12	Chicken gizzards	40.97311	0.007776	7.776398	0.960385
	Min	34.14426	0.00648	6.480332	0.800321
	Max	64.87409	0.012313	12.31263	1.52061
	Mean	**44. 9565**	**0.0085324**	**8.53243**	**1.05291**

IRAQI JOURNAL OF APPLIED PHYSICS Vol. 20, No. 3, July-September 2024, pp. 557-560

Islam N. Yousif
Malak J. Ali
Ismael T. Tlayea

Department of Physics,
College of Education for
Pure Science,
University of Al-Hamdaniya,
Nineveh, IRAQ

Study the Effect of Etching Time on the Morphology of Porous Silicon Surfaces Manufactured via Photochemical Etching

Given the importance of silicon nanocrystals in many applications of microelectronics, energy storage, and biomedicine, porous silicon was prepared from a n-type silicon wafer with a crystal orientation (100), negative conductivity, and low resistance (4.3 x 10^-4 ohm*cm) by photochemical etching technique in the presence of a halogen lamp (1000 W) and concentrated hydrofluoric acid (HF 40%). The effect of changing the etching time (70 minutes, 80 minutes, and 90 minutes) on the morphology of their surfaces was studied, and the results of atomic force microscopy (AFM) showed the formation of porous layers (392.8 nm, 491.3 nm, and 566.3 nm) and average diameters of the grains and nanoparticles (101.4 nm, 106.9 nm, and 44.85 nm) respectively. The results indicated that the surface roughness and thickness of the porous layer of the samples prepared increases when the etching time increases and decreases when the etching time decreases.

Keywords: Porous Silicon; Etching Time; Photochemical Etching; Nanoparticles
Received: 04 April 2024; **Revised:** 25 April 2024; **Accepted:** 01 May 2024

1. Introduction

The importance of silicon nanofabrication technology has emerged through the great efforts that have been made to organize the structures of atoms and the compositions of materials that fall within the nanoscale [1], in order to benefit from them in many laser [2] and optoelectronic applications [3], in addition to their nanoscale optical properties [4], which led to the appearance of a quantum confinement effect on its crystals through the movement of electrons and holes on its surfaces inside the crystal [5], which in turn led to an increase in its efficiency of electrical conduction, and the effectiveness of its light radiation resulting from the processes of controlling its wavelengths [6].

Through the multiple modifications made by researchers to the properties to develop silicon to produce optical and electronic properties completely different from the properties of the parent silicon material, what is called porous silicon appeared [7], which is forked and complex networks of isolated pores that are separated from each other by thin walls [8]. As a result of material reduction and miniaturization processes that lead to very small dimensions and sizes, we have the formation of nanoporous silicon [9].

The formation of porous silicon has given new dimensions to technologies based on crystalline silicon [10], as it has become of wide and great interest as a result of the changes and transformations that occur in the nature of its indirect energy gap, which turns into an energy gap direct, leading to improving the efficiency of its photoluminescence [11]. Enlarging the energy gap brings about changes in the resistance of the material, that increases with a decrease in the size and dimensions of the pores [12], in addition to the depletion processes of charge carriers accompanying the preparation process [13].

There are many techniques for preparing porous silicon, such as electrochemical etching [14], photoelectrochemical etching [15], spot etching [16], and photochemical etching technique using different light sources, such as using types of lasers or using spherical or flat halogen lamps [17-19]. It is possible to control its porosity and atomic dimensions [20,21], in order to work in a wide range of the electromagnetic spectrum which extends from infrared to the entire visible spectrum and even near ultraviolet [22-25].

We will show in this article the extent of time effect on the morphology of the porous surface of silicon produced through the process of preparation by the photochemical method, relying on a halogen lamp as one of the light sources to melt random areas of the silicone surface that determined through the atomic force microscope (AFM). Thus improving its properties and developing it to benefit from it more widely in applications of integrated circuits and electronic devices.

2. Experimental Part

The experiment is carried out on a single-sided n-type silicon chip whose surfaces are completely polished, with a resistivity of 4.3×10^{-4} Ω.cm and a crystalline orientation of (100), so the slice is cut into dimensions of 0.7x0.5 cm to be prepared for preparing porous silicon samples through using the photochemical etching system.

The samples are washed in diluted hydrofluoric acid (HF 10%) for 8 minutes to remove the layers of oxide stuck on it. Then, the samples are immersed in acetone and ethanol for 6 minutes to wash and clean them of the impurities stuck on them and to remove the remaining diluted hydrofluoric acid (HF 10%) from their surfaces. The samples are then left to dry.

The preparation system consists of a Teflon container, which is a solid polymeric material characterized by its high resistance to acids. The diameter of the container ranges 5.5 cm, its height is 3.5 cm, and the drilling depth from the inside is 1.5 cm. In the middle of container from the inside is a circular protrusion with a diameter of 1.5 cm, and the height of the protrusion ranges 0.7 cm from the surface of the drilling depth. The circular protrusion contains a support engraved in its face in the shape of the letter (U) to place the sample on it, while the Teflon container is filled with hydrofluoric acid (HF 40%) and the sample to be prepared is placed on the support so that it is covered by the HF solution, and a halogen lamp is shined (1000 W) on it vertically.

Silicon samples are prepared with variable etching times (70, 80, and 90 min) and constant resistivity (4.3×10^{-4} Ω.cm) as well as constant concentration of HF (40%) using light source (halogen lamp 1000 W). This ensures that the process of etching, dissolving, and formation of pores has occurred on the upper surface of the sample facing the light source, by observing the appearance of hydrogen bubbles on the surface of the sample resulting from chemical reactions leading to the dissolution of the silicon, or through the change in the color of its surface approaching the reddish-brown color that indicates the formation of the porous layer [26,27].

After the etching process is completed, we lift the sample with iron tweeze and place it in a tightly closed plastic container filled with methanol to prevent oxidation and preserve its properties.

The fine details of the surface morphology and the structures of the nanoparticles formed on the surface of the prepared samples are studied through an atomic force microscope (AFM) for the purpose of analyzing them and knowing the nanostructure of the porous layer, its thickness range, and roughness rate of its surface and particle sizes.

3. Results and Discussion

The process of decomposition of silicon molecules takes place as a result of the rapid exchange of silicon-fluoride bonds Si-F, which interact with water molecules H_2O, when placed in a dilute HF acid solution to form strong and stable covalent bonds. As a result, dense groups of silicon-hydroxyl bonds Si-OH, are formed that lead to formation of bridges and stable structures from Si-O-Si bonding to reveal oxide nuclei [28,29].

The precise dissolving mechanism of silicon occurs through the presence of important gaps for electronic polishing and etching to occur. When samples are immersed in a concentrated HF acid solution at different etching times (70, 80, and 90 min), porous layers of nanoporous silicon are formed, which is shown by 3D imaging of the morphology of silicon surfaces through the AFM examination shown in Fig. (1), where the silicon surface is saturated with hydrogen.

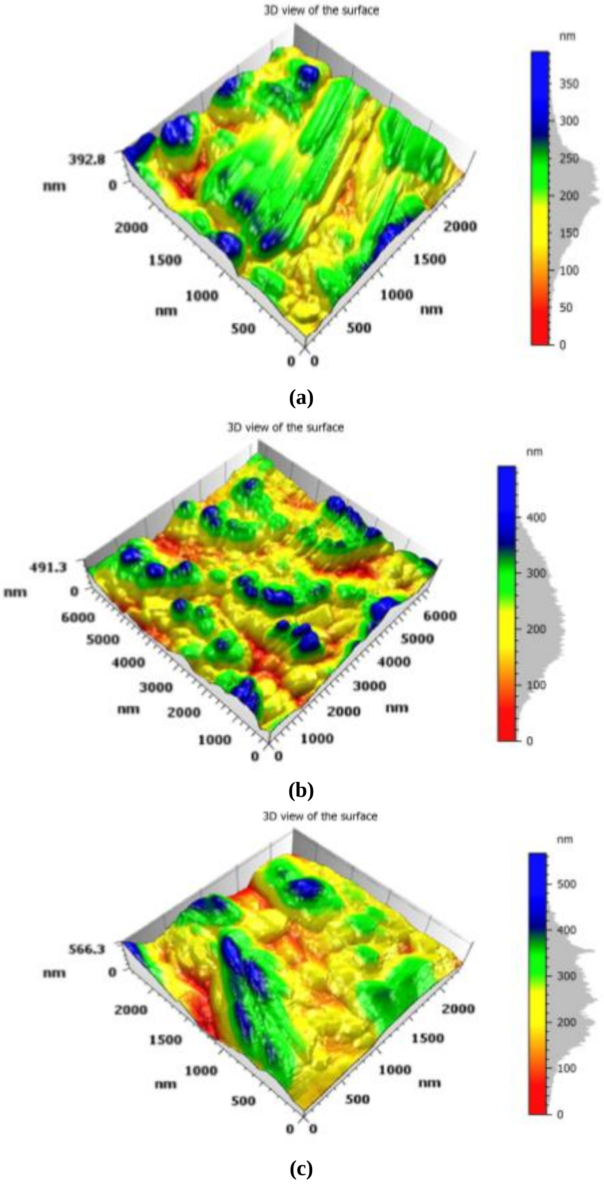

(a)

(b)

(c)

Fig. (1) 3D AFM examination of the morphology of silicon surfaces prepared at different etching times: (a) 70 min, (b) 80 min, and (c) 90 min

As soon as the surface is illuminated by the light of the source directed at it, it will begin to generate electron-gap pairs as a result of the absorption of light inside the chip, which in turn helps in the formation of the depletion layer in the illuminated area that It removes the silicon atom from its surface, leaving behind a hole or freckle to change the surface geometry and distribution of the electric field, which causes irregularities in its surface and the formation of holes [30,31].

The thickness of the porous layer and the average roughness surface of the prepared samples increase as the etching time increases and decrease when the etching time decreases, which leads to an increase in the root mean square (RMS) roughness, and shows the surface shape of the sample in the form of a semi-squishy structure and they are separated from each other by empty pore grooves and contain structures with pointed heads as shown in Fig. (1). This is a result of agglomerations of nanoparticles due to the continuation of etching processes, which leads to a change in the sizes and dimensions of the nanostructures of the prepared samples.

The surface kurtosis (S_{sk}) of the prepared samples shows a Gaussian distribution containing high peaks and low valleys that reflect the homogeneity of the surface skewness (S_{ku}) that gives a logarithmic distribution to show the differences of nanostructures in the distributions of surface heights.

Figure (2) shows the number of particles formed on the surface of the prepared sample due to the large transfer of positive charges accompanying the increase in etching time, which leads to a process of etching and gouging in multiple directions on the surface, sides and walls, and randomly, leading to an increase in the movement of the gaps and their numbers, and thus the production and formation of nanostructures particles of different compositions distributed with a certain homogeneity along the surface of the sample. The average diameters of the formed nanostructure are 101.4 nm, 106.9 nm, and 44.85 nm, which contributes to increasing the surface area, which in turn helps in increasing photovoltaic generation, enabling us to obtain spectral emissions within the visible region. These variables related to the distribution of the formed particles, the sizes of the surface pores, and the diameters of their nanostructures are used in many applications of nanotechnology, materials science, and micro-optoelectronics.

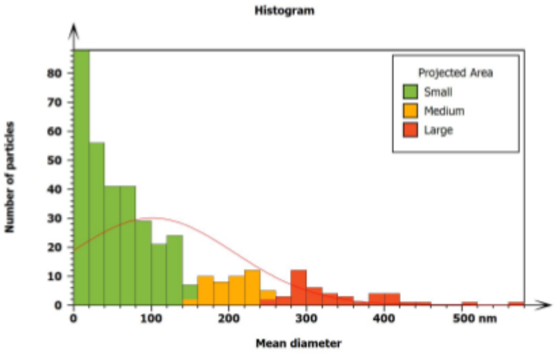

(a)

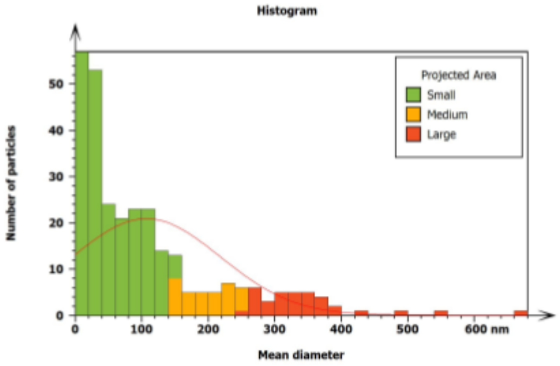

(b)

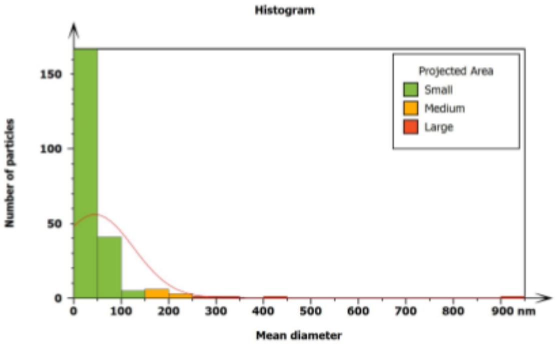

(c)

Fig. (2) Statistical distribution of the numbers of particles formed on the surfaces of the prepared samples with their mean diameters nanoscale at different etching times (a) 70 min, (b) 80 min, and (c) 90 min

4. Conclusion

Photochemical etching using a 1000W halogen lamp as the light source is an effective way to obtain porous silicon layers with multiple structures and properties. The results showed that increasing the etching time in the preparation processes when the concentration of hydrofluoric acid, the resistivity, and the light source are constant will lead to an increase in the sizes and diameters of the nanoparticles, which is useful in photodetectors, energy storage, and the manufacture of diodes.

References

[1] L. Meng et al., “A novel nanofabrication technique of silicon-based nanostructures”, *J. Nanoscale Res. Lett.*, 11 (2016) 1-9.

[2] S.M. Huang, Z. Sun and Y.F. Lu, “Nanofabrication by laser irradiation of polystyrene particle layers on silicon”, *J. Nanotech.*, 18(2) (2006) 025302.

[3] D. Wu et al., “Construction of high-quality CdS: Ga nanoribbon/silicon heterojunctions and their nano-optoelectronic applications”, *J. Nanotech.*, 22(40) (2011) 405201.

[4] S.H. Zaidi, C. An-Shyang and S.R.J. Brueck, “Optical properties of nanoscale, one-dimensional silicon grating structures”, *J. Appl. Phys.*, 80(12) (1996) 6997-7008.

[5] E.G. Barbagiovanni et al., “Quantum confinement in Si and Ge nanostructures:

Theory and experiment”, *J. Appl. Phys. Rev.*, 1(1) (2014) 011302.
[6] N. Koshida and M. Nobuo, “Fabrication and quantum properties of nanostructured silicon”, *J. Mater. Sci. Eng. R: Reports*, 40(5) (2003) 169-205.
[7] V. Torres-Costa and R.J. Martín-Palma, “Application of nanostructured porous silicon in the field of optics. A review”, *J. Mater. Sci.*, 45 (2010) 2823-2838.
[8] P. Granitzer and R. Klemens, “Porous silicon - a versatile host material”, *J. Mater.*, 3(2) (2010) 943-998.
[9] V.V.E. Starkov et al., “Nanoporous Layers and the Peculiarities of Their Local Formation on a Silicon Wafer”, *J. Processes*, 10(1) (2022) 163.
[10] L. Canham, “Routes of formation for porous silicon”, in **“Handbook of Porous Silicon”**, (2018) 3-11.
[11] M.J. Sailor and C.W. Elizabeth, “Photoluminescence-based sensing with porous silicon films, microparticles, and nanoparticles”, *J. Adv. Funct. Mater.*, 19(20) (2009) 3195-3208.
[12] G. Korotcenkov and B.K. Cho, “Silicon porosification: state of the art”, *Critic. Rev. Solid State Mater. Sci.*, 35(3) (2010) 153-260.
[13] M.K. Sahoo and K. Paresh, “Restructured porous silicon for solar photovoltaic: a review”, *J. Micropor. Mesopor. Mater.*, 289 (2019) 109619.
[14] O. Kuntyi, Z. Galyna and S. Mariana, “Porous silicon formation by electrochemical etching”, *J. Adv. Mater. Sci. Eng.*, 2022 (2022) 1-15.
[15] L. Koker and W.K. Kurt, “Photoelectrochemical etching of Si and porous Si in aqueous HF”, *Phys. Chem. Chem. Phys.*, 2(2) (2000) 277-281.
[16] É. Vázsonyi et al., “Porous silicon formation by stain etching”, *Thin Solid Films*, 388(1-2) (2001) 295-302.
[17] M.L. Ngan, K.C. Lee and K.W. Cheah, “Photochemical etching of silicon”, *J. Porous Mater.*, 7 (2000) 41-45.
[18] L. De Stefano et al., “Porous silicon-based optical biochips”, *J. Opt. A: Pure Appl. Opt.*, 8(7) (2006) S540.
[19] H.A. Mohammed, H.A. Kadhem and I.N. Yousif, “Effect of etching time on gallium arsenide surfaces morphology produced by photochemical etching method using sunlight”, *Coll. Basic Edu. Res. J.*, 17(2) (2021) 1550-1570.
[20] M.B. Gongalsky et al., “Biodegradation model of porous silicon nanoparticles”, *Colloids Surf. B: Biointerfaces*, 190 (2020) 110946.
[21] O. Bisi, S. Ossicini and L. Pavesi, “Porous silicon: a quantum sponge structure for silicon based optoelectronics”, *Surf. Sci. Rep.*, 38(1-3) (2000) 1-126.
[22] N.O. Länk, M. Käll and T.J. Antosiewicz, “Electromagnetic energy distribution in resonant quasi porous silicon nanostructures”, *ACS Photon.*, 6(7) (2019) 1706-1714.
[23] M. Kopani et al., “Morphology and FT IR spectra of porous silicon”, *J. Electr. Eng.*, 68(7) (2017) 53-57.
[24] S. Setzu, F. Patrick and R. Romestain, “Optical properties of multilayered porous silicon”, *Mater. Sci. Eng. B*, 69 (2000) 34-42.
[25] B. Gelloz and N. Koshida, “Stabilization and operation of porous silicon photonic structures from near-ultraviolet to near-infrared using high-pressure water vapor annealing”, *Thin Solid Films*, 518(12) (2010) 3276-3279.
[26] E. Galeazzo et al., “Porous silicon patterned by hydrogen ion implantation”, *Sens. Actuat. B: Chem.*, 76(1-3) (2001) 343-346.
[27] J. Ciosek and J. Ratajczak, “Influence of temperature–pressure treatment on heavily hydrogenated silicon surface”, *Appl. Surf. Sci.*, 252(18) (2006) 6115-6118.
[28] R. Hidayat et al., “Selective etching mechanism of silicon oxide against silicon by hydrogen fluoride: a density functional theory study”, *Phys. Chem. Chem. Phys.*, 25(5) (2023) 3890-3899.
[29] V.P. Ulin et al., “Surface of porous silicon under hydrophilization and hydrolytic degradation”, *Semiconductors*, 48(9) (2014) 1211-1216.
[30] P.G. Sennikov et al., “Laser induced dielectric breakdown in reactive mixture SiF^{4+} H_2", *Spectrochimica Acta B: Atom. Spectro.*, 179 (2021) 106099.
[31] K.P. Sreejith et al., “Etching methods for texturing industrial multi-crystalline silicon wafers: A comprehensive review”, *Sol. Ener. Mater. Sol. Cells*, 238 (2022) 111531.

Environmental and Radioactive Contamination in the Village of Kabarli in the Nineveh Plain Region in Iraq

Aaraf Kh. Thannon [1]
Malik H. Kheder [2]
Yasir Y. Kassim [3]
Hanaa N. Azeez [2]

[1] *Department of Sensing and Nano-Photonics, Laser and Photonics Research Center, University of Al-Hamdaniya, Al-Hamdaniya, IRAQ*
[2] *Department of Physics, College of Education for Pure Sciences, University of Al-Hamdaniya, Al-Hamdaniya, IRAQ*
[3] *Department of Physics, College of Education for Pure Sciences, University of Mosul, Mosul, IRAQ*

Iraqi Journal of Applied Physics
Q4 Electronic, Optical and Magnetic Materials
best quartile
SJR 2022
0.19
powered by scimagojr.com

Radioactive pollution in the environment is produced by uranium and its progeny. The obtained value of average radon concentrations levels in soil was 164.640 Bq/m^3, for water samples was 208.950 Bq/m^3. Total intake uranium is dependent mostly on the uranium content in the consumed water. The mean uranium concentrations value for soil samples was 18.130 µg/kg, and for water samples average was 21.255 µg/kg, were generally lower than the standard level rate of uranium concentrations in the drinking water, which was set at 30000 µg/kg according to WHO guidelines, still not dangerous. The findings show that the values of the water samples are greater than those of the soil samples because the water originated in the earth's crust's deeper layers, which are home to a large number of heavy minerals that contain radioactive nuclides. Although there is no risk to human life, the high incidence of uranium availability in particular areas poses a risk to public safety and health. The studied area is safe.

Keywords: Uranium; Radioactive pollution; Soil pollution; Water pollution
Received: 06 April 2024; **Revised:** 23 April 2024; **Accepted:** 30 April 2024

1. Introduction

Environmentally damaging battles were fought in Iraq, and there is a connection between those conflicts and an increase in cancer cases, as well as a predicted rise in these diseases in the future due to the pollutants from those conflicts [1]. The environment was impacted by these conflicts in both direct and indirect ways. Chemicals used in warfare as well as garbage and pollution from bombs and missiles were among the immediate effects. Infrastructure damage, however, pointed to the indirect effects [2] Uranium and its byproducts constitute the most major waste contaminant. The heaviest and longest-living element is uranium. Because of its radioactivity, it is one of the most dangerous pollution issues. Because uranium and its compounds are so poisonous, they are dangerous for the environment and human health [3,4]. One of the most prevalent elements in nature, uranium can be found in a variety of solid, liquid, and gaseous forms. It can be found in food, water, air, rocks, soil, and natural materials. With ease, uranium may combine with other elements to form carbonates, silicates, hydroxides, and uranium oxide [5]. The solubility of uranium compounds largely determines their physiological action. While insoluble (less soluble) uranium is regulated because of its radioactive characteristics, soluble uranium is controlled because of its chemical toxicity. However, rather than the potential for serious chemical damage to the renal system, its primary harm will be radiological damage (risk of cancer mortality) to internal organs due to its delayed absorption through the lungs and prolonged retention duration in the body tissues [6]. The human body can absorb uranium in a variety of ways. It can enter the body directly by ingesting uranium-contaminated water or by inhaling uranium-containing dust particles. Additionally, it may inadvertently penetrate via the layer of fertile soil and the food chain [7]. Soil is a major natural source of radioactivity because of its mineral richness. It also makes people more vulnerable to radiation and helps release radioactive materials into the environment. For these reasons, soil's inherent radioactivity is thought to be a key sign of radioactive contamination [8]. Concentration of radionuclides in soil is a primary indicator of natural background radiation [9]. Different types of soil can have dramatically varied natural radioactivity levels. One of these naturally occurring radionuclides that has been on Earth since the beginning is uranium. All uranium isotopes are radioactive, hence there needs to be control over their quantity [10]. Water is the other fundamental element for life, along with soil, and its supply and continued existence depend on other elements. The direct comprehensiveness of the water is essential to the existence of a wide variety of living organisms and is also necessary to meet their demands. Water is useful to humans since it may be used for food and drink, direct cleanliness, and maintaining good health. But we can't deny that contaminated water can spread illness [11]. Growing water use coupled with population growth indicates that the risk of uranium poisoning typically increases with exposure time and, as a result, the limit of 30 µg/L. When compared to the parent material, the natural background values of uranium in soil range from 0.79 to 11 mg/kg as per WHO guidelines [12]. Keeping daily uranium intake as low as feasible is necessary to minimize the danger of developing uranium-related hazards because uranium ingestion cannot be avoided and the negative effects of uranium have no lower limit [13].

The study aimed to measure the environmental and radioactive contamination, as uranium and its progeny radium and radon in soil and water samples of the Kabarli village thought it has cancer risks.

2. Experimental Part

Samples of soil and water were taken from village of Kabarli. Measurements with the CR-39 detector are made using a plastic can radon dosimeter (7 cm in diameter and 10 cm in length). The detector is put on the bottom of the dosimeter cover and is used to measure the radon concentration in samples, shown in (Fig. 1).

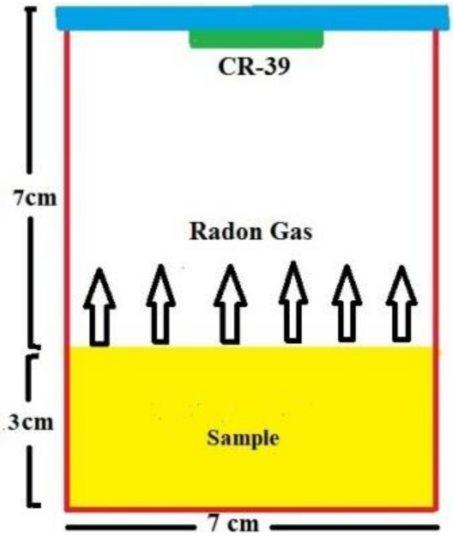

Fig. (1) The dosimeter

Samples with a volume 115.4x10^{-6} m^3 and the height of 3 cm were placed in dosimeter; the distance from the water samples to the surface of detector was 7 cm. Samples were filled and kept in the plastic can for duration of 60 days. Following a 60-day exposure period, the detectors were taken out of the dosimeter and etched chemically in a 6.25N solution of NaOH at 70°C for seven hours. Utilizing a 400X optical microscope, the tracks were counted.

The concentration of radon in the air volume within the container, as determined from the equation [14].

$$C_{Rn=}\rho[KT]^{-1} \qquad (1)$$

where K (=0.05916 Tr/cm^2.d/Bq/m^3) is the radon dosimeter utilized in this study's CR-39 detector calibration factor, ρ is the density of tracks, and T is exposure period [15]

Radon concentrations in water samples determined using the formula [16]

$$C_S = \lambda_{Rn} C_{Rn} HT[l]^{-1} \qquad (2)$$

where C_S is the radon concentration in samples (Bq/m^3), C_{Rn} is the concentration of radon in air space (Bq/m^3), and λ_{Rn} is the radon constant of decay (0.1814 day^{-1}), the T stands for exposure time (60 days), H is for height of air gap in the plastic can (7 cm), and l stands for sample thickness (3 cm)

The uranium contents were calculated by the secular activity equilibrium between the uranium and its daughters, and the concentration of radon measured with using the CR-39 detector. Activity of radon A_{Rn} in sample may calculated thanks to the correlation between C_{Rn} and the amount of radon in the sample [17]

$$A_{Rn} = C_{Rn} V \qquad (3)$$

The volume of sample volume is (V=πr^{2}L) 115.4x10^{-6} m^3, its thickness (L) is 0.03 m, and its radon dosimeter radius (r) is 0.035 m.

$$\lambda_{Rn} N_{Rn} = A_{Rn} \qquad (4)$$

The equation of the equilibrium between the uranium with its daughter (the uranium activity equals the activity of radon) was used to compute the uranium atoms number (N_U) in samples [18]

$$\lambda_U N_U = \lambda_{Rn} N_{Rn} \qquad (5)$$

In this case, the uranium decay constant is λ_U (=4.883x10^{-18} s^{-1}). The uranium atom number N_U was then used to compute the uranium weight in samples using the equation

$$W_U = \frac{N_U a_U}{N_{avo.}} \qquad (6)$$

where W_U is measured in micrograms (µg), N_{avo}= (6.02x10^{23} atom/Mol) is number of Avogadro, a_U is uranium mass number 238. Uranium content is determined by [19]

$$C_U = \frac{W_U}{W_S} \qquad (7)$$

Here, C_U represents the uranium concentration in (µg/kg) units, with W_S equal to 200g for soil and 170g for water

3. Results and Discussion

Outcomes of soil and water samples are listed in table (1), which contains data on the amounts of uranium in the samples C_U in (µg/kg) and radon in the samples (C_{Rn} in units of Bq/m^3). Radon concentration levels in soil ranged from 131.532 to

209.102 Bq/m^3 with average value 164.640 Bq/m^3, and for water samples ranged 152.990 to 236.770 Bq/m^3 with average value 208.950 Bq/m^3. The level of radon in the water samples was higher than in the soil samples because of differences in the earth's geological features. This is because the water comes from deep underground mining, where mineral metals were present in its journey. The US Environmental Protection Agency's recommended acceptable international concentration limit for radon contamination of drinking water is 11000 Bq/m^3, which is lower than any measured radon concentration in the samples. The uranium concentrations ranged from 14.484 to 23.026 µg/kg on average 18.130 µg/kg for soil samples and from 15.562 to 24.085 µg/kg on average 21.255 µg/kg for water samples, as illustrated in Fig. (2), were generally lower than the standard level rate of uranium concentrations in drinking water, which was set at 30000 µg/kg in accordance with WHO guidelines, but still not dangerous.

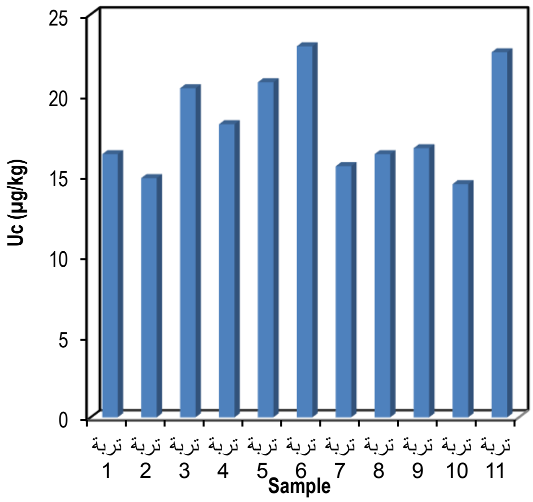

(a) Soil

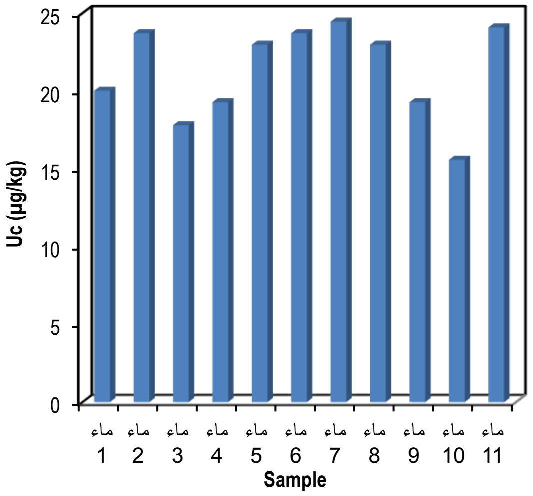

(b) Water

Fig. (2) Uranium concentrations: (a) in soil samples, and (b) in water samples

The findings demonstrated that the water samples had greater values than the soil samples. Radioactive nuclides can be found in many heavy minerals found in the Earth's deeper crustal layers. Public safety and health are at danger due to the high prevalence of uranium availability in certain places, even if there is no harm to human life. Significant health effects linked to uranium have been observed, akin to high-level radon exposure; treatment is not required.

4. Conclusion

The objective of this investigation was to measure the levels of radiation and uranium in soil and water samples from the Iraqi village of Kabarli, which is located in the Nineveh plain. Water with a high radiation level is one of the research area's sources of dangers to the public's health. This makes figuring out the radiation levels in the surrounding important. The study location is safe since the danger of increased uranium intake from drinking tap water is practically very minimal due to very low uranium intake from water.

References

[1] H.K.A. Ridha and J.S. Al-Safi, “The future vision to the cancer incidence in Iraq, a comparative analytical study to the effect of Iraq-Iran war”, *Baghdad Coll. Econ. Sci. Uni.*, 25 (2010) 91-102.

[2] K.M. Muhannad, “Risk assessment related to contamination of terrestrial food chains by atmospherically deposited lead particles”, *Al-Mustansiriyah J. Sci.*, 21(3) (2010) 103-116.

[3] A. Al-Hamzawi, M. Jaafar and N. Tawfiq, “Concentration of uranium in human cancerous tissues of Southern Iraqi patients using fission track analysis”, *J. Radioanal. Nucl. Chem.*, 303(3) (2015) 1703-1709.

[4] W. Zou et al., “Characterization and properties of zeolite as adsorbent for removal of uranium (VI) from solution in fixed bed column”, *J. Radioanal. Nucl. Chem.*, 288(3) (2011) 779-788.

[5] D. Banks et al., “Radioelement (U, Th, Rn) concentrations in Norwegian bedrock ground waters”, *Enviro. Geo.*, 25(3) (1995) 165-180.

[6] P. Todorov and E. Ilieva, “Contamination with uranium from natural and anthropological sources”, *Romanian J. Phys.*, 50(9-10) (2005) 25-30.

[7] A. AL-Hamzawi et al., “Uranium concentration in human blood using fission track etch technique”, *J. Nat. Sci. Res.*, 13 (2013) 176-181.

[8] S. Rahman and M. Faheem, “Natural radioactivity measurements in Pakistan an overview”, *J. Radiol. Prot.*, 28 (2008) 443.

[9] K. Kapanadze, A. Magalashvili and P. Imnadze, “Distribution of natural radionuclides in the

soils and assessment of radiation hazards in the Khrami Late Variscan crystal massif (Georgia)", *Heliyon*, 5(3) (2019).

[10] G. Graetz, "Energy for whom? Uranium mining, Indigenous people, and navigating risk and rights in Australia", *Ener. Res. Soc. Sci.*, 8 (2015) 113-126.

[11] A.S. Al-Zahrani, "The Water Situation in the Arab World and its Economic and Political Repercussions in a Geographical Perspective", 2nd Forum of Arab Geographers, Cairo, 30-20 November 2000, Part 1 (2002).

[12] World Health Organization (WHO), "Uranium in drinking-water, background document for development of WHO Guidelines for Drinking-water Quality" (2004).

[13] Agency for Toxic Substances and Disease Registry (ATSDR), "Public health statement for uranium", World Health Organization (1999) CAS# 7440-61-1.

[14] B. Al-bataina et al., "Radon measurements in different types of natural waters in Jordan", *Rad. Measur.*, 28(1-6) (1997) 591-94.

[15] M.H. Kheder et al., "Radioactivity concentrations in barley and wheat crops in Nineveh plain region in Iraq", *Int. J. Nucl. Ener. Sci. Technol.*, 14(1) (2020) 50-60.

[16] M.H. Kheder, H.N. Azeez and F.M. Al-Jomaily, "Alpha emitters radioactivity concentrations in some cosmetics used in Iraq using LR-115 detector", *J. Eureka Phys. Eng.*, 2 (2020) 65-70.

[17] H. Cember and T.E. Johnson, **"Introduction to health physics"**, 4th ed., McGraw-Hill (2009).

[18] M.H. Kheder, "Radium and Uranium Concentrations in Some Fruits and Vegetables Cultivated in Nineveh Governorate, Iraq", *Iraqi J. Appl. Phys.*, 19(3B) (2023) 15-19.

[19] M.H. Kheder, H.N. Azeez, and M.A. Al-Jubbori, "Measurement of Uranium and Radon Concentrations in Wells Water Samples of Some Farms near the Mosul City in Iraq", *Iraqi J. Appl. Phys.*, 19(3B) (2023) 3-8.

Table (1) The radon concentrations, uranium concentrations, and the radium concentrations

No	Soil		Water	
	C_{Rn} (Bq/m^3)	C_U (µg/Kg)	C_{Rn} (Bq/m^3)	C_U (µg/Kg)
S1	148.395	16.341	196.702	20.009
S2	134.905	14.855	233.128	23.714
S3	185.494	20.426	174.846	17.785
S4	165.258	18.198	189.416	19.268
S5	188.867	20.797	225.843	22.973
S6	209.102	23.026	233.128	23.714
S7	141.650	15.598	240.413	24.455
S8	148.395	16.341	225.843	22.973
S9	151.768	16.712	189.416	19.268
S10	131.532	14.48	152.990	15.562
S11	205.730	22.654	236.770	24.085
min	**131.532**	**14.484**	**152.990**	**15.562**
max	**209.102**	**23.026**	**236.770**	**24.085**
average	**164.640**	**18.130**	**208.950**	**21.255**

Unraveling the Influence of Hydrofluoric Concentration on the Morphology of Porous Silicon Surfaces Fabricated through Photochemical Etching using Sunlight

Islam N. Yousif
Ahmed T. Abdulhameed
Amenah M. Essmat
Abdulrahman I. Ahmed

Department of Physics,
College of Education for
Pure Science,
University of Al-Hamdaniya,
Nineveh, IRAQ

Samples of n-type porous silicon samples with negative conductivity, low resistivity (4.3x10^{-4} Ω.cm) and crystalline orientation (100) were prepared by photochemical etching method using sunlight as a light source. The intensity of the incident sunlight was collected and focused on the surface of the sample through a telephoto lens with a diameter of 7.5 cm and a focal length of 30 cm. The effect of changing concentrations of hydrofluoric acid (20%, 30%, and 40%) when using etching time of 30 min and illumination intensity of 6181 mW/cm^2 was studied. The results of surface morphology showed forming porous layers with thicknesses 527.7, 594.7, and 663.4nm and mean grain diameters of 104.9, 121.1, and 99.80 nm, respectively.

Keywords: Porous Silicon; Photoluminescence; Sunlight; Photochemical Etching
Received: 04 April 2024; **Revised:** 25 April 2024; **Accepted:** 01 May 2024

1. Introduction

The discovery of the phenomenon of photoluminescence in porous silicon prepared from crystalline silicon wafers at room temperature led to increasing interest in porous silicon structures that are characterized by an indirect energy gap [1,2], in order to give it a broad spectrum that extends from infrared radiation, and continues to the entire visible spectrum and may reach near ultraviolet spectrum by controlling the porosity of their surfaces and their atomic dimensions [3-5].

The processes of reducing the sizes of the pores and decreasing them to extremely small sizes and dimensions during the processes of preparing porous silicon will form complex and isolated networks of pores that lead to their separation and independence from each other with thin walls and the creation of pits and trenches between them [6-8], forming very small and patterned areas in the form of different nanostructures with semi-spherical or irregularly shaped heads to achieve quantitative confinement. Then, what is called nanoporous silicon is formed [9,10].

As a result of the photoluminescence processes that occur on the surfaces of porous silicon, its porous structures are stimulated to increase its ability to absorb light, which is used in the applications of photodetectors [11-13], which leads to an increase in the amount of light energy, and thus reduces the losses resulting from recombination, enabling us to convert the absorbed solar energy into electrical energy for use in solar cell applications and generating renewable energy [14-16]. Because of their porous surfaces of different sizes and distributions it provides large areas for contribute to processes of storing and preserving electrical charges, and works to rearranging them to be highly efficient in applications of energy storage systems such as electrical capacitors and batteries [17,18].

The changes which occur in the concentrations of chemicals used in their preparation processes, including the change in hydrofluoric acid concentration, which produces their porous structures using the photochemical etching technique occurs without applying any external effort to provide their surfaces with the gaps [19,20]. It is processes opposite to the preparation processes using the electrochemical etching technique, which requires an applied external effort on it and which makes it of great importance in optical sensing applications [21,22].

This article seeks to shed light on the importance of changing the concentration of hydrofluoric acid in light of the stability of other influences and its effective role in shaping porous silicon surfaces and the changes that occur to them when they are prepared using the photochemical etching technique, by taking advantage of the energy of sunlight that is absorbed by the prepared porous silicon surfaces because It is considered one of the most important sources of renewable energy.

2. Experimental Part

Based on the photochemical etching system and using sunlight as a light source, as shown in Fig. (1), n-type single-sided silicon slices were prepared with electrical resistance of 10^{-4} Ω.cm. Their surface is completely polished with crystalline orientation of (100). The material is cut into small samples with dimensions of 1.0x0.5 cm. It is then placed in a solution of acetone and ethanol for 5 minutes to remove the impurities stuck to it and get rid of the remaining diluted HF solution on it. After that, the samples are left to dry in order to configure them for the preparation process.

Fig. (1) Photochemical etching system of this work using sunlight as a light source

Through the light source (sunlight), the optical power of the lens with a diameter of 7.5 cm and the illumination intensity is calculated by multiplying the total lens area by the intensity of solar radiation. The average radiation intensity of 140 mW/cm^2 was adopted. So the value of both the optical power and the illumination intensity per (cm^2) are 6181 mW and 6181 mW/cm^2, respectively.

Porous silicon samples are prepared at different hydrofluoric acid concentrations (HF 20%, HF 30%, and HF 40%) at constant etching time (30 min), resistivity (10^{-4} Ω.cm), and illumination intensity (6181 mW/cm^2). Therefore, the samples are placed inside a cylindrical Teflon container known for its high resistance to acids and corrosion. The diameter of the Teflon container is 5.5 cm, an external height of 3.5 cm, and an internal drilling depth of 1.5 cm. In the middle of its internal design is a cylindrical protrusion with an engraved face in the shape of the letter (U) to hold the samples, where a container is filled with HF 40%, so that immersed of the surface of the sample, and then sunlight is shined on it, which in turn produces a light intensity of 6181 mW/cm^2 to contribute to the formation of the porous layer.

The formation of pores and the etching processes are confirmed through the chemical reactions that occur on the upper surface of the samples, since we notice the appearance of small hydrogen bubbles as a result of the dissolution of the silicone and their surface reddening in a color close to brown as a result of the continuing etching processes on their surface [23,24].

After the preparation process is completed, the sample is lifted with iron forceps to preserve its surface morphology. It is then placed in a plastic container filled with methanol and closed tightly to preserve its nano-porous structure. Its characteristics of the formed pores and the compositions of its particles are analyzed through an atomic force microscope (AFM), which shows us the shape of the porous layer and its thickness, its nanoparticles, their particle sizes, and their surface roughness.

3. Results and Discussion

The precise dissolution process occurs on silicon surfaces through the presence of gaps when sunlight is shed and focused on them to complete the process of electronic polishing and the formation of pits whose molecules dissolve when they interact with water (H_2O) molecules by placing them in HF acid solution. So, Si-F bonds are formed, which leads to the formation of stable and dense bridges from the Si-OH bond, to reveal the oxide nuclei emerging are formed from the Si-O-Si bonds [25-27].

The effect of changing the concentrations of HF acid (20%, 30%, and 40%) is evident on the morphology of their surfaces at an etching time of 30 min and an illumination intensity of 6181 mW/cm^2, porous layers of nanoporous silicon are formed with structures separated by grooves, pits, and semi-spherical heads, which is shown by the 3D AFM images shown in Fig. (2).

The thickness of the porous layer of the etched samples increases as the concentration of HF acid increases and decreases when the concentration decreases. The surface roughness rate is proportional to the root mean square (RMS) roughness in the form of a Gaussian distribution, due to the occurrence of agglomerations of nanoparticles due to the continuity of etching and removal processes on their surfaces, which leads to change the sizes and dimensions of nanostructures.

The surface kurtosis and surface skewness of the produced samples are shown in a logarithmic distribution because it contains low valleys and grooves extending with a certain homogeneity in relation to the distribution of surface heights and in a curved pattern that is close to the average values and gradually decreases when moving away from them. This distribution is used in many electronic industries related to technologies surface because it resists corrosion and reduces pressure and stress on the surface.

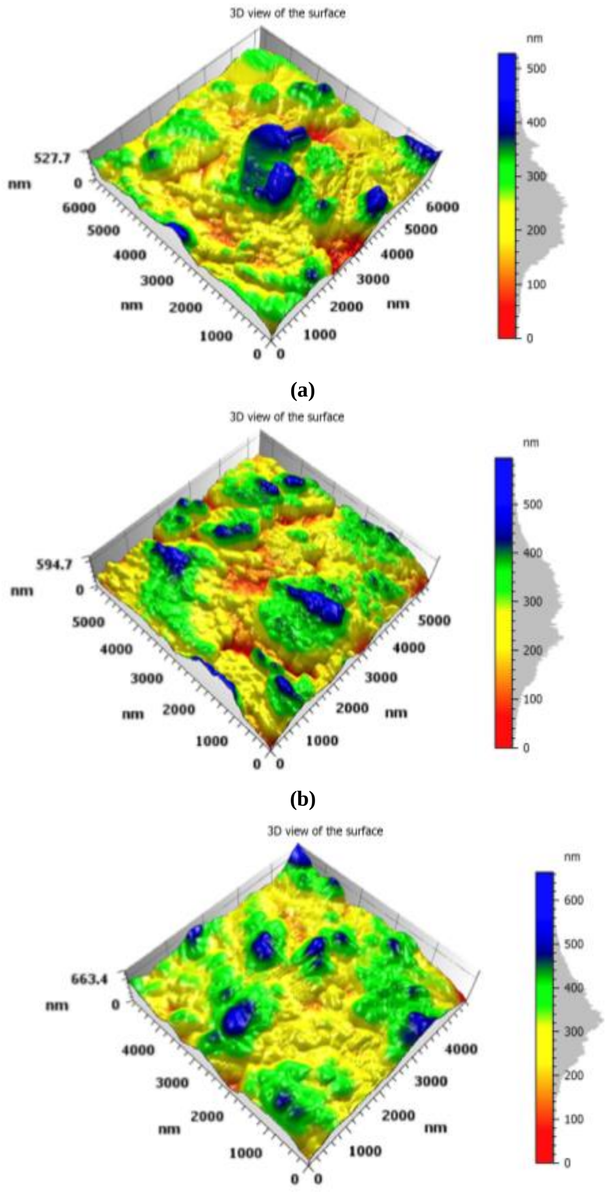

Fig. (2) 3D AFM images of silicon surfaces produced at different HF acid concentrations: (a) 20%, (b) 30%, and (c) 40%

Figure (3) shows that etching operations occur randomly on the surface or on the walls or sides, leading to a significant increase in the number of flowing gaps, so different nanoparticles with multiple compositions are formed along the surface of the sample by mean diameters 104.9 nm, 121.1 nm, 99.80 nm, which increases the surface area and generates high photovoltaic to emit spectral emissions within the visible region, which can be utilized in many materials science, optoelectronics, and nanotechnology applications.

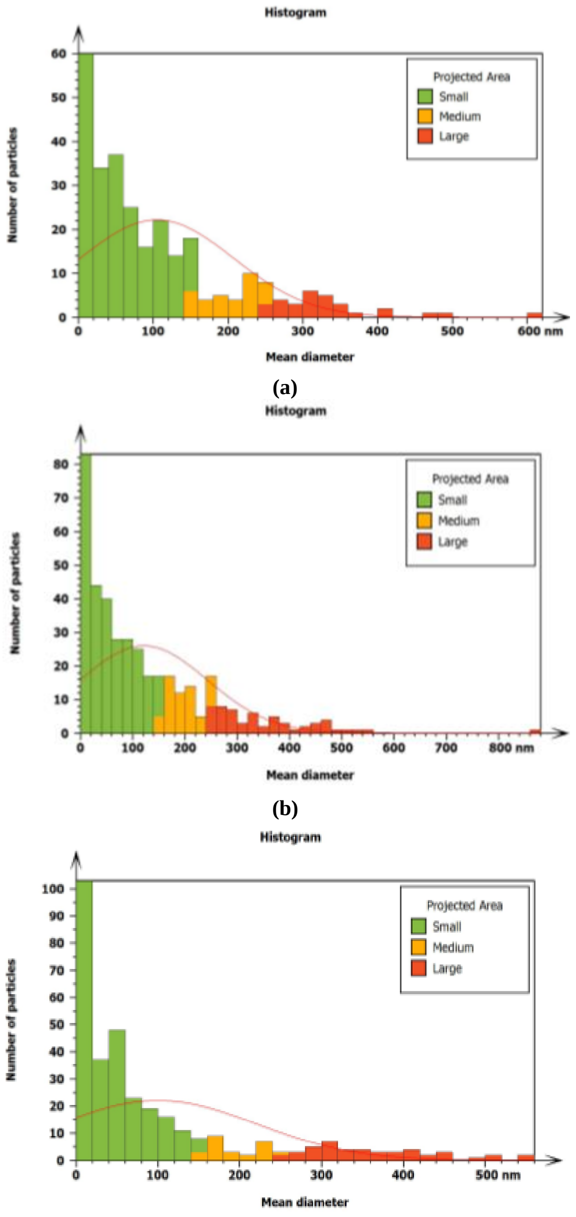

Fig. (3) Statistical distribution of the numbers of particles formed on the surfaces of the produced samples with their mean diameters nanoscale at different HF acid concentrations: (a) 20%, (b) 30%, and (c) 40%

4. Conclusion

Sunlight is one of the most promising and effective light sources in the process of preparing porous silicon slices using the photochemical etching method. It is one of the most important renewable and environmentally friendly sources of energy, and is considered as a successful alternative to other industrial sources. The results showed that increasing the concentration of hydrofluoric acid will lead to an increase in the thickness of the porous layer, and reducing it will lead to reducing the thickness of the porous layer when the etching time, resistivity, and illumination intensity are constant. It is considered useful in the applications of sensors and photodetectors, improving the efficiency of solar cells, and sensing diodes.

References

[1] S.M. Hossain et al., "Stability in photoluminescence of porous silicon", *J. Lumines.*, 91(3-4) (2000) 195-202.

[2] A. Mortezaali, S.R. Sani and F.J. Jooni, "Correlation between porosity of porous silicon and optoelectronic properties", *Non-Oxide Glasses*, 1 (2009) 293-299.

[3] M. Kopani et al., "Morphology and FTIR spectra of porous silicon", *J. Electr. Eng.*, 68(7) (2017) 53-57.

[4] S. Setzu, F. Patrick and R. Romestain, "Optical properties of multilayered porous silicon", *Mater. Sci. Eng. B*, 69 (2000) 34-42.

[5] B. Gelloz and N. Koshida, "Stabilization and operation of porous silicon photonic structures from near-ultraviolet to near-infrared using high-pressure water vapor annealing", *Thin Solid Films*, 518(12) (2010) 3276-3279.

[6] P. Granitzer and R. Klemens, "Porous silicon - a versatile host material", *Materials*, 3(2) (2010) 943-998.

[7] V.V.E. Starkov et al., "Nanoporous Layers and the Peculiarities of Their Local Formation on a Silicon Wafer", *Processes*, 10(1) (2022) 163.

[8] E. Monaico, I. Tiginyanu and V. Ursaki, "Porous semiconductor compounds", *Semicond. Sci. Technol.*, 35(10) (2020) 103001.

[9] E.G. Barbagiovanni et al., "Quantum confinement in Si and Ge nanostructures: Theory and experiment", *Appl. Phys. Rev.*, 1(1) (2014) 011302.

[10] B. Bera, "Nanoporous silicon prepared by vapour phase strain etch and sacrificial technique", *Int. J. Comput. Appl.*, 975 (2015) 8887.

[11] M. Sharifi et al., "Role of graphene on the optoelectrical stability of photodetectors based on porous silicon", *Sens. Actuat. A: Phys.*, 310 (2020) 112065.

[12] D. Banerjee et al., "High performance photodetectors using porous silicon-TiO_2 heterostructure", *Eng. Res. Exp.*, 2(3) (2020) 035021.

[13] D.H. Kim, W. Lee, and J.M. Myoung, "Flexible multi-wavelength photodetector based on porous silicon nanowires", *Nanoscale*, 10(37) (2018) 17705-17711.

[14] J.M. Martínez-Duart and R.J. Martín-Palma, "Photodetectors and solar cells based on porous silicon", *phys. stat. sol. (b)*, 232(1) (2002) 81-88.

[15] H.A. Mohammed, H.A. Kadhem and I.N. Yousif, "Effect of etching time on gallium arsenide surfaces morphology produced by photochemical etching method using sunlight", *Coll. Basic Edu. Res. J.*, 17(2) (2021) 1550-1570.

[16] S. Chandrasekaran et al., "Porous silicon nanoparticles as a nanophotocathode for photoelectrochemical water splitting", *RSC Adv.*, 5(104) (2015) 85978-85982.

[17] K. Grigoras et al., "Porous silicon for energy storage at microscale: Supercapacitors", *ECS Trans.*, 75(1) (2016) 97.

[18] I. González et al., "Lithium effect on the electronic properties of porous silicon for energy storage applications: a DFT study", *Dalton Trans.*, 47(22) (2018) 7505-7514.

[19] S. Yae et al., "Formation of porous silicon by metal particle enhanced chemical etching in HF solution and its application for efficient solar cells", *Electrochem. Commun.*, 5(8) (2003) 632-636.

[20] M.L. Ngan, K.C. Lee and K.W. Cheah, "Photochemical etching of silicon", *J. Porous Mater.*, 7 (2000) 41-45.

[21] E.A. Saverina et al., "Porous silicon preparation by electrochemical etching in ionic liquids", *ACS Sustain. Chem. Eng.*, 8(27) (2020) 10259-10264.

[22] V. Torres-Costa et al., "Porous silicon optical devices for sensing applications", *Opt. Mater.*, 27(5) (2005) 1084-1087.

[23] V.P. Ulin et al., "Surface of porous silicon under hydrophilization and hydrolytic degradation", *Semiconductors*, 48(9) (2014) 1211-1216.

[24] O. Bisi, S. Ossicini and L. Pavesi, "Porous silicon: a quantum sponge structure for silicon based optoelectronics", *Surf. Sci. Rep.*, 38(1-3) (2000) 1-126.

[25] E. Galeazzo et al., "Porous silicon patterned by hydrogen ion implantation", *Sens. Actuat. B: Chem.*, 76(1-3) (2001) 343-346.

[26] R. Hidayat et al., "Selective etching mechanism of silicon oxide against silicon by hydrogen fluoride: a density functional theory study", *Phys. Chem. Chem. Phys.*, 25(5) (2023) 3890-3899.

[27] K.P. Sreejith et al., "Etching methods for texturing industrial multi-crystalline silicon wafers: A comprehensive review", *Sol. Ener. Mater. Sol. Cells*, 238 (2022) 111531.

Asmaa A Aziz [1]
Nada F Tawfiq [2]
Lukman A. Hussein [3]

[1] *Department of Physics, College of Education for Pure Science, Tikrit University, Tikrit, IRAQ*
[2] *Department of Physiology and Medical Physics, College of Medicine, Al-Nahrain University, Baghdad, IRAQ*
[3] *Amerli Education, General Directorate of Salah al Din Education, Ministry of Education, Salah al Din, IRAQ*

Determination of radon concentrations, surface emission rate and mass emission rate radon in the surface soils of the city of Tuzharmatu in Governorate of Salah Al-Din

CN-85 is used to measure the levels of radon. A total of twenty-one surface soil samples were distributed around Tuzkormato's outskirts, while six samples were gathered from the city center. The radon concentration in Tuzhurmato, Imam Ahmad district, ranged from 18.96 $Bq.m^{-3}$ to 61.99 $Bq.m^{-3}$, while the radon concentration in the Albu Sabah village was 37.09 $Bq.m^{-3}$. The surface emission rate (Ex) was $1.14x10^{-4}$ $Bq.M^{-2}.h^{-1}$ (Albu Sabah) to $3.73x10^{-4}$ $Bq.M^{-2}.h^{-1}$ (Albu Hassan). The mass emission rate (Em) ranged between 0.12 x 10^{-4} $Bq.M^{-2}.h^{-1}$ in Albu Hassan village and $2.81x10^{-4}$ $Bq.M^{-2}.h^{-1}$ in Tuzhurmato-Iqsu district. When these results are compared to the allowable quantity of (ICRP) radon in the soil, which is (200) $Bq.m^{-3}$. The comparison revealed that all locations of study agree with these boundaries.

Keywords: Radon concentration; Surface emission; CN-85 detector; Pollution
Received: 04 April 2024; **Revised:** 25 April 2024; **Accepted:** 01 May 2024

1. Introduction

The most important element of the environment that allows humans access to food sources is soil. It is the thin, fragile layer that lies between a few millimeters and several meters above crustal rocks. It consists of a mixture of air, water, organic and mineral components. The plant has the ability to cling to the soil with its roots and extract the components necessary for life. The presence of radioactive radon gas in the soil, with high radioactive concentrations, is considered a source of long-term environmental pollution, leading to the pollution of food, water, air, and thus humans [1]. Radon is a colorless, odorless, natural gas that is emitted when uranium series U-238 radioactively decays. Radon is mostly found in rocks and soil near the surface. Therefore, there is a direct danger to human life as a result of the presence of radioactive radon gas in the soil in proportions exceeding the normal limit [2, 3]. We looked at the effect of radon gas on the lives of individuals directly through food, drink and even air, and indirectly through the soil and irrigation water, and from there to plants and animals and then to humans. Numerous studies have been conducted to determine the concentration of radon in various fields [4-6]. Uranium and radon gas exposure is a significant health concern, linked to increased cancer incidence, kidney failure, and other dangerous diseases due to uranium presence in patients' blood and urine [7-10]. The long-term measurement method for measuring radon concentration was adopted in models of surface soils it uses solid-state nuclear impact detectors, the method is more effective in detecting the concentration of radon [11]. Where the detector are placed in sealed diffusion Chamber in a cylindrical shape and placed against a sample is used to measure radon concentration and tightly sealed to prevent leakage or air exchange with the ocean [12].

The study aims to determine the concentration and rate of surface and mass radon emission. in 27 samples of the surface soil of the city of Tuzkhurmatu and its outskirts in Salah al-Din Governorate, with Six samples were collected from the city center, while 21 samples were distributed in the areas located on the outskirts of the city using trace detector CN-85 which is an organic detector. Its chemical formula is N(C6H8N2) and it has exceptional sensitivity to alpha particles and other heavy particles. [13].

2. Experimental Part

Twenty-seven surface soil samples were collected from the center and outskirts of Tuzkhurmatu city. The study area included about 600 km^2, including the center of Tuzkhurmatu city, with 6 samples and 22 samples distributed over 20 areas on the outskirts of Tuzkhurmatu city. Nuclear track detectors are electrically insulating materials, and charged particles (protons, alpha particles, and fission fragments) produce tracks as they pass through these materials where they generate narrow paths of radiation damage consisting of atomic defects, clonal gaps, and molecular chain breaks [14]. These defects are called latent tracts, and the damaged areas can be seen using an optical microscope after being treated with a chemical that etches and shows the areas of damage formed. Important properties of SSNTDs are the possibility of extending the minimum damage intensity along the impact core by etching technique [15]. Irradiation dramatically changes the properties of polymers by splitting or mixing their molecules, leading to significant changes in their overall structure. Radiation falling on these polymers causes them to ionize and break the bonds between them, leading to damage or defects. This stored defect is known as the hidden effect. Also, the areas affected by ionizing radiation show a the individual has a greater capacity to interact with alkaline solutions such as NaOH compared to the healthy areas, because the affected areas have more energy than the healthy areas, so the chemical solution quickly penetrates the areas exposed to radiation, which leads to an increase in the depth of the visible path and an expansion of its diameter with the etching time increases, and the hidden ionization path after chemical treatment can be seen using an optical microscope[16]. After the end of the microscopic viewing phase, the radon concentration in the samples can be determined using the following equation [17].

$$C_s = \lambda_{Rn} C_a ht/L \qquad (1)$$

where C_s concentration of Rn-222 within samples in Bq.m^{-3}. C_a The concentration of Rn-222 in the air space of Bq.m^{-3}. λ_{Rn} Fixed Rn-222 dissolution equals 0.1814 day^{-1}. h Height of the aerospace equal to 5.3 cm. L Thickness estimated value is about 1 cm. t Irradiation time is 55 d

The concentration of radon was determined using the following equation for its surface emission rate. [18]:

$$Ex = \frac{\mathrm{C}\,\lambda\,\mathrm{V}}{A[T+(e^{-\lambda T}-1)\lambda^{-1}]} \qquad (2)$$

where Ex: radon emission rate in terms of area(Bq/m^2.h). C: concentration of radon in unit (Bq/m^3), λ: radon decay constant and its value is 0.1814 day^{-1}. V: The size of the irradiation mug is 71.41 cm^3, A: The area of the cylinder is 75.17 m^2, T: The irradiation time in hours is 1320 hr.

The mass emission rate of radon was determined using the following equation [19]:

$$Em = \frac{\mathrm{C}\,\lambda\,\mathrm{V}}{M[T+(e^{-\lambda T}-1)\lambda^{-1}]} \qquad (3)$$

Here, Em Rn-222 emission rate in terms of mass (Bq.(kg.h)$^{-1}$), M: Models block is 10 gm

The samples were left in the sun for about a week to remove the moisture from them, then grind and sieve to keep the smooth part only to ensure the homogeneous distribution of the radioactive material. Use the CN-85 and 100 µm (1 x 2 cm^2 Solid-state nuclear path detectors are used to monitor the effects of alpha particles emitted by radon gas. Use a 10^{-2} gm sensitivity scale to calculate the weight of the soil models at 10 gm of each samples.

Samples were left for 22 days in enclosed test glasses to reach 98% of the balance between Ra226 radium and Rn222 radon. This time was calculated using the equilibrium relationship of radioactivity [20]:

$$A_{Rn} = A_{Ra}(1 - e^{-t\lambda_{Ra}}) \qquad (4)$$

Here, A_{Rn} the efficiency of radon, A_{Ra} the efficiency of radium, λ_{Ra} the decay of radium, 8.73× 10^{-8} s^{-1} and t the time needed to reach equilibrium state.

After the equilibrium state period ended, we quickly removed the cup lid to avoid changing the air inside the cup and replaced it with another lid with a piece of CN-85 reagent. The distance between the sample surface and the detector is approximately 5.3 cm and the sample is left for 55 days. The detector was then installed to prepare for the chemical etching process. The etching solution is created by dissolving a specific amount of NaOH granules in distilled water to obtain the required standard using a specific formula [21]

$$N = \frac{W(g)x000}{WeqV(ml)} \qquad (5)$$

N standard of solution, w(g) mass NaOH, V(ml) distilled water volume, weq equivalent weight of NaOH equal 40, the 6.25N Standardization was used for the etch solution for detector where 62.5g of sodium hydroxide granules were dissolved in 250ml of distilled water. Use the water bath to heat the NaOH solution to the required temperature of 60 °C, the etching process is carried out by placing the detector in the etching solution, which is placed in a flask inside the water bath after the finishing time of 2.5 hours. The detector is washed with distilled water and dried. The microscopic phase of the detector is then started. The ligands and synthesized complexes were characterized as follows.

3. Results and Discussion

Apart from the radiological background, the concentration of Rn-222 gas was determined for 27 soil samples using the CN-85 nuclear track detector. The surface and mass emission as well as the intensity of radon concentration were computed as shown in table (1).

According to the investigation, sample S3 had the greatest radon concentration (61.996 Bq.m^{-3}), sample S1 had the lowest value (18.961 Bq.m^{-3}) and the rate (37.09 Bq.m^{-3}) (Fig. 1). Also showed highest concentration of surface emission was recorded in sample S3 (3.732 Bq.m^{-2}.h^{-1}) and lowest in sample S1 (1.141 Bq.m^{-2}.h^{-1}) and 2.23 Bq.m^{-2}.h^{-1}) as shown in (Fig. 2), either As can be shown in (Fig. 3), sample S3 had the highest mass emission rate (2.810 Bq.kg^{-1}.h^{-1}), sample S21 had the lowest value (0.121 Bq.kg^{-1}.h^{-1}), and the average was 1.65 Bq.kg^{-1}.h^{-1}. According to the International Commission on Radiological Protection (ICRP), a comparison of these data with the allowable revealed a soil radon concentration of 200 Bq.m^{-3} [14]. Comparison revealed that all research locations concurred with these limitations.

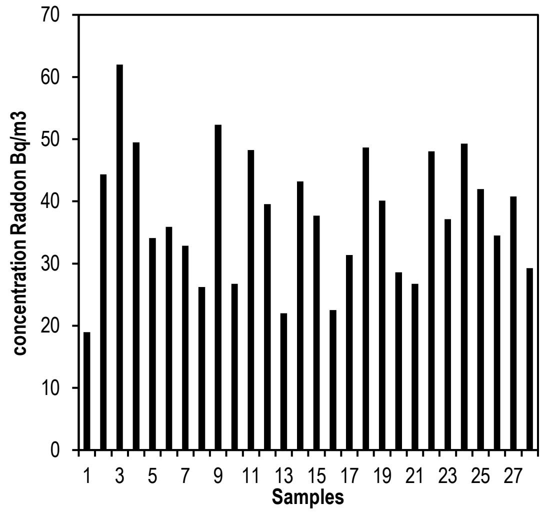

Fig. (2) Concentration of radon gas in surface soil models

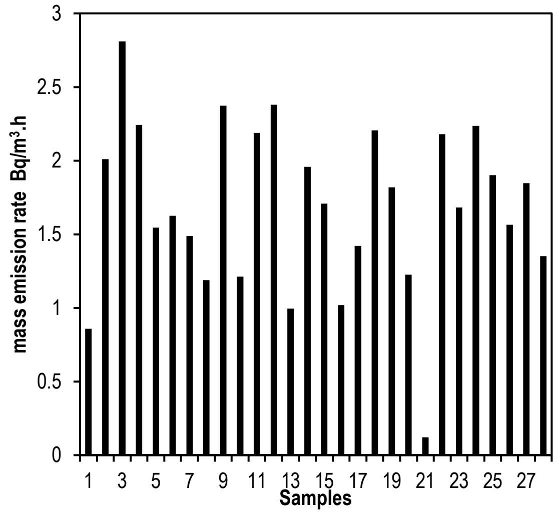

Fig. (3) Mass emission rate for radon

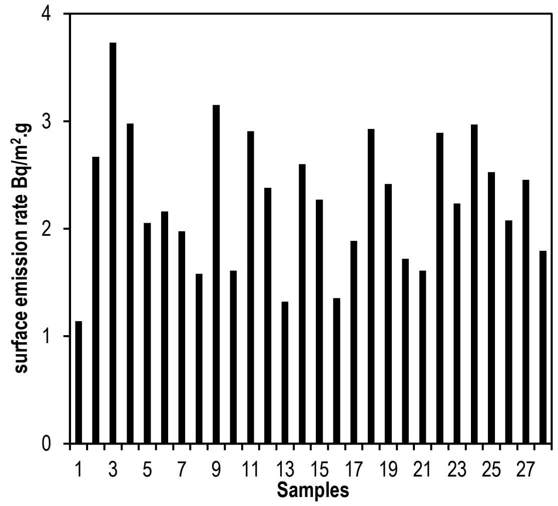

Fig. (4) Surface emission rate of radon

4. Conclusion

Along with the radiological background, the concentration of radon gas, its intensity, and its surface and mass emission were calculated, and the concentration of Rn-222 gas was determined for twenty-seven soil samples using the CN-85 nuclear track detector. Based on a comparison of these findings with the allowable level, the International Commission on Radiological Protection (ICRP) reported a radon concentration of 200 Bq.m^{-3} in soil. The comparison revealed that these limitations were accepted by all research locations.

References

[1] K.M. Ahmed, "**Land Pollution, (1999)**", Dar al-Shehabi Printing House (2001) p. 47.

[2] A.A. Al Saad, "Radon Risks and Benefits", *Corn Develop. J.*, 9(3) (1997) 81-88.

[3] R. Barillon et al., "Comparison of Effectiveness of three Radon Detectors (LR-115, CR-39 & Silicon Diode PIN) placed in Cylindrical Device – Theory and Experimental Techniques", *Nucl. Track Rad. Measur.*, 22(1-4) (1993) 281-282.

[4] A.A. Aziz, "Evaluation of radioactivity of cereals and legumes using a nuclear impact detector CN-85", *Iraqi J. Phys.*, 16(38) (2018) 139-146.

[5] N.F. Tawfiq, N.O. Rasheed and A.A. Aziz, "Measurement of Indoor Radon Concentration in Various Dwellings of Baghdad Iraq International", *J. Phys.*, 3(5) (2015) 202-207.

[6] N.F. Tawfiq, A.A. Aziz and L.A. Hussein, "Natural Radioactivity and Risk Assessment in Soil Samples of Tuzkhormato District Salahdin Governorate-Iraq", *J. Rad. Nucl. Appl. Int. J.*, 2(3) (2017) 109-114.

[7] A.A. Aziz, F.M. Majed and N.F. Tawfiq, "Determination of Uranium Concentration in Blood Samplesfor Patients with Kidney Failure in Salah din Governorate", *IOP Conf. Ser. Earth Enviro. Sci.*, 877 (2021) 012010.

[8] A.A. Aziz, N.F. Tawfiq and F.M. Majed, "Evaluation the concentration of lead in urine of cancer patients in Salah din Governorate using FAAS", *AIP Conf. Proc.* 2404 (2021) 070004.

[9] A.A. Aziz, F.M. Majed and N.F. Tawfiq, "Evaluation of Uranium Concentration in the Blood of Cancer Patients in Salah Al-Din Governorate", *Tikrit J. Pure Sci.*, 26 (2) (2021).

[10] O.W. Mohammad and A.A. Aziz, "Calculating uranium concentrations in some urine samples of cancer patients and comparing them with healthy people using the nuclear trace detector CR-39", *J. Genet. Enviro. Resour. Observ.*, 11(2) (2023) 91-95.

[11] N.A. Abdul Rahman, "Solid Reagents of Nuclear Impact and its Uses", *Corn Develop.*

J., 9(3) (1997) 101-106.

[12] H. Al-Wondawi, "Radon and its impact on the environment and man", *Corn Develop. J.*, 9(3) (1999) 38-41.

[13] S.A. Durrani and R.K. Bull, "**Solid State Nuclear Track Detection**", Pergamon Press (Oxford, 1987).

[14] B.A.-D. Maarouf, "Natural Radioactivity in Iraq," studies and researches selected from the scientific conference on the effects of the use of depleted uranium weapons on humans and the environment in Iraq., 129-145-26-27 March, 2002 Baghdad - Iraq, issued by the Ministry of Higher Education.

[15] C. Hepburm and A.H. Windle, "Solid state nuclear track detectors", *J. Mater. Sci.*, 15 (1980) 279-301.

[16] K.N. Yu et al., "Measurement of parameters of tracks in CR-39 detector from replicas", *Rad. Protect. Dosim.*, 111(1) (2004) 93-96.

[17] S. Sinch, and H.S. Vrk, "Determination of Natural Heavy Radioactivity in Soil", *Indian J. Pure Appl. Phys.*, 25 (1987) 127-129.

[18] A. Al-Kinani, "Determination of the Natural Radioactivity in Soil, Water and Air for Some Sections in Al-Sader City", MSc thesis, University of Baghdad (2015).

[19] A. Jose et al., "Analysis of the K-40 levels in soil using gamma spectrometry", *J. Brazilian Arch. Biol. Technol.*, 48 (2005) 221-228.

[20] B.G. Cartwright and E.K Shirk, "A nuclear Track Recording Polymer of Unique Sensitivity and Resolution", *Nucl. Instrum. Meth*, 153 (1978) 457-460.

[21] ICRP, Lung Cancer Risk from Radon and Progeny and Statement on Radon (2010).

Table (1) The intensity of the effects, the concentration of radon and the surface and mass emission rate

Symbol	Intensity of effects (track/mm^3)	Concentration of radon C_{Rn}(Bq/m^3)	Surface Emission Rate (EX) x10^{-4} Bq/m^2.hr	Mass emission Rate (EM) x10^{-4} Bq/kg.hr
S 1	445±1.34	18.961	1.141	0.859
S 2	1042±1.67	44.357	2.670	2.010
S 3	1455±1.16	61.996	3.732	2.810
S 4	1162±1.21	49.486	2.979	2.243
S 5	800±1.63	34.087	2.054	1.545
S 6	842±2.77	35.877	2.160	1.626
S 7	771±1.03	32.852	1.977	1.489
S 8	616±1.46	26.247	1.580	1.189
S 9	1228±1.82	52.324	3.150	2.372
S 10	628±1.66	26.758	1.611	1.213
S 11	1133±4.34	48.276	2.906	2.188
S 12	928±1.38	39.541	2.380	2.380
S 13	516±0.68	21.986	1.323	0.996
S 14	1014±1.24	43.206	2.601	1.958
S 15	885±1.95	37.709	2.270	1.709
S 16	528±0.88	22.497	1.354	1.019
S 17	737±0.99	31.351	1.887	1.421
S 18	1142±1.59	48.660	2.929	2.206
S 19	942±0.90	40.138	2.416	1.819
S 20	671±0.88	28.591	1.721	1.226
S 21	628±1.66	26.758	1.611	0.121
S 22	1128±1.03	48.063	2.893	2.179
S 23	871±1.66	37.112	2.234	1.682
S 24	1157±0.33	49.299	2.968	2.235
S 25	985±2.16	41.970	2.526	1.902
S 26	811±1.66	34.524	2.078	1.565
S 27	957±2.25	40.777	2.455	1.848
Radiation back ground	700±1.19	29.286	1.795	1.352
Min.	445±0.33	18.961	1.141	0.121
Max.	1455±4.34	61.996	3.732	2.810
Ave.	882.92±1.51	37.09	2.23	1.65

Mohammed K. Jawad
Farah T.M. Noori
Seenaa I. Hussein
Nadia A. Ali
Zainab R. Muslim
Manal A. Saleh

Department of Physics,
College of Science,
University of Baghdad,
Baghdad, IRAQ

Polypyrrole-Functionalized MWCNT Heterojunctions for Gas Detection

The current study is critical in examining the performance of a new nanocomposite sensor capable of detecting NO_2 and H_2S using a combination of PPy, NiO, and f-MWCNT. The f-MWCNT addition to the polymer matrix increases film roughness and the surface-to-volume ratio of the film, hence increasing adsorption of gas molecules on nanotube surfaces. The resistance change of the nanocomposite after exposure to H2S shows a very high sensitivity to the detection of gas, and the f-MWCNT has enhanced the sensing ability of the PPy sensor. This combination of PPy and f-MWCNT also exhibits a fast response time for both NO_2 and H2S gases. The paper analyses the sensitivity, response, and recovery time of the sensor, along with operating temperatures from 50, 100, 150, and 200°C, giving a survey of the different operating conditions that the sensor may operate efficiently. The uniqueness of this paper is in the specific nanocomposite structure based on the unique properties of PPy, NiO, and f-MWCNT to enhance the detection of gas. The innovative approach to the design of sensors guarantees an efficient and highly responsive solution to monitor toxic gases.

Keywords: Polypyrrole; f-MWCNT; Gas sensor; Contact angle; DTA
Received: 27 March 2024; **Revised:** 13 May 2024; **Accepted:** 20 may 2024

1. Introduction

Gas sensing technology has revolutionized the measurement and monitoring of a large number of gases in their different aspects. Gas sensing has found research and practical applications in a variety of areas, including environmental research, the automotive industries, medical diagnostics, and indoor air quality management. Chemo-resistive gas sensors have become a very important transduction unit for a variety of reasons, including easy readout interface circuitry, portability, low power consumption, and low cost. A gas sensor having active sensing material has been showed to be very versatile in terms of detection gases with a variety of different active sensing materials [1-2].

Hydrogen sulfide (H_2S) and Nitrogen oxide (NO) are naturally occurring and health hazards to human beings. Of the two, the most poisonous one is H2S, which causes symptoms like headaches and dizziness at low concentrations, and it is lethal at concentrations above 250 ppm. Its occurrence is found in mines, petroleum fields, and natural gas production, so detection is of utmost importance in oil and gas exploration, automotive ventilation, and dentistry.

Although most of the available sensors are based on inorganic metal oxide semiconductor technology, such as ZnO, Fe_2O_3, and WO_3, these materials often are very sensitive to high operating temperatures and poor selectivity. There is a great necessity for operating at room temperature [3-5].

Major applications in the field of sensing are assigned to conducting polymers, such as polypyrrole (PPy) as active layers of gas sensors, for which significant advantages arise from operation at room temperature, cost-effectiveness, flexibility, and very high sensitivity. Exceptionally high surface-to-volume ratio and hollow structure of nanomaterials, such as carbon nanotubes (CNTs), bring the ideal medium to adsorb gas molecules. CNTs have to a large extent driven significant advancements in gas sensor technology due to their unique geometries, morphologies, and material properties, making it possible to detect the changes of the gas induced through various techniques. NiO is regarded as a model of p-type semiconductors and is highly valued for its chemical stability and outstanding optical and electrical properties. The potential of NiO thin films as electrochromic device or sensing layers is appreciated by other studies [6]. Heinig et al. prepared a PPy–Au coated NiO nanocomposite to improve the electrocatalytic properties. Jia et al. prepared a PPy–Au coating on NiO nanoparticles to produce multifunctional nanocomposites for electroanalysis applications [7].

The aim of this study is to evaluate the performance of a nanocomposite sensor, composed of Polypyrrole (PPy), nickel oxide (NiO), and functionalized multi-walled carbon nanotubes (f-MWCNT), for the detection of NO_2 and H_2S gases, focusing on its sensitivity, response time, and efficiency across various temperatures.

2. Experimental Work

A nanocomposite film of PPy, f-MWCNT, and NiO was prepared on FTO substrates by using pulsed laser ablation (PLA). The substrate was heated to 400°C during deposition with a Nd:YAG laser, operating at a wavelength of 1064 nm, with a pulse duration of 10 ns and a frequency of 6 Hz. Before laser deposition, the sample powder was compressed into disk form under a pressure of 5 tons, resulting in a disk with 0.2 cm thickness and 1.5 cm radius.

The surface characteristics of the prepared nanocomposite film were characterized: the contact angle was measured by means of a special program and a high-resolution camera. This data gave insights into the hydrophobic or hydrophilic nature of the film, and these are the main characteristics to point to a possible application in gas sensing.

The electrical properties are measured using sensitive digital electrometer, Keithley 616, using a 2V power source to find the film resistance. A differential temperature test was also carried out, considering how the fluctuation of temperature would impact the performance of the sensor.

To see how the sensor should work in detecting poisonous gases, the films were exposed to NO_2 and H_2S gases in a controlled environment. This was achieved with the help of a specially designed system that controlled the concentration and flow of gas in an accurate manner, thus providing reliable test environments to test the sensor reaction to these given gases.

With some comprehensive tests and analyses, it was possible to determine the suitability of the nanocomposite film for gas sensing applications, with the objective of providing valuable data, which, in turn, help for improved design and functionality of the nanocomposite film.

3. Results and Discussion

The contact angle measurement indicates changes in surface wettability. The contact angle of the film decreased from 92° to 81°, as illustrated in Fig. (1), suggesting a shift from hydrophobic to hydrophilic characteristics. This change in wettability may result from the presence of lone pairs of electrons in the nitrogen atoms within the heterocyclic pyrrole structure, allowing hydrogen bonding with water molecules. This observation aligns with previous studies [10,11].

The direct current (DC) conductivity of the nanocomposite varies with the concentration of NiO, f-MWCNTs, and temperature. An increase in both NiO and f-MWCNT concentrations, as well as temperature, resulted in a fourfold increase in conductivity, as shown in table (1). Figure (2) demonstrates the exponential relationship between conductivity and temperature, consistent with the Arrhenius equation [12,13]. The activation energy for doped PPy was found to be between 0.89 and 0.11 eV within a temperature range of 303 to 453 K, indicating that increased MWCNT concentrations lead to improved conductivity due to the formation of a conductive path through the PPy/NiO matrix, as explained by percolation theory [14,15].

Table (1) The values of σ_{dc} and E_a for PP/MWCNT nanocomposites

PPy/NiO/f-MWCNT Ratio (wt.%)	1	2	3	4
σ (S/cm)	4.8×10^{-3}	3.1×10^{-2}	31.58	61.8
E_a (eV)	0.89	0.72	0.46	0.11

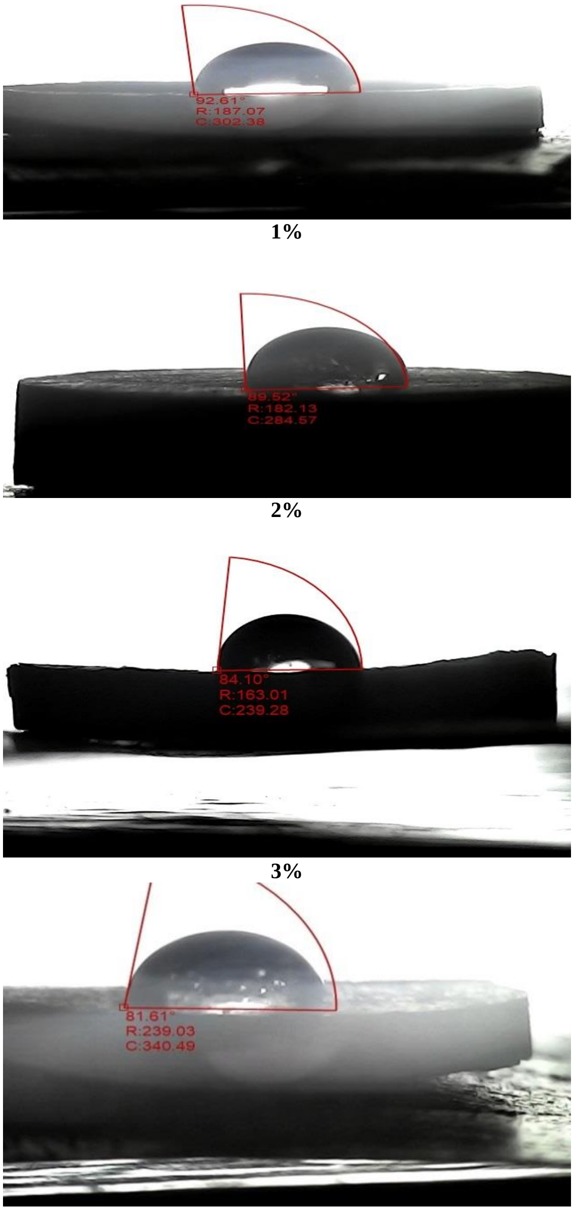

1%

2%

3%

4%

Fig (1) Contact angle measurements of PPy/NiO/f-MWCNT (1, 2, 3, 4%) samples

The differential thermal analysis (DTA) thermograms for PPy and PPy/NiO/f-MWCNT nanocomposites are shown in Fig. (3). The first stage of thermal analysis occurs in the temperature range of 50-75°C, likely due to the loss of moisture. The second stage, observed between 150-175°C, might be attributed to the loss of oligomeric molecules, with additional endothermic activity around 190-200°C. A weight loss between 200 and 300°C could result from the loss of dopants. The incorporation of f-MWCNT into PPy increased the thermal stability of the composites compared to PPy alone, suggesting that well-dispersed MWCNTs prevent rapid heat transmission [16,17].

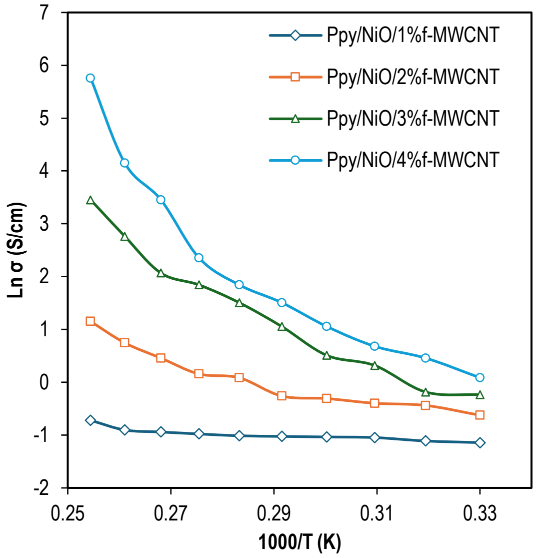

Fig (2) Variation of Ln(σ) versus 1000/T for PPy/NiO/f-MWCNT(1, 2, 3, and 4%)

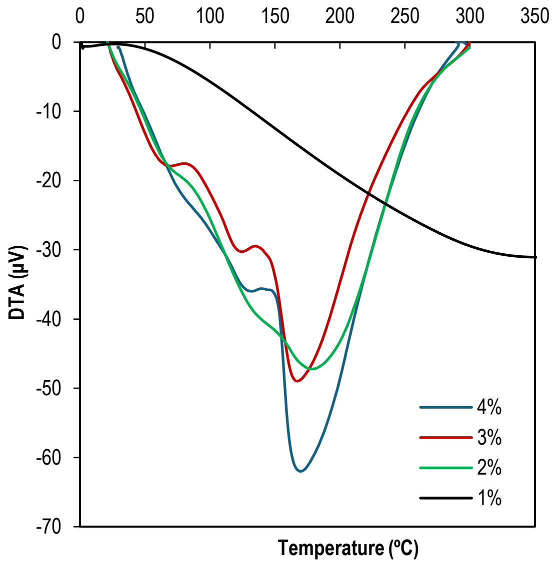

Fig (3) DTA curves of PPy/NiO/f-MWCNT (1, 2, 3, 4%) samples

The gas sensing performance of the nanocomposite was examined using oxidizing (NO_2) and reducing (H_2S) gases at different operating temperatures (25, 100, 150, and 200°C), as shown in Fig. (4). The sensitivity of the PPy/NiO/4% f-MWCNT film to H_2S at 50 ppm was approximately 14% at temperatures up to 200°C, whereas the sensitivity to 86 ppm NO_2 was about 13% at 100°C. This high sensitivity is attributed to the nano-sized structure of the films and the ability of the sample surface to adsorb oxygen [18-20].

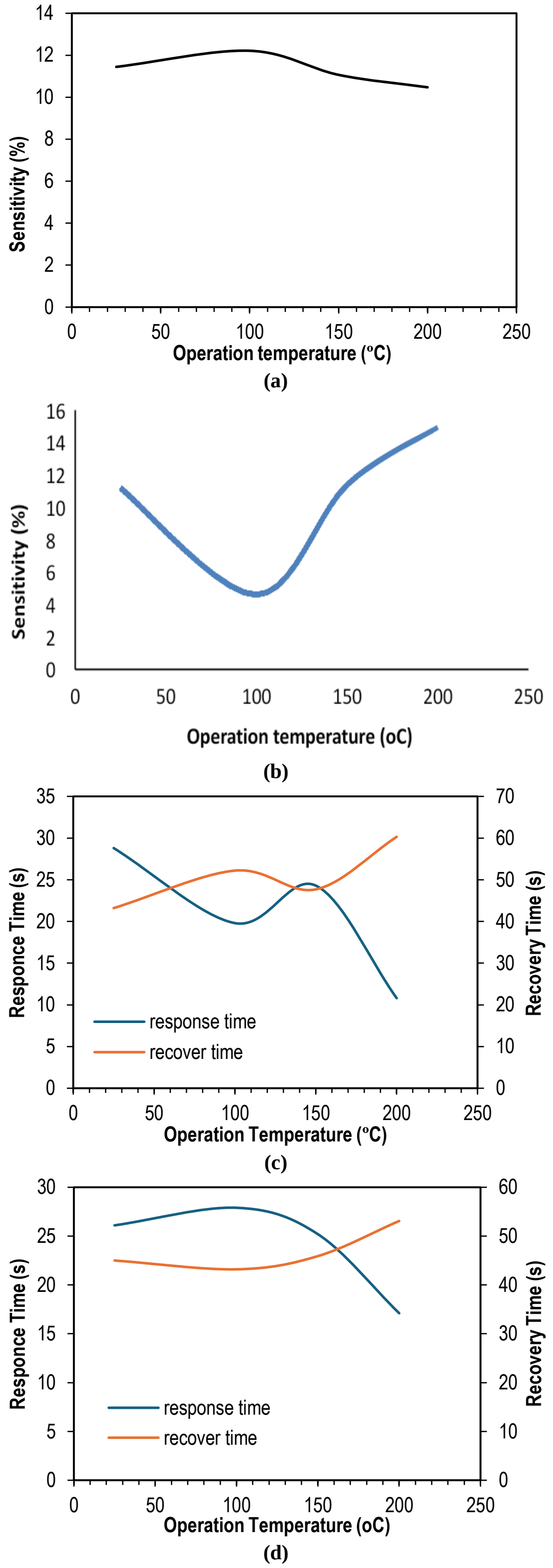

(a)

(b)

(c)

(d)

Fig. (4) The sensitivity of PPy/NiO/4% f-MWCNT to NO_2 (a),(c) and H_2S gases (b),(d)

These results highlight the potential of the PPy/NiO/f-MWCNT nanocomposite as a versatile material for gas sensing applications, demonstrating high sensitivity and thermal stability under varying conditions.

4. Conclusion

This study undoubtedly demonstrates proof of concept for the development of a nano-based sensor for the detection of NO_2 and H_2S, using a combination of PPy, NiO, and the f-MWCNT in the polymer matrix. The addition of f-MWCNT to the polymer matrix increases the roughness of the film and, therefore, the surface-to-volume ratio, in which gas adsorption is increased and yields greater sensitivity. The f-MWCNT-based sensor is capable of quick response to both NO_2 and H_2S, with different sensitivity, response, and recovery times for distinct operating temperatures (50, 100, 150, and 200°C), which shows versatility. The novel design of this sensor is very responsive and effective for the detection of toxic gases and has broad applications in industries where gas monitoring is of utmost importance.

References

[1] S. Feng et al., “Review on Smart Gas Sensing Technology”, *Sensors*, 19(17) (2019) 3760.

[2] M. Das and S. Roy, “Polypyrrole and associated hybrid nanocomposites as chemiresistive gas sensors: A comprehensive review”, *Mater. Sci. Semicond. Process.*, 121 (2021) 105332.

[3] M.R. Jwameer et al., “Antiproliferative Activity of PEG-PEI-SWCNTs against AMJ13 breast cancer cells”, *J. Nanomater.*, 2023 (2023) 1-8.

[4] A. Kadhim, F.T.M. Noori and N.D. Hamza, “Laser induced forward transfer of In_2O_3:ZnO:Au nanocomposite thin film for gas sensitivity application”, *ARPN J. Eng. Appl. Sci.*, 12(23) (2017) 6657-6662.

[5] D.M. Nerkar, S.E. Jaware and G.G. Padhye, “Fabrication of a novel flexible room temperature hydrogen sulfide (H_2S) gas sensor based on polypyrrole films”, *Int. J. Sci. Res.*, 5(3) (2016) 106-111.

[6] Y. Wang and J.T. Yeow, “A review of carbon nanotubes-based gas sensors”, *J. Sens.*, 2009 (2009) article ID 493904.

[7] I. Hotovy et al., “Sensing characteristics of NiO thin films as NO_2 gas sensor”, *Thin Solid Films*, 418(1) (2002) 9-15.

[8] N.F. Heinig et al., “The growth of nickel nanoparticles on conductive polymer composite electrodes”, *Mater. Lett.*, 62(15) (2008) 2285-2288.

[9] D. Jia et al., “Preparation and characterization of multifunctional polypyrrole–Au coated NiO nanocomposites and study of their electrocatalysis toward several important bio-thiols”, *Sens. Actuat. B*, 160(1) (2011) 168-173.

[10] M. Kılıç, “Natural additive material for desirable dielectric properties of polypyrrole: limestone”, *Synth. Met.*, 260 (2020) 116297.

[11] S.M. Jasim and N.A. Ali, “Properties characterization of plasticized polylactic acid/Biochar (bio carbon) nano-composites for antistatic packaging”, *Iraqi J. Phys.*, 17(42) (2019) 13-26.

[12] M.A. Salman and S.M. Hassan, “A Study of Crystallographic and DC Electrical Characteristics of PPy/Ag Nanocomposites”, *Iraqi J. Phys.*, 19(49) (2021) 15-21.

[13] F.M. Ahmed and M.K. Jawad, “FTIR and Electrical Behavior of Blend Electrolytes Basedon (PVA/PVP)”, *Iraqi J. Phys.*, 21(1) (2023) 1-9.

[14] V.R. Feig et al., “Mechanically tunable conductive interpenetrating network hydrogels that mimic the elastic moduli of biological tissue”, *Nat. Commun.*, 9 (2018) 2740.

[15] J.M. Rzaij, “Characterization of CuO thin films for gas sensing applications”, *Iraqi J. Phys.*, 14(31) (2016) 1-12.

[16] K.H. Musa and T.M. Al-Saadi, “Investigating the Structural and Magnetic Properties of Nickel Oxide Nanoparticles Prepared by Precipitation Method”, *Ibn Al-Haitham J. Pure Appl. Sci.*, 35(4) (2022) 94-103.

[17] R. Afshari, S. Mazinani and M. Abdouss, “Nanohybrid Nanoparticles Based on Chitosan/ Functionalized Carbon Nanotubes as Anti-HIV Nanocarrier”, *NANO Brief Rep. Rev.*, 10(1) (2015) 1550010.

[18] A. Imani, G. Farzi and A. Ltaief, “Facile synthesis and characterization of polypyrrole-multiwalled carbon nanotubes by in situ oxidative polymerization”, *Int. Nano Lett.*, 3 (2013) 52.

[19] M.A. Alborisha et al., “Investigations on TiO_2–NiO@ In_2O_3 nanocomposite thin films (NCTFs) for gas sensing: synthesis, physical characterization, and detection of NO_2 and H_2S gas sensors”, *J. Mater. Sci.*, ?? (2024) 1-6.

[20] K.-S. Teh and L. Lin, “MEMS sensor material based on polypyrrole–carbon nanotube nanocomposite: film deposition and characterization”, J. Micromech. Microeng., 15(11) (2005) 2019.

Saad A. Essa [1]
Kareem K. Mohammad [2]
Yaseen H. Mahmood [1]

[1] *Department of Physics, College of Science, Tikrit University, Tikrit, IRAQ*
[2] *Al-Nahrain Research Center for Renewable Energy, Al-Nahrain University, Baghdad, IRAQ*

Characterization of the Radioactivity of Natural Radionuclides in Some Building Materials using a High-Purity Germanium Detector

The main objective of the current study is to characterize radioactivity in selected samples of building materials by measuring the amounts of natural radionuclides (^{238}U, ^{232}Th, ^{40}K) using gamma spectroscopy with a high-purity germanium (HPGe) detector. Samples selected for the models were collected from different origins and subjected to analysis to confirm average concentrations of radionuclides. Then, risk factors were calculated and these results were compared to international values for further analysis. The results of the study indicate that the quantities of radionuclides fall within the established global natural limits, which indicates that the levels of natural radioactivity fall within the globally accepted range.

Keywords: Building materials; Radioactivity; Ceramics; Marble substitute
Received: 04 April 2024; **Revised:** 25 April 2024; **Accepted:** 01 May 2024

1. Introduction

Soil is a critical environmental component that plays a vital role in providing humans with a livelihood. When contamination occurs as a result of the addition or removal of certain components, it results in defects that alter inherent natural, biological, or chemical characteristics. These changes have direct or indirect effects on both humans and other species living in the affected environment [1]. The increasing number of sophisticated scientific inquiries pertaining to the generation of radioactive elements and the wide range of applications they possess in everyday existence poses a significant peril to the environment and its contamination [2]. Hence, it has become essential for researchers to gain knowledge regarding the properties and risks associated with these substances, as well as appropriate protocols for their safe handling and management. Radionuclides make up a large portion of naturally occurring radioactive materials [3]. The presence of these nuclides can be observed in various geological formations within the Earth's environment, encompassing the Earth's crust, subsurface rocks, soil, vegetation, hydrosphere, and atmosphere. The relative proportions of these nuclides, which serve as sources of radioactivity [4], show variations based on factors such as the geographic and geological characteristics of a given area, the spatial distribution of radionuclides, and the existing radiochemical conditions. The United Nations Scientific Committee on the Effects of Atomic Radiation (UNSCEAR) in 2000 stated that [5]. Radioactive contamination is widely recognized as an extremely dangerous form of environmental pollution. When radioactive elements infiltrate the body's cells, they cause visible and internal imbalances [6].

Building materials contribute to the construction of buildings and residential homes in which people live and spend most of their lives for a long period. These materials are made or taken from natural sources, whether rocks or soil from different regions. [7]. They have natural radioactivity that affects human life. This effect depends on the amount of radiation to which he/she is exposed, the type of ionizing rays contained in these materials, and the manner in which a person is exposed to them, whether internally or externally [8]. Among the health risks to which a person is exposed that are related to exposure to radiation are cancerous diseases that occur as a result of genetic mutations resulting from a change in the genetic codes due to exposure of living cells to radiation. Because of these and other effects, it has become important to focus on the control factor for these materials and examine them periodically to determine the extent of their danger and their impact on humans [9]. This is done by measuring their radioactivity and comparing it with international values for the amount of radiation permitted to be exposed to according to statistics set by the relevant international bodies.

This study seeks to validate the levels of inherent radioactivity and assess the radiation levels found in samples of the building materials under investigation [10]. To achieve this goal, measurements were carried out on five samples, including those sourced from different companies, to determine radium equivalents, internal and external risk indicators, annual absorbed dose, and gamma radiation risk indicators.

2. Experimental Part

A high-purity germanium detector (HPGe) it has an efficiency of 20% and an operating voltage of

400keV located in Al-Nahrain University, Al-Nahrain Research Center for Renewable Energy was used for quantitative and qualitative analysis of the samples of the studied materials in order to calculate the specific activity of natural radionuclides (^{238}U, ^{232}Th, ^{40}K) and industrial cesium (^{137}Cs) and analyze these results using a computer equipped with (SpectraLineGP) software to make appropriate changes.

The study included 5 samples of different types of ceramic, porcelain, and marble substitutes, as distributed in table (1). Samples were collected from different types in Iraqi local markets and from different industries. One kilogram for each sample is taken, after using a small-diameter sieve to obtain a homogeneous mixture, and then the samples are transferred to the laboratory to preserve them and measure the exact mechanism of action of radionuclides. In order to begin the measurement, an empty plastic container was placed in the detector system and the gamma ray spectrum was collected for a duration of 60 min. Following this, the radiation background of the laboratory was measured. After that, the device was calibrated as needed. Then, the samples under study were measured, The lead isotope ^{214}Pb specific activity was determined at an energy level of 351.9 keV, bismuth ^{214} Bi at an energy level of 609.32 keV, and radium ^{226}Ra at an energy level of 185.6 keV, which is equivalent to the specific activity of the uranium ^{238}U series. The most effective value was selected. The specific activity of ^{212}Pb was determined at an energy level of 238.6 keV, the specific activity of actinium isotope ^{214}Ac at an energy level of 911.16 keV, which is equivalent to the specific activity of the thorium series ^{232}Th, and the specific activities of potassium ^{40}K at an energy level of 1460.8 keV [11].

3. Results and Discussion

According to the results listed in table (1), sample Y3 had the greatest specific activity of uranium ^{238}U at 54.6 Bq/kg, while sample Y5 had the lowest at 7.80 Bq/kg, according to the findings of the specific radioactivity of radioactive isotopes acquired from ceramic, porcelain, and marble substitution samples. Sample Y3 had the greatest specific activity of ^{232}Th (42.25 Bq/kg), whereas sample Y5 had the lowest (1.1 Bq/kg). As indicated in Fig. (1), the specific activity of ^{40}K had a maximum value of 300 Bq/kg in sample Y5 and a minimum value of 100 Bq/kg in sample Y1. Radium equivalent effectiveness (Ra_{eq}). The results showed that the highest value is sample Y5 had the lowest value at 35.67 Bq/kg, whereas the overall rate of comparable radium efficacy was 83.21 Bq/kg. Sample Y3 had the highest value at 131.26 Bq/kg. The findings presented here show. There is a discrepancy between the radium equivalent efficacy rate and the worldwide average of 370 Bq/kg.

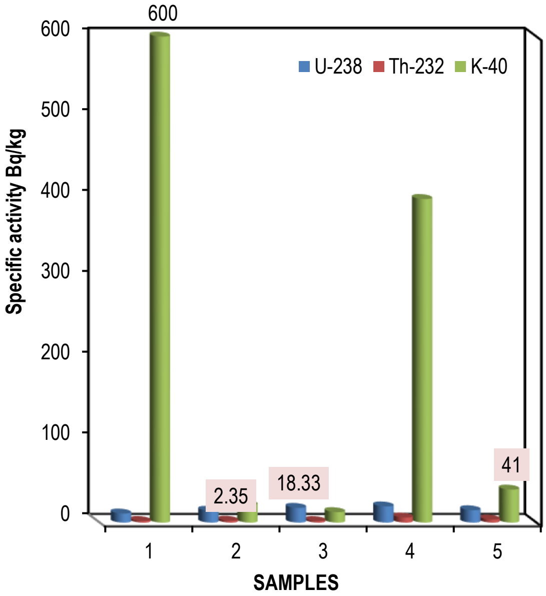

Fig. (1) Effect Hazard Index for the studied ceramic, porcelain, and marble substitute samples

The values of the absorption dose rate (D) range from 18.26 nGy/h in sample Y5 to 59.54 nGy/h in sample Y3. The average rate is 38.05 nanograms per hour. According to the latest findings, as seen in Fig. (2), the airborne absorbed dose rate is lower than the average worldwide value of 84 nGy/h.

In terms of the Annual Effective Dose Indoor ($AEDE_{in}$), the sample Y5 had the lowest value at 0.02 mSv/y, while Y3 had the highest value at 0.07 mSv/y. On average, it's 0.05 mSv/y. A lower value of 0.09 mSv/y was found in Y5, while the highest value of 0.29 mSv/y was in sample Y3, indicating that the present findings demonstrate that the yearly effective dose rate for internal exposure is lower than the worldwide average of 1 mSv/y. On average, it's 0.19 mSv/y. According to the latest findings, the yearly effective dosage rate from the outside is lower than the worldwide norm (1 mSv/y) .

Nuclear danger index for the interior H_{in} In sample Y3, the maximum value was 0.5 Bq/kg, whereas in sample Y5, the lowest value was 0.13 Bq/kg. The internal risk index rate is lower than the world average, which is 1 Bq/kg, with a typical rate of 0.32 Bq/kg. Additionally, the Hout external radiation risk index With a value of 0.35 Bq/kg, sample Y3 had the highest concentration. Also, in sample Y5 the lowest value was 0.10 Bq/kg). The findings show that the external risk index rate is lower than the general rate of 1 Bq/kg, whereas the general average is 0.22 Bq/kg.

Index of danger for Iγ gamma radiation. While the overall average was 0.59 Bq/kg, the findings showed that sample Y3 had the greatest value at 0.93 Bq/kg and sample Y5 had the lowest value at 0.28 Bq/kg. Figure (3) shows that the overall rate is 1Bq/kg, but the external risk index rate is lower [12].

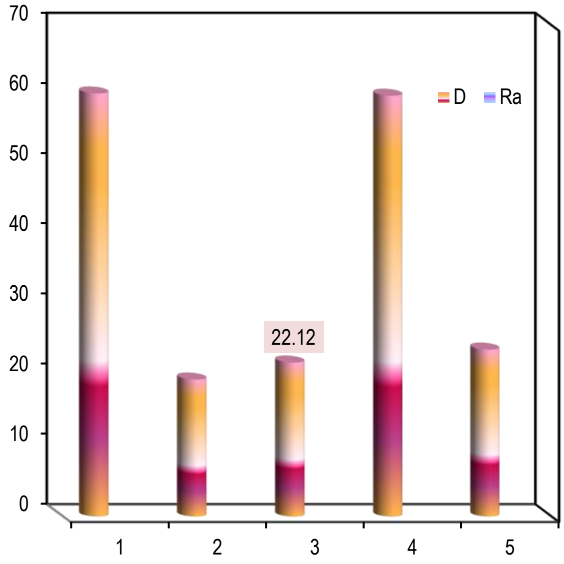

Fig. (2) Specific effectiveness for the studied ceramic, porcelain, and marble substitute samples

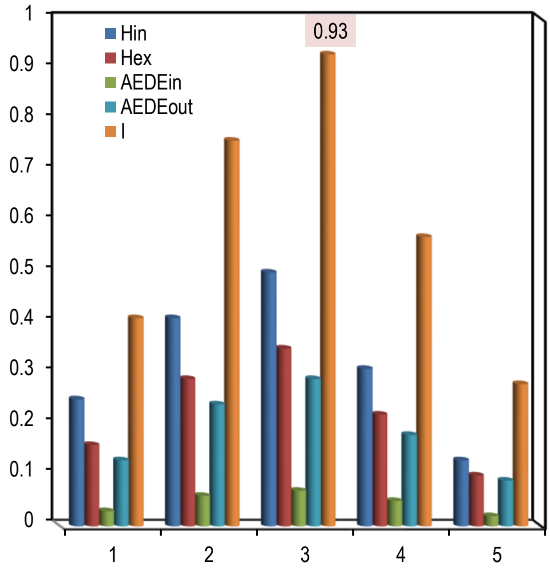

Fig. (3) Risk factors for the studied ceramic, porcelain, and marble substitute samples

4. Conclusions

Based on the data collected, the absorbed dose rate did not exceed the limitations set by UNSCEAR (2000) [22]. Internationally permitted levels, as determined by UNSCEAR (2000), are lower than the yearly effective dose rates. The radium equivalent likewise fell under the 370 Bq/kg level that is considered acceptable worldwide. The findings of this study indicate that the absorbed dose rate in the samples collected was within the acceptable limits set by the International Commission on Radiological Protection (ICRP, 1993). Hence, these varieties are deemed safe for use in building.

References

[1] F.F. Kaddoori et al., “Measurement of specific activity of natural radioactive materials and Cs-137 in soil samples for some areas in Al-doura city in Baghdad governorate”, *Iraqi J. Sci.*, 62(9) (2021) 2940-2947.

[2] Z.J. Kazem, “Radioactive contamination with uranium and radon gas, and concentrations of some heavy elements in the soil of the city of Nasiriyah”, MSc thesis, University of Baghdad (2012).

[3] Y.S. Khalf and K.K. Mohammad, “Measurement of natural radioactivity level in selected phosphate fertilizer samples collected from Iraqi Markets”, *Al-Nahrain J. Sci.*, 24(3) (2021) 43-49.

[4] IAEA Safety Glossary, “Terminology used in nuclear safety and radiation protection”, *Vienna* (2007).

[5] UNSCEAR Sources, “Effects of Ionizing Radiation”, United Nations (NY, 2000), 453-487.

[6] R.L. Clark, “US Environmental Protection Agency Radiation Protection Programs for Waste Management and Site Cleanup”, WM Symposia, 1628 E. Southern Avenue, Suite 9-332, Tempe, AZ 85282 (United States, 2008).

[7] IAEA, “Communications on nuclear radiation transport and waste safety”, Practical Handbook, (Vienna, 1999).

[8] N.F. Tawfiq, H.L. Mansour and M.S. Karim, “Natural radioactivity in soil samples for selected regions in Baghdad governorate”, *Int. J. Recent Res. Rev.*, 8(1) (2015) 1-7.

[9] M. Miglierini, “Detectors of radiation”, *React. Phys. Exper. J.*, 2(4) (2004) 1-67.

[10] Measurements, Scientific Committee 46-2 on Uranium Mining and Milling--Radiation Safety Programs, *Radiation Protection in the Mineral Extraction Industry: Recommendations of the National Council on Radiation Protection and Measurements*. No. 118. Ncrp, 1993.

[11] UNSCEAR Sources, “Effects of Ionizing Radiation”, United Nations (NY, 2000) 453-487.

[12] IAEA., “Communications on nuclear radiation transport and waste safety”, Practical handbook, Vienna, 1999. Angell, James Ross. "Practical perspectives on spent nuclear fuel transportation risks”, (2005).

Table (1) Specific effectiveness and risk factors for the studied ceramic, porcelain, and marble substitute samples

Sample	Samples name	Specific activity (Bq/kg)			HazardIndex (Bq/kg)		absorbed dose rate D(nGy/h	Annual effective dose (mSv/y)		I_γ (Bq/kg)	Ra (Bq/kg)
		^{238}U	^{232}Th	^{40}K	H_{IN}	H_{EX}		$AEDE_{IN}$	$AEDE_{OUT}$		
Y1	Ceramic Indian	33.2	16	40	0.25	0.16	26.67	0.03	0.13	0.41	59.16
Y2	Porcelain Indian	41.3	39.8	136	0.41	0.29	48.82	0.06	0.24	0.76	108.76
Y3	Ceramic Iranian	54.6	42.2	211	0.50	0.35	59.54	0.07	0.29	0.93	131.26
Y4	Porcelain Iranian	34.3	25.1	141	0.31	0.22	36.95	0.05	0.18	0.57	81.19
Y5	Marble alternative Turkish	7.8	1.1	300	0.13	0.10	18.26	0.02	0.09	0.28	35.67
Max		**54.6**	**42.2**	**300**	**0.5**	**0.35**	**59.54**	**0.07**	**0.29**	**0.93**	**131.26**
Min		**7.80**	**1.10**	**40.0**	**0.13**	**0.10**	**18.26**	**0.02**	**0.09**	**0.28**	**35.67**
Mean		**34.25**	**24.8**	**165.6**	**0.32**	**0.22**	**38.05**	**0.05**	**0.19**	**0.59**	**83.21**

Muayyad N. Fathula [1]
Azhaar A. Ali [2]
Malik H. Kheder [3]

[1] *Department of Electronic and Control Engineering/Techniques, Technical College, Northern Technical University, Kirkuk, IRAQ*
[2] *Department of Fuel and Energy, College of Oil and Gas Techniques Engineering, Northern Technical University, Kirkuk, IRAQ*
[3] *Department of Physics, College of Education, University of Al-Hamdaniya, Al-Hamdaniya, IRAQ*

The Optical and Structural Properties of Thermally Vaporized Composite Thin Films

In the current work, $CuAlSe_2$ alloys were fabricated by melting the stoichiometric weights of Cu, Al, and Se in a sealed quartz ampoule at a vacuum of about 3×10^{-2} mbar. The alloy is applied to a soda lime glass substrate, heated to various temperatures, and then thermally evaporated at a pressure of roughly 10^{-6} mbar. The thin layer has a thickness of 1200±100 Å. Thin films were polycrystalline with sphalerite structure but the bulk showed chalcopyrite structure throughout. An increase in the optical energy gap with substrate temperature and direct transitions in the thin layer were observed in the optical experiments. As the annealing period was raised to two hours, the films annealed at 200-400°C indicated an increase in the energy gap.

Keywords: $CuAlSe_2$; Thin films; Thermal evaporation; Optical energy gap
Received: 04 April 2024; **Revised:** 25 April 2024; **Accepted:** 01 May 2024

1. Introduction

The preparation technique of thin films from solid materials is one of the most crucial methods for studying their physical characteristics. Since thin films are used in the fabrication of integrated circuits like capacitors, resistors, and diodes as well as high-reflective mirrors and electromagnetic detectors, they are important to both advanced applications and solid-state physics research. One of the most significant and well-preferred uses of thin films is the fabrication of solar cells due to their low production cost as they require less production requirements than other energy sources [1]. Due to their high energy band gap (2.67eV) and tri-crystalline form in the orthogonal chalcopyrite structure, which is comparable to the structure of sapphirite, the $CuAlSe_2$ compound family has recently gained the interest of many researches. These compounds can be used in solar cells with efficiencies up to 11% and as electromagnetic radiation detectors too [2,3]. The group I-III-VI compounds, such as $CuAlSe_2$, $CulnSe_2$, and others, have great technical significance because of their remarkable optical sunlight absorption. The basic absorption edge of an ideal semiconductor is the region where photons with energy at least equal to the optical energy gap are employed to activate the valence band [4]. In crystalline and polycrystalline semiconductors, there are direct transitions, where electrons move from the top of the valence band to the bottom of the conduction band without changing their wave vector. The absorption coefficient of these transitions (α_{dir}) is related to the optical energy band gap (E_{gopt}) by the following relatioship

$$\alpha_{dir} = B(hv - E_{gopt})^{\frac{1}{2}} \qquad (1)$$

where B is a constant, and h is the energy of the incident photon

In crystalline and amorphous semiconductors, an indirect transition can occur when the electron wave vector is different before and after the transition. Transitions in semiconductors are unconstrained, however in crystalline semiconductors, the conservation of momentum principle imposes restrictions. The law of conservation of momentum is random because composition is unpredictable. The indirect absorption coefficient for each type of semiconductors is given if crystalline and polycrystalline semiconductors absorb photons to accomplish momentum conservation [3].

$$\alpha_{Ind} = \frac{c(hv - E_{gopt})}{e^{(E_{ph}/kT - s)}} \qquad (2)$$

where E_{ph} is the energy of the absorbed photon, E_{gopt} is the optical energy gap, and c is a constant

2. Experimental Part

The pure stoichiometric weights of the constituents (Cu:Al:Se = 1:2:3) were combined in a sealed quartz tube to produce the alloy. The quartz tube was evacuated using a rotary pump to 3×10^{-2} mbar getting an evacuated tightly-closed tube as a capsule with the three contents. A convection oven was gradually and gently heated to 1100°C and the tube was left there for three hours. To guarantee a homogenous molten mixture and complete fusion of the three elements, the oven is regularly stirred and set at 1100°C. After the capsule gradually cools to room temperature to extract the alloy ($CuAlSe_2$), some of its bulk is powdered and characterized by the x-ray diffraction (XRD) analysis to ensure the formation of the required alloy. A molybdenum (Mo) evaporation pot was continuously electrically charged and the evaporation chamber was evacuated to 10^{-6} mabr in order to perform the process at room temperature. This allowed for the growth of thin films by thermal evaporation using Balzer evaporation system. At a rate of 2 Å/s, the substance was evaporated. Consequently, the film preparation process was performed at room temperature. the film preparation process was carried out with variable deposition temperatures. The alloy was fabricated in the form of an ingot, which is then completely ground to produce usable alloy powder. A Phillips x-ray diffractomer was used in the scanning range (2θ) of 20°-70°, and the thin films prepared from the same alloy were examined using the same XRD apparatus. The film thickness was measured using a quartz crystal monitor and the optical interference method [5].

3. Results and Discussion

By comparing the Bragg's reflections of the deposited films and alloy powder with the American Standard for Testing Material (ASTM) cards, the composition of the alloy (bulk) was verified by analyzing the XRD patterns. It was found that these patterns belong to the compound $CuAlSe_2$. These patterns are displayed in Fig. (1) for substrate temperatures (T_s) of 150°C, 250°C, and 350°C.

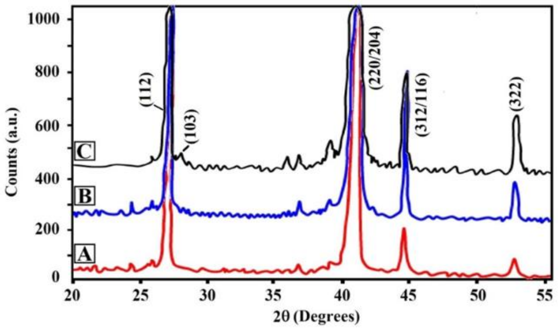

Fig. (1) XRD patterns of the samples deposited at different substrate temperatures (a) 150°C, (b) 250°C, and (c) 350°C

By increasing the substrate temperature, the composition of the prepared samples was sphalerite cubic with a lattice dimensions of a=5.0364Å and c=10.5440Å [6,7]. The substrate's composition is sphalerite cubic with a lattice dimension of a=5.0364Å, and by raising the temperature, the sample becomes much more porous (c=10.5440Å). The XRD patterns of the thin films annealed at 200°C or 400°C for two hours with thickness of 1200±1100Å are displayed in figures (2) and (3). These figures showed an increase in the intensity of some peaks and a decrease in the intensity of others when compared with Fig. (1) for unannealed films. The reason for this result is attributed to the growth of crystalline grains due to the coalescence of the grains with each other during the annealing process, which will lead to an increase in the diffraction intensity of some peaks, whereas the decrease in the intensity of some other peaks is due to the fact that this coalescence process will lead to the formation of separate islands (discrete islands), the distances between which are rather wide, especially when the thickness of the deposited film is small, and this is consistent with reference [9].

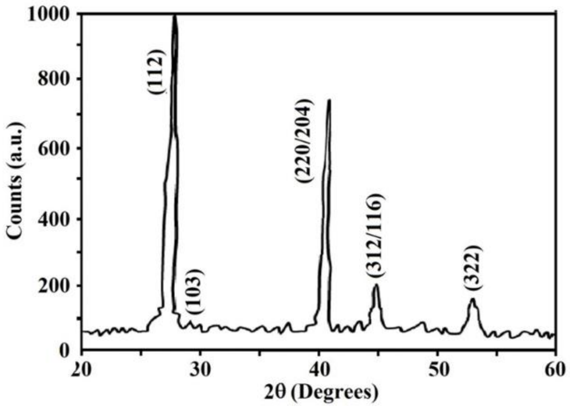

Fig. (2) XRD pattern of $CuAlS_2$ thin film annealed at 200°

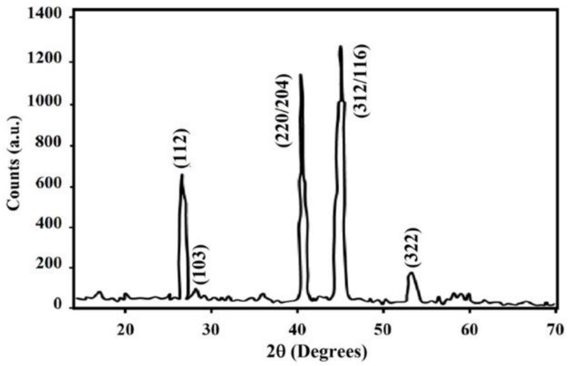

Fig. (3) XRD pattern of $CuAlS_2$ thin film annealed at 400°

The relationship between $(\alpha h\nu)^2$ and incident photon energy ($h\nu$) is depicted in Fig. (4). It is observed that the films prepared at high temperatures exhibit increased crystallization, as the composition of the $CuAlSe_2$ films is greatly influenced by the substrate temperature during film deposition. The activation energy of the deposited particles increases with the intensity and height of the Bragg's peaks. This energy is required for the deposited particles to reach sites on the substrate with the least energy loss in order to be more stable. As a result, during the evaporation process, the films prepared at temperatures 150-350°C exhibit phase transition from orthogonal chalcopyrite to cubic sphalerite. These findings agree with those of references [7,8], who found that deposition of thin films at lower temperatures results in the growth of films composed primarily of sphalerite. We observe that the $CuAlSe_2$ films are of direct transition, which is consistent with the results of references [4,10]. Also, the values of optical energy gap were in agreement with those of reference [4], who prepared $CuAlSe_2$ films at temperatures between 300 and 400°C using a spray deposition method. The rise in the number of crystalline grains and the increase in film crystallization were the reasons given for the increase in the optical energy gap with increasing deposition temperature. The absorption edge is obviously impacted by the annealing process. The effect of film annealing at 400°C for two hours is depicted in Fig. (5). The optical energy gap has changed to 2.65eV for films annealed at 200°C and 400°C, as shown in this figure. The annealing process removes structural flaws and increases the grain size, which explains the increase in absorbance due to the increase in granular boundaries. This is consistent with references [11-14].

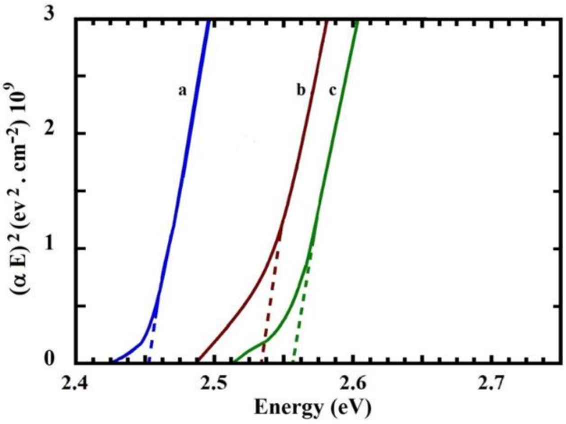

Fig. (4) Relationship of $(\alpha h\nu)^2$ with incident photon energy ($h\nu$) for thin films prepared at different substrate temperatures (a) 150°C, (b) 250°C, and (c) 350°C

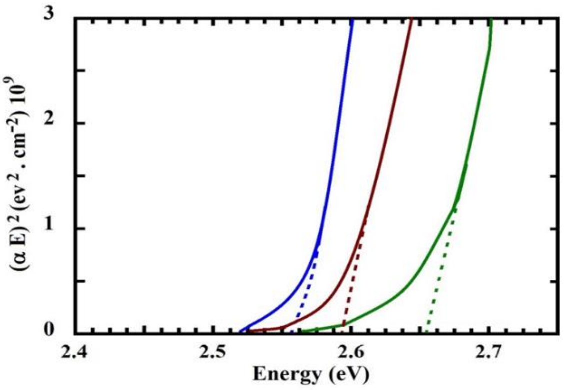

Fig. (5) Effect of annealing temperature on the energy band gap of the thin films: (a) not annealed, (b) annealed at 200°C, and (c) annealed at 400°C for two hours

4. Conclusion

The thin films deposited at high temperatures were found much more crystalline. During the evaporation process, the orthogonal chalcopyrite composition of the films formed at temperatures between 150 and 350°C has converted into cubic sphalerite, causing a phase transition. The growth of crystalline grains is a result of the grains coalescence during the annealing process. The absorption edge is clearly impacted by the annealing process, which decreases structural flaws and enlarges the grains.

Reference

[1] M. Strongin et al., “Thin Films”, in the Encyclopedia of Physics, R.G. Lerner and L. Trigg (eds.), VCH Publishers Inc. (NY, 1990) p.1276.

[2] S. Marsillac et al., “$CuAlSe_2$ Thin Films Obtained by Chalcogenization”, *J. Phys. III France*, 3 (1997) 2165-2196.

[3] S. Chichibu et al., “Low-Pressure metalorganic Chemical vapor deposition of $CuAlSe_2$”, *Jpn. J. Appl. Phys.*, 32 (1993) 139.

[4] C. Rincón et al., “Exergy analysis and development of flat plate solar collectors: A Review”, *IOP Conf. Ser.: Mater. Sci. Eng.*, 1253 (2022) 012009.

[5] M.N. Fathalla, “Study the effects of substrate temperature on the optical properties on the film $CuGaS_2$”, *J. Sci.*, 5(2) (1999) 32.

[6] R. Janam and D. Srivastava, “Solar energy materials”, *J. Solar Cells*, 24 (1989) 395.

[7] B. Tell et al., “Valence-band structure of $CuGa_xIn_{1-x}S_2$ alloys”, *Phys. Rev. B*, 10 (1974) 1748.

[8] H. Fujisawa et al., “Structural Properties of $CuInSe_2$ Thin Films for High Efficiency Solar Cells”, 10th Euro. Photovolt. Solar Ener. Conf., 8-12 April 1991, Lisbon, Purtogal.

[9] K.L. Chopra, **“Thin film phenomena”**, McGraw Hill (1989).

[10] T. Hama et al., “Structural properties of $CuInSe_2$ thin films for solar cell applications”, *Sol. Ener. Mater.*, 23(2-4) (1991) 380-387.

[11] K. Sugiyama, K. Mori and H. Miyake, “Epitaxial growth of $CuAlSe_2$ on $CuGaSe_2$ substrates”, *J. Cryst. Growth*, 113(3-4) (1991) 390-394.

[12] S. Chichibu et al., “$CuAlSe_2$ chalcopyrite epitaxial layers grown by low-pressure metalorganic chemical vapor deposition”, *J. Cryst. Growth*, 131(3-4) (1993) 551-559.

[13] S.H. You et al., “Growth and characterization of $CuAlSe_2(112)/GaAs(100)$ heteroepitaxial layers grown by hot wall epitaxy method”, *J. Cryst. Growth*, 290(1) (2006) 18-23.

[14] R.S. Kumar et al., “Structural studies of $CuAlSe_2$ and $CuAlS_2$ chalcopyrites at high pressures”, *J. Alloys Comp.*, 312(1-2) (2000) 4-8.

Muna Y. Slewa [1]
Fatin M. Hamam [2]
Rafal Z. Bahnam [3]

[1] *Laser and Photonics Research Center, Al Hamdaniya University, Nineveh, IRAQ*
[2] *Department of Basic Science, College of Dentistry, Mosul University, Nineveh, IRAQ*
[3] *Nineveh Education Directorate, Nineveh, IRAQ*

Evaluate the Output Radiation of Light Curing Sources in Dental Offices Across the Left Side of Nineveh Province

The research aims to evaluate the extent of the effect of optical processing sources and other factors on radiation outputs in dental clinics on the left side of Nineveh Governorate. Use a radiometer to measure the amount of radiation coming from polymerization devices. Radiation values were recorded at three locations in the clinics while the polymerase machines were operating. The mean radiation was determined after a short period of operation. The results showed that many dentists do not use curing lamps correctly and are not provided with sufficient information about the harm resulting from these devices and their impact on their health and the health of patients and the surrounding environment. Therefore, emphasis must be placed on appropriate education and training on the ideal light therapy technique. Improve photo curing performance at scale with detailed instructions on optimizing photo curing technology.

Keywords: Radiation; Light intensity; Light curing; Phototherapy units
Received: 04 April 2024; **Revised:** 25 April 2024; **Accepted:** 01 May 2024

1. Introduction

Radiation is a measure of the amount of radiation present in a given environment. The effective dose is the radiation dose to which tissues and the environment are exposed, taking into account the different biological effects resulting from different types of radiation. Blue light therapy has increased in popularity in the past few years. It is a painless, comfortable, non-invasive and highly effective biophysical treatment for many diseases [1,2]. There is no evidence that devices operating on mid-level blue light have harmful effects, but the potential effects of long-term cumulative exposure and dose-response effects are currently unknown[3].

A dental device used to polymerize composites based on photo curing, used to harden the composite material. There are four basic types of light sources for dental treatment: tungsten halogen, light-emitting diodes (LED), plasma arcs, and lasers. All these modules emit blue light in the wavelength range of 380-510 nm [4]. It emits appropriate light intensity. The consumption of light source and exposure to light radiation of materials can reduce the output intensity of the module. Therefore, it is recommended to evaluate the performance of optical processing units [5]. As the polymerization system ages, the light output diminishes due to prolonged use, resulting in decreased mechanical properties [6]. Blue light from therapy lights can cause eye damage; the risks depend on the radiation emitted, radiation geometry, exposure time, and degree of reflectance. The International Commission on Radiation Protection has stressed the application of special guidelines when exposed to blue light and its reflection from treatment lamps. Safety concerns are essential to avoid a work-related injury [3,7,8]. Regarding the principles of patient safety and radiation protection, the dentist must improve the treatment procedures. When exposed for a long time, the pulp and tissues of the tooth exposed to light are damaged [9]. On the contrary, applying low radiation or short treatment time leads to failure of the restoration. Although LED lamps are more commonly used compared to halogen lamps, the radiation of LED lamps decreases over time and causes technical failure. Therefore, curing lamps need constant maintenance and regular monitoring to control the beam coming from light sources [10].

This study aims to determine the amount of radiation resulting from light sources in dental clinics on the left side of the city of Nineveh and to determine the extent of its impact on the doctor, the patient, and the surrounding environment during and after treatment and to know the characteristics and correct usage of these devices.

2. Experimental Part

This study was conducted in the left side of Nineveh Governorate, and 45 private dental clinics were randomly selected, including 78 phototherapy devices that work to polymerize light-cured resin. The following information was collected: type of unit (LED and the QTH unit), age of the unit, and date of last maintenance. For the device, number of uses during the day, light output (light intensity in mW), and radiation from the clinic and units, use a radiation measuring device (1 pc An hour (μSv/h) to 150 mSv/h to measure the amount of radiation emitted by the polymerization devices in these offices.

Radiation values were recorded in three different locations in the clinics while the polymerization devices were operating. The average radiation emitted by each device was measured at different times. This was repeated three times and we obtained three readings from each LED unit and the QTH of all parameters, after which the average irradiance was determined after a short period of operation and all results were recorded in tables for analysis.

3. Results and Discussion

Tables (1) and (2) show the average radiation changes with the (age, last maintenance date, number of times used during the day, intensity) of the unit versus the number of curing units. The results showed that the radiation rate was not influenced by the last maintenance date of the unit, but the three variables (age, number of times used during the day, intensity) did have an effect on the unit versus the number of curing units. To maintain the safety of the patient and dentist and reduce radioactive contamination of the environment surrounding clinics, appropriate treatment units with appropriate characteristics must be chosen. This study highlights the importance of repeatedly evaluating the radiation rate of different treatment units used in dental clinics in the left side of Nineveh province. efficiency Continuous improvement in treatment unit technology may contribute to increased adoption by dentists of these curing units in clinics as they have numerous benefits such as narrow emission spectrum, specific energy density, improved treatment efficiency, durability, compact device form, and energy [11,12] and thus lead to a reduction in Emitted radiation is harmful to humans and the environment. When the intensity is low, the light radiation from light sources does not produce efficiency in treatment even if the treatment time is increased. However, the ray with a high intensity and the shortest treatment time produces high-precision mechanical properties, and increasing the treatment time can be an alternative to low intensity in some treatments, the fracture strength efficiency and hardness of the composite material increase [13-15].

This study demonstrated how easily errors can occur during the phototherapy process, leading to increased risks during restoration operations. However, photo curing performance can be extensively enhanced using detailed instructions on improving the technology used in photo-polymerization and detecting the resulting damage and radiation emitted by photo polymerization devices used in dental clinics and hospitals. This is a result of the incorrect use of some relevant features and understanding the technical knowledge in these devices and providing the necessary advice and guidance to the owners of these clinics, according to the survey data collected. The results of this study showed that many dentists do not use curing lamps correctly and are not provided with sufficient information about the harms resulting from these devices and their impact on their health and the health of patients, as well as their impact on the surrounding environment. To their clinics. Therefore, emphasis should be placed on appropriate education and training on the ideal phototherapy technique in all dental schools and even the inclusion of all dentists in special and periodic courses to understand the problems related to phototherapy.

Table (1) Average radiation changes with: Age and last maintenance date (c) the no. of times was used during the day (d) the intensity of the unit versus no. of curing unit

average Radiation μSv/h	Age of the unit (years)	Number of QTH lights (n=26)	Number of LED lights (n=52)
0.12	<1	6	19
0.15	1-4	9	24
0.18	>4	11	9
Average Radiation (μSv/h)	Last maintenance date of the unit (months)	Number of QTH lights (n=26)	Number of LED lights (n=52)
0.22	no	9	22
0.17	<3	2	3
0.20	3-6	6	5
0.15	6-12	5	18
0.21	>12	4	4

Table (2) Average radiation changes with: the no. of times was used during the day and the intensity of the unit versus no. of curing unit

Average Radiation (μSv/h)	The number of times the unit was used during the day	Number of QTH lights (n=26)	Number of LED lights (n=52)
0.17	<5	13	19
0.21	5-10	7	12
0.24	>10	6	21
Average Radiation (μSv/h)	Intensity (mW/cm^2)	Type of QTH lights (n=26)	Type of LED lights (n=52)
0.16	<250	15	17
0.18	250-1000	7	25
0.23	1000-1500	4	10

4. Conclusion

The typical treatment times with radioactive light were addressed, in addition to a typical number of daily treatments as well as maintenance, the danger of these devices to the surrounding people and the environment may exceed the limits, because dentists did not protect themselves and their patients adequately from these devices Requires the operator to know the characteristics and correct usage of these devices.

References

[1] F. Yoshino and A. Yoshida, “Effects of blue-light irradiation during dental treatment”, *Japanese Dent. Sci. Rev.*, 54(4) (2018) 160-168.

[2] M.Y. Slewa et al., “Influence of Light Intensity and Irradiation Time on Efficacy of Polymerization Temperature Using Diode Laser and Light-Emitting Diodes”, *Iraqi J. Appl. Phys.*, 19(3B) (2023) 35-38.

[3] A. Gregoire et al., “Blue light exposure: ocular hazards and prevention a narrative reviews”, *Ophthalmol. Therapy*, 12(2) (2023) 755-788.

[4] K. Mild, R. Lundström and J. Wilén, “Non-ionizing radiation in Swedish health care—exposure and safety aspects”, *Int. J. Enviro. Res. Public Health*, 16(7) (2019) 1186.

[5] R. Price, J. Ferracane and A. Shortall, “Light-curing units: a review of what we need to know”, *J. Dent. Res.*, 94(9) (2015) 1179-1186.

[6] S. Huson et al., “A genetic study of von Recklinghausen neurofibromatosis in south east Wales. I. Prevalence, fitness, mutation rate, and effect of parental transmission on severity”, *J. Med. Genet.*, 26(11) (1989) 704-711.

[7] World Health Organization (WHO), Ultraviolet radiation: an authoritative scientific review of environmental and health effects of UV, with reference to global ozone layer depletion. 1994.

[8] M. Rajeshree, S. Naidoo and J. Van, “The prevalence of occupational health-related problems in dentistry: A review of the literature”, *J. Occup. Health*, 60(2) (2018) 111-125.

[9] K. Neal and B. Kusnoto, “Soft-tissue lasers in orthodontics: an overview”, *Amer. J. Orthodon. Dent Facial Orthoped.*, 133(4) (2008) S110-S114.

[10] S. Kopperud et al., “Light curing procedures–performance, knowledge level and safety awareness among dentists”, *J. Dent.*, 58 (2017) 67-73.

[11] Y. Wedad, “The influence of temperature on the efficacy of polymerization of composite resin”, *J. Contemp. Dent. Pract.*, 8(6) (2007) 9-16.

[12] D. Jandt and W. Mills, “A brief history of LED photopolymerization”, *Dent. Mater.*, 29(6) (2013) 605-617.

[13] F. Rueggeberg et al., “A predictive model for the polymerization of photo-activated resin composites”, *Int. J. Prosthod.*, 7(2) (1994) 159-166.

[14] M. Miyazaki et al., “Effect of light exposure on fracture toughness and flexual strength of light-cured composites”, *J. Esthetic Restor. Dent.*, 11(6) (1999) 342.

[15] K. Hinoura, M. Miyazaki and H. Onose, “Effect of irradiation time to light-cured resin composite on dentin bond strength”, *Amer. J. Dent.*, 4(6) (1991) 273-276.

Aynoor B. Kamal [1]
Zainab Q. Mosa [1]
Abeer N. Kadhim [1]
Islam N. Yousif [2]

[1] *Department of Physics, College of Education for Women, University of Kirkuk, Kirkuk IRAQ*
[2] *Department of Physics, College of Education for Pure Science, University of Al-Hamdaniya, Nineveh, IRAQ*

A Study of Optical Properties of Tetraborate Glass Containing MgO

Glasses with compositions (65%) $Na_2B_4O_7$ – (35-x)%V_2O_5 – (x)% MgO, where x=10, 15, 20, or 25, is were produced using conventional melt quenching technique. The shifting rate of absorption edge position, band tails energy (E_o) and optical band energy (E_{opt}) were investigated. The results showed all the values of E_o and E_{opt} for the glass compound can be possibly treated and their characteristics can be compared with the values that correspond to their identical semiconductors.

Keywords: Band tails energy; Tetraborate Glass; MgO; Optical band energy
Received: 04 April 2024; **Revised:** 25 April 2024; **Accepted:** 01 May 2024

1. Introduction

Tetraborate glasses are a class of glasses that are technologically important and play an important role in various physical applications [1]. Optical absorption in solids occurs by several different mechanical processes, all of which involve the interaction between incident rays and the dipole moments of the material and thus the transfer of energy. Absorption likely occurs as a result of internal transitions between shell (D) electrons in transition metals. Optical absorption can also be created by transferring electrons from a neighboring atom to transition metal ions and vice versa [2].

Measurements of the dimensional optical absorption coefficient, in particular near the main absorption edge, have enhanced the study of optically induced electronic transitions, and also provide us with some insights into the beam structure and gap energy of crystalline and amorphous materials [2].

The optical absorption coefficient near the absorption edge in a number of amorphous semiconductors and insulators shows an exponential dependence on photon energy. It is subject to a quasi-experimental relationship [3]:

$$\alpha(\omega) = \alpha_0 \exp\,[\hbar\omega/E_0] \qquad (1)$$

Here, $\alpha(\omega)$ represents the absorption coefficient, ω the angular frequency of incident radiation, α_0 is constant, and E_0 represents the energy of the beam tails for localized states. The optical absorption coefficient can be calculated by the following relation [4]:

$$\alpha(\omega) = \frac{1}{d}\ln\left(\frac{I_0}{I_t}\right) \qquad (2)$$

where I_0 and I_t represent the intensity of the incident and penetrating rays, respectively and d represents the thickness of the sample under study. The optical gap energy (E_{opt}) in most semiconductors has been calculated using the following relationship [5]:

$$\alpha(\omega) = A\frac{(\hbar\omega - E_{opt})^r}{\hbar\omega} \qquad (3)$$

where A is a constant, ħω represents the photon energy, the exponent (r) is a coefficient depends on the type of emission or electronic transition responsible for absorption. The value of 1/2 represents the direct emission allowed, the value of 2 represents the permissible indirect emission, the value of 1/3 represents the direct emission present, while the value of 3 represents the indirect emission observed [6]

Borate glasses have been studied in recent years as there is a number of published research on how to prepare glass. Identify and identify the characteristics of these glassware through their compositions [7,8].

In this study, a number of laboratory experiments were conducted to study the optical gap energy, the beamwidth energy of the localized states, the refractive index, density and molar volume as functions of increasing the percentage of MgO oxide in the network of the glassware under investigation, as well as studying the infrared absorption spectra and knowing the beam positions and analyze it.

In addition, density of material, the most important to determining the mechanical and chemical properties, it is involved in determining the thermal and electrical insulation properties of materials [9].

2. Experimental Part

Glass aggregates have been prepared [65% $Na_2B_4O_7$ – (35-x)% V_2O_5 – x% MgO]. The values of x=10, 15, 20, and 25 were taken each time for oxide MgO. Highly-purified chemicals were used in the method of cooling the molten material suddenly and at room temperature. Each group was prepared after being weighed and mixed together in an alumina crucible, mixing using an alumina rod and melting using an electric furnace with a maximum temperature of 1200°C. Each sample was placed in a furnace installed at a temperature of 200°C for one hour to reduce volatile substances and then the sample was introduced into the melting furnace for one hour. It was observed through the experiment that the fusion of the samples of these group is in the range of 1000-900°C based on the ratio of oxide (MgO) where the higher its proportions in the glass lattice, the higher the melting point than 900°C. Finally, the molten material is poured onto a mold designed for this purpose to obtain a disc between 2 and 4 mm.

3. Results and Discussion

Figure (1) shows the optical absorption spectra of the glass compound $Na_2B_4O_7$–MgO as a function of the wavelength and within the wavelength range 190-900nm. It is clear that the main absorption edge deviates slightly towards the short wavelengths as the amount of MgO in the compound increases.

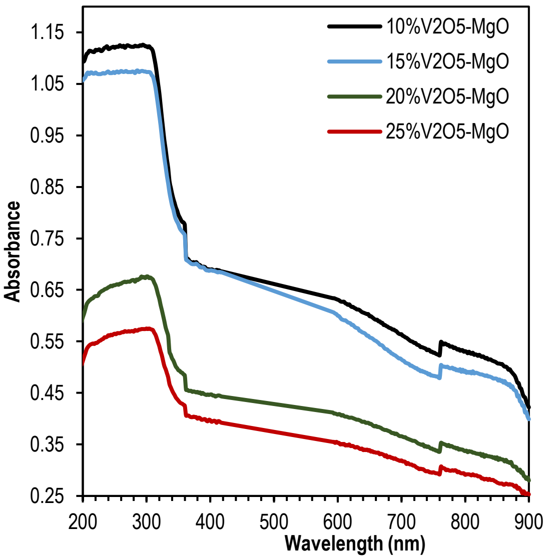

Fig. (1) Optical absorption spectra of the prepared glass as a function of the wavelength

Figure (2) shows the graph between $(\hbar\omega\alpha)^{1/2}$ and the energy of the incident photon where it is possible to calculate the optical gap energy from the same figure and the values of the optical gap energies (E_{opt}) have been drawn as a function of the oxide concentrations (MgO) in the glass compound under consideration as shown in Fig. (3). The log change of the optical absorption coefficient $\ln[\omega(\alpha)]$ as a function of the energy of the incident photon ($\hbar\omega$) is shown in Fig. (4) and from the diagram the energy of the beam tail is calculated using Eq. (1) as shown in Fig. (5).

Table (1) shows beam values as an optical function (E_{opt}), beam tail energy for localized states (E_o) and theoretically calculated values of refractive index with increasing oxide (MgO).

Table (1) Optical gap energy values, beam tail and refractive index of glass compound

MgO content (%)	E_o	E_{opt}
10%	0.998	3.352
15%	0.862	3.252
20%	0.771	3.058
25%	0.659	2.957

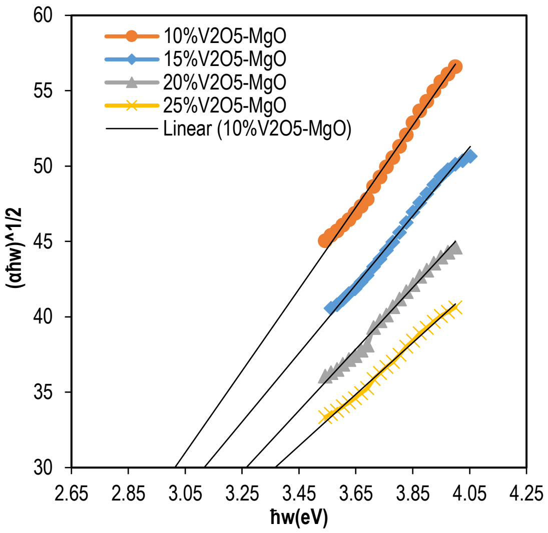

Fig. (2) Variation of $(\alpha\hbar\omega)^{1/2}$ as a function of the photon energy ($\hbar\omega$) for the prepared glass

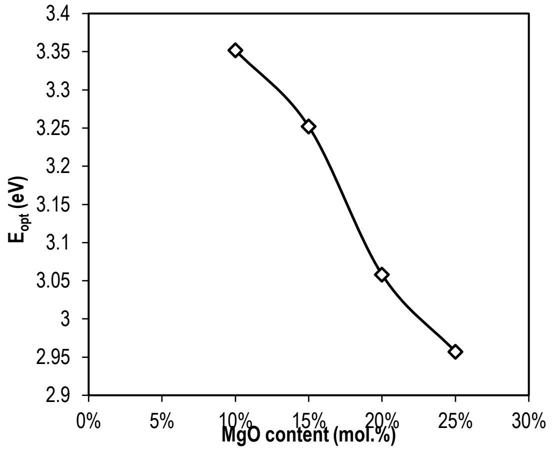

Fig. (3) The optical gap energy for the prepared glass as a function of the MgO content

4. Conclusions

The increase in density in the crystal structure of the models under investigation is closely related to the change in the composition of these glasses caused by the decrease in the atomic interval, which in turn produces tight and dense semiconductor glass. It is clear that the results of the optical absorption edge analysis of all glass lattices under research are well consistent with the theory of Mott & Davis [2] and this confirms with conclusive evidence the occurrence of indirect emission between beams in these glass aggregates.

It was found that the optical absorption edge deviates towards the longest wavelength in all binary glass aggregates with increasing concentration of MgO in all the glasses. This is likely due to a change in the amount of unbridged oxygen ion with an increase in the ions of the element Mg. A decrease in the energy of the optical gap with an increase in the concentration of the amount of oxides leads to an increase in the degree of loss of order (disorder) in these glasses and in turn supports the theory of Mott & Davis [2].

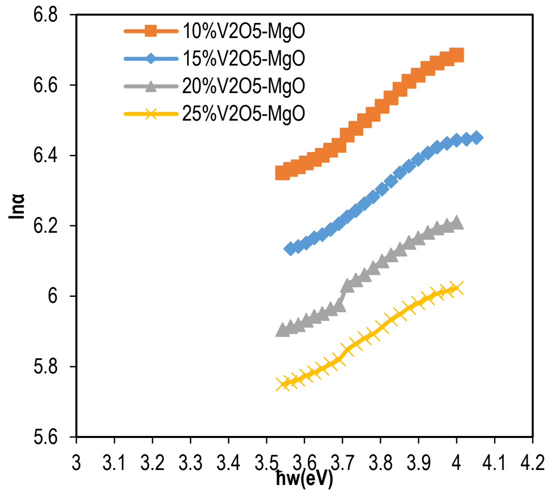

Fig. (4) Variation of Lnα for the prepared glass as a function of incident photon energy

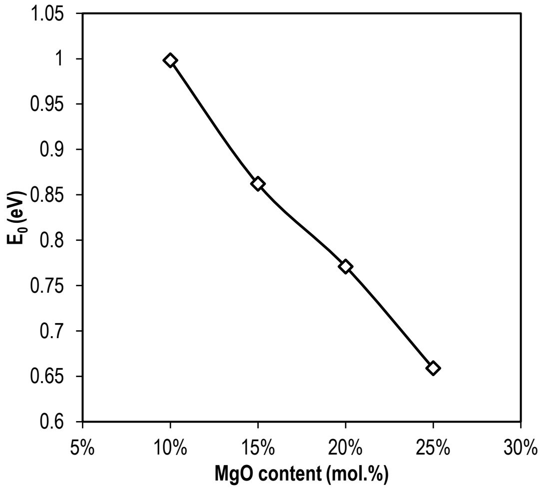

Fig. (5) The beam tail energy for the prepared glass as a function of the MgO content

References

[1] C. Gautam, A.K. Yadav and A.K. Singh, “A review on infrared spectroscopy of borate glasses with effects of different additives”, *ISRN Ceram.*, 2012 (2012) 1-17.

[2] N.F. Mott and E.A. Davies, **“Electronic processes in non-crystalline materials**”, Oxford University Press (2012).

[3] F. Urbach, “The long-wavelength edge of photographic sensitivity and of the electronic absorption of solids”, *Phys. Rev.*, 92(5) (1953) 1324.

[4] P. Chimalawong et al., “Optical properties of the SiO_2-Na_2O-CaO-Nd_2O_3 glasses”, *Amer. J. Appl. Sci.*, 7(4) (2010) 584-589.

[5] B. Eraiah and S.G. Bhat, “Optical properties of samarium doped zinc–phosphate glasses”, *J. Phys. Chem. Solids*, 68(4) (2007) 581-585.

[6] S.K.J. Al-Ani and A.A. Higazy, “Study of optical absorption edges in MgO-P_2O_5 glasses”, *J. Mater. Sci.*, 26 (1991) 3670-3674.

[7] V. Kundu et al., “Effect of V_2O_5 on structural, physical and electrical properties of bismuth borate glasses”, *J. Optoelectron. Adv. Mater.*, 10(10) (2008) 2765-2770.

[8] W.J. Gawande, S.S. Yawale and S.P. Yawale, “Study of physical and electrical properties of Cuo-MnO_2-B_2O_3 Glasses”, *Int. Res. J. Sci. Eng.*, 3(3) (2015) 77-83.

[9] E.J. Salih et al., “Study of some of the physical variables of a metal-based system using the powder method”, *IOP J. Phys.: Conf. Ser.*, 1999(1) (2021).

[10] M.A. Hassan, *2nd Sci. Conf. Wassit Univ.* (2009) 756-784.

[11] S.N.S. Yaacob et al., “The Polarizability and Optical Characteristics of Zinc Phosphate Glasses Doped Terbium Embedded with Copper Oxide Nanoparticles”, *Solid State Phenom.*, 290 (2019) 35-40.

[12] T. Tasheva and V. Dimitrov, “Synthesis, optical properties and structure of NiO-BaO-V_2O_5 glasses", *J. Chem. Technol. Metall.*, 52(2) (2017) 369-378.

Muayyad N. Fathula [1]
Azhaar A. Ali [2]
Siham J. Al-Faris [3]
Rajaa A. Basheer [3]

[1] *Department of Electronic and Control Engineering/Techniques, Technical College, Northern Technical University, Kirkuk, IRAQ*
[2] *Department of Fuel and Energy, College of Oil and Gas Techniques Engineering, North Technical University, Kirkuk, IRAQ*
[3] *Department of Physics, College of Education for Pure Sciences, University of Al-Hamdaniya, Al-Hamdaniya, IRAQ*

The Influence of Bi on Compounds on Their Structural and Electrical Properties

The high-temperature superconductivity of $Tl_{2-x}Bi_xBa_2Ca_2Cu_3O_{10}$ and its electrical resistivity were measured at temperatures ranging from 90 to 330K. According to the findings, when the Bi ions concentration is increased from 0.1 to 0.5, the zero resistivity's critical temperature rises from 121 to 146K. The x-ray diffraction has also been used to analyze the structure of the $Tl_2Bi_2Ba_2Ca_2Cu_3O_{10}$ compound. The analysis revealed that the compound structure type is tetragonal with a=b=5.36Å and c=36.09Å. In addition, the value of the c-axis increases to 37.8Å when the Bi ions concentration is elevated to 0.5.

Keywords: Compound structure; Critical temperature; XRD; superconductivity
Received: 04 April 2024; **Revised:** 25 April 2024; **Accepted:** 01 May 2024

1. Introduction

Since the discovery of mercury, there has been a great deal of interest in extremely high-temperature (HT) superconductivity in copper oxide. Initially, the first participant in the $HgBaCa_{n-1}Cu_nO_{2(n+2+8)}$ series has n=1, 2, 3, 4, and 5 and crucial temperatures Tc=94, 128, 135, 116, and 96 K, respectively [1,2]. Two more comparable HT superconductivity series with Tc>100K received undue attention. The first was the super conductivity about 105 K shown by the Bi-Sr-Ca-Cu-O compounds [3,4]. The systems shown above proved that the Tc values of the structural formulation superconductors $Bi_2Sr_2Ca_2Cu_3O_{10}$, $Bi_2Sr_2Ca_2Cu_3O_8$, and $Bi_2Sr_2Ca_2Cu_3O_6$ are 120, 110, and 108.5 K, respectively [5]. On the other hand, second series TI-Ba-Ca-Cu-O compound demonstrated superconductivity above 100 K [6]. The greater Tc of this series of superconductors gives them infinite X significance. The Tc values of $Tl_2Bi_2Ba_2Ca_2Cu_3O_6$, $Tl_2Bi_2Ba_2Ca_2Cu_3O_8$, and $Tl_2Bi_2Ba_2Ca_2Cu_3O_{10}$ compounds were found to be 80, 110, and 125 K, respectively. There are other series that exhibit superconductivity above 130 K when Hg is used in place of Tl. More investigation was done on the Hg-Ba-Ca-Cu-O combination, which resulted in increased Tc at 150K when subjected to pressures as high as 150 bar [7]. Given that the primary determinants of site tenancy in replacement studies are the valence state ionic radius and the ionic radius coordination number. The replacement effects in these materials have received a lot of interest in HTSC studies [8,9]. Here are some key points that highlight the significance of the substitutional results: (a) A number of replacement investigations lead to an increase in the materials' low Tc. New superconductors discovered at HT (b). (c) Can enable a more thorough comprehension of the HT superconductivity mechanism. Nearly all high Tc systems are made of co-based materials, which have two key characteristics: (a) A crystal structure that is partially or entirely orthorhombic or tetragonal with a high C-parameter value. (b) The cause of HT superconductivity in these systems is thought to be the very conducting 2D Cu-O layers.

The aim of this work is to investigate the effects of Bi substitution instead of Tl on the electrical resistivity in the HT and Tc of $Tl_{2-x}Bi_xBa_2Ca_2Cu_3O_{10}$ superconductors.

2. Experimental Part

Samples of HT superconducting technology were produced using solid state reaction technology of the $Tl_{2-x}Bi_xBa_2Ca_2Cu_3O_{10}$ compounds (where x=0, 0.1, 0.2, 0.3, 0.4, and 0.5). The correct stoichiometric ratio of Ba, Ca, and Cu is 2:2:3. With the help of the isopropanol fluid, these ingredients were combined, ground in a manually operated gate mortar, and thoroughly dried for 20 minutes at 60°C. For 12 hours, the appropriate mixture of these oxide powders was heated in an electric resistance furnace to 950°C. The resulting mixture was then further ground and compressed into pellets with a radius of 1.4 cm and a thickness of 0.1 cm while operating at a pressure of 3 tons per square centimeter. For 30 hours, the pellets were sintered in an oxygen gas stream at a flow rate of 1.1 liters per hour at 850°C. After that, the pellets were cooled at a rate of 30°C per hour to reach room temperature. Conventional four-probe method used to find the electrical resistance. Using conductive silver paste, the samples and probes were connected by thin copper wires. The samples are being cooled to a low temperature using a closed cycle helium refrigerator. Those samples were subjected to room-temperature x-ray diffractometer (XRD) analysis utilizing a Phillips device equipped with a Fe K-α source and a wavelength 1.937Å.

3. Results and Discussion

The expected Tc_0 values along with the resistance drop's midpoint temperature displayed in table (1). The electrical resistivity of $Tl_{2-x}Bi_xBa_2Ca_2Cu_3O_{10}$ compounds was evaluated in response to temperature for x = 0, 0.1, 0.2, 0.3, 0.4, and 0.5, as shown in Fig. (1). Using the MATLAB computer language, the lattice parameters values of the a, b, and c were determined and are provided in table (2). The transition temperature of superconducting (Tc_0) is the temperature at which the sample resistance drops to zero. The sample that yielded the ideal Tc_0 value was the one when x=0.5. The fluctuations in the superconducting electron carrier density are responsible for the rise in Tc values seen in those samples. Moreover, the normal spacing between the Bi ions in the network matrix coherence length in the c-direction and at the a-b planes is impacted by partial replacement of Bi rather than TI. These effects facilitate easier movement in the direction of a to b for the 2D Cu-O planes, which govern HTSC. Higher Tc values must follow from a fractional substitution of Bi in TI. Furthermore, the resistively temperature curves' slope is not much altered, even if increasing the x-value to 8.5 seems to have a large effect on Tc values. These patterns suggest a transition mechanism based on electron-phonon interaction. Increases in Tc values resulting from partial substitution of Bi in TI-Ba-Ca-Cu-O compounds have been associated with changes in the superconducting electron carrier density. These changes change the usual ion spacing in the network matrix, with the coherence length of the a-b planes in the c-direction aiding simpler movement in the Cu-O planes and increasing Tc values [11].

Table (2) Values of lattice parameters a, b, and c were calculated using the MATLAB programming language

Sample composition	Lattice parameters (Å)			Tc (K)	
	a	b	c	Tc_o	Tc_m
$Tl_2Bi_2Ba_2Ca_2Cu_3O_{10}$				125	125
$Tl_{1.9}Bi_{0.1}Ba_2Ca_2Cu_3O_{10}$	5.361	5.361	36.12	121	136
$Tl_{1.8}Bi_{0.2}Ba_2Ca_2Cu_3O_{10}$	5.361	5.361	36.22	129	145
$Tl_{1.7}Bi_{0.3}Ba_2Ca_2Cu_3O_{10}$	5.362	5.362	36.56	133	147
$Tl_{1.6}Bi_{0.4}Ba_2Ca_2Cu_3O_{10}$	5.361	5.361	37.67	137	149
$Tl_{1.5}Bi_{0.5}Ba_2Ca_2Cu_3O_{10}$	5.361	5.361	37.80	146	156

According to this, increasing Tl with Bi results in higher c-values, which makes electron mobility across the Cu-O planes of those compounds easier. At 0.5 Bi in Tl, it seems that the substitution worked. For the compound $Tl_{2-x}Bi_xBa_2Ca_2Cu_3O_{10}$, adding more than 0.5 Bi concentration causes the Tc values to drop towards 133 K [12]. Table (2) displays the values of the a, b, and c parameters. As the Bi concentration grows, so does the length of the c-axis in comparison to the lengths of the other cell sides. The findings are interpreted as follows. There will be few opportunities because the TI roles are not entirely filled. According to the first idea, cations such as Bi can reside in such regions, increasing HT superconductivity. The c-axis values reported in this study are in good agreement with the findings for the Bi-2223 compounds, which demonstrate a linear increase in Tc values with compound-level Pb concentration. Results of partial substitutions of Sn, Eu, and Zn in Ba, Sm, and Cu metals for the crystal structure, transition temperature, and oxygen concentration of the HT $SmBa_2Cu_3O_7$ superconductor [13-15]. These results showed that the limited replacement of Eu and Sm metals increased the Tc from 88 to 107 K without changing the type crystal structure. In contrast, the limited replacement of Sn and Ba metals resulted in lower Tc values and a different shape of the crystal structure. The orthorhombicity and superconductivity of the structure were lost when Cu was replaced with Zn metal.

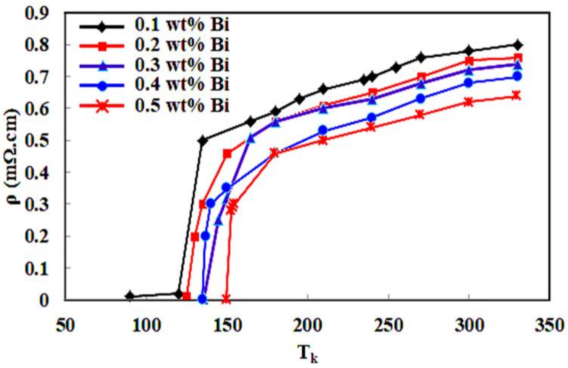

Fig. (1) The temperature dependence of electrical resistivity for varying Bi wt.%

4. Conclusion

High-temperature $Tl_{2-x}Bi_xBa_2Ca_2Cu_3O_{10}$ superconductors have had their electrical resistivity tested in the 90-330 K temperature range. The following points serve as a summary of the primary findings. As the concentration of Bi rose from zero to 0.5, the critical temperature rose from 121 to 146 K. The lattice parameters of the crystal structure, a=b=5.36Å and c=36.09Å, were determined to be tetragonal. When the c-axis is raised to 0.5 elevation, its magnitude rises to 37.8Å.

References

[1] R. Wesche, “**Physical properties of high-temperature superconductors**”, John Wiley & Sons (2015) 87-97.

[2] R. Han, “**Superconductivity Centennial**”, World Scientific, 6 (2018) 13-19.

[3] S.J. Fathi, “Effect of Nano-sized ZnO on electrical & structural properties of high temperature $Tl_{2-x}Hg_xBa_2Ca_2Cu_3O_{10-\delta}$ superconductors”, *Adv. Mater. Res.*, 925 (2014) 436-441.

[4] C. Chu, L. Deng and B. Lv, “Hole-doped cuprate high temperature superconductors”, *Physica C: Supercond. Appl.*, 514 (2015) 290-313.

[5] R. Hazen, “**Perovskites**”, Scientific American, 258 (1988) 74-81.

[6] F. Masinde, “Field Dependence of The Properties of High-Temperature Superconductors”, PhD dissert., University of Eldoret (2016).

[7] T. Pereg-Barnea, “Phenomena in unconventional superconductivity: d-wave quasiparticles, pseudogap, QED_3 theory and Andreev edge states”, PhD dissert., University of British Columbia (2005).

[8] Y. Zhuo et al., “Creating a green-emitting phosphor through selective rare-earth site preference in $NaBaB_9O_{15}:Eu^{2+}$”, *Chem. Mater.*, 33 (2021) 3304-3311.

[9] L. Chen et al., “Readiness level of sodium- ion battery technology: a materials review”, *Adv. Sustain. Syst.*, 2 (2018) 1700153.

[10] M. Sadovskii, “Superconductivity and localization”, *Phys. Rep.*, 282 (1997) 225-348.

[11] M. Gürsul et al., “Significant enhancement of superconducting performances of Bi-2212 fibers through combined sodium substitution and LFZ process”, *J. Mater. Sci.: Mater. Electron.*, 32 (2021) 17686-17699.

[12] M. Paranthaman and A. Manthiram, “**Chemical Characterization of Thallium Cuprate Superconductors**”, in Thallium-Based High-Temperature Superconductors, CRC Press (2020) 147-176.

[13] Q. Guo, “Understanding and control of the metallic state in epitaxial $NdNiO_3$”, PhD dissert., University of Groningen (2021).

[14] B. Wang et al., “Single crystal growth of relaxor ferroelectric $Ba_2PrFeNb_4O_{15}$ by the optical floating zone method”, *Update*, 19 (2019) 7249-7256.

[15] R. Tilley, “**Perovskites structure-property relationships**”, John Wiley & Sons (2016) 258-261.

Table (1) Lattice parameter values as the Bi concentration increases

T (K)	ρ (mΩ.cm) x=0.1	T (K)	ρ (mΩ.cm) x=0.2	T (K)	ρ (mΩ.cm) x=0.3	T (K)	ρ (mΩ.cm) x=0.4	T (K)	ρ (mΩ.cm) x=0.5
330	0.8	330	0.76	330	0.74	330	0.7	330	0.64
300	0.78	300	0.75	300	0.72	300	0.68	300	0.62
270	0.76	270	0.7	270	0.68	270	0.63	270	0.58
255	0.73	240	0.65	240	0.63	240	0.57	240	0.54
240	0.7	210	0.61	210	0.60	210	0.53	210	0.5
235	0.69	180	0.56	180	0.56	180	0.46	180	0.46
210	0.66	150	0.46	165	0.51	150	0.35	155	0.3
195	0.63	135	0.3	150	0.32	140	0.3	154	0.29
180	0.59	130	0.2	145	0.25	137	0.2	153	0.28
165	0.56	125	0.01	136	0.00	135	0.0	150	0
135	0.5								
120	0.02								
90	0.01								

IRAQI JOURNAL OF APPLIED PHYSICS

Volume (20) Issue (3) July 2024

CONTENTS

Contents